

A Search for Radio Pulsars: from Millisecond Pulsars to Magnetars

Lina Levin

Presented in fulfillment of the requirements
of the degree of Doctor of Philosophy

June 2012

Faculty of Information and Communication Technology
Swinburne University

Abstract

The southern High Time Resolution Universe (HTRU) survey for pulsars and fast transients is currently underway at the Parkes Radio Telescope in Australia. In this thesis we describe a search for pulsars in the intermediate latitude part (medlat) of this survey, which is now complete. With higher time and frequency resolution than previous surveys carried out in this region of the sky, the medlat survey was more sensitive to millisecond pulsars (MSPs) at higher distances from the Sun. We discuss the survey strategy and set up, the instrumentation used to collect data as well as the processing pipeline and search techniques used to discover pulsars in the data set. In total this survey has returned 104 newly discovered pulsars, including 26 MSPs. Some of these pulsars are particularly interesting, including an MSP with a Jupiter-mass companion, an eclipsing binary pulsar and an MSP suitable for the Pulsar Timing Array projects.

A major find from the HTRU medlat survey was the radio magnetar PSR J1622–4950, which is described in detail in this thesis. Magnetars are slowly rotating neutron stars with extremely large surface magnetic field strengths, that occasionally undergo large outbursts of radiation. PSR J1622–4950 is one of 23 known magnetars and one of only 3 to have confirmed radio pulsations. The radio magnetars differ from ordinary rotation-powered pulsars e.g. by their highly variable flux densities, changing pulse profiles and flat radio spectrum. Evidence of a decrease by a factor of ~ 2 over the last 700 days in the peak flux density of PSR J1622–4950 is observed, indicating a transient nature. A fit of the rotating vector model to the position angle of the linear polarisation of the emission from the magnetar suggests a nearly aligned geometry of the pulsar.

Finally, we have used the large number of MSPs discovered in the HTRU medlat survey to carry out a population study of MSPs in the Galaxy. Pulsar population studies make use of the observed properties of the known pulsar sample to derive the numbers and properties of the underlying Galactic population of pulsars. We have performed a large-scale flux-limited pulsar population synthesis study. At the derived best estimate of the scale height, $z = 500 \text{ pc}$, the simulation implies an underlying population of $\sim 150,000$ MSPs with luminosities above $L_{1400} = 0.07 \text{ mJy kpc}^2$. The results from the simulation predict that the two remaining parts of the southern HTRU survey will discover ~ 85 previously unknown MSPs.

Acknowledgements

The preparation and writing of this thesis has been an amazing journey, and many people have been a great help and support to me during my PhD.

Firstly, I owe a huge thanks to my supervisors: Matthew Bailes, Simon Johnston, Willem van Straten and Michael Kramer. Thank you for teaching me about pulsars and astronomy, for pushing and encouraging me to always do better, but most of all for believing in me and my ability to become a good scientist and researcher.

Matthew, thank you for taking the time to sit down with me and teach me all from basic programming and scripting to complicated astronomy principles and instrumentation. Your contagious enthusiasm for pulsars and pulsar searching helped me make the decision to move across the world to do a PhD and I haven't regretted it for a second. You have shared my excitement for every new discovery and good looking candidate - I am always going to hear your voice in my head shouting "Pulsar!" as a nice looking pdmp plot of a pulsar pops up on my screen.

Simon, you have been a great support to me, especially during the last year. Our weekly meetings have helped me tremendously to get my work and ideas sorted, and to discuss any issue that has come up straight away. Thank you for pushing me to set deadlines and also for pushing me to keep them! Willem, your sense of detail and your ability to dig down to the bottom of every problem gives me faith in research. Thank you for teaching me the secrets of polarisation and the subtleties of the English language. Michael, thank you for inviting me to visit you in Bonn and for helping me with both survey and magnetar related issues.

I am very grateful to have been part of the awesome pulsar gang at Swinburne: Matthew, Willem, Ramesh, Andrew, Jonathon, Sarah, Stefan, Paul and Ben. Thank you for always being around to help out with anything anytime it might come up or just for a coffee and a chat!

I have also been very lucky to be backed up by the great HTRU team. Thank you all for sharing excitement over new discoveries, for finding pulsars, for confirming pulsars, for solving pulsars and for making long observing hours a lot easier. In particular, I would like to thank the people that I have worked closer together with: Mike (thank you for always helping me out with anything I needed, through countless numbers of emails with questions and discussions), Sam, Sabrina, Marta, Andrea, Ben and Cherry. Keep up the good work!

To the wonderful staff at Parkes, always happy to help out with any issue that might come up, observing related or not so observing related (such as driving to Forbes on a Friday night to pick up my missing bag, thanks again John!). Special thanks to Ettore Carretti, Brett Preisig and John Sarkissian.

I have had great teachers and mentors also during the years leading up to the start of my PhD. I would like to thank Jan Åke Nilsson, for believing I could do bigger and better things than I ever thought myself; P-O Fredriksson, for making me excited about physics and astronomy; Marek Abramowicz, for sharing your enthusiasm for research and for being committed to help me do well in my career. Thank you for helping me get to where I am today.

My time in Australia has let me make amazing friends: Stefan, I am going to miss our random chats about everything from pulsars to giant woodpeckers (sometimes that step isn't even very large!); Paul, thank you for coffee breaks and Friday chocolate and lunch at Grill'd, all with lots of chats and laughs; Sabrina, I am so glad you came to stay with me, you are a wonderful friend; Jono, thank you for taking care of me anytime I visited Sydney, and for all the card games! A special thank you also to Sarah and Max, Christina and Mike, Catarina, Ben, Evelyn, Emily, Caro and Frik, Vince, Chris, Francesco, Kathrin, Glenn, Anna, Adrian, Lee, Juan, Max, Carlos and all of the students at Swinburne. A huge thank you also to all of the Shooting Stars, I look forward to soccer nights all week!

Sara, thank you for sharing my interest in astronomy and for always pushing me (or competing with me!) to do better. Those long hours of studying for physics exams in your kitchen, trying to resist the temptation of the deck of cards, seem to have paid off for both of us! Helena and Kristofer, I know you are glad that I am happy where I am, but I still appreciate you making me feel missed by trying to find me any job you can in Sweden. Thank you all for being such lovely friends!

Without the encouragement from my family at home, this work would have been a lot harder. Mamma and Pappa, thank you for supporting me in my decision to move to Australia to do my PhD, even if you hated the thought of me being so far away. Thank you also to Daniel and Frida, simply for being the best siblings in the world!

Ian and Tricia, thank you for your warm welcome into your family and all the interest you show both in me and in what I do.

Graeme, thank you for holding my hand both through the happy and the rough times. You are an amazing friend and I am happier than ever. This is only the beginning of the big adventure!

Cheers everyone - I couldn't have done it without you!

Statement of originality

The work presented in this thesis has been carried out in the Centre for Astrophysics and Supercomputing at the Swinburne University of Technology (Hawthorn, VIC) and the Australia Telescope National Facility/CSIRO Astronomy and Space Sciences (Marsfield, NSW) between 2008 and 2012. During the last year, part of this work has been funded by the ARC Centre of Excellence for All-sky Astrophysics (CAASTRO), through project number CE110001020. This thesis contains no material that has been accepted for the award of any other degree or diploma. To the best of my knowledge, this thesis contains no material previously published or written by another author, except where due reference is made in the text of the thesis or included in this statement.

The pulsar survey, on which the most of the work in this thesis is based, is a collaboration of a large number of researchers, initially comprised of the authors of Keith et al. (2010) and with another few scientists added during the course of the project. All members of the survey team have been contributing to the collection of data for the survey. I have personally visited the telescope >15 times during my PhD and spent more than 100 days observing.

Although I have written the first draft of this entire thesis, my advisors have assisted in proof reading and revising of this text. Many of the details in Chapter 2 have been published by the survey team in Keith et al. (2010). The pipeline described in this chapter consists of a combination of newly developed and existing software. It was originally put together by Michael Keith, Samuel Bates and Matthew Bailes. My main contribution to the pipeline was connected to the de-dispersion code *dedisperse_all*, optimising RFI rejection routines, debugging and testing of the pipeline as well as candidate selection. The previously known pulsar section in Chapter 3 was carried out in collaboration with Simon Johnston and Michael Keith.

In Chapter 4, the high radio frequency data collected with ATCA was reduced by Michael Keith and the X-ray data collected with Chandra was analysed by Nanda Rea. Chapter 4 and 5 have been published in full in refereed journals; references for these are listed below. Minor alterations have been made to the published papers in order to maintain argument continuity and consistency of spelling and style.

The pulsar population modelling program *psrevolve* used in Chapter 6 was developed by Fanel Donea and Matthew Bailes, and modified to use new subroutines written by Michael Keith. Finally, the ideas and future work in Chapter 7 are results of discussions and collaboration with the survey team and many of these tasks will be addressed by the

team in the near future.

- Chapter 4 was published in *Astrophysical Journal*, **721**, L33, 2010, as “A Radio-loud Magnetar in X-ray Quiescence”, authored by L. Levin, M. Bailes, S. D. Bates, N. D. R. Bhat, M. Burgay, S. Burke-Spolaor, N. D’Amico, S. Johnston, M. Keith, M. Kramer, S. Milia, A. Possenti, N. Rea, B. Stappers, W. van Straten
- Chapter 5 was published in *Monthly Notices of the Royal Astronomical Society*, **422**, 2489, 2012, as “Radio emission evolution, polarimetry and multifrequency single pulse analysis of the radio magnetar PSR J1622–4950” authored by L. Levin, M. Bailes, S. D. Bates, N. D. R. Bhat, M. Burgay, S. Burke-Spolaor, N. D’Amico, S. Johnston, M. Keith, M. Kramer, S. Milia, A. Possenti, B. Stappers, W. van Straten



Lina Levin
Melbourne, Australia
2012

*To mamma Bine and pappa Lars
for always encouraging me to follow my heart.*

Contents

Abstract	i
Acknowledgements	ii
Statement of Originality	v
List of Figures	xii
List of Tables	xv
1 Introduction	1
1.1 Pulsar Properties and Observables	2
1.1.1 The Pulsar Emission	2
1.1.2 Pulsar Parameters	2
1.1.3 Interstellar Medium Propagation Effects	5
1.1.4 Polarised Pulsar Emission	7
1.2 The Known Pulsar Population	10
1.2.1 Ordinary Pulsars	10
1.2.2 Millisecond Pulsars	12
1.2.3 Magnetars	13
1.2.4 Other Pulsar Subgroups	14
1.3 Pulsar Surveys	14
1.3.1 Previous Pulsar Surveys	14
1.3.2 Present Pulsar Surveys	16
1.4 The Millisecond Pulsar Population	18
1.5 Thesis Outline	18
2 The High Time Resolution Universe Survey - Strategy and Analysis	21
2.1 Parkes Radio Telescope and its Pulsar Search Hardware	21
2.1.1 The Multibeam Receiver	23
2.1.2 The Berkeley Parkes Swinburne Receiver Backend	25
2.2 HTRU Survey Setup	26
2.2.1 Survey Sensitivity	27
2.3 Processing Details	29
2.3.1 The HITRUN Search Pipeline	29
2.3.2 Processing Setup and Run Times on the Green Machine	34

2.3.3	Candidate Selection	35
3	The High Time Resolution Universe Survey - Discoveries and Detections	39
3.1	HTRU Medlat Discoveries	39
3.1.1	Ordinary Pulsars	40
3.1.2	Millisecond Pulsars	43
3.2	Previously Known Pulsars in the Medlat Survey Region	47
3.2.1	Detections	47
3.2.2	Non-detections	51
3.3	Conclusions	54
4	A Radio-loud Magnetar in X-ray Quiescence	59
4.1	Introduction	59
4.2	Observations and Historical Data	60
4.2.1	Parkes Observations	60
4.2.2	Archive Mining	62
4.2.3	ATCA and Chandra Observations	62
4.3	Analysis, Results and Discussion	63
4.3.1	Radio Light Curve	63
4.3.2	Timing	63
4.3.3	Polarization	65
4.3.4	Radio Spectrum	68
4.3.5	X-ray Emission	68
4.3.6	Possible SNR Association	69
4.4	Conclusions	70
5	Multifrequency Radio Observations of the Magnetar PSR J1622–4950	71
5.1	Introduction	72
5.2	Observations and Analysis	74
5.3	Radio Light Curve	75
5.4	Timing	76
5.5	Polarimetry	79
5.5.1	Polarisation Categories	79
5.5.2	Rotating Vector Model Predictions on the Neutron Star Geometry .	81
5.5.3	Pulse Profile Alignment	84
5.5.4	Depolarisation	86

5.6	Single Pulses	87
5.6.1	Scattering	87
5.6.2	Single Pulse Characteristics	88
5.6.3	Width of Single Emission Spikes	90
5.6.4	Pulse-Flux Distribution	91
5.6.5	Pulse Modulation	92
5.7	Conclusions	93
6	Millisecond Pulsar Population Study	97
6.1	Introduction	98
6.1.1	Previous Studies	98
6.1.2	Selection Effects in Pulsar Surveys	99
6.2	Millisecond Pulsar Data Set	100
6.2.1	Pulsar Flux Densities	101
6.3	Model	112
6.3.1	The Scale Factor Method	112
6.3.2	Analysis	113
6.4	Results	115
6.5	Discussion	118
6.5.1	S/N Variations	118
6.5.2	Choice of Scale Height	118
6.5.3	Luminosity Distribution	120
6.5.4	DM Distance Errors	122
6.5.5	Pulsars with $P \lesssim 1.5$ ms	123
6.5.6	Estimation of Detections for the Other HTRU Sub-surveys	124
6.6	Conclusions	126
7	Conclusions and Future Work	127
7.1	The High Time Resolution Universe Survey	127
7.2	Millisecond Pulsar Population Studies	130
7.3	PSR J1622–4950 and Radio Magnetars	132
	Bibliography	136
	A Tables of Previously Known Pulsars	149

List of Figures

1.1	Dipole model	3
1.2	Interstellar medium effects	5
1.3	Beam geometry	8
1.4	Pulsar emission cone and position angle	9
1.5	P - \dot{P} diagram	11
2.1	Parkes Radio Telescope	22
2.2	Multibeam Receiver	23
2.3	Beam pattern of the multibeam receiver	24
2.4	IBOB	26
2.5	HTRU medlat survey sensitivity as function of period and DM	28
2.6	<i>hitrun</i> pipeline flow chart	30
2.7	The effects of de-striping data	36
2.8	Example of pulsar candidates	37
3.1	Spatial distribution of HTRU medlat discoveries	40
3.2	Period-DM distribution of HTRU medlat discoveries	41
3.3	P - \dot{P} diagram including HTRU medlat discoveries	42
3.4	Histogram of DM values for MSPs	43
3.5	Binary pulsar minimum companion mass - spin period	45
3.6	Spatial distribution of detected previously known pulsars	48
3.7	Period and DM distribution of detected previously known pulsars	48
3.8	P - \dot{P} diagram for detected previously known pulsars	50
3.9	S/N of previously known pulsars	52
3.10	Theoretical S/N of non-detections	53
4.1	1.4 GHz light curve and pulse profile variations for PSR J1622–4950	61
4.2	Chandra and ATCA images	64
4.3	Extract of the P - \dot{P} diagram: long periods	66
4.4	Polarimetric profiles of PSR J1622–4950 at 3.1 GHz and 1.4 GHz	67
5.1	Radio emission evolution	75
5.2	Timing model	77
5.3	Polarisation categories	80
5.4	Pulse profile alignments	85

5.5	3.1 GHz single pulse characteristics	89
5.6	3.1 GHz pulse phase histogram	90
5.7	Pulse-flux distribution at 3.1 GHz	92
5.8	Modulation index and R-parameter	94
6.1	S/N histograms for MSPs in the sample	103
6.2	Luminosity - Period distribution	111
6.3	Comparison of the discovery S/N to the average S/N	119
6.4	Cumulative histogram of scale heights	121
6.5	Luminosity histogram	122

List of Tables

2.1	Multibeam receiver specifications	25
2.2	HTRU survey parameters	26
2.3	HTRU survey regions	27
2.4	HTRU survey processing times	34
3.1	HTRU medlat discoveries	55
4.1	Parameter summary of PSR J1622-4950	68
5.1	PSR J1622–4950 RVM fits	82
5.2	Widths of single pulse spikes	91
6.1	Millisecond pulsar sample	102
6.2	Millisecond pulsar average flux density and luminosity	110
6.3	Scale factors	116
6.4	Average detection numbers	117
6.5	Scale factors for pulsars with $P \lesssim 1.5$ ms	117
A.1	Known pulsars detected in the pipeline	149
A.2	Weak pulsars only detected by direct folding	166

1

Introduction

The first pulsar was serendipitously discovered in late 1967 by Hewish et al. (1968) while analysing the angular structure of compact radio sources in the Galaxy. What was first thought to be radio frequency interference turned out to be an extremely accurate pulsating radio source associated with a rotating neutron star. Since then, pulsars have been used to study a wide variety of physical and astrophysical phenomena, such as efforts to detect gravitational waves (Hobbs et al. 2009, van Haasteren et al. 2011, Yardley et al. 2011), to test predictions made by general relativity (Kramer et al. 2006) and other theories of gravity (Bhat et al. 2008), to perform astrometry (Deller et al. 2009) and estimate the electron distribution of the Galactic interstellar medium (Cordes & Lazio 2002), and many other applications.

This thesis will present a search for previously unknown pulsars as part of the High Time Resolution Universe survey (Keith et al. 2010) currently underway at the Parkes Radio Telescope. At the time of writing this survey has discovered over 100 radio pulsars, and the thesis will explain the research and analysis undertaken to achieve this, from acquiring the astronomical data to viewing possible pulsar candidates to follow-up work on new discoveries. Some focus will be directed at the discovery and detailed study of one particular source: PSR J1622–4950 (Levin et al. 2010, 2012). This pulsar belongs to the group of magnetars, a category of pulsars with extremely high surface magnetic field strengths, and it is the first magnetar ever discovered in the radio band. Finally we will explore how the large number of millisecond pulsars discovered in the survey can be used to put limits on the millisecond pulsar population in our Galaxy.

This first chapter will cover general pulsar properties as well as describe the different kinds of known pulsars and how they enable various scientific research projects. It will also review current and past surveys conducted for previously unknown pulsars in our Galaxy, and discuss how we can use the detection and discovery of millisecond pulsars to

estimate how many of these sources should exist in the Galaxy.

1.1 Pulsar Properties and Observables

Pulsars are generally accepted to be rapidly rotating neutron stars, that emit radiation in beams observable at various wavelengths. Neutron stars are highly compact objects, with radii of only tens of kilometers and masses of $\sim 1.4 - 2.0 M_{\odot}$. There are currently about 2000 pulsars known with spin periods ranging over 4 orders of magnitude (from 1.4 ms to ~ 10 s).

1.1.1 The Pulsar Emission

The emission properties of pulsars are explained by the acceleration of charged particles along the field lines in the highly magnetized neutron star. Due to an offset between the rotation and magnetic axes, pulses are observed when the beam of emission sweeps past the observer's line of sight once every rotation, in the so-called lighthouse effect. Observers describe the pulsar magnetosphere with a simple model, shown in Fig 1.1. It consists of the rotating neutron star, with its open and closed dipolar magnetic field lines. The radio emission beam is thought to arise from near the surface of the star and is limited by the widest closed field lines. The observed pulse is dependent on the angle between the line of sight and the beam. The size of the neutron star magnetosphere is limited by the light cylinder, with a radius defined as the point where the co-rotation speed is equal to the speed of light.

1.1.2 Pulsar Parameters

The pulse period of a pulsar is observed to increase with time and by measuring the value of the spin-down rate, $\dot{P} = dP/dt$, other physical parameters for the pulsar can be derived.

The spin-down luminosity, \dot{E} , describes the rate at which the neutron star loses its rotational kinetic energy. It is given by

$$\dot{E} \equiv -\frac{dE_{rot}}{dt} = -\frac{d(I\Omega^2/2)}{dt} = 4\pi^2 I \dot{P} P^{-3} \quad (1.1)$$

where the rotational angular frequency $\Omega = 2\pi/P$ and I is the moment of inertia. Only a small fraction of the rotational energy is converted into radio emission ($L_{radio} \sim 10^{-5} \dot{E}$), while most of \dot{E} is converted into high energy radiation, magnetic dipole radiation and a pulsar wind. This is an important value especially for research on magnetars, a sub-class

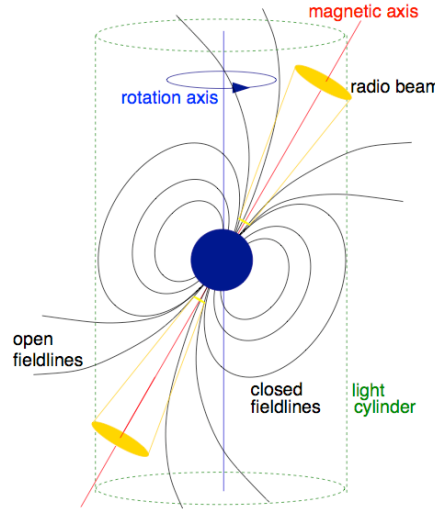


Figure 1.1 Sketch of the model for the rotating neutron star and its dipolar magnetic field. Figure taken from Lorimer & Kramer (2005).

of pulsars with extremely high magnetic field strength described in detail in Sec 1.2.3 below. One of the defining properties of this group of pulsars is that the energy loss rates measured for these sources during outburst often exceeds the spin-down luminosity, and hence the rotational kinetic energy loss cannot be the only power source for the pulsar.

By adopting the assumption that pulsars have very strong dipole magnetic fields, we can compare the spin-down luminosity to the energy loss due to magnetic dipole braking. The radiation power can be written as

$$\dot{E}_{\text{dipole}} = \frac{2}{3c^3} |m|^2 \Omega^4 \sin^2 \alpha \quad (1.2)$$

where m is the magnetic moment and α is the angle between the magnetic and rotational axes. Assuming a source in vacuum we can set $\dot{E}_{\text{dipole}} = \dot{E}_{\text{rot}}$, and derive an equation for the evolution of the rotation frequency as

$$\dot{\Omega} = \frac{2|m|^2 \sin^2 \alpha}{3Ic^3} \Omega^3. \quad (1.3)$$

The more general pulsar spin-down model assumes that the evolution of the spin frequency, $\nu = 1/P$, can be expressed as a power law

$$\dot{\nu} = -K\nu^n \Rightarrow \dot{P} = KP^{2-n} \quad (1.4)$$

where n is the braking index and K is a constant. Comparing this result with eq 1.3 above, we can see that for pure magnetic dipole braking, $n = 3$.

The age of a pulsar can be derived by integrating eq 1.4 with respect to pulse period, assuming a constant K and a braking index $n \neq 1$, giving

$$T = \frac{P}{(n-1)\dot{P}} \left[1 - \left(\frac{P_0}{P} \right)^{n-1} \right]. \quad (1.5)$$

Assuming that the current spin period is much longer than the pulsar spin period at birth ($P_0 \ll P$) and a braking index $n = 3$, we can write the characteristic age of a pulsar as

$$\tau_c \equiv \frac{P}{2\dot{P}}. \quad (1.6)$$

However, other reasons for rotational energy loss than magnetic dipole braking may be present, e.g. stellar winds or variations of the moment of inertia or magnetic field (Manchester et al. 1985, Blandford & Romani 1988), each of which would change the value of n . Indeed, by measuring the braking index for a few pulsars observers have found braking indices ranging from $n = 1.4$ to $n = 2.9$ (e.g. Kaspi & Helfand 2002). This can be done by differentiating eq 1.4, resulting in

$$n = \frac{\nu \ddot{\nu}}{\dot{\nu}^2}. \quad (1.7)$$

Another physical parameter that can be inferred assuming that the spin-down is due to magnetic dipole braking is the surface magnetic field strength, B . Using the relation $B \approx |m|/r^3$ between the magnetic field strength and the magnetic moment together with eq 1.3, we derive the magnetic field strength at the surface of the neutron star ($r = R$) as

$$B = \sqrt{\frac{3c^3}{8\pi^2} \frac{I}{R^6 \sin^2 \alpha} P \dot{P}}. \quad (1.8)$$

Many of the variables in the magnetic field strength equation are hard to measure (α , R and I), however, values calculated with this equation are useful as order of magnitude estimates. In practice it is usually used in the form

$$B = 3.2 \times 10^{19} \text{ G} \sqrt{P \dot{P}} \simeq 10^{12} \text{ G} \left(\frac{\dot{P}}{10^{-15}} \right)^{1/2} \left(\frac{P}{s} \right)^{1/2} \quad (1.9)$$

where a neutron star radius, $R = 10 \text{ km}$, a moment of inertia, $I = 10^{45} \text{ g cm}^2$ and an angle between the magnetic and rotational axis $\alpha = 90^\circ$ is assumed.

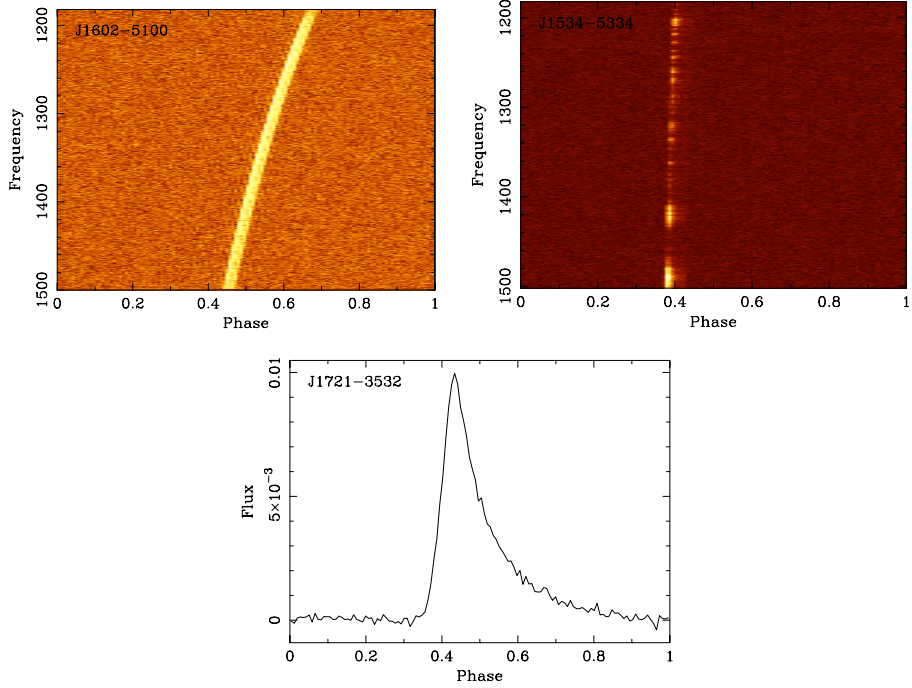


Figure 1.2 Effects on pulsar signal after propagation through the interstellar medium.
Top left: Pulse delay in PSR J1602–5100 over a frequency band due to dispersion.
Top right: Scintillation in the signal from PSR J1534–5334, which can be seen as intensity variations over the frequency band.
Bottom: Pulse scattering tail in PSR J1721–3532.

1.1.3 Interstellar Medium Propagation Effects

The interstellar medium (ISM) affects the pulsar signal on its way to earth. In this chapter we will give a brief overview of three ISM effects: dispersion, scintillation and scattering, examples of which are shown in Fig 1.2.

Pulse dispersion refers to the frequency dependence of the group velocity of radio waves as they propagate through the ISM, which causes pulses at higher radio frequencies to arrive earlier at the telescope than pulses at lower radio frequencies. A relation between this time delay and the observing frequency can be derived by defining the index of this refraction as

$$\mu = \sqrt{1 - \left(\frac{f_p}{f}\right)^2} \quad (1.10)$$

where f is the observing frequency and f_p is the plasma frequency, which in turn is defined

as

$$f_p = \sqrt{\frac{e^2 n_e}{\pi m_e}} \simeq 8.5 \text{ kHz} \left(\frac{n_e}{\text{cm}^{-3}} \right)^{1/2} \quad (1.11)$$

where n_e is the electron density number, e is the electron charge and m_e is the electron mass (Lorimer & Kramer 2005). From eq 1.10 it follows that $\mu < 1$, with the logical consequence that the group velocity of a propagating wave $v_g = c\mu$ is always smaller than the speed of light c . Hence, the time delay with respect to a signal at infinite frequency for a radio signal propagating from a pulsar to Earth along a path of length d is given by

$$t = \left(\int_0^d \frac{dl}{v_g} \right) - \frac{d}{c}. \quad (1.12)$$

Using eq 1.10 and assuming that $f_p \ll f$, we can write the time delay as

$$t = \frac{1}{c} \int_0^d \left[1 + \frac{f_p^2}{2f^2} \right] dl - \frac{d}{c} = \frac{e^2}{2\pi m_e c} \frac{\int_0^d n_e dl}{f^2} \equiv D \frac{\text{DM}}{f^2} \quad (1.13)$$

where the dispersion measure

$$\text{DM} = \int_0^d n_e dl \quad (1.14)$$

and D is the dispersion constant given by

$$D = \frac{e^2}{2\pi m_e c} = (4.148808 \pm 0.000003) \times 10^3 \text{ MHz}^2 \text{ pc}^{-1} \text{ cm}^3 \text{ s}. \quad (1.15)$$

In practice, by using these equations and observing a pulsar at two different frequencies or across a reasonable frequency band, we can infer the DM of the pulsar. The DM can then be used to estimate the distance to the pulsar, by numerically integrating eq 1.14 and assuming a model for the Galactic electron density. The current model that is generally used, and will be used throughout this work, is the NE2001 model by Cordes & Lazio (2002).

Turbulence in the interstellar medium has both diffractive and refractive effects on the pulsar radiation. Diffractive scintillation can be observed as short timescale (\sim minutes) fluctuations in the intensity of the pulsar signal at narrow (~ 1 MHz) frequency bands (e.g. Cordes & Rickett 1998). Diffractive scintillation in pulsars was first observed by Lyne & Rickett (1968) and shortly thereafter Scheuer (1968) developed a basic model to explain this scintillation. The model assumes that the interstellar medium is a thin screen of inhomogeneous matter, placed midway between the pulsar and the observer. The phase perturbations of the signal produced by such a screen are correlated over a scintillation

bandwidth $\Delta f \propto f^4$, where f is the observing frequency. Refractive scintillation causes longer term, less deep variations in the flux density. In pulsars, it was first observed by Sieber (1982), who noticed a strong correlation between the time scales of long term intensity modulations and source distance. Rickett et al. (1984) later suggested that these modulations were due to refractive interstellar scintillation.

Scintillation can also be observed as pulse broadening, which to first order manifests itself as exponential tails in the pulse profiles of distant pulsars. It can be explained as scattering of the emitted rays by the irregularities in the interstellar medium, which will cause different rays to travel different path lengths and ultimately possess different arrival times at the telescope. This causes an intrinsically narrow pulse to be broadened by the time it arrives at the observer. The scattering time scale, τ_s , is inversely proportional to the scintillation bandwidth as $\tau_s \sim 1/(2\pi\Delta f)$. Measurements of τ_s show that this value is strongly correlated with DM such that more distant pulsars with higher DM in general will be more scattered (Bhat et al. 2004). The scattering time scale is also strongly frequency dependent and in the thin screen model scales approximately as $\tau_s \propto f^{-4}$. However, measurements of actual scattering show that the value of τ_s deviates from the model, and could even go down to $\tau_s \propto f^{-2.8}$ (Löhmer et al. 2001).

1.1.4 Polarised Pulsar Emission

The pulsar radio emission is in general highly polarised. We can decompose the emission into the four Stokes parameters I, Q, U and V , where I is the total intensity, $L = \sqrt{Q^2 + U^2}$ is the linear polarisation and V is the circular polarisation. The total amount of polarised emission varies greatly between pulsars, with some having close to 100% polarised emission, but the average degree of linear polarisation $\langle L/I \rangle$ is about 20% and circular polarisation $\langle |V|/I \rangle$ about 10% (Gould & Lyne 1998). The linear polarisation position angle (PA) is given by

$$\Psi = \frac{1}{2} \tan^{-1} \left(\frac{U}{Q} \right) \quad (1.16)$$

and normally follows a smooth and regular S-shaped curve throughout the pulse phase in ordinary pulsars. When studied as a function of pulse phase, the PA can be used to determine the pulsar beam size and inclination angle with respect to the rotation axis. This is done by fitting the PA to the Rotating Vector Model (RVM; Radhakrishnan & Cooke 1969) described below. However, not all pulsars exhibit a smooth PA curve. Many millisecond pulsars in particular have flatter and/or discontinuous PA curves (e.g. Xilouris

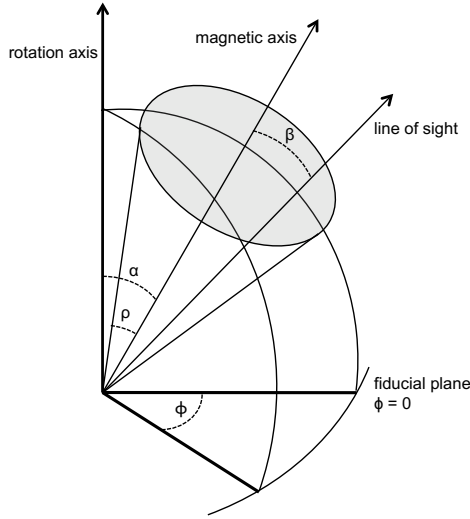


Figure 1.3 Beam geometry for pulsar emission. The emission beam is centered around the magnetic axis and has an opening angle ρ . The angle between the rotation axis and the magnetic axis is denoted by α and the angle between the magnetic axis and the pulsar-observer line of sight is β . The fiducial plane determines the zero point of the rotational phase ϕ . Figure inspired by figures in Lorimer & Kramer (2005).

et al. 1998). In addition, some pulsars exhibit jumps in the PA swing from one S-curve to another, which is a result of the presence of two orthogonal polarisation modes in the radiation. In some cases, non-orthogonal jumps have also been observed (Backer & Rankin 1980). Although this phenomenon is usually observed in the behavior of the linear polarisation, circular polarised radiation can undergo similar jumps between left-handed and right-handed emission (Cordes et al. 1978, McKinnon 2003, Edwards & Stappers 2004).

Rotating Vector Model

Shortly after the discovery of pulsars, Radhakrishnan & Cooke (1969) proposed a model to explain the S-shaped sweep of the PA in terms of the geometry of the pulsar emission beam. Generally the beam geometry is explained as a cone-shaped beam centered on the magnetic axis, as seen in Fig 1.3. Here the the emission cone has an angular radius ρ and is inclined to the rotation axis by an angle α . The closest angle between the line of sight and the magnetic axis, β , is denoted the impact parameter and is always smaller than (or equal to) ρ , since the beam sweep otherwise would miss the Earth. The line of sight follows a curved path through the beam as the pulsar rotates, which results in the observed pulse profile and width. This also causes the projected direction of the magnetic field within

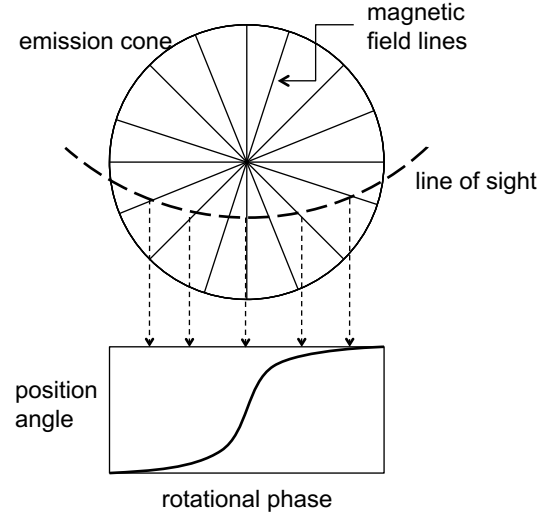


Figure 1.4 The top plot shows the pulsar emission cone viewed towards the magnetic pole, with its magnetic field lines. As the plane of linear polarisation passes through the beam along the line of sight curve, it produces the S-shaped position angle curve in the bottom plot. The steepest gradient in the PA curve is expected to be the point of the fiducial plane. Figure inspired by figures in Lorimer & Kramer (2005).

the beam to rotate with the pulsar as the beam sweeps across our line of sight, see Fig 1.4. The direction of the magnetic field determines the plane of the polarised emission and leads to measurement of a slowly varying PA at the edges of the beam and a faster one towards the middle, resulting in the S-shaped PA curve. The RVM predicts the PA swing from these arguments as

$$\tan(\Psi - \Psi_0) = \frac{\sin \alpha \sin(\phi - \phi_0)}{\sin(\alpha + \beta) \cos \alpha - \cos(\alpha + \beta) \sin \alpha \cos(\phi - \phi_0)} \quad (1.17)$$

where ϕ is the rotational phase, α is the axis between the magnetic and rotation axis and β is the impact parameter (Radhakrishnan & Cooke 1969). The position angle $\Psi = \Psi_0$ is determined by the longitude of the fiducial plane ϕ_0 , which in turn is defined as the plane that contains the rotation and magnetic axis as well as the line of sight vector.

Fits of PAs to the RVM give values of α and β , however in practice it can be hard to find well constrained values for these angles as the range of pulse phases with reliable PAs are limited by the duty cycle of the mean pulse profile. The steepest gradient of eq 1.17 can be easier to determine and is given by

$$\frac{d\Psi}{d\phi} = \frac{\sin \alpha}{\sin \beta} \quad (1.18)$$

when measured at the fiducial plane, $\phi = \phi_0$. From this equation we can see that the gradient is largest if $\beta \rightarrow 0$, hence if the line of sight is passing close to the middle of the beam, whereas a shallow PA swing generally means a large β , hence the beam is cut at the outer edge.

1.2 The Known Pulsar Population

The \sim 2000 known pulsars in our Galaxy and nearby globular clusters all have certain general properties, such as emission over a broad bandwidth, stable rotation with well defined spin periods (at least in most cases, see rotating radio transients (RRAT) in Ch 1.2.4 below for exceptions) and measurable spin down rates. However, we can also divide the pulsar population into several sub-populations. The separation between these subgroups can be visualised in the $P - \dot{P}$ diagram (see Fig 1.5) and this chapter will briefly describe each of them. Most of the known pulsars and their properties can be found in the ATNF Pulsar Catalogue¹.

1.2.1 Ordinary Pulsars

The ordinary pulsars are found as the large cluster of sources in the middle of the $P - \dot{P}$ diagram. They range from recently born pulsars with periods of $P \sim 80 - 100$ ms to old and slow pulsars with periods of $P \sim 2 - 10$ s. Some of the young pulsars have associated supernova remnants, which confirms their low characteristic age. Most of the ordinary pulsars ($> 99\%$) are solitary stars, and they have spin down rates in the range $10^{-17} \lesssim \dot{P} \lesssim 10^{-11}$ ss $^{-1}$ and surface magnetic field strengths $10^{10} \lesssim B \lesssim 10^{13}$ G.

A likely path describing the “life” of an ordinary pulsar would start with a position around $P \sim 80$ ms, $\dot{P} \sim 10^{-12}$ ss $^{-1}$ at the birth of the pulsar. Thereafter the pulsar would rapidly spin down and enter the ordinary pulsar “island” on a timescale of $\sim 10^{5-6}$ years where it would continue to spin down until it would switch off after $\sim 10^7$ years. The limit at which the pulsar emission energy is too low to produce beamed radiation (or possibly a signal too weak to detect) is usually referred to as the “death line” in the $P - \dot{P}$ diagram. Once a pulsar has passed that line, it “dies” in the pulsar “graveyard”. Theoretical models predict that no emission should be seen from pulsars in the graveyard, however the discovery of pulsars on the “wrong” side of the death line (e.g. J2144–3933; Young et al. 1999) challenges these simple emission models, suggesting that a death line model might be too simplistic and perhaps a “death valley” would be more suitable.

¹see <http://www.atnf.csiro.au/research/pulsar/psrcat/>

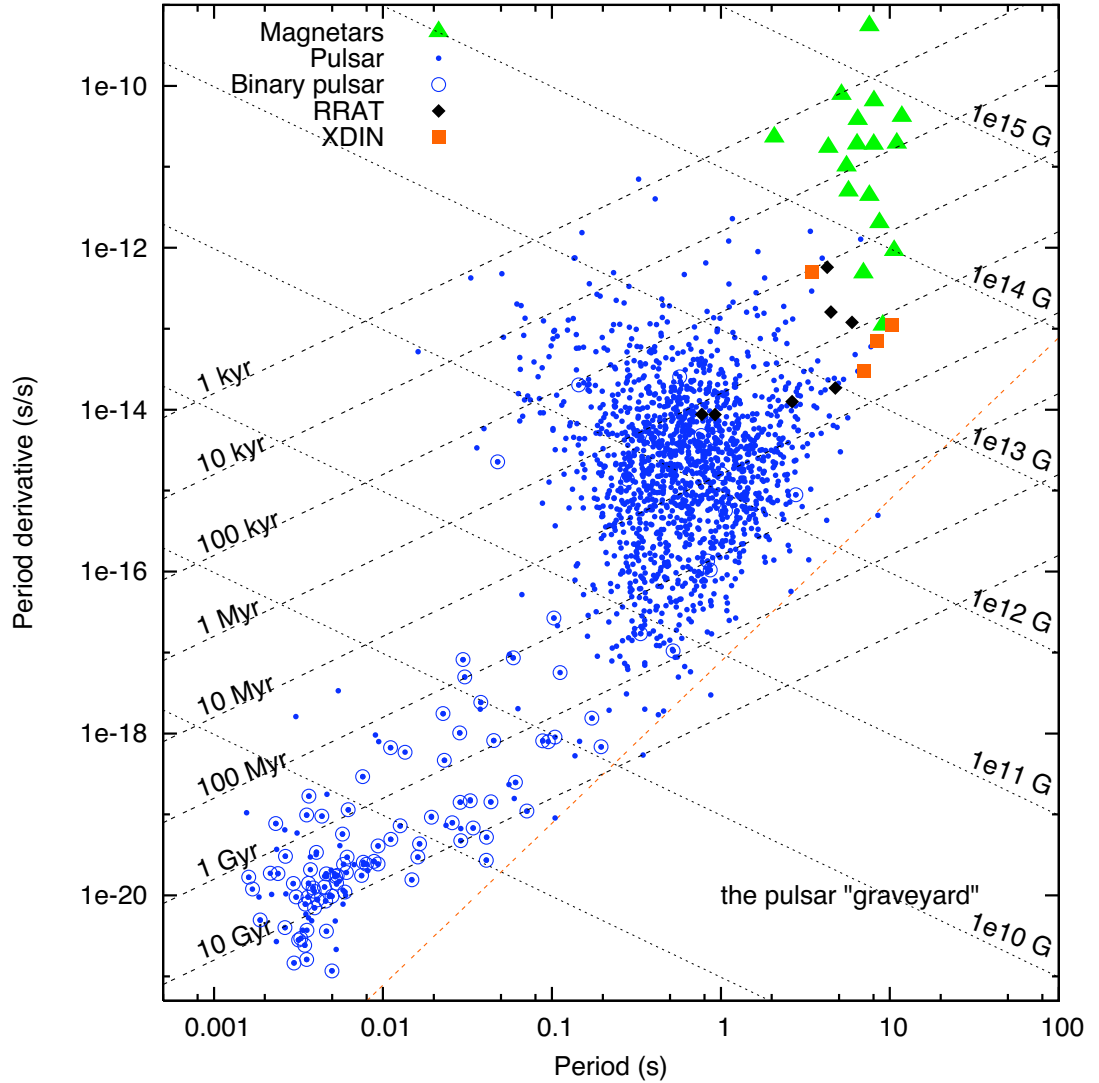


Figure 1.5 $P-\dot{P}$ diagram. Blue dots represent ordinary pulsars, with the circled ones being pulsars in binary systems. Green triangles represent the magnetars, black diamonds the rotating radio transients and red squares the X-ray dim isolated neutron stars, as defined in the text. Dashed lines correspond to lines of constant characteristic age and dotted lines to constant magnetic field strength. The orange dotted line is the death line, which represents the border of the pulsar graveyard.

1.2.2 Millisecond Pulsars

The bottom left corner of the $P - \dot{P}$ diagram hosts the millisecond pulsars (MSPs). They generally have periods $1 \lesssim P \lesssim 30$ ms, spin down rates $10^{-21} \lesssim \dot{P} \lesssim 10^{-18}$ ss $^{-1}$ and surface magnetic field strengths $10^8 \lesssim B \lesssim 10^{10}$ G. Their position in the $P - \dot{P}$ diagram suggests that MSPs are old neutron stars that have been spun-up by the accretion of matter and angular momentum from a binary companion to the pulsar. This process can potentially revive an otherwise dead pulsar by spinning it up to millisecond periods, which has led to that MSPs often are referred to as “recycled” pulsars.

The preferred scenario in which an MSP is created can be explained as follows: The more massive of two main sequence stars in a binary system evolves faster than the less massive star and will explode in a supernova to form a neutron star before the less massive star comes to the end of its main sequence lifetime. In most cases, the kick from the supernova explosion will disrupt the binary and leave a single ordinary pulsar and a single main sequence star. However, some systems will stay bound and the neutron star will keep spinning down as an ordinary pulsar until its companion star starts its red giant phase. At this stage the pulsar will begin to accrete matter from the red giant to form an accretion disk, and the system can be observed as an X-ray binary. In the accretion process, orbital angular momentum will be transferred to the pulsar and start spinning it up to short periods. This will significantly reduce its magnetic field and continue until the co-rotation radius is equal to the so called Alfvén radius, at which the energy density of the magnetic field equals the kinetic energy density of the inflowing plasma (Bhattacharya & van den Heuvel 1991). At this stage the pulsar’s minimum spin period is reached and we are left with a recycled millisecond pulsar.

The life of the companion star depends on the mass of the star. If it is massive enough, also the companion will go through a supernova explosion and become a neutron star. Examples of systems that have survived this second supernova are B1913+16 (Hulse & Taylor 1975), B1534+12 (Wolszczan 1990, 1991) and of course the double pulsar J0737–3039 (Burgay et al. 2003, Lyne et al. 2004). A less massive companion will become a white dwarf. This process is slower than the double neutron star scenario, and the mass transfer can continue for a longer time, leaving a faster rotating pulsar.

Some cases of isolated MSPs are also known, and their formation process is still not fully understood. One theory is that the strong relativistic particle wind from the pulsar during the X-ray binary phase destroys the companion (Ruderman et al. 1989). Another possibility is that the pulsar completely accretes its companion. This would be possible for systems with sufficiently small separation between the two stars and also depend on

the mass of the companion and the orbital period of the system (Bailes et al. 2011).

1.2.3 Magnetars

The group of pulsars in the top right corner of the P - \dot{P} diagram is the magnetars. They have very long spin periods with $P \gtrsim 2$ s and high spin down rates, $\dot{P} \gtrsim 5 \times 10^{-13}$ ss $^{-1}$. In contrast to ordinary pulsars, the magnetars are not powered by their spin-down, but by the energy stored in their extremely large magnetic fields, typically $\gtrsim 10^{14}$ G (Duncan & Thompson 1992). They are divided into two groups, Soft Gamma-ray Repeaters (SGRs) and Anomalous X-Ray Pulsars (AXPs), whose relation to each other and to other kinds of neutron stars is still a matter of debate (Mereghetti 2008).

SGRs were discovered as sources emitting short repeating bursts in the hard X-ray/soft γ -ray band and were initially thought to be a sub-class of gamma-ray bursts (e.g. Laros et al. 1986). In a few different SGR sources, giant flares with luminosities up to 10^{47} erg s $^{-1}$ have also been observed (e.g. Mazets et al. 1979). With more observations of the SGR bursts, better positions of the sources were obtained and the detections of their X-ray counterparts revealed that they are also pulsating at these energies. The AXPs were first detected in the soft X-ray band as bright pulsars that were believed to be part of the group of accreting X-ray binaries. More observations in the X-ray and optical/IR bands ruled out the presence of binary companions in all these sources and because of their unusual properties, such as pulse profile changes and extreme flux variations, they were classified as a separate group of pulsars. Recently sources have been found that show properties of both groups, suggesting that AXPs and SGRs belong to the same family (Rea et al. (2009), Mereghetti et al. (2009)).

After the discovery of magnetars many attempts were made to find pulsed radio emission from these sources (e.g. Burgay et al. 2006) but it was not until 2006 that the first detection was reported (Camilo et al. 2006). Currently three magnetars have confirmed radio pulsations, namely XTE J1810–197 (Halpern et al. 2005) and 1E1547–5408 (Camilo et al. 2007b) and PSR J1622–4950 (Levin et al. 2010). The first two sources are transient AXPs, hence they occasionally undergo very bright X-ray outbursts. Their pulsed radio emission was discovered in connection with these outbursts, and is observed to fade with time after an outburst. PSR J1622–4950 on the other hand was first discovered in the radio band and observations of its X-ray counterpart show more moderate variations in the X-ray emission.

The three known radio-emitting magnetars are found in the lower parts of the magnetar group in the P - \dot{P} diagram, with periods that are short in comparison to the other

magnetars and inferred magnetic field strengths in the lower half of the magnetar range, adjacent to the ordinary radio pulsars with the highest surface magnetic fields. The gap between these two groups of pulsars have been narrowing with new discoveries, such as the detection of magnetar-like X-ray bursts from PSR J1846–0258 (Gavriil et al. 2008), which for a long time was thought to be a purely rotation-powered pulsar.

1.2.4 Other Pulsar Subgroups

There are also a few other groups of neutron stars that have been discovered recently and belong to the pulsars, but their origin and part of the big picture is still fairly unclear.

The Rotating Radio Transients (RRATs; McLaughlin et al. 2006) seemed to be a separate class of neutron stars when they were discovered. They emit radiation very sparsely, typically through short, narrow pulses often detectable for less than a second per day. This makes them very hard to discover even if the total population might be large and hence only a comparatively small number of them are currently known (~ 70 sources, but only 19 with phase-connected timing solutions; Keane & McLaughlin 2011). It is currently under discussion whether these sources are actually a special class of neutron stars, or if they are just very sparsely emitting nulling pulsars (Burke-Spolaor & Bailes 2010), or maybe they are steady emitters but only the brightest pulsations are detectable (Weltevrede et al. 2006b). It has also been suggested that the RRATs might be "exhausted magnetars" (Lyne et al. 2009), a link which could explain the intermittency in both groups of sources and their tendency to go through glitches in their spin down. For further discussion on the nature of RRATs see e.g. Keane et al. (2011) and Burke-Spolaor et al. (2011).

The X-ray dim isolated neutron stars (XDINS; Kaplan 2008, Kaplan & van Kerkwijk 2009) make up another special group. Currently only 7 of these sources are known, and they are all slow, radio-quiet pulsars with a soft X-ray black body-like spectrum and very faint optical counterparts. They can be found close to the magnetars in the $P-\dot{P}$ diagram, and their link to ordinary pulsars, magnetars and RRATs is still unclear.

1.3 Pulsar Surveys

1.3.1 Previous Pulsar Surveys

Since the discovery of the first pulsar in late 1967 (Hewish et al. 1968) a large number of pulsar surveys have been carried out, some more successful than others. There are two main groups of pulsar surveys: targeted surveys and blind surveys.

A large number of MSPs and binary pulsars have been discovered through targeted searches of globular clusters, e.g. observations of 47 Tucanae (Manchester et al. 1991, Camilo et al. 2000) and Terzan 5 (Ransom et al. 2005) have led to the discovery of 23 and 34 MSPs respectively. This is as expected, since the progenitors of the MSPs, the low-mass X-ray binaries (LMXBs), have a higher population density in the cores of globular clusters than in most parts of the Galaxy. Targeted searches are usually an efficient use of telescope time, since a single globular cluster often fits in one telescope beam. On the other hand, the globular clusters are usually more distant than average millisecond pulsars discovered in large area searches, so longer, deeper observations are required to detect the pulsars, which in turn makes the data reduction more complex. In addition, to discover MSPs in close binary systems it is often required to perform a search also in acceleration space, a process that is computationally intensive and highly time consuming even for short observations. To date 143 pulsars in 27 globular clusters are known. Targeted surveys have also discovered 21 pulsars in the Magellanic Clouds and 48 pulsars associated with supernova remnants.²

As successful as the targeted surveys have been, the largest number of pulsars have been found in blind searches of the Galaxy. The kind of pulsars found in these surveys is highly dependent on the survey parameters. Different areas of the sky may need to be approached differently for optimal use of telescope time.

The region near the Galactic plane contains the largest number of known pulsars, and in particular young pulsars are expected to be found there, close to their birthplace. Interstellar propagation effects, such as scattering and dispersion, are severe in this part of the sky and the sky background radiation, T_{sky} , is high. This has an adverse effect on the sensitivity at lower observing frequencies (<1 GHz). That, balanced by that pulsars in general have a steep, negative radio spectrum ($\alpha \simeq -1.6$, where $S \propto \nu^\alpha$; Lorimer et al. 1995b), has resulted in that most surveys in this region are undertaken in the 1–2 GHz band. The most successful survey near the Galactic plane (and also by far the most successful survey in general) is the Parkes Multibeam (PM) pulsar survey (Manchester et al. 2001), carried out at Parkes Radio Telescope in the late 1990’s, which discovered over 700 new pulsars (Lorimer et al. 2006). The PM survey was the first pulsar survey to use the 13-beam, 1.35-GHz receiver at Parkes (the 21-cm Multibeam receiver; Staveley-Smith et al. 1996). It employed an observed frequency bandwidth of 288 MHz divided into 96 frequency channels and a 35 min integration time, sampled every 250 μ s, resulting in about 5 TB of data.

²See the globular cluster pulsar webpage at <http://www.naic.edu/~pfreire/GCpsr.html> for details.

Older pulsars are often found further away from the Galactic plane, as they have had more time to move away from their place of birth. Millisecond pulsars are typically several billions of years old, and are expected to be found at high Galactic latitudes, which has been proven through the many MSPs found by all-sky surveys at these latitudes. Since the sky background effects are less severe away from the Galactic plane, high latitude surveys profit from observing at lower frequencies. Two of the first high Galactic latitude recycled pulsars were discovered at 430 MHz with the 305-m radio telescope at Arecibo by Wolszczan in the early 1990's. Both of these pulsars turned out to be very exciting objects: B1534+12 (Wolszczan 1991) is in a double neutron star binary system and B1257+12 (Wolszczan & Frail 1992) is orbited by three planets. These findings started a trend of millisecond pulsar searching at high latitudes, and has led to the discovery of many MSPs by several other pulsar groups at the large radio telescopes. The only previous all-southern-sky survey was the Parkes Southern Pulsar Survey (PSPS), carried out in the 1990's (Manchester et al. 1996). This very successful survey discovered a large number of millisecond pulsars: 17 sources out of 101 pulsars discovered in total (Lyne et al. 1998). PSPS was a low frequency survey, with a 32-MHz bandwidth centered on 436 MHz divided into 125 channels.

In addition, pulsar surveys have been carried out at intermediate galactic latitudes (about $5^\circ < |b| < 15^\circ$) in order to search for pulsars more deeply than is possible at high Galactic latitudes in a finite amount of telescope time. One successful survey in this region was the Swinburne intermediate-latitude pulsar survey, which discovered 69 new pulsars, including 8 MSPs (Edwards et al. 2001).

1.3.2 Present Pulsar Surveys

Large scale pulsar surveys require large computing and data storage resources, and as technology evolves pulsar surveys can be undertaken with higher sensitivity and higher spectral and temporal resolution than before.

The southern High Time Resolution Universe (HTRU) survey for pulsars and fast transients (Keith et al. 2010) is currently underway at the Parkes 64-m radio telescope, using the 21-cm Multibeam receiver (Staveley-Smith et al. 1996). It uses a new 13-recorder digital backend system, which gives HTRU four times the time resolution and eight times the frequency resolution of the previous Parkes Multibeam survey: the frequency bandwidth of 340 MHz, centered at 1.35 GHz, is divided into 870 channels with 2-bit sampling every 64 μ s. HTRU is planned to be an all-sky survey, where the southern sky is covered at Parkes and a parallel survey with similar sensitivity is carried out for the northern sky

with the 100-m Effelsberg radio telescope in Germany. The southern survey is divided up into three regions, to make the search as effective as possible, with all parameters but the integration time and the sky coverage identical between the three parts. Close to the Galactic plane, at $|b| < 3.5^\circ$ and $-80^\circ < l < 30^\circ$ (HTRU deep), the observing time is chosen to 4200 s, which is twice that of the Parkes Multibeam survey and makes it the deepest Galactic plane survey to date. At intermediate latitudes, $|b| < 15^\circ$ and $-120^\circ < l < 30^\circ$ (HTRU medlat), the integration time is 540 s and at high latitudes, the entire sky south of declination $+10^\circ$ (HTRU hilat), the observing time is 270 s.

This thesis will describe the southern HTRU medlat survey in great detail, but HTRU is not the only large scale pulsar survey that is currently being carried out; there are more surveys underway at other radio telescopes.

One of them is a pulsar survey at the Arecibo telescope using the Arecibo L-band Feed Array (ALFA), a seven-beam receiver system operating at 1.4 GHz. The Pulsar ALFA (PALFA) survey is planned to search most of the sky accessible at Arecibo (declinations between -1° and $+38^\circ$) but concentrate on the Galactic plane with $|b| < 5^\circ$ (Cordes et al. 2006). This implies that the PALFA survey will mainly cover a different part of the sky than the southern HTRU survey, making the two surveys complementary rather than competing. The PALFA survey commenced in 2005 and is still ongoing.

While tracks of the Green Bank Telescope (GBT) were refurbished over the northern summer of 2007, a research team carried out a drift scan survey for pulsars (Boyles 2008, Boyles et al. 2011) at 350 MHz. It covered about 10,300 square degrees of the sky between declinations of -21 and 26 degrees. The data from this survey is still being searched for pulsars, and has discovered 30 pulsars including 7 MSPs³ to date.

The Fermi collaboration is also searching for pulsars, using the Large Area Telescope (LAT) onboard the Fermi Gamma-ray Space Telescope (Abdo et al. 2010). This survey applies two different search strategies to find gamma-ray emission from pulsars: one searches for gamma-rays from known pulsars, using the ephemerides from radio and X-ray observations, and the other is a “blind period search” that is looking for gamma-ray pulsations from neutron star candidates. There is also an effort being made trying to find the radio counterparts of the LAT sources using some of the large radio telescopes (Camilo et al. 2009, Keith et al. 2011b, Ransom et al. 2011, Ray et al. 2012). The Fermi Pulsar Search Consortium has currently detected 101 γ -ray pulsars, including more than 30 MSPs⁴.

³<http://www.as.wvu.edu/~pulsar/GBTdrift350/>

⁴For the latest updates, please see:
<https://confluence.slac.stanford.edu/display/GLAMCOG/Public+List+of+LAT-Detected+Gamma-Ray+Pulsars>

1.4 The Millisecond Pulsar Population

Population synthesis studies of pulsars attempt to use the properties of the known pulsar population to derive the underlying total population of pulsars in our Galaxy. This has been done for ordinary isolated pulsars by a number of authors using data from various pulsar surveys and has resulted in different models describing e.g. pulsar velocities (e.g. Faucher-Giguère & Kaspi 2006, Hobbs et al. 2005) and luminosities (e.g. Faucher-Giguère & Kaspi 2006, Ridley & Lorimer 2010), and the Galactic distribution of pulsars (e.g. Lorimer et al. 2006).

In the case of millisecond pulsars, the situation is a bit different. For a long time, all Galactic MSP population studies carried out were badly affected by small-number statistics (Kulkarni & Narayan 1988, Johnston & Bailes 1991). With the Parkes Southern Pulsar Survey, the number of known MSPs increased significantly and made it possible to perform a millisecond pulsar population study for the local solar neighborhood. Lyne et al. (1998) carried out such an analysis using the 19 MPSs detected in the survey to estimate the local surface density of MSPs, the MSP birth rate and their space velocities.

More recently, Story et al. (2007) performed an MSP population study of radio and γ -ray pulsars from the Galactic disk by using 56 MSPs discovered in one of 10 different radio surveys. Their model predicts the numbers of radio-loud and radio-quiet millisecond pulsars detectable as γ -ray sources. They estimate the Galactic birthrate of MSPs to be $4 - 5 \times 10^{-4}$ MSPs per century.

One large issue in pulsar population studies is biases introduced by the necessity of using pulsars discovered in different surveys using different telescopes, receivers and back-ends. With the new discoveries in the current large-scale surveys, we can improve the results from previous pulsar population studies, both because of the higher total number of MPSs known and because with the higher sensitivity we can get data on a larger number of detected MSPs within the same survey. We have made an attempt to model the Galactic population of millisecond pulsars using the discovered and detected MSPs in the intermediate latitude part of the southern HTRU survey, which is described in Ch 6 in this thesis.

1.5 Thesis Outline

This thesis will describe work done in connection with the southern HTRU survey. It will mainly focus on pulsar searches in the intermediate latitude part of the survey and discuss what the results from this survey can tell us about the general millisecond pul-

sar population. It will also discuss one particular source in detail, the radio magnetar PSR J1622–4950, which was discovered in the HTRU survey.

The structure of the thesis is as follows:

Chapter 2

The HTRU survey setup is described, as well as details about the HITRUN processing pipeline, processing times and pulsar candidate selection.

Chapter 3

The discovered pulsars in the HTRU medlat survey are presented, together with a discussion of their properties, both for some individual sources and for the HTRU sample as a whole. This chapter will also include an analysis of the previously known pulsars detected in the medlat survey and discuss the survey sensitivity and overall performance.

Chapter 4

The discovery of the radio magnetar PSR J1622–4950 is discussed. This chapter has been published in full in the *Astrophysical Journal Letters* (Levin et al. 2010)

Chapter 5

Continued multifrequency radio band observations of PSR J1622–4950 are presented, including polarisation properties and single pulse analysis. This chapter has been published in full in the *Monthly Notices of the Royal Astronomical Society* (Levin et al. 2012).

Chapter 6

A millisecond pulsar population analysis is described, based on the discoveries from the HTRU medlat survey combined with all detections of previously known MSPs in the survey data set.

Chapter 7

A summary of the major findings in this thesis is presented along with suggestions for future research.

2

The High Time Resolution Universe Survey - Survey Strategy and Analysis

The High Time Resolution Universe survey for pulsars and fast transients (HTRU) commenced its southern survey at the Parkes 64-m Radio Telescope in November 2008 and shortly thereafter the northern survey achieved first light at the Effelsberg 100-m Radio Telescope. Since then, both the northern and the southern surveys have covered a large part of the sky and made many discoveries. Both surveys are still underway at the time of writing. This chapter will describe the details of the southern survey, including instrumentation at the telescope, survey parameters, processing pipeline and pulsar candidate selection. Many of the details in this chapter were previously published by the survey team (Keith et al. 2010). Here we focus on the Swinburne pipeline and more deeply discuss the processing details and the candidate selection strategy used at Swinburne.

2.1 Parkes Radio Telescope and its Pulsar Search Hardware

The 64-m dish of the Parkes Radio Telescope is located in New South Wales, Australia. It was opened in 1961, and has since gone through a number of upgrades and refurbishments to keep up to date with the advances in instrumentation and technology and to maintain its status as a world-class research facility. It became famous to the world as it was part of the tracking of the Apollo 11 moon landing in 1969. In the pulsar community however, it is well-known for discovering more than half of the currently known pulsars. One of the reasons for its great success in pulsar astronomy is its location. It is not the largest single radio dish in the world, but it is the largest one dedicated to astronomy in the southern hemisphere, and hence a large part of the Galactic plane that is below the horizon for the other large radio telescopes in the world is visible at Parkes.



Figure 2.1 Parkes Radio Telescope. Photo credit: John Sarkissian, CSIRO

By far the most successful pulsar survey carried out to date is the Parkes Multibeam survey (PM; Manchester et al. 2001), which discovered over 700 pulsars and almost doubled the known population. The reason for the success of this project was a combination of the choice to observe at higher frequencies than previous surveys and the use of the 13-beam 21-cm multibeam receiver (Staveley-Smith et al. 1996), which provided lower system temperatures and 13 times the normal 20-cm field of view. The 21-cm multibeam receiver is described in more detail in Ch. 2.1.1.

Though highly successful, the PM survey had limited frequency resolution, which affected its ability to detect short duration pulses from MSPs at larger distances. This was due to the analogue filters in the backend and also to the processing power available at the time of the survey (in the 1990s). Today this is different. As technology advances, analogue systems are replaced by digital equipment that provide higher time and frequency resolution at lower cost than before. Increased frequency resolution allows us to better compensate for the dispersive effects of the interstellar medium and, in combination with higher time resolution, provides increased sensitivity to short duration pulses, such as those from MSPs. We are also able to store and process substantially larger data sets today than was possible 15 years ago, which is a key factor in designing improved pulsar surveys. The HTRU survey has taken advantage of these technological improvements in the design and



Figure 2.2 Photo of the Parkes 21-cm Multibeam Receiver. Photo credit: CSIRO¹

implementation of the Berkeley-Parkes-Swinburne-Recorder (BPSR) backend, described in Ch. 2.1.2 below.

2.1.1 The Multibeam Receiver

The ability to quickly cover a large area of the sky was made possible by the use of the Parkes 21-cm Multibeam Receiver (Staveley-Smith et al. 1996). It consists of a central feed surrounded by two hexagonal rings of six feeds each, creating a star-like pattern of 13 beams as shown in Fig 2.3. This pattern can be tessellated on the sky to efficiently cover the sky with little loss of sensitivity between beams. The central feed has a symmetric beam pattern with a system temperature of ~ 23 K at 1400 MHz (Keith et al. 2010). The other feeds have slight ellipticities and gain degradation that increase with the distance from the centre beam (see Table 2.1). Both polarisations for each beam are down-converted from 1182–1582 MHz to 0–400 MHz.

Unfortunately, due to a very strong source of radio frequency interference (RFI) we have been forced to block a part of our frequency band. This interference is caused by the Thuraya 3 geostationary communications satellite, which transmits a space-to-earth signal in the 1525 – 1559 MHz band. We installed low-pass hardware filters after the receiver to

¹<http://www.atnf.csiro.au/research/multibeam/>

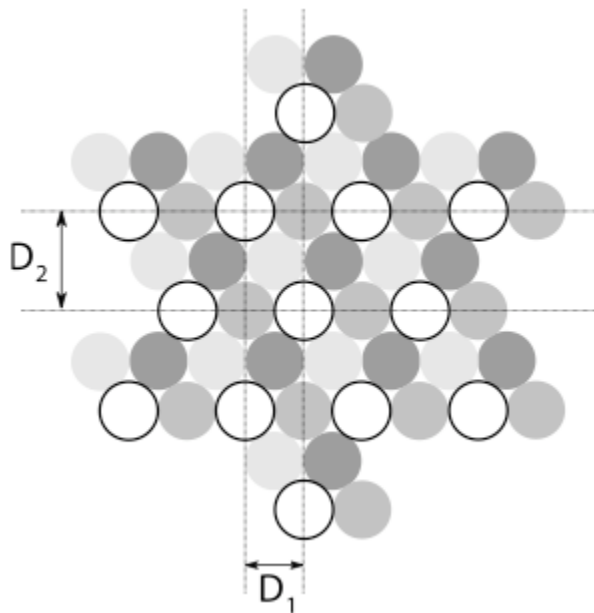


Figure 2.3 The beam pattern of the multibeam receiver. The black unfilled circles indicate the 14-arcmin half-power beam width of each of the 13 beams of the receiver. The separation D_1 is also equal to this 14-arcmin width and $D_2 = \sqrt{3}D_1$. The filled circles show three further pointings interleaved to make up the shape with which the entire survey region is tessellated. Figure is taken from Keith et al. (2010).

Table 2.1 Multibeam receiver specifications, showing the centre feed, the inner ring and outer ring of feeds. Values are taken from Manchester et al. (2001)

Beam	Centre	Inner ring	Outer ring
Telescope gain (K Jy ⁻¹)	0.735	0.690	0.581
Half-power beamwidth (arcmin)	14.0	14.1	14.5
Beam ellipticity	0.0	0.03	0.06
Coma lobe (dB)	none	-17	-14

filter this part of the band, which limits the upper end of our observing band to 1522 MHz. Hence the effective observing bandwidth is 340 MHz, centered on 1352 MHz.

2.1.2 The Berkeley Parkes Swinburne Receiver Backend

The astronomical signal collected with the multibeam receiver is down converted and recorded on the Berkeley Parkes Swinburne Receiver (BPSR) backend. BPSR consists of 13 dual-polarisation digital spectrometers, which are implemented using the IBOB² platform developed by the CASPER group³ as described in McMahon (2008). The spectrometers are connected to 13 server-class workstations, that format the data and write it to disk. The 13 IBOBs have two analogue-to-digital converters and two polyphase filters each, implemented on an FPGA⁴. Each IBOB samples orthogonal polarisations at 800 MHz using 8 bits per sample, then divides each signal into 1024 spectral channels of width 390 kHz using a 2-tap polyphase filterbank. Each channel is then detected and integrated over 25 samples, yielding output with 64 μ s time resolution. The spectrometer outputs 32 bits per sample, which are linearly scaled, decimated to 8 bit samples and written to a single UDP⁵ packet with a 2048-byte payload containing 1024 channels times two polarisations. Each packet is sent to a 10 Gb/s Ethernet interface connected directly to a Dell PowerEdge 1950 server via a CX4 cable. Thereafter the data is collected in 10 s blocks on the server. Both polarisation streams are summed and normalised by subtracting the mean and dividing by the standard deviation. Finally the data are decimated to 2 bits per sample and written to disk at a rate of 32 Mb s⁻¹.

All data is duplicated and written to two sets of magnetic tapes. One of them is written directly in the control room at Parkes, while the other is written at the Green Machine

²Internet Break-Out Board

³the Center for Astronomy Signal Processing and Electronics Research at the University of California, Berkeley

⁴Field Programmable Gate Array

⁵User Datagram Protocol

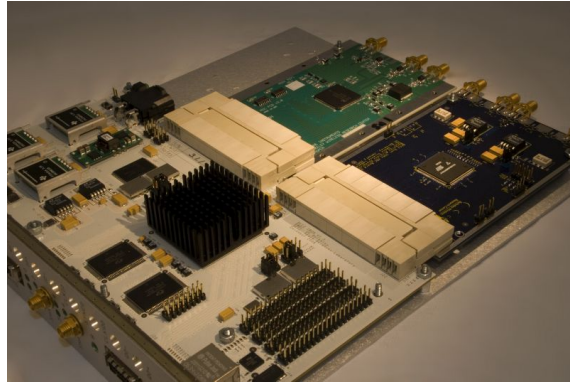


Figure 2.4 Example of an IBOB. In the top right are two analogue to digital converters. The heat sink covers the FPGA. See text for more detail. Photo credit: CASPER⁶

Table 2.2 Summary of the survey parameters.

Parameter	Value
τ_{samp}	$64 \mu\text{s}$
ν_{centre}	1.352 GHz
B	340 MHz
$\Delta\nu_{\text{chan}}$	390.625 kHz
N_{chan}	870

supercomputer at Swinburne. A 1 Gb s^{-1} fibre link is dedicated to transfer survey data directly from Parkes to Swinburne, where the data get temporarily stored on disk and then written to tape. While on disk, some of the data are immediately picked up and processed by the pipeline at the Green Machine, depending on availability of free computer cluster nodes. The remaining data are read off tape and processed at a later stage.

2.2 HTRU Survey Setup

The HTRU survey is aimed at covering the entire southern sky. To enable this and at the same time optimise the scientific return in a finite amount of telescope time, it is divided into three sub-surveys. Except for sky coverage and observing time, all survey parameters are equal for all three parts. A summary of the survey parameters can be found in Table 2.2 and the division of the sub-survey regions are in Table 2.3. The low latitude section (deep) covers the Galactic plane in a 7-degree wide strip with parameters $-80^\circ < l < 30^\circ$,

⁶<https://casper.berkeley.edu/wiki/IBOB>

Table 2.3 Division of the HTRU survey regions.

Survey Region	Deep	Medlat	Hilat
	$-80^\circ < l < 30^\circ$	$-120^\circ < l < 30^\circ$	$\delta < +10^\circ$
	$ b < 3.5^\circ$	$ b < 15^\circ$	
τ_{obs} (s)	4300	540	270
N_{beam}	15 990	95 056	443 287
Data length (samples)	$\sim 2^{26}$	$\sim 2^{23}$	$\sim 2^{22}$
Data/beam (GB)	16.0	2.0	1.0
Total observing time (hrs)	1469	1096	2557
Total data (TB)	256	190	443

$|b| < 3.5^\circ$, where (l, b) is Galactic longitude and Galactic latitude respectively. The low latitude survey is aimed at finding weak, distant pulsars by using a long observation time of 70 minutes, which is twice as long as the integration time used for the PM survey. The intermediate latitude (medlat) survey has a wider span and covers $-120^\circ < l < 30^\circ$, $|b| < 15^\circ$. In this region, old recycled millisecond pulsars are expected to be found and with the improved frequency resolution of the HTRU survey we should detect pulsars discovered during the PM survey, despite the much shorter observation time of 9 minutes of the medlat survey. In addition, in this part of the project we should be able to discover MSPs at higher dispersion measures than previously known, again due to the better frequency resolution. The short integration time allows us to survey this important part of the sky quickly. The majority of the work carried out for this thesis is connected to the HTRU medlat survey. The remaining visible southern sky, with a equatorial declination, δ , lower than $+10^\circ$, will be covered in the high latitude region (hilat). The 4.5-minute observations will give us a snapshot of the transient sky at our high resolution.

2.2.1 Survey Sensitivity

Estimating the minimum detectable flux density is essential for both planning a pulsar survey and evaluating the results of a completed survey. However, the survey sensitivity varies with different regions of the sky and with respect to different pulsars. This makes absolute determination of the limiting flux density complicated. An estimate of the theoretical limit can be made by assuming the values for a “typical” pulsar put at various positions in the Galaxy. For this analysis the radiometer equation is used, giving the minimum detectable flux density in the centre of the central beam of the 21-cm Multibeam

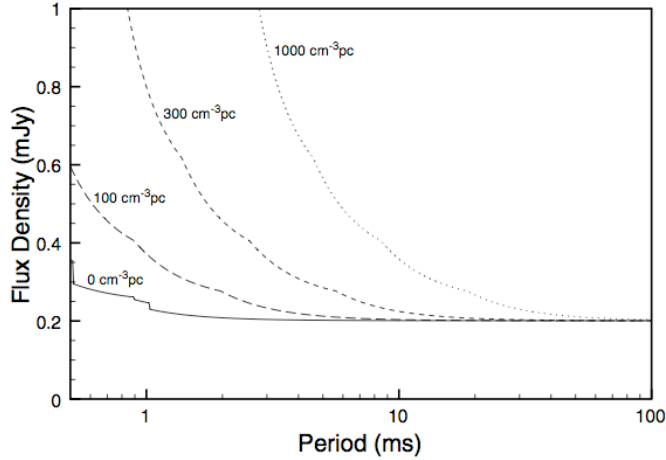


Figure 2.5 The medlat survey sensitivity is shown as function of pulsar spin period for four different values of DM. A pulse duty cycle of 0.05 is assumed. Figure taken from Keith et al. (2010).

Receiver as

$$S_{\min} = \frac{S/N_{\min}(T_{\text{rec}} + T_{\text{sky}})}{G \sqrt{n_{\text{pol}} t_{\text{int}} \Delta\nu}} \quad (2.1)$$

where S/N_{\min} is the minimum acceptable signal-to-noise, T_{rec} and T_{sky} are the receiver and sky noise temperatures, G is the system gain, n_{pol} is the number of polarisations recorded, t_{int} is the integration time and $\Delta\nu$ is the observed frequency bandwidth. The sky noise temperature is strongly dependent on the observed sky region, and contributes significantly to S_{\min} only at low Galactic latitudes. Using mean values of $T_{\text{sky}} = 7.6, 2.5$ and 1.0 K for the deep, medlat and hilat surveys, together with $S/N_{\min} = 8$, $T_{\text{sys}} = 23\text{ K}$, $n_{\text{pol}} = 2$ and $G = 0.735$ results in values for S_{\min} of $0.20, 0.47$ and 0.61 mJy for the three surveys respectively (Keith et al. 2010).

However, the practical limiting flux density also depends on the pulse duty cycle for each pulsar, which will lower the values of S_{\min} calculated above. The sensitivity of the Fourier-based detection algorithm used in the survey pipeline depends on the spin period, the pulse duty cycle and the DM for each pulsar. In Fig 2.5 the mean limiting flux density for the medlat survey is shown as function of pulse period for four different values of the DM, assuming a pulse duty cycle of 0.05.

To measure the actual sensitivity limit, we have analysed data for previously known pulsars detected in the HTRU data and compared the theoretical S/N values for each pulsar to the values from the processing pipeline. This analysis is discussed in more detail

in Sec 3.2.

2.3 Processing Details

The very large data set produced by the HTRU survey creates challenges during data processing, both in management of the large data sizes and in processing times. This chapter will describe the processing pipeline and routines that I have used to process the intermediate latitude part of the survey to search for regularly emitting pulsars. Other members of the survey team have processed different parts of the survey and/or searched for transient sources using different methods, which are presented elsewhere(e.g. Burke-Spoliar et al. 2011)

2.3.1 The HITRUN Search Pipeline

When searching for pulsars, a standard strategy is frequently used and is well tested on different data sets. This search procedure involves de-dispersing the raw data at a number of DM trials, which produces time series that can be searched for periodicities using a Fast Fourier Transform (FFT). The highest Signal to Noise (S/N) periodicity candidates are then chosen and the raw data is folded at the period and DM of the candidate, in order to visualise the signal. Following this general strategy, the HITRUN search pipeline is composed by a number of steps outlined below. For an overview of these step, a flow chart for the entire processing pipeline is shown in Fig 2.6.

RFI mitigation

The first part of the pipeline is a routine that identifies short duration or narrow channel radio frequency interference in the data and remove these signals from the search. In the HITRUN pipeline this is done in two parts, called *debird* and *tzap*.

The first routine, *debird*, cleans each frequency channel from strong RFI signals, by first dividing the data up into its separate 1024 frequency channels. It then performs an FFT on each of those single channel files to search for strong periodic signals. If the strongest signal in an individual channel has a S/N above a certain threshold, it gets flagged as a bad channel and will not be included in the search. After all of the channels have been checked, a list of bad channels is created. At this stage, if $\geq 50\%$ of the channels are flagged as bad channels, the threshold is raised and the FFT procedure starts over. In the first pass through the data, the threshold is set to S/N=15, and it is then incremented by $\sqrt{2}$ per every new pass. This is done to account for very strong pulsars at low DM, which

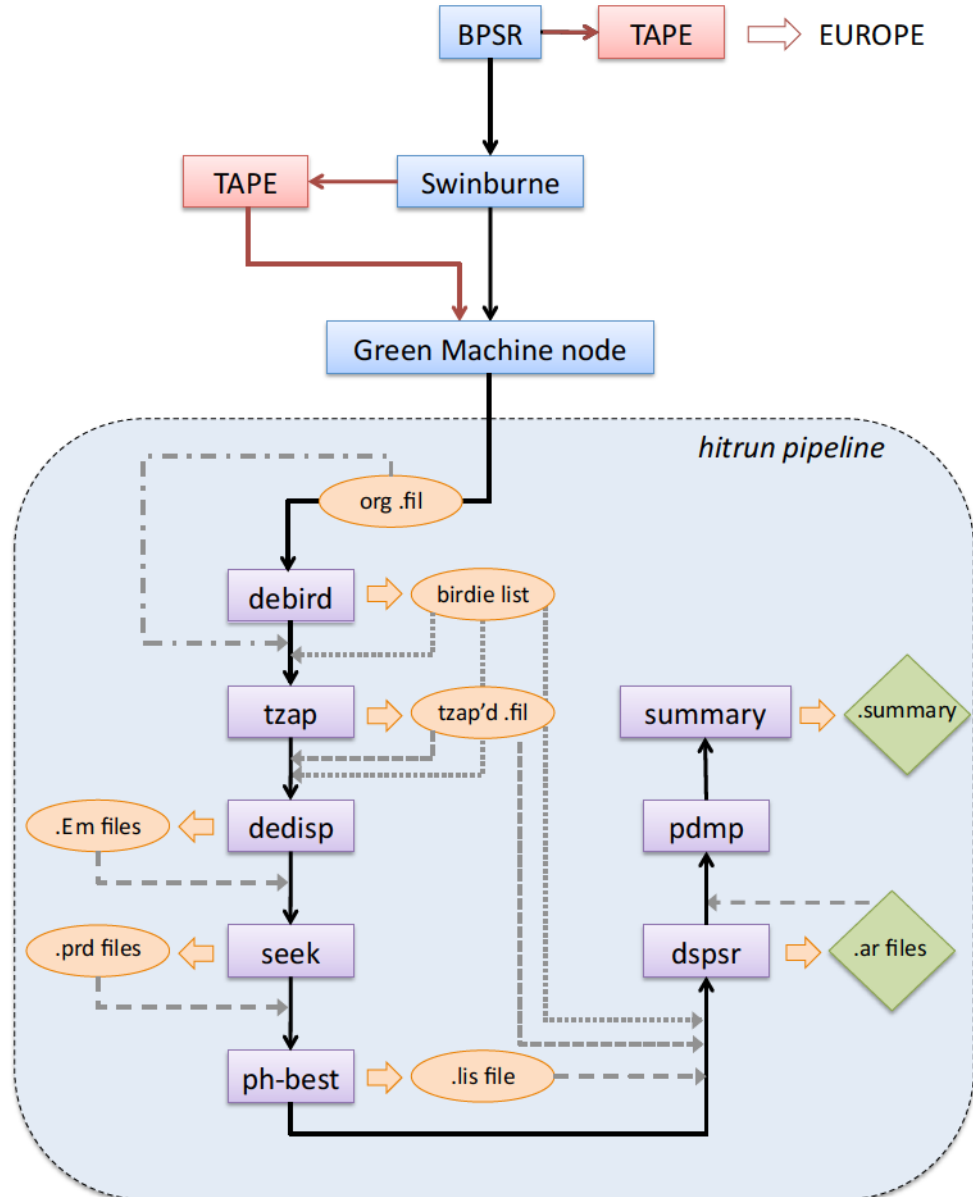


Figure 2.6 Flow chart for the HITRUN pipeline. The black arrows show the order of processing steps, represented by purple rectangles, in the pipeline. For each step, new files that are created are shown in ellipses and dashed/dotted lines show where these files are being used. The final output of the pipeline are shown as green diamonds. See text for details on each step.

might show up even in individual frequency channels. Due to the RFI from the Thuraya 3 satellite and the filters installed in the top of our frequency band, we have chosen to always flag these 145 channels as bad. The list of bad channels will be used to blank out those channels later in the search pipeline, which will remove a large fraction of narrow band RFI from the search.

The second part, *tzap*, searches for individual time samples with excessive power. It begins by creating a time series at $DM = 0$ by summing the data over the frequency band. This 0 DM time series is searched for samples that deviate from the mean by more than 5σ . Each time sample with a value higher than this threshold will get flagged as bad, and will be replaced by a random noise value in the raw data file. This removes any short duration RFI signals from the data file. To remove longer duration RFI bursts, 2, 4, 8, 16 and 32 adjacent samples are summed together and the search is repeated.

De-dispersion

Since the dispersion measure of the pulsar signals for which we are searching are unknown, we need to search through a number of DM trial values for each data file. De-dispersing the data is a time consuming task, hence optimization of the interval between these DM trials is very important. In the HITRUN pipeline we use the program *dedisperse_all* for de-dispersing the data. This program is based on the *dedisperse* routine in the SIGPROC package⁷ and was modified to run on a range of DM values at once and the possibility to use several CPU cores in parallel. We have also added a routine that uses a new algorithm to calculate the steps between DM trial values. This routine determines the next DM trial value by considering the amount of pulse broadening caused by the size of the DM step. The effective width of a pulse at the new trial value, DM , with respect to the last trial value, DM' , is:

$$w_{\text{eff}}(DM, DM') = \varepsilon \cdot w_{\text{eff}}(DM', DM') \quad (2.2)$$

where ε is the pulse broadening fraction due to the DM step. We have chosen to tolerate a total pulse width smearing of 25% due to the DM step in comparison to the value at the last DM, hence we put $\varepsilon = 1.25$. The effective pulse width is given by:



$$w_{\text{eff}}^2 = t_{\text{scatt}}^2 + t_{\text{samp}}^2 + t_i^2 + t_{\text{DM}}^2 + t_{\Delta \text{DM}}^2 \quad (2.3)$$

⁷<http://sigproc.sourceforge.net/>

where t_{scatt} is the scattering time, t_{samp} is the sampling time and t_i is the intrinsic width of the pulse. $t_{\Delta \text{DM}}$ is the broadening due to the dispersion measure given by:

$$t_{\Delta \text{DM}} = 8.3 \frac{B \cdot DM}{\nu^3} \quad (\mu\text{s}) \quad (2.4)$$

where B is the channel bandwidth [MHz], and ν is the center frequency [GHz]. $t_{\Delta \text{DM}}$ refers to a pulse broadening over all frequency channels due to the dispersion measure step size and is given by

$$t_{\Delta \text{DM}} = \frac{8.3}{4} \frac{N_{\text{chan}} \cdot B \cdot \Delta DM}{\nu^3} \quad (\mu\text{s}) \quad \boxed{\text{---}}$$

where N_{chan} is the number of frequency channels and $\Delta DM = DM - DM'$ is the dispersion measure interval. Combining eq 2.2 – 2.5 we can derive an expression for the new dispersion measure as a function of the last DM value, which we can write as

$$DM = N_{\text{chan}}^2 \alpha DM' + \sqrt{16\alpha(\varepsilon^2 - N_{\text{chan}}^2 \alpha) DM'^2 + 16\alpha\beta(\varepsilon^2 - 1) \left(\frac{\nu^3}{8.3B} \right)^2} \quad \boxed{\text{---}} \quad (2.6)$$

where $\alpha = 1/(16 + N_{\text{chan}}^2)$ and $\beta = (t_{\text{scatt}}^2 + t_{\text{samp}}^2 + t_i^2)$. Note that the first two terms in this equation depend on only N_{chan} and ε , implying that the values of B and ν as well as the values for t_{scatt} , t_{samp} and t_i become less important for high DM values. Using the parameters for the HTRU survey in Table 2.2 and assuming $t_{\text{scatt}} = 0$ and $t_i = 40\mu\text{s}$, we get approximately 1200 DM steps for values $0 < DM < 1000 \text{ pc cm}^{-3}$.

The output from *dedisperse_all* is one time series per DM step, in which the data has been corrected for inter-channel dispersion delay and summed in frequency. The time series are saved on disk for further processing.

Periodicity search

The search for periodic signals in the time series is performed using the SIGPROC program *seek*. It converts the time series into a power spectrum using an FFT. The power spectrum generally has a strong red-noise component at frequencies $< 10 \text{ Hz}$, which is removed by subtraction of a running mean and division by a running variance, which simultaneously normalises the spectrum. After this is done, the power spectrum is searched for signals with $S/N > 6$. To reclaim power in the harmonics of narrow pulses, we also search spectra that have had 2, 4, 8 and 16 harmonics summed. Every signal above the S/N threshold in each of the DM trials is recorded for later sorting and cross-checking.

To speed up the search process we run multiple instances of *seek* simultaneously, usually

one for each CPU core.

Periodicity sorting

All the periodic signals found by *seek* are then sorted and grouped together by frequency. This is done with the program *ph-best* from the PULSARHUNTER package. *ph-best* collects all the periodic signals with the same frequency from different DM trials, and signals that are harmonically related, into one candidate periodicity. It returns a list of the 100 pulsar candidates with the greatest S/N from each data file.

Candidate folding

Each candidate period and DM found in the sorting step is then used to produce average pulse profiles of the candidate by folding the RFI-mitigated data file. In the HITRUN pipeline, we use the *dpsr* software⁸ to create candidate archives containing 128 phase bin pulse profiles for each of 16 frequency bands and 32 sub-integrations, added together into one archive per candidate. The *dpsr* program can run on multiple processing cores to speed up the processing.

Period and DM optimisation

The program *pdmp* from the PSRCHIVE package (Hotan et al. 2004) is used to search for the optimal period and DM in a small range around the values found in the Fourier domain search. The values of period and DM that give the highest folded S/N are then used to make the final plots of the candidate.

Creating summary files

For easier viewing of the candidates as well as for long-term archival purposes, we extract a number of relevant properties from each pulsar candidate archive and collect those in summary lists, one for each observed beam. The entries in the summary list are: candidate name, telescope beam number, galactic latitude, galactic longitude, MJD of observation, period, period error, DM, DM error, pulse width in seconds, pulse width as a percentage of pulse period, harmonic fold number, folded S/N, spectral S/N and three scintillation diagnostics.

⁸<http://dpsr.sourceforge.net/>

Table 2.4 HTRU survey processing times

Routine	Processing time (s)	Processing time (min)
RFI mitigation	1,081	18
De-dispersion	3,289	55
Periodicity search and sorting	931	15
Candidate folding	1,257	21
Period and DM optimisation	97	2
Total processing time per medlat beam	6,655	111
Total processing time all medlat	$\sim 6.3 \times 10^8$	$\sim 1.1 \times 10^7$
Total processing time on cluster	= 7321	4-CPU days

Separate folding of known pulsars

The last step in the pipeline is a check for any previously known pulsars in each survey beam. Here we cross-check the position of the current beam with the pulsar catalogue (psrcat⁹) for any known pulsars within a 15' radius around the centre of the current beam. If a known pulsar is found, the relevant data are folded at the period and DM recorded in the catalogue. We then compare the period and DM of the pulsar with those of the candidates in the summary list, to check if the pipeline detected the known pulsar, and finally we make an entry in a known pulsar database for later reference.

2.3.2 Processing Setup and Run Times on the Green Machine

The majority of the data processing for the HTRU survey in Australia, and all processing of the data used in this thesis, has been carried out on the *Green Machine* computer cluster at Swinburne University. The Green Machine consists of 160 nodes, each with 2 quad-core 64-bit processors, 16 GB of RAM and 2×500 GB of disk space.

The first step in the processing setup is to locate data on disk that are ready to be processed. This is done in two ways. During observing sessions, survey data are automatically transferred to Swinburne from Parkes. At Swinburne, the data are temporarily stored on disk, from which the data are then written to tape for storage. During this time, the pipeline can pick up the new data files directly from disk and process as many as possible before the disks fill up with new data. The rest of the data files can then be read off tape during periods without telescope time, and processed in the same way.

After the pipeline processing has finished, we save the candidate folded profiles and

⁹<http://www.atnf.csiro.au/research/pulsar/psrcat/>

summary lists for each data file on disk and start over with a new file. Using the queue system on the Green Machine the HTRU project was granted access to up to 512 CPU cores running simultaneously, depending on cluster availability. The processing times for each part of the pipeline as well as the total processing times for the intermediate latitude survey can be found in Table 2.4.

2.3.3 Candidate Selection

A large-scale survey like HTRU will naturally return a large number of pulsar candidates. In the medlat survey alone each of the 95 056 beams return 100 candidates, giving us more than 9.5 million pulsar candidate plots. It is therefore very important to find a time effective and yet thorough way to sift through the candidates and sort out promising pulsar candidates from the interference and noise. In this thesis, the approach we have chosen is to automatically select candidates that have a combination of certain properties and then visually inspect the most likely of those.

The candidate selection process is as follows:

Candidates are grouped into sets depending on observing day. We have found this grouping criteria very useful, as a lot of RFI is present during limited periods of time. That is, if a particular interference signal is present in one observation, it is very likely present also in the next observation, but not necessarily in an observation collected one week later.

Each group of candidates is then run through a selection mask in a first attempt to remove the most unlikely candidates. The criteria built into this mask select candidates with $DM > 0$, folded S/N > 9 and pulse width $w < 0.4P$ if the candidate period $P > 100\text{ ms}$ (and all widths at shorter periods). In this analysis, we have also chosen to only consider candidates with periods between 1 ms and 5 s. This step eliminates around 95% of the pulsar candidates, and saves the surviving $\sim 410\,000$ candidates in new “selected” lists.

After that, the lists of selected candidates from a given day are divided up into shorter and more manageable lists of 1000 candidates, that are read into the plotting program *mbplot*. The values in the lists, which consist of “summary list” style columns as described in Sec 2.3.1, can be plotted in 2D graphs with user selected axes and each candidate diagnostic plot can easily be viewed by selecting and clicking with the mouse. The first step in the viewing process is to remove candidates with the same pulse period from different parts of the sky, since we expect pulsars to be unique while RFI often is not. This is done by manually viewing one of the candidates with a reoccurring period, to check it is

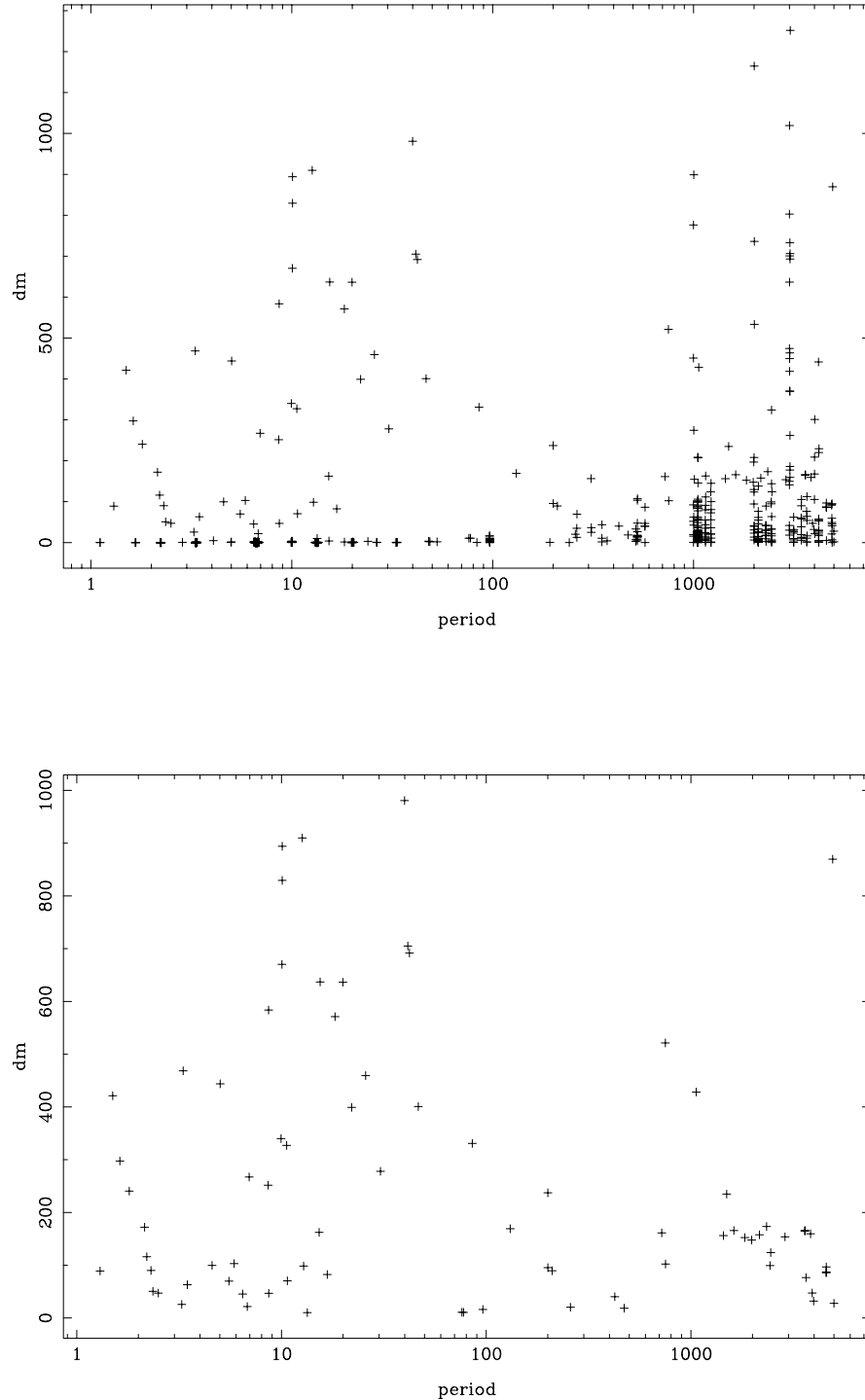


Figure 2.7 Example of output from the graphical candidate viewer mbplot. The top panel shows data loaded into the viewer before de-striping and the bottom plot shows the candidates that are left after de-striping (see text for more details).

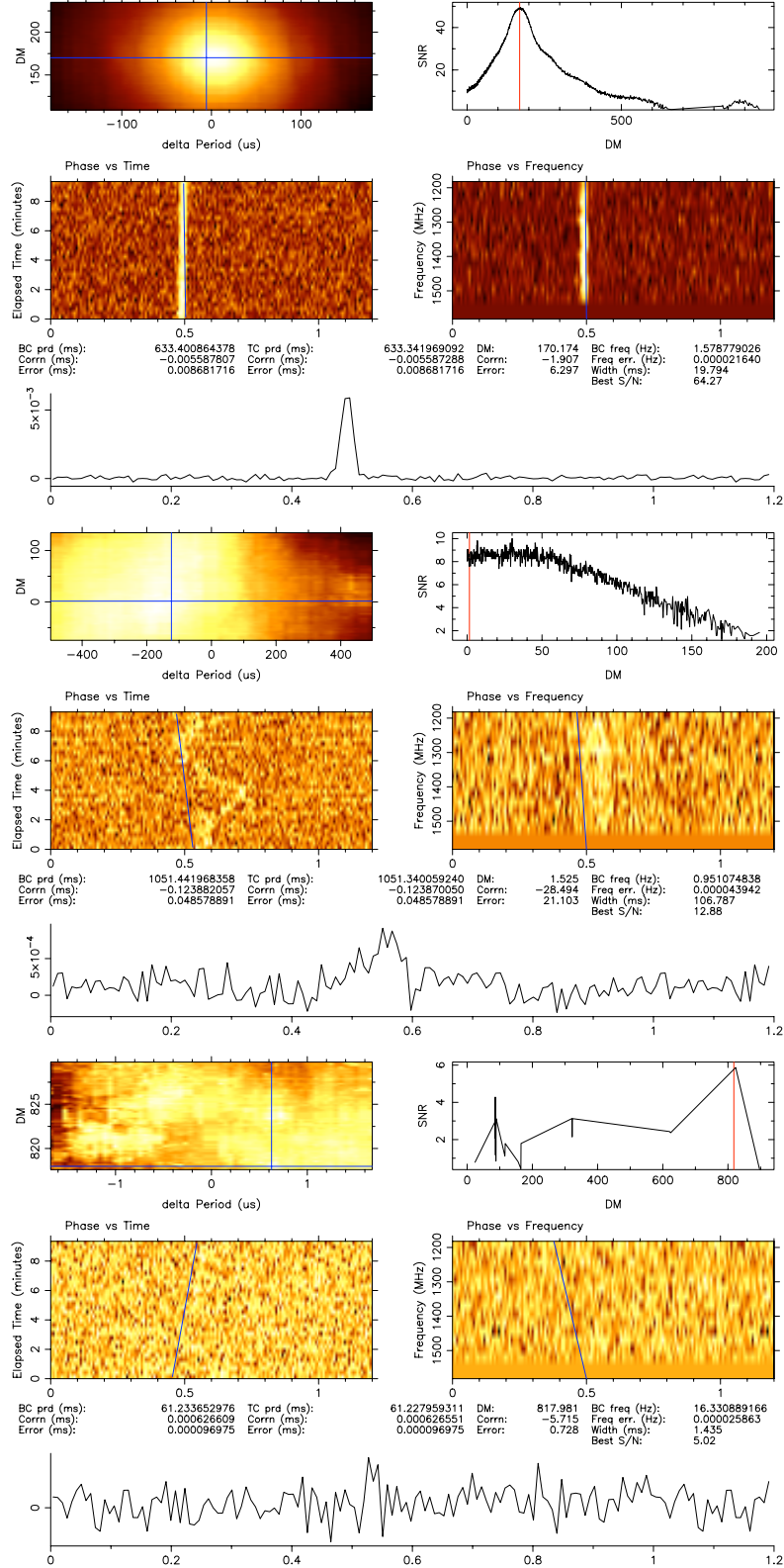


Figure 2.8 Example of pulsar candidates. The top panel contains the bright and slow HTRU pulsar J1803-3328, the middle panel is an example of pulsar-like RFI at $DM=0$ and the bottom panel shows a random noise-like candidate.

not a very strong pulsar that has shown up in several nearby observing beams, and then “de-striping” the candidate graph by removing all candidates with the same period. The effect of the de-striping process is shown in Fig 2.7. We then remove all pulsar candidates with $DM < 5 \text{ pc cm}^{-3}$. This criteria is justified by the very low numbers of pulsars known with $DM < 5 \text{ pc cm}^{-3}$ in the HTRU medlat survey region (only 2 of the 1124 pulsars in the catalogue) and since this part of the parameter space is highly contaminated by interference signals, it significantly decreases the number of spurious candidates.

The next step is to manually view the pulsar candidate plots, starting with the most likely ones and moving down in probability. This is done by choosing a point on the *mbplot* graph, viewing the corresponding *pdmp* diagnostic plot and finally deciding the fate of the candidate by putting it into one of three categories: possible new discovery, previously known pulsar or RFI. Examples of a few different types of candidates can be found in Fig 2.8. The candidates that are considered RFI are immediately removed from the graph to not be confused for an unseen candidate. Points corresponding to potential discoveries or previously known pulsars are updated on the display by changing in shape and color, and a duplicate copy of their diagnostic plot is saved for future reference.

3

The High Time Resolution Universe Survey - Discoveries and Detections

Using the techniques outlined in the previous chapter, the HTRU medlat survey has been processed in full using the Green Machine at Swinburne. At the time of writing the HTRU medlat survey has returned 104 pulsar discoveries, with another ~ 10 very promising pulsar candidates awaiting confirmation at the telescope. A large part of those discoveries (26 sources) are of millisecond pulsars. This chapter will present an overview of all discoveries and discuss some of the more interesting sources individually. In addition, the medlat survey area covers the positions of 1108 previously known pulsars. An analysis of the detectability of these pulsars by the HITRUN pipeline is also presented.

3.1 HTRU Medlat Discoveries

The HTRU medlat survey has so far confirmed 104 new pulsar discoveries. The basic properties of all of these pulsars are listed in Tab 3.1. References to the discovery papers for the published pulsars are also listed, in which more detailed information on particular pulsars can be found.

The spatial distribution of the HTRU medlat pulsars is shown in Fig 3.1 together with the previously known pulsar sample. The medlat survey region is shown as a grey box. It is clear from this plot that we have discovered more new pulsars at higher latitudes than we have at low latitudes. The reason for this is primarily that previous surveys covering the Galactic plane region had a higher sensitivity than the surveys at higher galactic latitudes. In particular in the Parkes Multibeam survey, which covered $|b| < 3.5^\circ$ with 35 minute observations, a large number of pulsars was discovered (> 700 ; Lorimer et al. 2006). However, even though the HTRU medlat survey has shorter integration time and is less

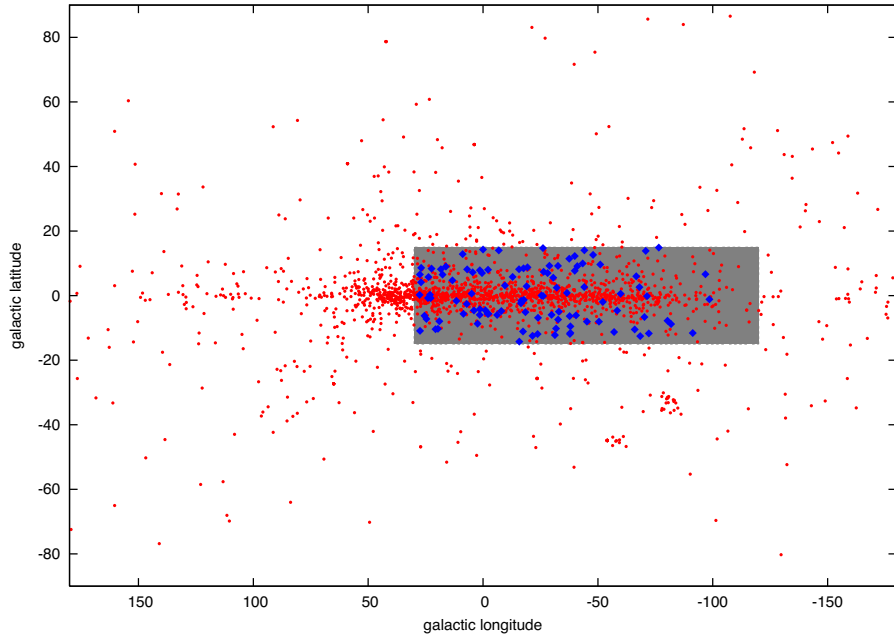


Figure 3.1 Spatial distribution of HTRU medlat discoveries. Red points represent previously known pulsars from the pulsar catalogue and blue diamonds represent HTRU medlat discoveries. The grey box shows the medlat survey region.

sensitive to slow pulsars than the PM survey, we have made a number of new discoveries in this area of the sky. These pulsars could have been missed in the PM survey due to the pulsar position being on the edge of the survey beam or the corresponding beam included a large amount of interference. Another possible reason is that the pulsars were missed due to scintillation. However, only a few of the newly discovered pulsars in the PM survey region have $DM \lesssim 100 \text{ pc cm}^{-3}$, making scintillation an unlikely cause.

3.1.1 Ordinary Pulsars

The HTRU medlat sample includes 78 newly-discovered ordinary, slow pulsars. Here we define a slow pulsar as a source with $P > 100 \text{ ms}$.

The dispersion measures of the new slow pulsar discoveries are mainly clustered in the range $DM < 200 \text{ pc cm}^{-3}$ with only a few new pulsars above $DM = 400 \text{ pc cm}^{-3}$, as shown in Fig 3.2. This is expected since the largest part of the known pulsars with such high values of DM was discovered in the PM survey and with its higher sensitivity to slow pulsars, it could find sources that are further away in the Galactic plane. We instead expect that the HTRU deep survey will discover a large number of pulsars in this region of parameter space, since it will have both higher frequency and time resolution as well as

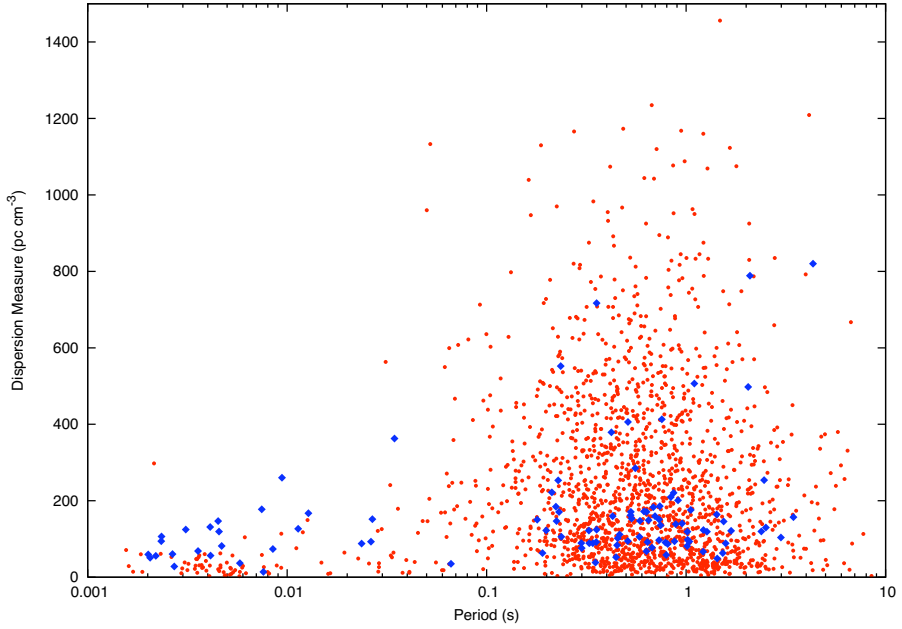


Figure 3.2 Period-DM distribution of HTRU medlat discoveries. Red points represent all previously known pulsars not in globular clusters in the pulsar catalogue and blue diamonds represent HTRU medlat discoveries.

twice as long integration times in comparison to the PM survey.

The follow-up observations of the HTRU pulsars are carried out at one of two different telescopes depending on their position on the sky. All pulsars that are visible from Jodrell Bank observatory (with $\delta > -35^\circ$) have been observed and timed there, while the pulsars further south have been followed-up at the Parkes Telescope. All of the pulsars that have been timed for at least 300 days and for which we have a stable timing solution, are plotted in the $P - \dot{P}$ diagram in Fig 3.3 on top of the previously known sample. Looking at the long period pulsars in this plot, all sources except one belong to the main pulsar island. The exception is the radio magnetar PSR J1622–4950, described in detail in Ch 4 and Ch 5 in this thesis.

It is worth noting the absence of young pulsars (with $\tau < 100$ kyr and $P < 1$ s) among the HTRU discoveries. Since young pulsars are found very close to their birthplace in the Galactic plane, all of these sources should have been discovered already in the PM survey. Hence we did not expect to discover any new young pulsars in the medlat portion of the HTRU survey, but we do expect to discover this kind of sources in the deep HTRU survey.

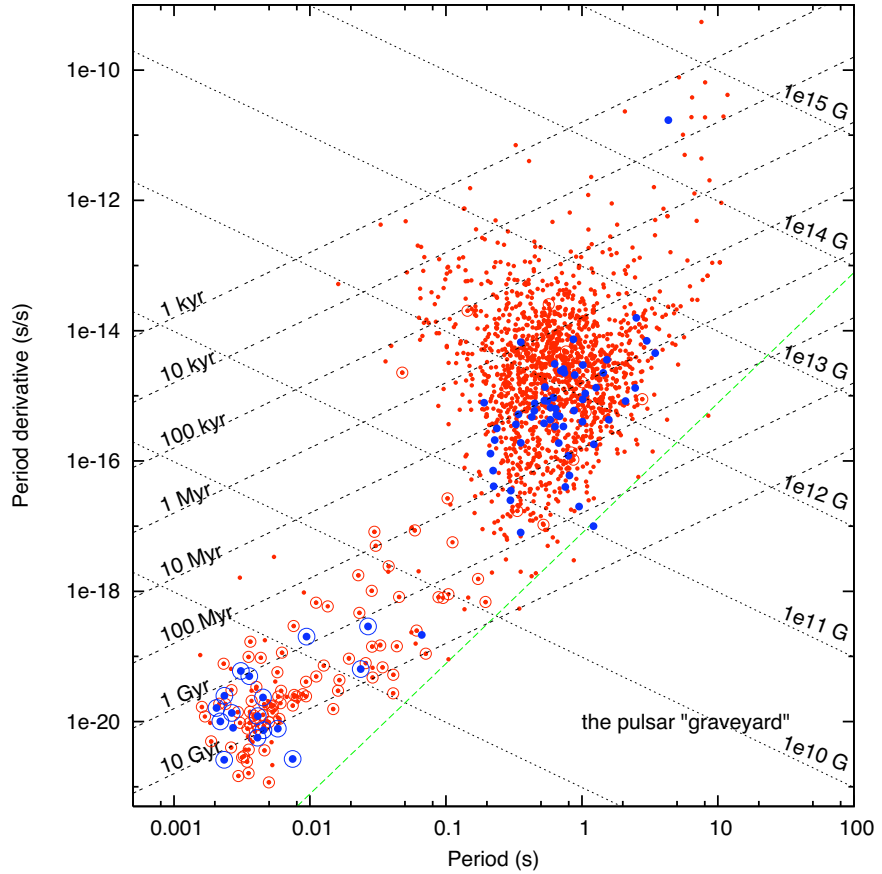


Figure 3.3 $P - \dot{P}$ diagram including HTRU medlat discoveries. The red dots represent the previously known pulsars and the blue diamonds represent the pulsars that were discovered in the HTRU medlat survey. The encircled points represent binary systems. The black dashed lines show lines of constant characteristic age and the dotted black lines show lines of constant surface magnetic field strength. The green line represents the proposed pulsar graveyard boundary.

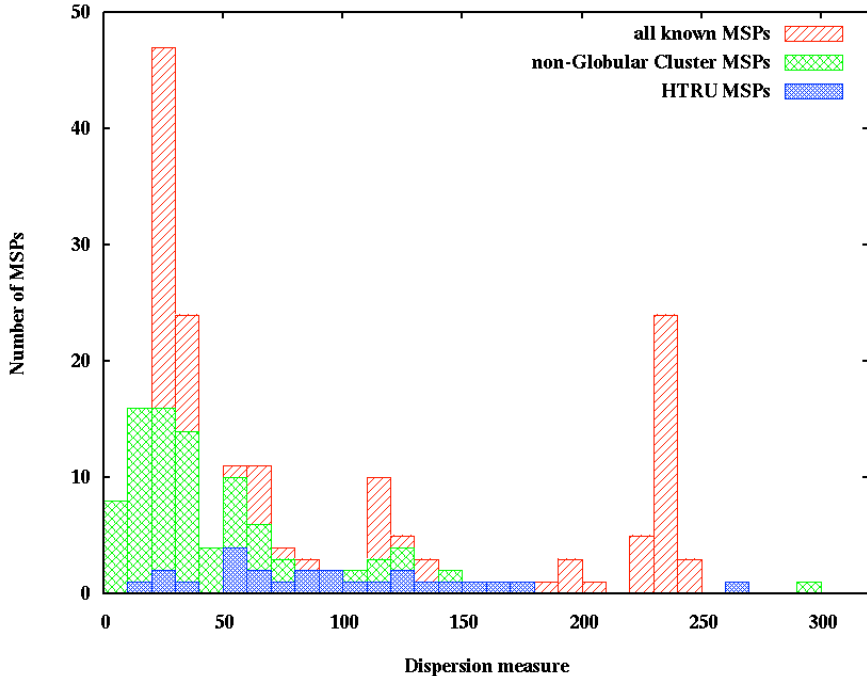


Figure 3.4 Histogram of DM values for MSPs. The red bars show values for all known MSPs and the green bars include only MSPs not associated with globular clusters. The blue bars show the MSPs discovered in the HTRU medlat survey.

3.1.2 Millisecond Pulsars

A large fraction of the discoveries (26 out of 104 sources) are recycled pulsars with periods ranging from 2 ms to 66 ms.

In contrast to the slow pulsars, the millisecond pulsars discovered in the medlat survey are generally found at higher DM values than previously known MSPs outside of globular clusters, as shown in Fig 3.2. This is a result of the higher frequency resolution in the HTRU survey compared to previous surveys, and provides a nice confirmation that the survey is meeting its design targets. A histogram of the DM values for all known MSPs is shown in Fig 3.4, clearly showing how the HTRU discoveries are more frequently found at higher DMs than the previously known non-globular cluster MSPs.

Most of the HTRU MSPs (24 of 26 pulsars) are in binary systems with another star. The minimum mass of the binary companion as a function of spin period of the MSP is shown in the top panel of Fig 3.5. Here we can see that there are two different groups of binary systems in the previously known sample (the red dots), separated by a gap in the diagram. The first type of system has a companion of minimum mass of $\gtrsim 0.1 M_{\odot}$ and the

pulsar period can range over the entire period range of known pulsars, while the second type of system has a minimum companion mass $< 0.05M_{\odot}$ and all known pulsars of this type are in the millisecond range. Looking at the HTRU sample however (the blue dots), there are two pulsars that lie outside of these two groups which will be described below.

MSPs with Low Mass Companions

The first outlier in Fig 3.5, PSR J1502–6752, was discovered in the Swinburne pipeline. It is an MSP with a spin period of 26.7 ms and a minimum companion mass of $0.02M_{\odot}$ (Keith et al. 2012). All other known systems in this companion mass group have very short spin periods ($P < 7$ ms). These systems are believed to have formed when mass transfer from the companion begins before the large degenerate core of the companion has formed. The early start of the mass transfer is due to short distance between the neutron star and the companion. This stable process leads to a long period of spin up of the pulsar, which explains the short spin periods of the pulsars and the low mass of the companions.

However, the longer spin period of PSR J1502–6752 clearly differentiate this pulsar from the other binary systems with very low mass companions. The unknown inclination angle of the system could possibly explain the low companion mass. However, for the companion mass to be $> 0.1M_{\odot}$ (which is the lowest value for other known pulsar binaries in this spin period range) the inclination angle must be less than 13° , which has a probability of only 2.5% (Keith et al. 2012).

The binary period for PSR J1502–6752 is much longer than the rest of the group (2.5 days compared to < 0.5 days). Since the mass transfer in a wider orbit happens later in the companion’s life and hence for a shorter period of time, this might explain the slow spin period of PSR J1502–6752. However, it can not explain the low mass of the companion. One possible scenario for the formation of this system could be a collision between the neutron star and a main sequence star due to an asymmetric kick in the supernova explosion, which could lead to the disruption of the companion star and an only mildly spun-up pulsar (Bailes 1989). The discovery of more pulsars with very low mass companions will help us to understand if PSR J1502–6752 really is a unique system or if the spin period distribution of pulsars in systems with low-mass companions is actually wider than currently thought.

With the right geometry, the systems with low-mass companions can be observed as eclipsing binaries. The HTRU medlat survey has discovered one such eclipsing binary pulsar, J1731–1847 (Bates et al. 2011a), once again originally discovered on the Swinburne supercomputer. It has a spin period of 2.34 ms and orbits its $0.03M_{\odot}$ companion every

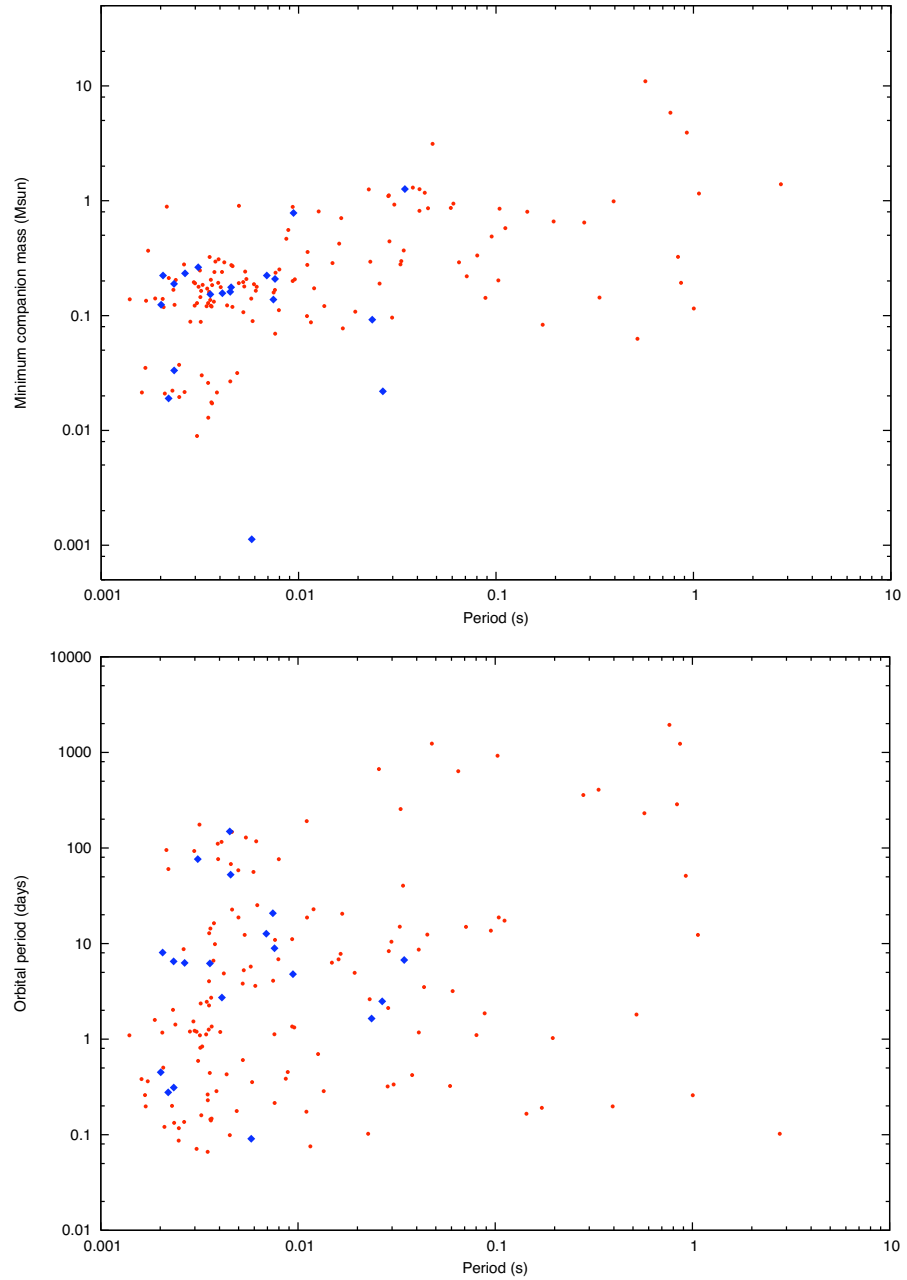


Figure 3.5 Binary pulsar minimum companion mass versus spin period, assuming a pulsar mass of $1.4 M_{\odot}$. The red dots represent the previously known pulsars and the blue diamonds represent the pulsars that were discovered in the HTRU medlat survey.

7.5 hours, spending ~ 1 hour in eclipse. When this pulsar was discovered, it was one of only four eclipsing binary systems known outside of globular clusters. Subsequently more sources of this kind have been found, many associated with Fermi γ -ray sources (Roberts 2011).

The other outlier in Fig 3.5 is the 5.79 ms pulsar J1719–1438 (Bailes et al. 2011), which was discovered in the pipeline running on the green machine at Swinburne. This MSP is in a 2.2 hour binary orbit around a Jupiter mass companion. By calculating the Roche lobe radius, we get the maximum size of the companion and can calculate the lower limit of the density of the companion to $\rho = 23 \text{ g cm}^{-3}$. This value is much higher than the density of gaseous planets like Jupiter, which has $\rho < 2 \text{ g cm}^{-3}$. The mass and radius are highly dependent on the unknown inclination angle of the binary system. If J1719–1438 is a face-on system, this could explain its low mass function. Comparing this system to the known binary pulsar population, its mass function is ~ 1000 times smaller than that for any other known system. For the mass function of J1719–1438 to increase to similar values, a maximum inclination of 5.7 degrees is required, which has a chance probability of only 0.5%. Hence, it is unlikely that the system is very close to face-on. We believe that this binary system was once an ultra-compact low mass X-ray binary where most of the companion mass and angular momentum has been transferred to the pulsar. If just a slightly larger fraction of the companion mass would have been lost to the pulsar, the system would have been disrupted, leaving behind a solitary millisecond pulsar.

Isolated MSPs

Two of the 25 MSPs in the HTRU medlat discoveries are isolated. One of them is the 2.72 ms pulsar J1832–0835. This pulsar was discovered using the version of the HITRUN pipeline set up at Cagliari Observatory in Sardinia. The other is PSR J1729–2121, which with its 66 ms period could have been mistaken for a young pulsar before the timing solution was obtained. However, with its small period derivative of 2.3×10^{-19} , it is most likely an old, disrupted binary pulsar. This pulsar was discovered in the pipeline running at Jodrell Bank in Manchester.

High Precision Timing Pulsars

The Pulsar Timing Array projects around the world are using arrays of millisecond pulsars to search for the gravitational wave background. They use high precision timing of the most accurately pulsating sources to search for variations in the pulse times of arrival at the telescope due to gravitational waves. The success of these projects rely on a large

number of stable pulsars being timed frequently for a long period of time and new MSP discoveries have the potential to increase the sensitivity of the timing arrays. A good timer is usually indicated by a high S/N, a short pulse period and a narrow profile. PSR J1017–7156 is one such pulsar discovered in the HTRU medlat survey. It has a period of 2.3 ms, a duty cycle of 0.03 and is typically observed with a S/N ~ 50 in a 9-min observation (the HTRU medlat integration time). PSR J1017–7156 has already been added to the target list of the Parkes Pulsar Timing Array (Hobbs et al. 2009).

3.2 Previously Known Pulsars in the Medlat Survey Region

The region of the sky covered by the medlat survey contains a total of 1108 previously known pulsars and we have analysed the detectability of all of these pulsars in the survey. The closest survey beam for each of the pulsars has been both searched for the pulsar through the HITRUN pipeline and folded at the catalogue period and DM. They have been divided up in four categories depending on their detectability:

1. **Detections:** Pulsars that were found by the pipeline. (725 sources)
2. **Weak:** Pulsars that were detected by folding the data file with the catalogue period and DM, but not detected in the pipeline. These sources are usually very weak, which is the reason for the non-detection in the pipeline. (96 sources)
3. **RFI:** Pulsars that were not found, most likely due to heavy radio frequency interference. (70 sources)
4. **Undetected:** Pulsars that were detected neither in the pipeline nor by direct folding, and no obvious RFI was present. (214 sources)

3.2.1 Detections

The details for all of the pulsars in the two first categories are listed in Table A.1 and Table A.2 in Appendix A and an overview and analysis of their properties are presented in this section.

The spatial distribution of the detected pulsars is shown in Fig 3.6. Here we can see that the detections follow the total distribution well, with a concentration on the Galactic plane but also with detections spread over the entire search region. The weak pulsars (from group 2 above, represented by green diamonds) also follow the same distribution as the rest of the sample.

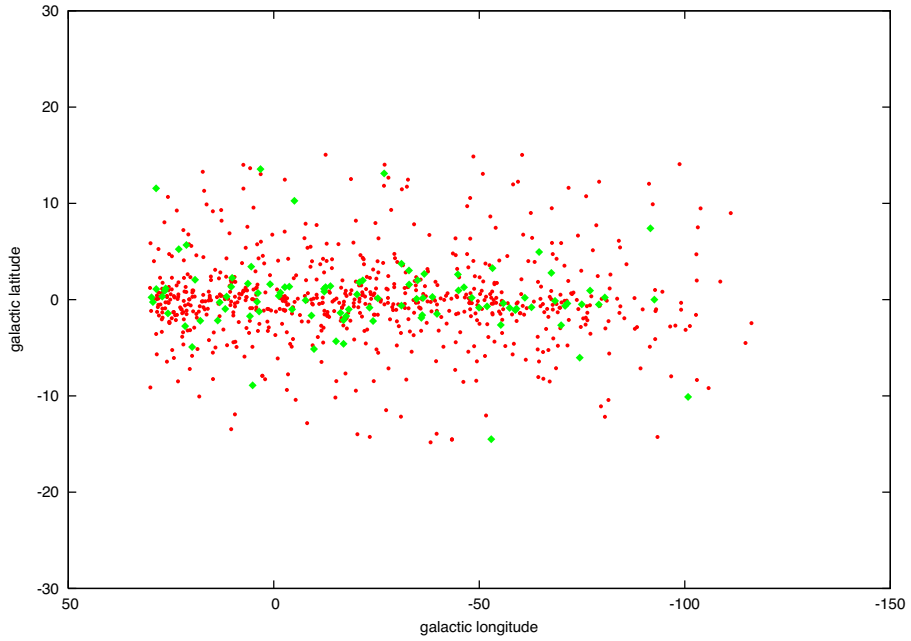


Figure 3.6 Spatial distribution of detected previously known pulsars. The red dots represent the pulsars that were detected in the pipeline and the green diamonds represent the pulsars that were only detected by direct folding.

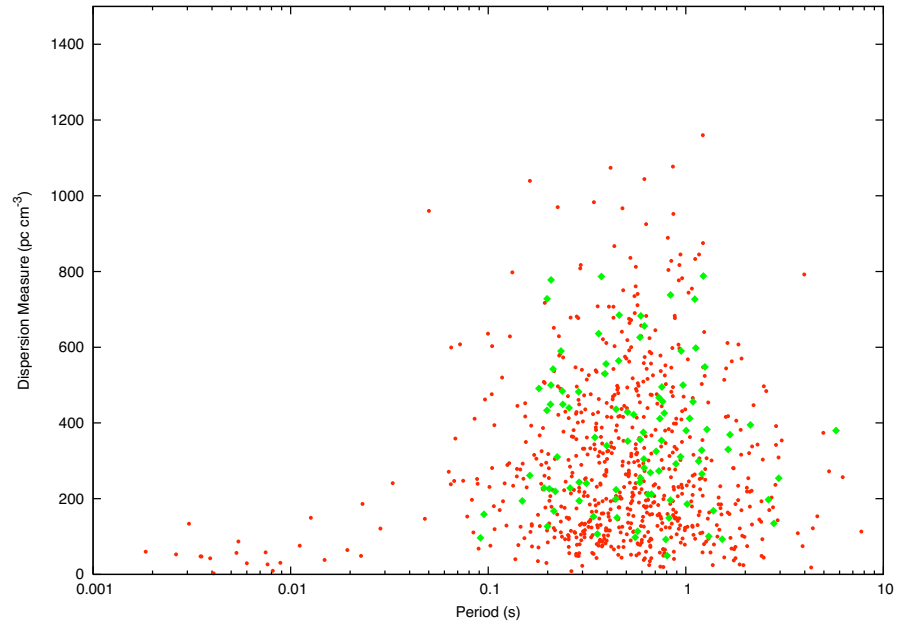


Figure 3.7 Period and DM distribution of detected previously known pulsars. The red dots represent the pulsars that were detected in the pipeline and the green diamonds represent the pulsars that were only detected by direct folding.

There is also good agreement between the period - DM distribution of the slow pulsars in the sample, see Fig 3.7. Both the weak pulsars and the pulsars detected in the pipeline follow the total pulsar distribution well, if we compare with Fig 3.2. In the case of the millisecond pulsars, the pipeline detected all of the pulsars that are detected by direct folding. This is a good confirmation that the pipeline is well optimised for finding MSPs, but is also a result of the higher sensitivity for shorter period pulsars in HTRU compared to previous surveys. Since the frequency resolution of the Parkes Multibeam survey (Manchester et al. 2001) and the Swinburne Intermediate Latitude Survey (Edwards et al. 2001) only provided enough sensitivity to find bright, nearby MSPs it is not surprising that the HTRU survey also detected the same sources.

Also the $P - \dot{P}$ diagram (see Fig 3.8) shows that the survey does not discriminate against any particular kind of pulsar. The sample detected in the survey follows the complete known population well.

A crucial part of evaluating the results of a pulsar survey is to analyse the survey sensitivity performance. Here we do that by analysing how the S/N of the folded data compares to the theoretical S/N, which is calculated using the radiometer equation (eq 2.1), assuming the catalogue flux value, spin period and pulse width as well as taking the beam number and distance from the beam centre into account. In the top panel of Fig 3.9 we have plotted these two values in a graph containing both the detected and the weak pulsars. Most of the pulsars end up nicely scattered around a straight line through $x=y$ (the direct folded S/N = the theoretical S/N). There are some outliers that have direct folded S/N ~ 10 times higher or lower than the theoretical S/N, which could indicate that the catalogued value of the flux is over-/underestimated in those cases. Other possible reasons include an offset between real and recorded pulse width, or that the pulsars are prone to scintillate, which would result in similar offsets in S/N value.

The weak pulsars (represented by green diamonds) are clustered in the low direct folded S/N range. The spectral S/N attained from the FFT is often lower than the S/N after folding (as described in e.g. Kondratiev et al. 2009), which means that many of these pulsars would have a spectral S/N below our detection threshold.

The bottom panel in Fig 3.9 shows the direct folded S/N versus the folded S/N from the pipeline output. Also here we expect the pulsars to follow a straight line through $x=y$. The scatter in this plot is less than the previous one and show that the pipeline is returning candidates with accurate S/N estimates. The apparent bi-modality of the points in this plot is not very well understood, but could originate from a combination of how the software calculates the S/N values and the resolution chosen when plotting the pulsar

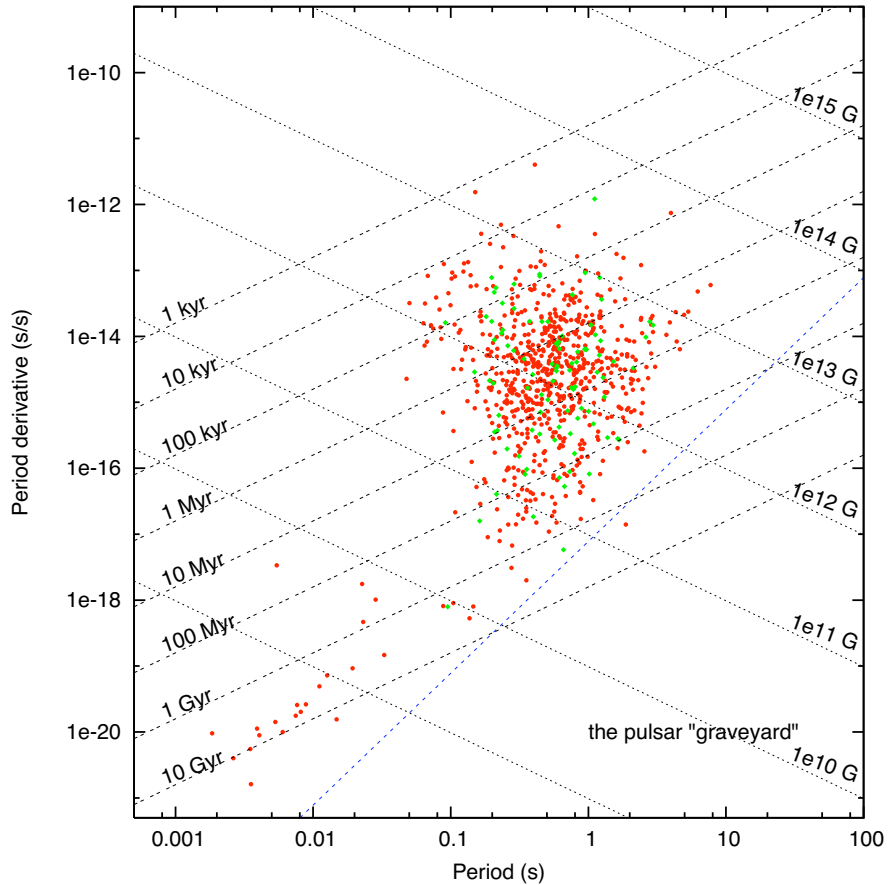


Figure 3.8 $P - \dot{P}$ diagram for detected previously known pulsars. The red dots represent the pulsars that were detected in the pipeline and the green diamonds represent the pulsars that were only detected by direct folding. The black dashed lines show lines of constant characteristic age and the dotted black lines show lines of constant surface magnetic field strength. The blue dashed line represent the pulsar graveyard boundary.

profiles.

Some of the pulsars that end up with significantly lower folded S/N in the pipeline than via direct folding from the catalogue ephemeris are the accelerated pulsars. Since this thesis does not include any acceleration searching, this is not unexpected. Particularly in the case of the double pulsar, J0737–3039, the effect of the acceleration is very prominent. In our data, the pulsar is very bright after direct folding with the ephemeris ($S/N = 28$). It is also found in the search pipeline, but only with a much lower S/N and at a harmonic of the true period. The profile is extremely broadened due to the acceleration smearing and by eye it is not possible to distinguish from the noise, so that the pulsar was not selected in the candidate viewing process. Acceleration searching is crucial for finding this interesting kind of pulsar and will be carried out on all the HTRU data by other members of the research team in the near future.

3.2.2 Non-detections

In the remainder of this chapter, the pulsars that belong to category 3 (RFI) and 4 (Undetected) in the list above are collectively defined as non-detections. The 70 pulsars in the RFI group include both bright and weak sources and provide a rough estimate of the total number of beams in the survey that were so heavily affected by RFI that they are unusable. By assuming that the 1108 beams that contain known pulsars are representative of the entire survey, we expect that about 6.3% of the total beams in the survey are ruined by RFI.

The largest fraction of the group of undetected pulsars is sources with low luminosity that are too weak to be detected with the sensitivity of the medlat survey. A histogram of the theoretical S/N of the non-detections is shown in Fig 3.10. This group includes (almost) all globular cluster pulsars, which were discovered in targeted searches that used very long integration times. In addition, these pulsars are often highly-accelerated MSPs which would have required acceleration searching to be detected in any survey. In this group, there are also nulling pulsars, that happened to be off at the time of our observation. PSR J1717–4054 is one of these intermittent pulsars that is very bright when it is on (O’Brien et al. 2006), but was undetected in our data set. Another pulsar that has a high theoretical S/N calculated from its catalogue flux is PSR J1550–5418. This pulsar is one of the three known radio magnetars (Camilo et al. 2007b), which is known to have a highly variable flux density. It might have been in a low state at the time of the HTRU observation, which would explain why it was not detected.

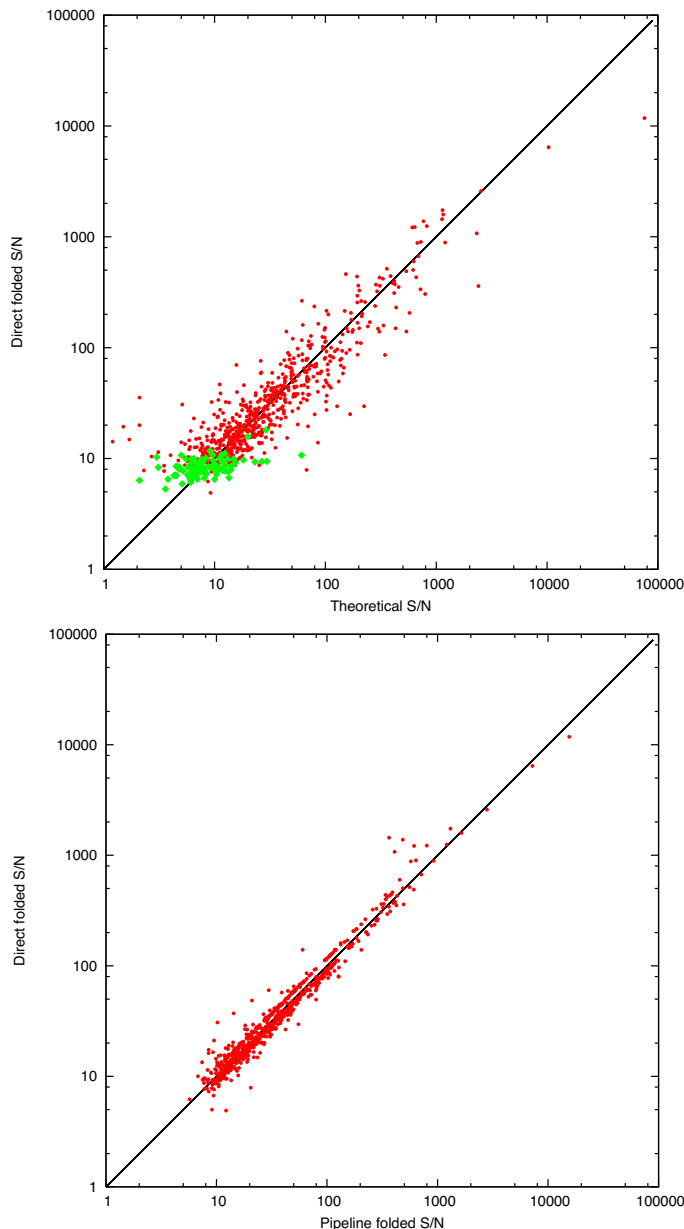


Figure 3.9 S/N of previously known pulsars. The red dots represent the pulsars that were detected in the pipeline and the green diamonds represent the pulsars that were only detected by direct folding. The black line, $x=y$, is plotted for reference. The top panel shows S/N when the data is folded with the catalogue ephemeris versus the calculated theoretical S/N, and the bottom panel shows the catalogue ephemeris folded S/N versus the folded S/N from the processing pipeline. The apparent bi-modality of the points in the bottom panel is not very well understood, but could originate from a combination of how the software calculates the S/N values and the resolution chosen when plotting the pulsar profiles.

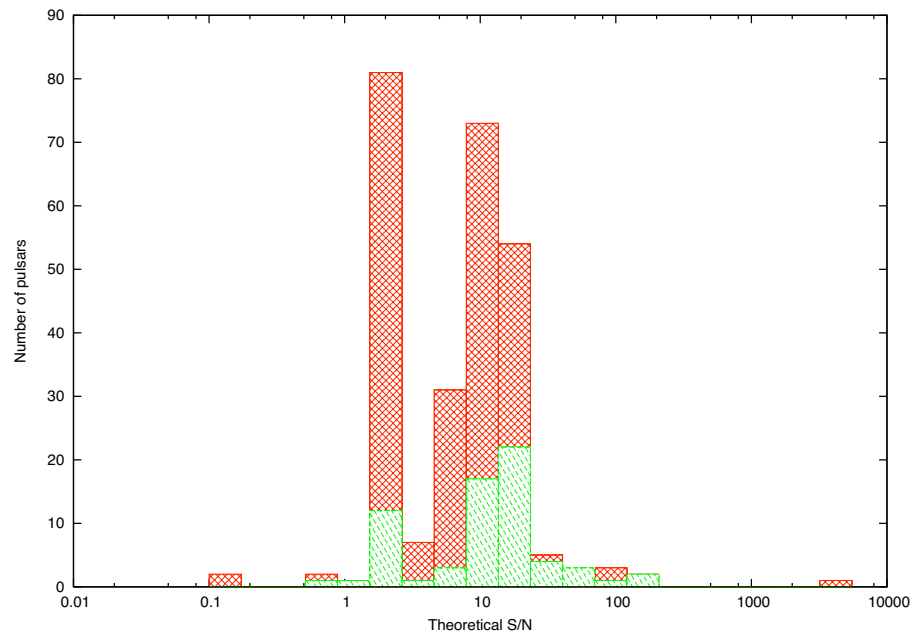


Figure 3.10 Histogram of theoretical S/N of non-detections. The red bars show all non-detections and the green bars show only the observations that were ruined by RFI. The missed pulsars with theoretical S/N>20 in observations not ruined by RFI include the nulling pulsar J1717–4054, the radio magnetar J1550–5418 and a globular cluster pulsar.

3.3 Conclusions

The HTRU medlat survey has discovered 104 previously unknown pulsars, with another ~ 10 promising candidates still to be confirmed. The new discoveries include 26 MSPs, a large fraction compared to the known population ($\sim 9\%$ of all pulsars in the pulsar catalogue are MSPs). The HTRU MSPs are on average found at higher DM than the known MSP population. This is a result of the higher frequency resolution of the HTRU survey compared to earlier surveys and one of the design targets of the survey.

In addition to the new discoveries, the HTRU medlat survey region covers the position of 1108 previously known pulsars. An analysis of the relevant survey data for those pulsars shows that 725 of them were detected by the processing pipeline. 96 sources were weak pulsars found by folding the data with the catalogue ephemeris but not detected by the pipeline. The remaining 284 sources were not detected at all in the data, but for 70 of those sources the non-detection was due to the presence of heavy RFI. From this we estimate that $\sim 6\%$ of the total observations in the survey are ruined by RFI.

In general, the HTRU medlat survey performs as expected. The large number of MSPs discovered as well as the higher DM of the MSP discoveries were two of the aims of the medlat survey set up prior to the commencement of the observations. As a bonus, some of the discoveries have turned out to be very interesting objects, for example PSR J1719–1438 and its planetary mass companion, the eclipsing binary PSR J1731–1847 and the radio magnetar PSR J1622-4950.

Table 3.1: HTRU medlat discoveries.

Pulsar	<i>l</i>	<i>b</i>	<i>P</i>	DM	Ref.
J0808-5422	268.72	-11.57	0.526647	161.9	6
J0835-4232	261.47	-1.17	0.738423	185.8	6
J0904-6022	278.16	-8.79	0.340853	88.9	6
J0912-3848	263.17	6.62	1.526114	63.2	6
J0919-6047	279.73	-7.77	1.217008	66.9	6
J0949-6900	287.83	-11.69	0.640022	92.0	6
J1017-7156	291.56	-12.55	0.002339	94.3	3
J1036-6600	289.76	-6.62	0.533502	153.3	6
J1054-5944	288.64	-0.16	0.228323	253.4	6
J1056-7118	293.95	-10.47	0.026310	92.8	
J1105-4357	283.51	14.89	0.351113	38.3	6
J1125-5825	291.89	2.60	0.003102	124.8	2
J1132-4655	289.20	13.84	0.325636	121.9	6
J1142-5539	293.32	6.00	0.685360	183.1	6
J1226-6202	300.09	0.58	0.034528	362.6	8
J1239-6728	301.60	-4.63	1.055480	175.9	6
J1253-7408	302.98	-11.28	0.327056	89.0	6
J1330-5251	308.97	9.64	0.648104	149.0	1
J1337-6423	307.89	-1.96	0.009423	260.3	3
J1346-4927	312.08	12.61	0.299620	76.0	6
J1406-4656	315.91	14.05	0.007602	13.7	8
J1409-6954	309.55	-8.04	0.528581	171.1	6
J1417-5036	316.60	9.97	0.794875	58.2	6
J1431-4717	320.06	12.26	0.002012	59.4	8
J1431-5736	315.96	2.66	0.004111	131.2	7
J1433-5029	318.95	9.14	1.017495	98.0	1
J1442-5122	320.09	7.68	0.732061	97.0	1
J1446-4701	322.50	11.43	0.002195	55.8	3
J1502-6752	314.80	-8.07	0.026744	151.8	3
J1517-4636	327.38	9.22	0.886610	139.0	6
J1525-5544	323.50	0.85	0.011357	126.8	
J1528-3835	333.90	14.72	0.008486	73.6	
J1530-6336	319.51	-6.11	0.910310	201.2	6
J1535-4432	331.14	9.26	1.221429	123.4	6
J1540-4829	329.43	5.54	1.272842	119.0	1
J1543-5149	327.92	2.48	0.002057	50.9	3
J1546-4552	331.89	6.99	0.003575	68.4	7
J1552-4433	333.62	7.40	0.674068	77.4	6
J1552-6213	322.29	-6.34	0.198839	122.2	6
J1607-6447	321.99	-9.52	0.298116	89.3	6
J1612-5811	327.00	-4.96	0.615520	172.0	1
J1614-3846	340.66	8.77	0.464098	111.7	6
J1622-3752	342.37	8.47	0.731471	151.2	6

Table 3.1 – Continued

Pulsar	l	b	P	DM	Ref.
J1622-4950	333.85	-0.10	4.326450	820.0	4
J1622-6617	321.98	-11.56	0.023623	87.9	3
J1625-4914	334.57	0.03	0.355856	717.0	1
J1625-6620	322.20	-11.88	0.450868	83.6	6
J1627-5933	327.33	-7.44	0.354239	92.0	1
J1629-3635	344.31	8.18	2.988134	104.0	6
J1634-5638	330.18	-5.95	0.224202	146.7	6
J1635-2616	353.12	14.02	0.510455	94.5	6
J1638-4233	341.02	2.91	0.510930	406.0	6
J1648-3605	347.12	5.79	0.212316	222.0	1
J1650-6046	328.24	-10.18	0.583693	105.6	1
J1653-2056	359.99	14.28	0.004129	56.5	8
J1701-4419	342.28	-1.32	0.755535	413.0	1
J1705-4335	343.38	-1.57	0.222561	184.6	1
J1705-5230	336.06	-6.85	0.230708	170.5	6
J1705-6137	328.70	-12.24	0.808546	87.0	1
J1708-3506	350.47	3.12	0.004505	146.8	2
J1708-4406	343.47	-2.40	0.865242	220.6	6
J1709-2613	357.83	8.03	0.954167	140.7	6
J1715-4703	341.55	-5.13	0.555822	285.2	6
J1719-1438	8.86	12.84	0.005790	36.8	5
J1719-2334	1.37	7.84	0.453990	101.8	6
J1720-2451	0.42	7.00	0.874263	94.1	6
J1729-2121	4.50	7.22	0.066293	35.0	8
J1731-1847	6.89	8.15	0.002345	106.5	2
J1733-5516	336.22	-11.90	1.011225	81.4	6
J1745-3816	352.05	-4.78	0.698356	159.6	6
J1745-5342	338.46	-12.46	0.355666	124.4	6
J1748-1024	16.18	9.00	1.578515	88.6	6
J1749-4928	342.59	-11.11	0.445826	52.4	6
J1754-2421	4.98	0.65	2.090263	788.8	1
J1755-0900	18.33	8.18	0.190710	63.3	6
J1755-3715	353.87	-6.01	0.012786	167.4	
J1757-1503	13.35	4.72	0.179354	150.6	6
J1759-1025	17.62	6.51	2.512312	129.9	6
J1801-3210	358.92	-4.58	0.007454	177.7	2
J1802-0521	22.40	8.37	1.680657	121.5	6
J1802-3349	357.65	-5.62	2.461052	254.0	6
J1803-3328	358.02	-5.64	0.633412	171.0	1
J1805-2949	1.42	-4.22	0.428343	159.6	6
J1810-0120	26.96	8.61	0.744976	135.5	1
J1811-2405	7.07	-2.56	0.002661	60.6	1
J1811-4930	344.24	-14.25	1.432704	49.0	1
J1812-2749	3.97	-4.59	0.236983	105.7	1

Table 3.1 – Continued

Pulsar	l	b	P	DM	Ref.
J1812-3046	1.43	-5.97	0.587468	147.5	6
J1814-0528	23.76	5.76	1.014346	119.0	1
J1816-1938	11.59	-1.64	2.046845	497.8	6
J1818-0152	27.50	6.54	0.837547	209.7	6
J1825-0322	27.00	4.12	0.004554	119.5	7
J1825-3103	2.40	-8.70	2.382205	119.7	6
J1826-2413	8.54	-5.62	0.004696	81.8	
J1832-0835	23.10	0.26	0.002719	28.2	7
J1835-0921	22.80	-0.75	0.235245	552.4	
J1837-0820	23.96	-0.77	1.099200	506.6	6
J1840-0438	27.59	0.24	0.422321	379.1	6
J1854-1559	19.02	-7.95	3.453121	157.0	1
J1900-0928	25.47	-6.24	1.424005	164.0	6
J1902-1039	24.62	-7.23	0.786770	91.0	6
J1904-1624	19.65	-10.28	1.541460	145.8	6
J1906-1525	20.68	-10.40	0.632231	67.8	6
J1920-0946	27.46	-10.93	1.037830	93.2	6

REFERENCES:

- (1) Keith et al. (2010); (2) Bates et al. (2011a);
- (3) Keith et al. (2012); (4) Levin et al. (2010)
- (5) Bailes et al. (2011); (6) Bates et al. (2012)
- (7) Burgay et al. (2012); (8) Thornton et al. (2012)

4

A Radio-loud Magnetar in X-ray Quiescence

This chapter was published in full in *Astrophysical Journal*, 721, L33, 2010, authored by L. Levin, M. Bailes, S. D. Bates, N. D. R. Bhat, M. Burgay, S. Burke-Spolaor, N. D'Amico, S. Johnston, M. Keith, M. Kramer, S. Milia, A. Possenti, N. Rea, B. Stappers, W. van Straten.

As part of a survey for radio pulsars with the Parkes 64-m telescope we have discovered PSR J1622–4950, a pulsar with a 4.3-s rotation period. Follow-up observations show that the pulsar has the highest inferred surface magnetic field of the known radio pulsars ($B \sim 3 \times 10^{14}$ G), exhibits significant timing noise and appears to have an inverted spectrum. Unlike the vast majority of the known pulsar population, PSR J1622–4950 appears to switch off for many hundreds of days and even in its on-state exhibits extreme variability in its flux density. Furthermore, the integrated pulse profile changes shape with epoch. All of these properties are remarkably similar to the only two magnetars previously known to emit radio pulsations. The position of PSR J1622–4950 is coincident with an X-ray source that, unlike the other radio pulsating magnetars, was found to be in quiescence. We conclude that our newly discovered pulsar is a magnetar - the first to be discovered via its radio emission.

4.1 Introduction

Magnetars are slowly rotating neutron stars that, in contrast to ordinary pulsars, are not powered by their spin-down energy losses, but by the energy stored in their extremely large magnetic fields, typically $\gtrsim 10^{14}$ G (Duncan & Thompson 1992). They are divided into two groups, Soft Gamma-ray Repeaters (SGRs) and Anomalous X-Ray Pulsars (AXPs), whose relation to each other and to other kinds of neutron stars is still a matter of debate

(Mereghetti 2008). SGRs were discovered as sources emitting short repeating bursts in the hard X-ray/soft γ -ray band, while AXPs were first detected in the soft X-ray band. Recently, sources have been found that show properties of both groups, suggesting that AXPs and SGRs belong to the same family (Rea et al. 2009; Mereghetti et al. 2009). Many attempts have been made to find pulsed radio emission from magnetars (see e.g. Kriss et al. 1985; Gaensler et al. 2001; Burgay et al. 2006) but it was not until 2006 that the first detection was reported (Camilo et al. 2006). To date only two AXPs have confirmed radio pulsations, namely XTE J1810–197 (Camilo et al. 2006) and 1E 1547–5408 (Camilo et al. 2007b). Both of these sources are transient AXPs, a subgroup of magnetars that occasionally undergo very bright X-ray outbursts. Their pulsed radio emission was discovered in connection with these outbursts, and is observed to fade with time after an outburst.

Here we report on the discovery of PSR J1622–4950, the first magnetar discovered in the radio band, and discuss its properties in relation to the two magnetars previously known to emit radio pulsations.

4.2 Observations and Historical Data

4.2.1 Parkes Observations

The High Time Resolution Universe (HTRU) survey for pulsars and fast transients is currently being carried out at the Parkes 64-m radio telescope (Keith et al. 2010), using the 20-cm multibeam receiver (Staveley-Smith et al. 1996). In brief, an effective bandwidth of 341 MHz, centered around 1.35 GHz, is divided into 874 frequency channels and sampled using 2 bits every $64\,\mu\text{s}$. In April 2009 (MJD = 54939) a bright radio pulsar, PSR J1622–4950, was discovered. It has a period (P) of 4.326 s and a dispersion measure (DM) of $820\,\text{cm}^{-3}\,\text{pc}$, corresponding to a distance of $\sim 9\,\text{kpc}$, if the Cordes–Lazio model for the distribution of the electrons in the interstellar medium is assumed (Cordes & Lazio 2002).

After the HTRU discovery we embarked on a timing campaign, observing PSR J1622–4950 a total of 110 times at 1.4 GHz and 10 times at 3.1 GHz, obtaining polarimetric information on most occasions. The digital filterbank system (DFB3) used to create the folded profiles first converts the analogue voltages from each polarization channel of the linear feeds into digital signals. It then produces 1024 polyphase filterbank frequency channels that are folded at the apparent topocentric period of the pulsar into 1024 pulsar phase bins, and written to disk every 20 s. Four Stokes parameters are recorded. To determine the relative gain of the two polarization channels and the phase between them,

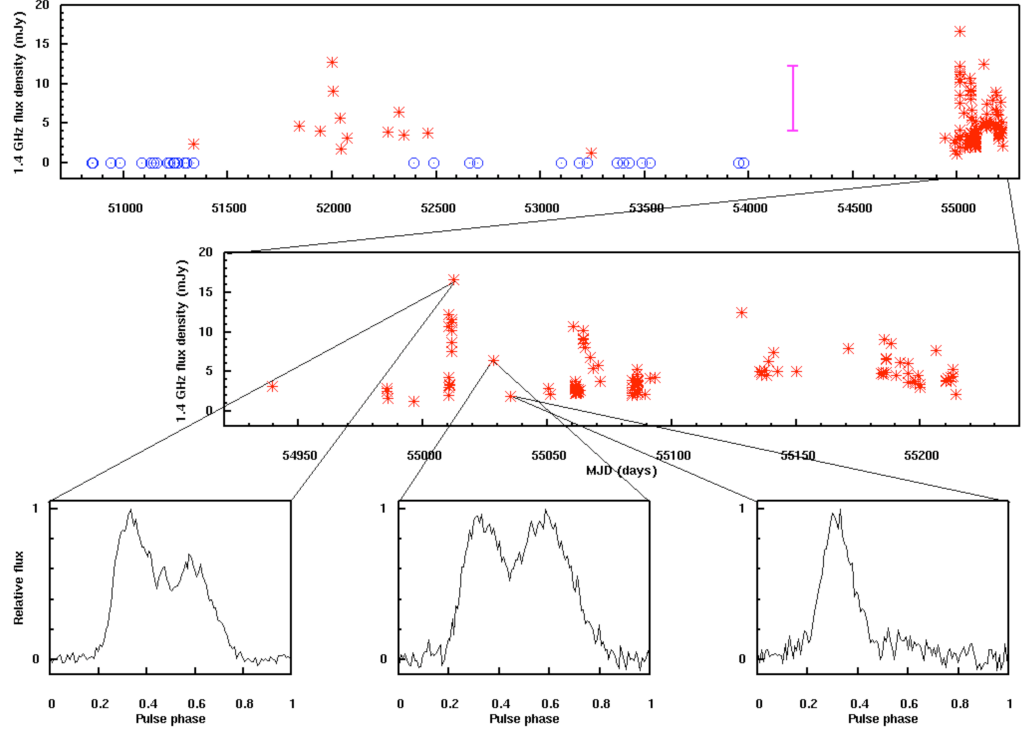


Figure 4.1 Light curve and profile variations for PSR J1622–4950. The top plot shows the temporal variation of flux density at 1.4 GHz. Archival timing data collected within the framework of the Parkes Multibeam Survey ends just before MJD = 54000, and the discovery of PSR J1622–4950 by the HTRU pulsar survey was made on MJD = 54939. The red asterisks show the detections (with errors smaller than the size of the points), and the blue circles indicate observations during which PSR J1622–4950 was not detected (down to a limiting flux density of 1.2 mJy). The purple error bar indicates the observation centered at 6.3 GHz from the Methanol Multibeam survey that detected PSR J1622–4950. When converted into a 1.4 GHz flux density, the large error is dominated by the uncertainty in the spectral index; the top value of the bar corresponds to a flat radio spectrum and the bottom value is derived from our best estimate of the spectral index. The bottom plots show three different pulse profiles from three consecutive observations, taken on 30 June 2009, 16 July 2009 and 23 July 2009.

a calibration signal is injected at an angle of 45° to the feed probes. The data are analyzed off-line using the PSRCHIVE package¹ (Hotan et al. 2004) and corrected for parallactic angle and the orientation of the feed. The position angles are also corrected for Faraday rotation through the interstellar medium using the nominal rotation measure.

4.2.2 Archive Mining

The area of sky containing PSR J1622–4950 was covered previously by the Parkes Multi-beam Pulsar Survey (Manchester et al. 2001) but, somewhat surprisingly given its large apparent flux density and DM, the pulsar was not detected in these data. However, that survey did find two other radio pulsars in close proximity to PSR J1622–4950 and monitored them for a number of years, namely PSRs J1623–4949 and J1622–4944 at an angular separation of 11' and 7' respectively. These archival data were reprocessed using the period and DM of PSR J1622–4950. The first detection was made in observations recorded in June 1999 (MJD = 51334), and it was then detected in 11 observations between October 2000 (MJD = 51844) and July 2002 (MJD = 52458) (see the top panel of Fig. 4.1). However, in the 14 subsequent observations preceding August 2006 (MJD = 53975), the pulsar was detected only once. No further archival data of the two nearby pulsars were available after that date. The Methanol Multibeam pulsar survey at 6.3 GHz (Bates et al. 2011b) also covered the part of the sky containing PSR J1622–4950, and by reprocessing the relevant data, the pulsar was detected in an observation taken in April 2007 (MJD = 54211).

4.2.3 ATCA and Chandra Observations

Observations of the pulsar were made on 8 Dec 2009 and 27 Feb 2010 with the Australia Telescope Compact Array (ATCA), an east-west synthesis telescope located near Narrabri, NSW, which consists of six 22-m antennas on a 6-km track. The observations were carried out simultaneously at 5.5 and 9.0 GHz with a bandwidth of 2 GHz at each frequency subdivided into 2048 spectral channels, and full Stokes parameters. The source was tracked for 12-hours in each of the EW352 and 750B array configurations.

Initial data reduction and analysis were carried out with the MIRIAD package² using standard techniques. After flagging bad data, the primary calibrator (PKS 1934-638) was used for flux density and bandpass calibration and the secondary calibrator (PKS J1613-586) was used to solve for antenna gains, phases and polarization leakage terms.

¹See <http://psrchive.sourceforge.net>

²See <http://www.atnf.csiro.au/computing/software/miriad>

We also obtained a 20-ks *Chandra* observation performed with ACIS-I on 10 July 2009 to search for an X-ray counterpart. Figure 4.2 shows the resultant radio and X-ray images. Although there are a number of radio and X-ray sources present in the field of view, a highly polarized radio point source is coincident with the brightest X-ray source, CXOU J162244.8–495054, which is also the counterpart of a source seen in archival ASCA data, AX J162246–4946. We note that CXOU J162244.8–495054 was one of only two X-ray sources in the field without an optical/infrared counterpart. We are therefore confident that the polarized source seen in the radio is indeed the pulsar and that it has an X-ray counterpart.

4.3 Analysis, Results and Discussion

4.3.1 Radio Light Curve

Throughout the HTRU timing campaign, the pulsar was detected in every observation with a greatly varying flux density, which fluctuated by as much as a factor of ~ 6 within a 24-hour period. These flux variations cannot be attributed to interstellar scintillation and must be intrinsic to the source, as at 20cm wavelengths, pulsar flux densities are reasonably stable at such large DMs (Stinebring et al. 2000). The pulse profile averaged over each observation (typically 5–10 minutes) also changes shape on short timescales, often from day to day. Although such variability in both the integrated profile and the flux density is very uncommon in pulsars, it is a distinctive feature of the two magnetars whose pulsed emission has been detected in the radio band (Camilo et al. 2007b; Serylak et al. 2009; Kramer et al. 2007). The light curve for PSR J1622–4950 and three representative pulse profiles are shown in Fig. 4.1.

4.3.2 Timing

To attain a stable timing solution of a source that is changing its pulse profile from observation to observation, special care needs to be taken in the timing procedure. In conventional pulsar timing a standard profile is created and used to calculate each pulse’s time of arrival (TOA) at the telescope. In the case of PSR J1622–4950 each pulse profile is different, but we noticed that all profiles seem to consist of the same components, only differing by their amplitudes (and sometimes the amplitude for a specific component was indistinguishable from zero). Software from the PSRCHIVE package (Hotan et al. 2004) was used to fit gaussians to one of the profiles that showed all the different components and a model was made to describe how the components build up the profile. This model

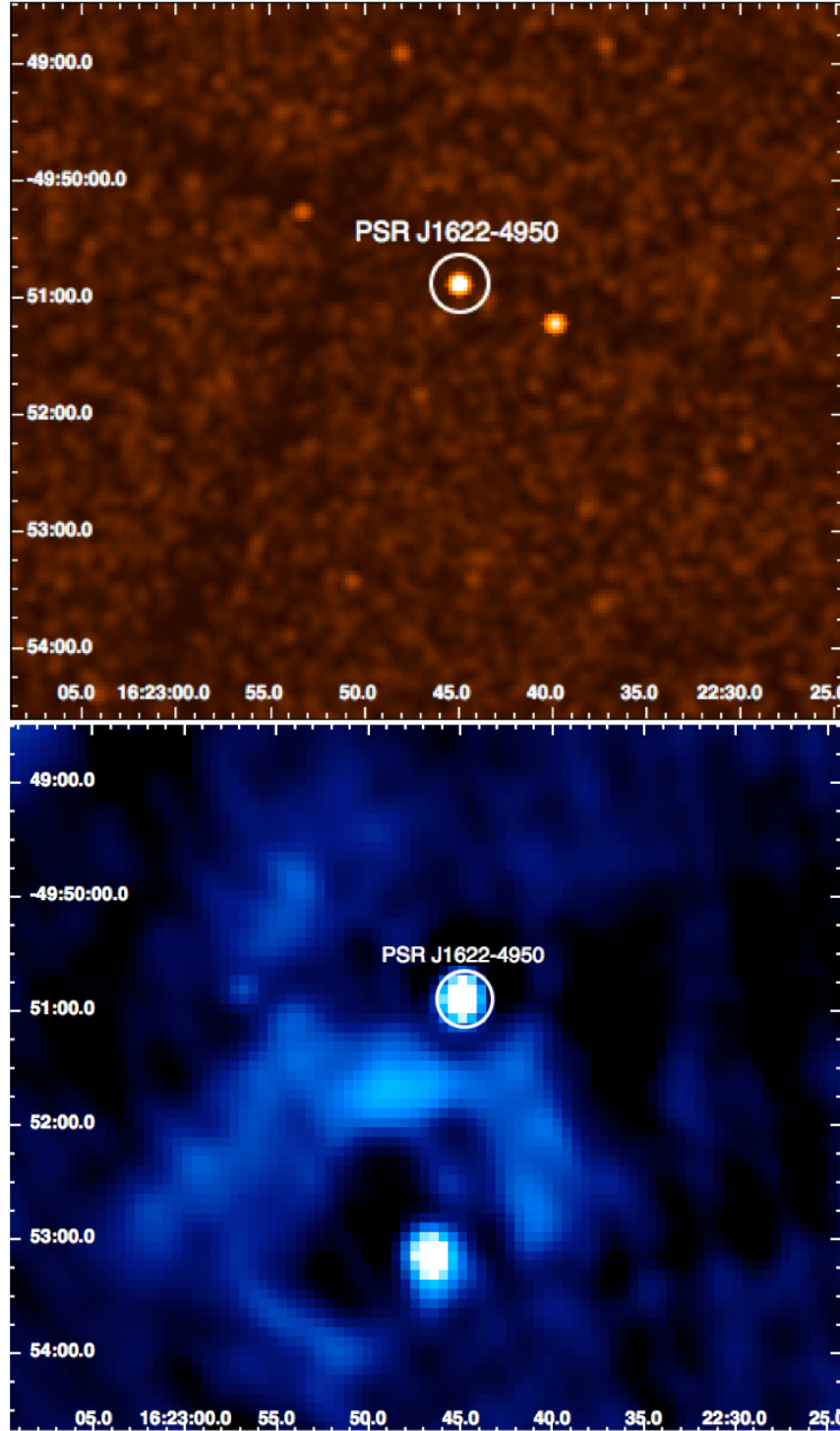


Figure 4.2 *Top:* *Chandra* X-ray observations of the region around PSR J1622–4950. The source encircled with a $15''$ marker, CXOU J162244.8–495054, is coincident with the radio point source in the ATCA image. *Bottom:* ATCA radio observations at 5.5 GHz. The encircled source is PSR J1622–4950. South of the magnetar is a faint ring of extended emission that appears to be non-thermal and may be a supernova remnant (see text for details).

was then used to calculate TOAs, by letting the amplitudes of the different components vary.

When TOAs for all our observations were calculated, the TEMPO software³ was used to analyze the rotational history of PSR J1622–4950. The resultant fit requires at least 9 period derivatives to obtain reasonable phase connection for all our data, which is not uncommon for magnetars (Camilo et al. 2008). To monitor variations of the period derivative with time, we have also measured P and \dot{P} over several time intervals separately. The time spans were chosen to be as long as possible while keeping phase connection without adding higher period derivatives. This usually resulted in groups of TOAs spanning about 40 days each. It appears that \dot{P} is fluctuating within a factor of ~ 2 in time. From this analysis we derived an average period derivative, $\dot{P} = 1.7 \times 10^{-11} \text{ ss}^{-1}$. The parameters from the timing analysis are listed in Table 4.1.

The timing solution for PSR J1622–4950 implies a very high surface magnetic field strength of $B \equiv 3.2 \times 10^{19} \text{ G} \sqrt{P\dot{P}} \approx 2.8 \times 10^{14} \text{ G}$ and a characteristic age of $\tau_c \equiv P/(2\dot{P}) \approx 4000$ years (e.g. Lorimer & Kramer 2005). This is the highest surface magnetic field of any radio pulsar known to date. Figure 4.3 shows an extract of the P - \dot{P} diagram, where the currently known magnetars are clustered in the upper right corner, with $P \gtrsim 2 \text{ s}$ and $\dot{P} \gtrsim 5 \times 10^{-13} \text{ ss}^{-1}$. The two radio emitting magnetars are found in the lower parts of the magnetar group, with periods that are short in comparison to the other AXPs and inferred magnetic field strengths in the lower half of the magnetar range, adjacent to the ordinary radio pulsars with the highest surface magnetic fields. The gap between these two groups of pulsars is narrowing with new discoveries, such as the detection of magnetar-like X-ray bursts from PSR J1846–0258 (Gavriil et al. 2008), which was previously thought to be solely rotation-powered. PSR J1622–4950 is found in the same region of the plot as the two radio emitting magnetars.

4.3.3 Polarization

The emission from the magnetar is often highly linearly polarized, typically with greater polarization at 3.1 GHz than at 1.4 GHz (see Fig. 4.4). The pulsar also intermittently shows significant circular polarization. The Faraday rotation measure derived from these observations is very large, $\text{RM} = -1484 \pm 1 \text{ rad m}^{-2}$. A detailed analysis of these polarization data will be reported elsewhere but we note the similarity between the polarization properties of PSR J1622–4950 and the other radio pulsating magnetars 1E 1547–5408 (Camilo et al. 2008) and XTE J1810–197 (Kramer et al. 2007; Camilo et al. 2007d).

³See <http://www.atnf.csiro.au/research/pulsar/tempo/>

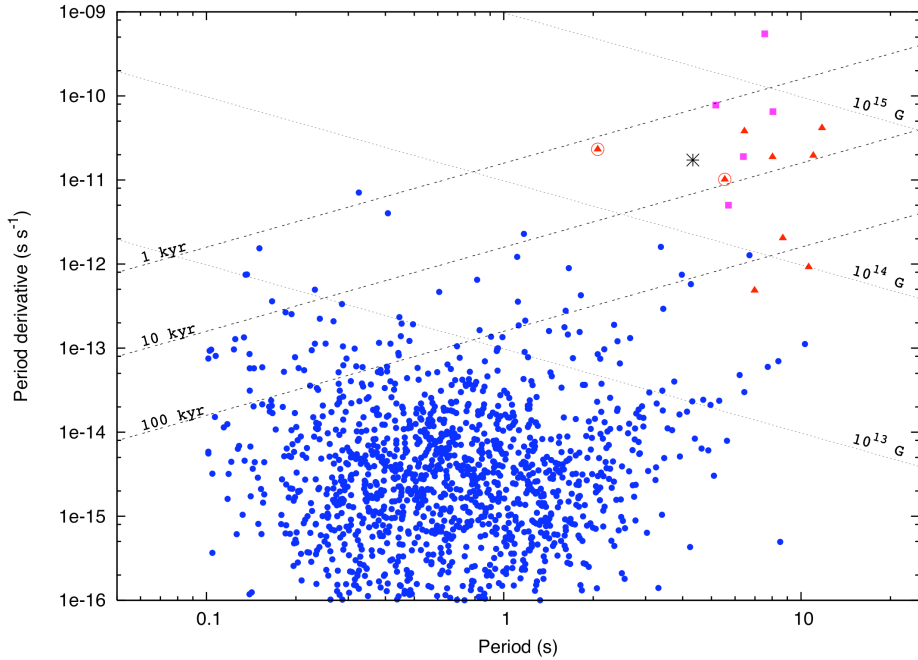


Figure 4.3 Extract of the $P-\dot{P}$ diagram, showing the longer period pulsars and those with higher inferred magnetic field strengths. Blue dots represent ordinary pulsars, red triangles are AXPs, purple squares are SGRs, and the black asterisk represents PSR J1622–4950. The two encircled AXPs are the magnetars that are observed to emit radio pulsations. Dashed lines correspond to lines of constant characteristic age and dotted lines to constant magnetic field strength. PSR J1622–4950 has a slightly higher magnetic field strength than the AXPs that are pulsating in the radio band, but clearly higher than that of any of the ordinary pulsars.

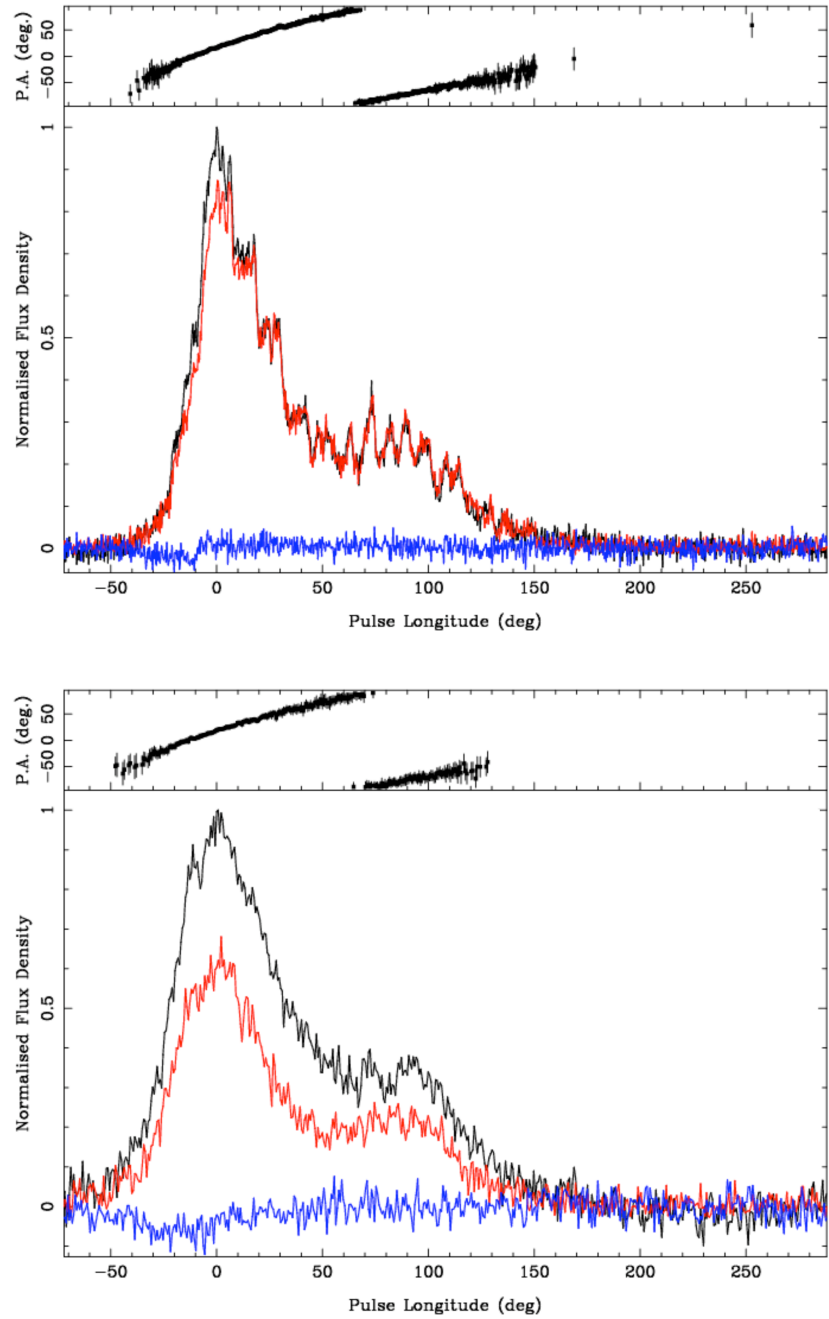


Figure 4.4 Polarimetric profiles of PSR J1622–4950 at 3.1 GHz (top) and 1.4 GHz (bottom) observed at Parkes on the same day (MJD = 55197). The blue and red lines represent circular and linear polarization respectively, while the black lines represent the total intensity. The full 360° of pulse rotation are shown, with the zero point of the pulse longitude set at the peak value of the flux density. Absolute position angles at infinite frequency are shown after correction for a rotation measure of -1484 rad m^{-2} .

Table 4.1 Parameter summary of PSR J1622-4950.

Parameter	Value
<hr/>	
Observed	
Right ascension (J2000) ^a	16 ^h 22 ^m 44 ^s .80(3)
Declination (J2000) ^a	-49°50'54".4(5)
Galactic longitude ^a	333.85
Galactic latitude ^a	-0.10
Epoch	MJD 55080
Spin period (P)	4.3261(1) s
Period derivative (\dot{P})	1.7(1) $\times 10^{-11}$ s s ⁻¹
Dispersion measure (DM)	820(30) cm ⁻³ pc
Flux density at 1400 MHz (S_{1400})	4.8(3) mJy
Rotation measure (RM)	-1484(1) rad m ⁻²
<hr/>	
Derived	
Distance ^b	\approx 9 kpc
Surface magnetic field (B)	2.8×10^{14} G
Characteristic age (τ_c)	4 kyr
Spin down luminosity (\dot{E})	8.5×10^{33} erg s ⁻¹
X-ray luminosity (L_X) ^c	2.5×10^{33} erg s ⁻¹

^aThe position refers to the coordinates of the X-ray source.

^bThe distance is calculated from the dispersion measure with the Cordes–Lazio model.

^cAssuming the dispersion measure derived distance.

4.3.4 Radio Spectrum

We combined the various flux density measurements to estimate the spectral index of the pulsar in the radio band. The average flux density at 1.4 GHz is $\langle S_{1400} \rangle = 4.8$ mJy (with standard deviation $\sigma_{S_{1400}} = 2.8$ mJy) and at 3.1 GHz is $\langle S_{3100} \rangle = 4.9$ mJy ($\sigma_{S_{3100}} = 2.5$ mJy). The ATCA measurements yield $\langle S_{5500} \rangle = 13 \pm 1$ mJy and $\langle S_{9000} \rangle = 14.3 \pm 0.8$ mJy, similar to the flux density of 12 ± 2 mJy obtained from the Methanol Multibeam pulsar survey at a centre frequency of 6.3 GHz. The spectrum therefore appears to have a positive spectral index, highly unusual for pulsars which have a mean spectral index of about -1.6 (Lorimer et al. 1995b). Again, this peculiar spectral behaviour is observed in the other two radio pulsating magnetars, which both have a flat (or inverted) radio spectrum (Camilo et al. 2008; Lazaridis et al. 2008; Camilo et al. 2007c).

4.3.5 X-ray Emission

For ordinary rotation-powered pulsars, the X-ray luminosity (L_X) is much smaller than the spin-down luminosity, $\dot{E} \equiv 4\pi^2 I \dot{P} P^{-3}$; on average $L_X \approx 10^{-3} \dot{E}$ (Becker & Truem-

per 1997). In contrast, magnetars are observed to have $L_X \gtrsim \dot{E}$. An estimate of the unabsorbed 0.3–10 keV flux for CXOU J162244.8–495054 gives $2.6 \times 10^{-13} \text{ erg cm}^{-2} \text{ s}^{-1}$, assuming a Galactic hydrogen column density in that direction of $N_{\text{H}} = 2 \times 10^{22} \text{ cm}^{-2}$ (Dickey & Lockman 1990) and a blackbody spectrum with $kT = 0.4 \text{ keV}$, typical of a quiescent magnetar. This implies $L_X(0.3\text{-}10 \text{ keV}) \approx 2.5 \times 10^{33} \text{ erg s}^{-1}$ at the estimated distance of 9 kpc and, given $\dot{E} \approx 8.5 \times 10^{33} \text{ erg s}^{-1}$ for this magnetar, $L_X \sim 0.3\dot{E}$. Since the distance calculated from the DM has a large uncertainty and is known only to within a factor of two or so, the derived X-ray luminosity may be in error by up to a factor of four. Even within these errors, the ratio is significantly higher than for ordinary pulsars, but well within the range for the magnetars 1E 1547–5408 and XTE J1810–197 which have $L_X \sim 0.1\dot{E}$ and $L_X \sim 4\dot{E}$ (Mereghetti 2008; Camilo et al. 2007b; Halpern et al. 2005) in quiescence and larger ratios in outburst.

The radio emission from XTE J1810–197 was discovered immediately following a strong X-ray outburst. It has since faded, both in the radio and the X-ray band, and the radio pulsations are no longer visible. For 1E 1547–5408, the radio emission is also highly variable and appears to be ‘revived’ in the periods after its X-ray outbursts. PSR J1622–4950 on the other hand, has had at least two episodes of non-detections in the radio band lasting hundreds of days followed by periods of bright radio emission (see Fig. 4.1). In addition to the new *Chandra* observation, we searched archival data from *Chandra*, *XMM Newton*, *Rosat*, *ASCA*, *Beppo-SAX*, *Rossi-XTE* and *Swift* for an outburst, however no evidence for X-ray flux variability and no X-ray outburst at the level of the outbursts seen in XTE 1810–197 and 1E 1547–5408 in connection to the radio pulsations ($\gtrsim 10^{36} \text{ erg s}^{-1}$) were found since at least as early as 2005. It is possible therefore that an enhancement of X-ray activity is not a requirement for pulsed radio emission by magnetars, however, given the duty cycle of sensitive X-ray observations of the field containing PSR J1622–4950, we cannot constrain the occurrence of fainter X-ray enhancements of the source. What is instead certain is that the observed X-ray emission from PSR J1622–4950 is at variance with what is observed for the other two radio pulsating magnetars.

4.3.6 Possible SNR Association

If the true age of PSR J1622–4950 is similar to its characteristic age of 4 kyr, we might expect to see a supernova remnant (SNR) surrounding the pulsar. Indeed, 5 of the 9 AXPs and at least 1 of the 5 SGRs are located within SNRs (Mereghetti 2008; Gaensler et al. 2001). Inspecting the ATCA image in Fig. 4.2, we see a ring of emission centered $\sim 2'$ south of the pulsar location. This ring lacks an infra-red counterpart and appears

to be non thermal, whereas the extended radio source to the south of the ring is clearly thermal in nature. Could the ring be the SNR and the pulsar has escaped its bounds? If we assume a distance of ~ 9 kpc to the magnetar and further assume it was born in the centre of the ring, the magnetar would need a velocity of $\sim 1300 \text{ km s}^{-1}$ to reach its current location whereas the ring itself would have a lower expansion velocity. Such a velocity is high (though not impossible) for pulsars but rather low for expanding SNRs. Although the link between the ring and the magnetar is a possibility we consider it unlikely.

4.4 Conclusions

The HTRU survey has discovered a radio-luminous pulsar, which is highly polarized, has an inverted spectrum, and is highly variable in both its pulse profile and flux density. The radio pulsar has a faint X-ray counterpart that appears to be stable in flux, with a value that is typical of a quiescent magnetar. The pulsar shares many of the properties of the two known radio magnetars and we therefore conclude that PSR J1622–4950 is indeed a magnetar, the first discovered through its radio emission. This discovery not only adds a new member to the magnetar family, but also highlights unprecedented features of the emission of the magnetars across the electromagnetic band. At odds with what is observed in other sources, PSR J1622–4950 indicates that bright radio emission can be present even when a magnetar displays an X-ray luminosity typical of a quiescent state. Moreover, PSR J1622–4950 shows that *pulsed* radio emission can either exist without the occurrence of a strong X-ray outburst, or occur a long time ($\gtrsim 5$ years) after the outburst. Alternatively, the radio pulsations could be triggered by a modest increment of X-ray activity, that escaped detection in this case. We finally note that the extreme variability in the flux density of PSR J1622–4950 also demonstrates the advantages of surveying the radio sky at regular intervals with even modest sensitivity. This highlights the potential of the upcoming radio facilities like the LOFAR, ASKAP or the SKA which promise to characterize the dynamic radio sky at an unprecedented level.

5

Radio Emission Evolution, Polarimetry and Multifrequency Single Pulse Analysis of the Radio Magnetar PSR J1622–4950

This chapter was published in full in *Monthly Notices of the Royal Astronomical Society*, 422, 2489, 2012, authored by L. Levin, M. Bailes, S. D. Bates, N. D. R. Bhat, M. Burgay, S. Burke-Spolaor, N. D’Amico, S. Johnston, M. Keith, M. Kramer, S. Milia, A. Possenti, B. Stappers, W. van Straten.

We report here on observations of the radio magnetar PSR J1622–4950 at frequencies from 1.4 to 17 GHz. We show that although its flux density is varying up to a factor of ~ 10 within a few days, it has on average decreased by a factor two over the last 700 days. At the same time, timing analysis indicates a trend of decreasing spin-down rate over our entire data set, again of about a factor of two over 700 days, but also an erratic variability in the spin-down rate within this time span. Integrated pulse profiles are often close to 100 per cent linearly polarised, but large variations in both the profile shape and fractional polarisation are regularly observed. Furthermore, the behaviour of the position angle of the linear polarisation is very complex - offsets in both the absolute position angle and the phase of the position angle sweep are often seen and the occasional presence of orthogonal mode jumps further complicates the picture. However, model fitting indicates that the magnetic and rotational axis are close to aligned. Finally, a single pulse analysis has been carried out at four observing frequencies, demonstrating that the wide pulse profile is built up of narrow spikes of emission, with widths that scale inversely with observing frequency. All three of the known radio magnetars seem to have similar characteristics, with highly polarized emission, time-variable flux density and pulse profiles, and with spectral indices

close to zero.

5.1 Introduction

PSR J1622–4950 was discovered in the High Time Resolution Universe survey for pulsars and fast transients (Keith et al. 2010) currently underway at the Parkes and Effelsberg radio telescopes. The pulsar’s many similarities with the two previously known magnetars that emit radio pulsations have placed this source in the fast growing group of magnetars. Magnetars are commonly thought to be rotating neutron stars that in addition to their emission of pulsating radiation also undergo large bursts and outbursts of radiation in the X-ray and γ -ray bands (for more detailed reviews on magnetars see e.g. Mereghetti (2008) and Rea & Esposito (2011)). The magnetar group is built up by two subgroups: Anomalous X-ray Pulsars (AXP) and Soft Gamma-ray Repeaters (SGR). There is however no longer a strict division between the two classes, as new observations have shown that some of the sources simultaneously exhibit properties originally thought to belong exclusively to only one of the two classes (Gavriil et al. 2002, Mereghetti et al. 2009, Rea et al. 2009). The term magnetar originates in the sources’ extremely high inferred surface magnetic fields (typically $\geq 10^{14}$ G) and it is believed that their radiation is powered by the energy stored in the magnetic fields (Duncan & Thompson 1992) instead of by the spin-down as is the case for ordinary pulsars. Recently a new magnetar (SGR 0418+5729) with a considerably lower surface magnetic field ($B < 7.5 \times 10^{12}$ G) was discovered (Rea et al. 2010), casting doubts on the assumption that a high surface dipolar magnetic field strength is a requirement for magnetar-like activity.

Radio pulsations from a magnetar were first detected in 2006 from the source XTE J1810–197 (Camilo et al. 2006), and since then only two other sources have been found to belong to the group of radio-emitting magnetars: 1E 1547.0–5408 (Camilo et al. 2007b) and PSR J1622–4950 (Levin et al. 2010). XTE J1810–197 and 1E 1547.0–5408 are both so-called transient magnetars, that occasionally undergo large outbursts of X-ray emission. The radio properties of these two pulsars have been described in detail in a series of papers (e.g. Camilo et al. 2007d, 2008, Kramer et al. 2007, Lazaridis et al. 2008), which reported on features that make the radio magnetars stand out from the ordinary pulsar population. In addition to long pulse periods and high surface magnetic field strengths, these features include highly variable radio flux densities, changing pulse profiles on short time scales, large amounts of timing noise and a flat radio spectrum.

Both sources emit nearly 100% linearly polarised radiation at a large range of observing frequencies (Kramer et al. 2007, Camilo et al. 2007d, 2008). Analyses of the linear

polarisation position angle (PA) shows a preferred neutron star geometry for 1E 1547.0–5408 where the rotation and magnetic axes are close to aligned (Camilo et al. 2008), which at the time was supported by a low pulsed fraction in the X-ray (Halpern et al. 2008). Since then, X-ray monitoring has shown much higher pulse fraction values (Israel et al. 2010) and it has been shown that the low pulsed fraction in X-ray observed during high flux states may be due to a dust scattering halo (Israel et al. 2010, Bernardini et al. 2011, Scholz & Kaspi 2011). This is in conflict with the aligned geometry derived from the radio emission of 1E 1547.0–5408. The radio emission geometry analysis for XTE J1810–197 has proven difficult and different groups have reported on different results. Camilo et al. (2007d) report on two possible solutions for the geometry: Either the magnetic and rotation axes are nearly aligned, or the emission originates high above the surface of the star. Kramer et al. (2007) on the other hand derive a geometry where two emission cones must be present in the neutron star magnetic field. This is interpreted as either an offset dipole or a non-dipolar field configuration. Analyses of the X-ray data from XTE J1810–197 seem to favor a non-aligned geometry for this source (Perna & Gotthelf 2008).

Single pulse studies of XTE J1810–197 are covered in great detail in Serylak et al. (2009). They show that the integrated pulse profile consists of strong spiky sub-pulses, with an overall high modulation index that varies between components of the pulse. Their analysis concludes that the radio emission from XTE J1810–197 is clearly different to that from ordinary pulsars.

The radio magnetar PSR J1622–4950 was discovered by Levin et al. (2010). That paper reports on the high variability of this pulsar in the shape of the integrated pulse profile and in radio flux density on time scales of hours. The X-ray counterpart of the pulsar is identified, with an observed X-ray luminosity $L_X(0.3\text{--}10 \text{ keV}) \approx 2.5 \times 10^{33} \text{ erg s}^{-1}$, which is in the lower end of the range of X-ray luminosities observed for quiescent magnetars ($1.8 \times 10^{33} < L_X(1\text{--}10 \text{ keV}) < 1.2 \times 10^{36}$; Rea & Esposito (2011); or see the McGill SGR/AXP Online Catalogue¹). The same paper also mentions that PSR J1622–4950 has highly linear polarised radio emission and an inverted radio spectrum. Further studies of the radio spectrum of this magnetar have been carried out by Keith et al. (2011a), who observed it at bands centered at 17 GHz and 24 GHz, and concluded that the spectral index is close to zero when the flux densities from these observations are added in the radio spectrum calculation.

In this paper we will present the continued observations and analysis carried out for PSR J1622–4950 with the Parkes Radio Telescope. We will focus on four different aspects

¹<http://www.physics.mcgill.ca/~pulsar/magnetar/main.html>

of the emission: First we will have a look at the flux density evolution over \sim two years of observations to see if the source is still as variable in flux density as has been measured previously and if there are any trends in how it is varying overall. The second part will treat the timing analysis of the source, with the complications that a highly varying pulse profile introduces to this process. We will investigate if the frequency (ν) and frequency derivative (i) that we observe demonstrate the true spin-down of the pulsar or if their changes are artifacts of the pulse profile variations. Thereafter we will report on the polarimetry of the integrated pulse profiles and compare the results to the two previously known radio magnetars. We will also attempt to derive the geometry of the radio emitting regions of the neutron star. Finally we will report on an analysis of single pulses from the magnetar at several observing frequencies. Throughout the paper we will review the similarities and differences between PSR J1622–4950 and 1E 1547.0–5408, XTE J1810–197 and ordinary pulsars. This discussion will be incorporated in each pulsar property section in the paper, and we will finish by summarising our findings in the last section.

5.2 Observations and Analysis

All data used for this analysis were collected with the 64-m dish at the Parkes Radio Telescope using different receivers and backends. Observations were made at frequency bands centered at: 1.4 GHz using the center beam of the Multibeam Receiver (Staveley-Smith et al. 1996), 3.1 GHz using the ‘10/50-cm’ receiver and 17 and 24 GHz using the ‘13-mm’ receiver.

The Parkes Digital Filterbank System (PDFB3) used to create the folded profiles first converts the analogue voltages from each polarisation channel of the linear feeds into digital signals. It then produces 1024 polyphase filterbank frequency channels that are folded at the apparent topocentric period of the pulsar into 1024 pulsar phase bins, and written to disk every 20 s. Four Stokes parameters are recorded. To determine the relative gain of the two polarisation channels and the phase between them, a calibration signal is injected at an angle of 45° to the feed probes. The data are analysed off-line using the PSRCHIVE package² (Hotan et al. 2004) and corrected for parallactic angle and the orientation of the feed. The position angles are also corrected for Faraday rotation through the interstellar medium using the nominal rotation measure.

For the single pulse analysis the baseband data recording and processing system known as the ATNF Parkes Swinburne Recorder (APSR; van Straten & Bailes 2011) was used.

²See <http://psrchive.sourceforge.net>

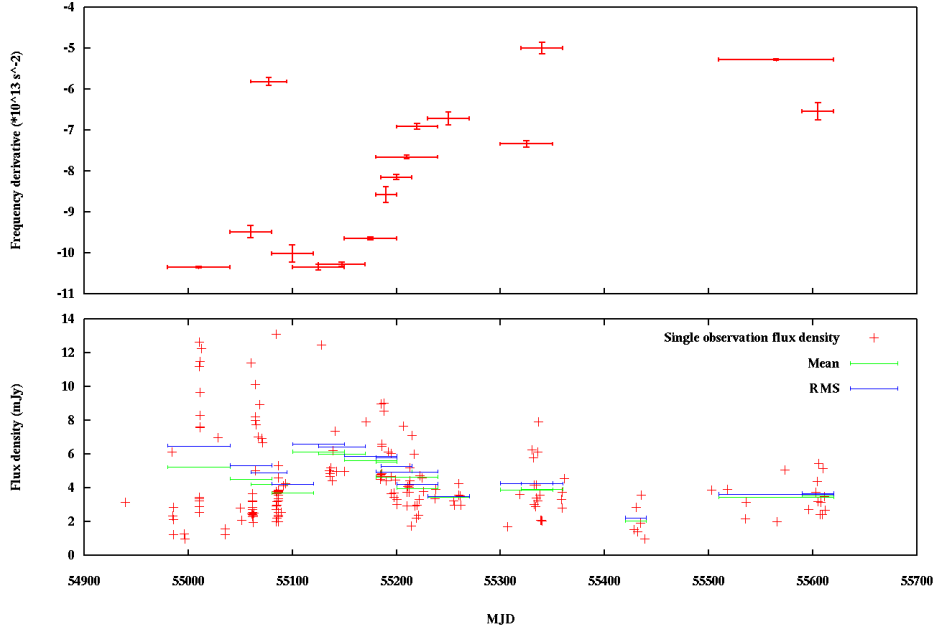


Figure 5.1 *Top plot*: Variation of frequency derivative with time. The error bars in the x-range indicate the time span of the included TOAs. The large variations in the value of the frequency derivative indicate changes in absolute value and sometimes also in sign of the second derivative. In some cases we have included a fit to a shorter data set, even if all the TOAs in that set are already included in a fit of a longer data set, to show the direction of the frequency derivative change. In total, the values of the frequency derivative varies up to a factor of ~ 2 . *Bottom plot*: Variation of flux density at 1.4 GHz with time. The mean and RMS values were calculated using the same sets of observations as were used in the frequency derivative analysis. In one case, around MJD 55440, the number of observations collected were not enough to attain a timing solution, and hence the corresponding point is missing in the top panel.

5.3 Radio Light Curve

As reported in Levin et al. (2010) the 1.4 GHz flux density of the integrated pulse profile varies greatly between observations. Since then we have collected about one more year of data on this source. Plotted in the bottom panel of Fig. 5.1 is the integrated flux density of each observation made at 1.4 GHz at Parkes since the discovery in April 2009. The new data points begin around MJD=55240. It is clear from this plot that the peak observed flux density during the last ~ 200 days is only about half the value observed during the first ~ 200 days after the discovery, suggesting an intrinsic long-term decay of the flux density. However, it is possible that the magnetar is still just as variable and with as high peak flux density as before but that the higher flux density points are missed during the

later time span due to the smaller sample. Simply fitting a line to the data points results in a slight slope, giving a decline of the average flux density of ~ 2 mJy for the 700 days of observing. To more easily visualise the flux density decline we have divided the data points into smaller sets of about 30 days each and calculated the mean flux density and the root mean square (RMS) for each of these data sets. The time span for each data set is the same as we used for calculating different rotation frequency derivatives as described in Sec. 5.4 below. The mean and RMS of each data set is plotted on top of the data points in the bottom panel of Fig. 5.1.

Anderson et al. (2012) report on recent observations of PSR J1622–4950 with the Chandra X-ray Observatory and the ATCA that were collected within the framework for the “ChIcAGO” project (Anderson et al. 2011). They observed the magnetar with the ATCA simultaneously at frequency bands centered at 5.0 GHz and 9.0 GHz on November 22, 2008 and December 5, 2008. The flux densities are 33.0 ± 0.3 mJy and 40.4 ± 0.3 mJy at 5.0 GHz and 30.9 ± 0.6 mJy and 31.9 ± 0.6 mJy at 9.0 GHz for the two observation sessions respectively. This is significantly higher flux densities than the values measured on December 8, 2009 and February 27, 2010 with the ATCA published in Levin et al. (2010): 13 ± 1 mJy at 5.0 GHz and 14.3 ± 0.8 mJy at 9.0 GHz. These values indicate a decrease in flux density of about 68% at 5.0 GHz and 55% at 9.0 GHz over one year (Anderson et al. 2012). With this in mind it seems likely that the flux density decline observed recently at 1.4 GHz with Parkes is a real intrinsic decay of flux density in the magnetar.

5.4 Timing

To analyse the rotational history of a pulsar, it is conventional to integrate over a set number of rotations, enough to create a stable pulse profile for each observation. These profiles are then aligned with the help of a standard profile, unique to that particular pulsar, to create a list of the pulse times of arrival (TOA) at the telescope. The list of TOAs is used to determine a more accurate period and spin down rate of the pulsar as well as its precise position in the sky, a more precise value of its DM, etc. When performed on data from a large enough time span, using this method generally results in values for the pulsar parameters with very high accuracy.

However, due to the variability of pulse profile at 1.4 GHz, the timing analysis of PSR J1622–4950 is more complex than for an ordinary pulsar. Here we have employed the same tools in the timing procedure as were used in Levin et al. (2010), i.e. TOAs for the pulses were calculated by using a model that describes the different components of

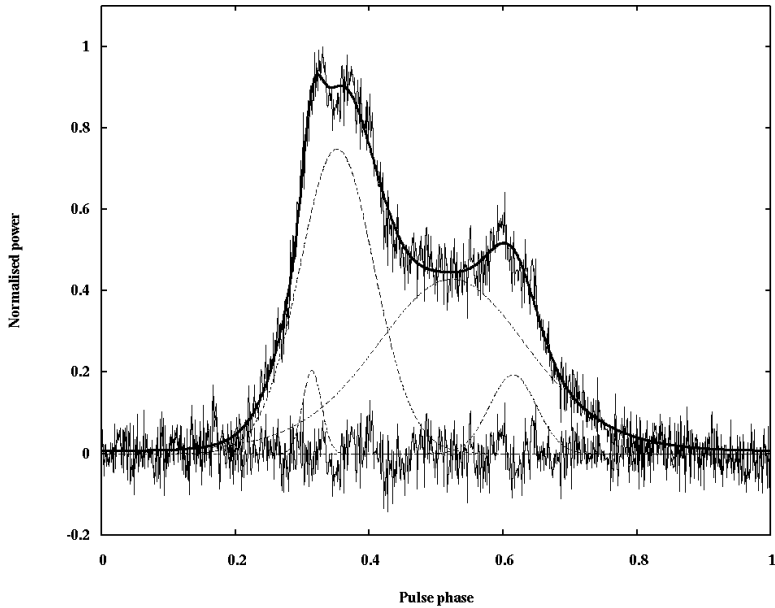


Figure 5.2 Timing model. The dashed lines show the von Mises functions used to build up the profile, which added together give the solid line that follows the pulse shape. The bottom noise level show the emission that is left after subtracting the model. Profile from 29 June 2009.

the profile, rather than using a standard profile. The model was created using software from the PSRCHIVE package (Hotan et al. 2004) by fitting scaled von Mises functions (von Mises 1918) to the pulse profile of one of the observations where all the components were present. This profile and the corresponding model is shown in Fig. 5.2. The TOAs are then created by letting the amplitudes of the components vary but keeping the separations fixed, while fitting the model to each observation. The timing analysis was made using the TEMPO software³.

However, we cannot obtain a coherent timing solution for our full data span even using this method. Instead we have looked at data from shorter time spans and fitted the observed frequency (ν) and frequency derivative ($\dot{\nu}$) for each set of timing points separately, in an attempt to quantify how much and in which direction the true spin-down is changing with time. The number of points included in each set is dependent on how long we could get a stable $\dot{\nu}$ with a reasonable error (largest error in Fig. 5.1 is $\dot{\nu}_{err} = 0.21 \times 10^{-13} \text{ s}^{-2}$). For this timing analysis the position is held fixed at that constrained by the X-ray counterpart: R.A. = 16:22:44.80, Dec. = -49:50:54.4 (Levin et al. 2010) and the dispersion measure is set to $820 \text{ cm}^{-3}\text{pc}$. The result of this analysis is shown in the

³See <http://www.atnf.csiro.au/research/pulsar/tempo/>

upper panel of Fig 5.1. It is evident from this plot that $\dot{\nu}$ has been changing with a factor of ~ 2 since the discovery, as was also stated in Levin et al. (2010). However, the second derivative of the frequency ($\ddot{\nu}$) is also changing rapidly in magnitude and direction with time.

A comparison of these results to the timing analysis carried out previously for the other two radio magnetars, 1E 1547.0–5408 (Camilo et al. 2007a) and XTE J1810–197 (Camilo et al. 2008) shows clear similarities, but also differences. In all three cases the $\dot{\nu}$ is changing greatly as a function of time. In both of the other sources the $\ddot{\nu}$ seems to vary more smoothly than it does for PSR J1622–4950 and they both have steady trends along a fairly straight line (allowing for some "wobbling" on the way). However, the sign of the estimated $\ddot{\nu}$ is different for the two sources: XTE J1810–197 has a positive $\ddot{\nu}$ and 1E 1547.0–5408 has a negative one. The timing analyses for both the other two magnetars were made using data that were collected more regularly and frequently than our observations, which may contribute to the smoother looking frequency derivative evolution.

Camilo et al. (2007a) quantify the timing noise by looking at the magnitude of the cubic term of a Taylor series expansion of rotational phase over a time interval t , i.e. $\ddot{\nu} t^3/6$ (Arzoumanian et al. 1994). By using this expression they get about 60 cycles over 6 months for 1E 1547.0–5408 and 20 cycles over 9 months for XTE J1810–197. The same calculation for PSR J1622–4950 yields about 250 cycles over the entire 20 months that the pulsar has been observed since the discovery. If we instead look at only the 100 days when the $\dot{\nu}$ is steadily increasing (from MJD \sim 55150 to MJD \sim 55250) the value is about 5 cycles over 3.3 months.

One option that could explain the unusual behavior of $\dot{\nu}$ in PSR J1622–4950, is if the source went through a glitch shortly before the discovery observation at MJD=54939. Glitches are more frequent for younger pulsars than for older sources, but in general unusual in ordinary pulsars (Espinoza et al. 2011). For AXPs however, glitches have been observed in nearly all known sources (Dib et al. 2008) and it would therefore be feasible to observe a glitch also for PSR J1622–4950. Unfortunately it is very hard to constrain if a glitch has occurred without any data from around or before the time of the possible glitch, but the possibility is worth noting for future timing efforts of this source.

By comparing the two panels in Fig. 5.1, there is an apparent correlation between reduced flux density and increased $\dot{\nu}$, again especially between MJD \approx 55100 and MJD \approx 55300. Calculating Pearson's correlation coefficient, $r_{(x,y)} = \text{cov}(x,y)/\sigma_x\sigma_y$ (where $\text{cov}(x,y)$ is the covariance of x and y , and σ is the standard deviation), for correlation between $\dot{\nu}$ and the mean values for each time span in Fig. 5.1 gives $r = -0.73$, which corresponds to

a 3 sigma correlation. It is however hard to constrain that these two features are direct consequences of each other, and we stress that care should be taken not to infer too much from these correlation results.

Beloborodov (2009) describes a model in which starquakes or glitches in the neutron star cause the magnetic field lines to twist. The author describes the electrodynamics of the untwisting of the field lines as they relax back towards their initial state. He considers this model in the context of the magnetars, in particular XTE J1810–197, where the reduction in the radio flux density over time, the changes to the torque and the X-ray observations all conform roughly with his calculations. This model may also be applicable here as we see a similar decrease in flux density over time and large variations to the torque although we are hampered by a lack of information in the X-ray band. It is also hard to see how the gradual untwisting of magnetic field lines can cause the rapid profile and polarization variations that we see as these appear to oscillate back and forwards between states on a timescale much shorter than the decay of the radio flux density.

5.5 Polarimetry

We have collected polarimetric data for PSR J1622–4950 with the Parkes Telescope at four different observing frequencies, with bands centered at: 1.4 GHz (the centre beam of the Multibeam receiver), 3.1 GHz (10/50 cm receiver) and 17 GHz and 24 GHz (13 mm receiver).

The high frequency observations (at 17 and 24 GHz) were reported on in Keith et al. (2011a), and we note some striking similarities in the polarised emission over all observed frequencies. As well as having a very wide ($\sim 50\%$) duty cycle for the integrated profiles, the linear polarisation is often close to 100% of the total intensity. However, similar to the flux density and pulse profile shape, also the polarisation of the integrated profiles is changing between observations.

5.5.1 Polarisation Categories

In an attempt to get an overview of the way the polarisation is varying we have collected observations with similar characteristics in groups, giving us four separate categories with different properties. Category I is the most frequent mode, with almost half (48%) of all categorised observations. It collects the observations where the linear polarisation is $> 50\%$ of the total intensity, the circular polarisation is low and the position angle (PA) has a steep and consistent swing. In category II the linear polarisation is much lower

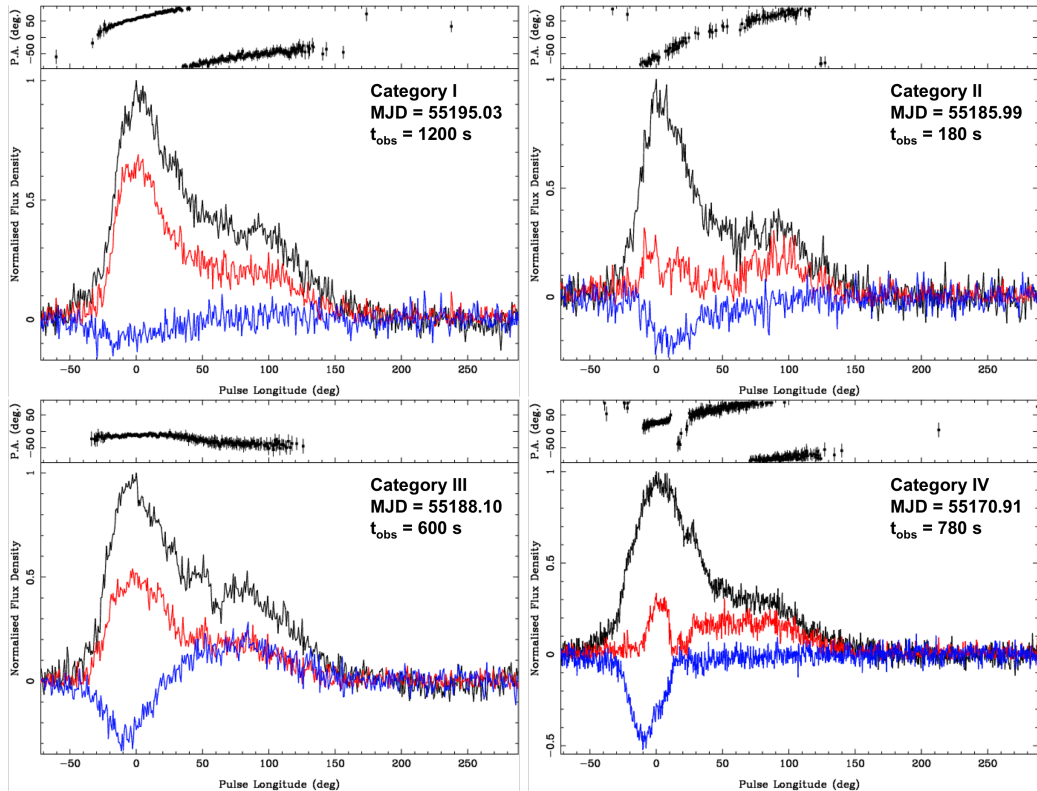


Figure 5.3 Examples of observations at 1.4 GHz from the four different polarisation groups described in Sec 5.5.1. Category I - IV are shown from top left to bottom right. Total intensity is shown in black, linear polarisation in red and circular polarisation in blue. The integration time for each observation is noted in the panels, however there are both shorter (~ 180 s) and longer (~ 600 s) observations present in all categories. Note the short time scale of the variations: all four observations were collected within the same calendar month (December 2009).

throughout the profile. In the cases where a second component is present, the fraction of linear polarisation is higher in the trailing edge than in the leading edge of the profile. Similar to category I, the circular polarisation is low and the PA swing is steep and consistent. 24% of our observations belong to this group. For category III (11% of the observations) the most prominent feature is the shallow PA curve. In addition the profiles also tend to have low linear polarisation in the leading edge of the profile and a higher value of the circular polarisation than for categories I and II. The last 17% of the observations do not fit into any of the first three groups, and hence will end up in category IV. Here we have collected the observations with jumps and other irregularities in the PA swing, change of handedness in the circular polarisation and large changes in linear polarisation within the pulse profile. Examples from all four groups are shown in Fig 5.3.

When looking at the time evolution of the polarised emission, by analysing observations from the different groups in time order, it does not seem like the variations are following any preferred order, but are fairly random in time. The large variations in linear polarisation and PA for PSR J1622–4950 are at odds with what is seen for XTE J1810–197 by Kramer et al. (2007). They observe an evolution in PA swing over a time-scale of weeks, but very few changes on shorter time-scales. Also Camilo et al. (2007d) observed that the general polarisation properties of XTE J1810–197 do not seem to vary with time as the total intensity changes. That is, the linear polarisation is always close to 100% of the total intensity, and the circular polarisation component is low. This suggests that the observed profile variations are not caused by changes in the magnetic field geometry of the emission regions for this source. Also in the case of 1E 1547.0–5408 there is little variation in linear polarisation and in measured PA swing with observing frequency and time (Camilo et al. 2008). The circular polarisation however increases with decreasing frequency, and is overall higher than for XTE J1810–197.

5.5.2 Rotating Vector Model Predictions on the Neutron Star Geometry

By analysing the linear polarisation and how its position angle is varying across the pulse profile, predictions on the angles of the rotation and dipole axes can be made. The rotating vector model (RVM; Radhakrishnan & Cooke 1969) states that the pulsar emission beam has its base close to the dipole axis of the pulsar magnetic field and is observed through rapid swings of the linear polarisation position angle over the pulse phase. When using the RVM there are a number of effects that are very difficult to take into account and hence are often ignored. These effects include rotational sweepback of the magnetic field lines (Dyks & Harding 2004), propagation effects in the pulsar magnetosphere (e.g.

Table 5.1 RVM fits to 3.1 GHz data. All angles are given in degrees.

Observation ID	MJD	χ^2	ψ_0	ζ	α	ϕ_0
s091230_210826	55195.88	1.47	-5.7±13.6	15.1±28.8	36.0±60.2	141.6±9.7
s091230_215432	55195.91	1.28	-11.6±3.4	15.5±9.8	28.6±17.2	137.5±2.0
s100101_201716	55197.85	1.01	-20.6±2.8	20.7±4.0	46.0±7.8	149.7±1.6
t100615_074911	55362.33	1.34	-20.5±1.8	14.7±5.8	28.3±10.4	137.0±1.1
t100825_102356	55433.43	1.62	-23.7±6.1	16.3±22.2	25.0±33.5	157.4±2.2
t110116_211759 ^a	55577.89	2.40	-4.8±1.5	13.2±7.0	22.2±11.3	192.9±0.9
s110410_210120	55661.88	1.69	-29.6±6.4	7.1±21.9	20.7±58.0	122.6±7.3
s110410_212455	55661.89	1.10	-26.5±3.2	9.9±9.7	24.7±21.8	128.9±3.3

Notes:

^a Observation with orthogonal PA jump

Petrova 2006), emission height differences (Dyks 2008) and multipolar components of the magnetic field. There are a number of papers discussing these effects on the magnetic field geometry for magnetars in particular, and the possibility that higher order multipoles are contributing to the magnetic field structure near the magnetar surface (e.g. Thompson et al. 2002, Beloborodov 2009, Rea et al. 2010, Turolla et al. 2011). We will disregard from these effects in this paper, but it is important to keep in mind that the magnetic field topology may well deviate from the simple dipole model.

In the case of PSR J1622–4950, the highly varying values of the PAs in the 1.4 GHz observations make it difficult to find a consistent solution to the geometry of the neutron star emission. RVM fits to data from different days give different answers depending on the parameters of the PA curve for that particular observation. The scatter broadening of the single pulses at 1.4 GHz (as described in section 5.6.2) could contribute to some of the large changes in linear polarisation and PA swing that we observe at this observing frequency, and hence we have focused the RVM fits to the less scatter broadened and apparently more stable 3.1 GHz data. Tab. 5.1 shows the values from the 3.1 GHz RVM fits. Even though the best fit angles vary between observations we are able to put some constraints from these fits. The angle between the spin axis and the pulsar-observer line of sight, ζ , is small in all observations with $\zeta \lesssim 20^\circ$ and the angle between the spin axis and the magnetic pole, α , is always just a few degrees higher than ζ with $20^\circ \leq \alpha \leq 46^\circ$. The resulting angle, β , places the line of sight between the magnetic pole axis and the positive rotation axis with values $-25^\circ \leq \beta \leq -8^\circ$. The results imply that the pulsar has close to aligned magnetic and rotation axes and that the line of sight remains within the emission beam for large parts of the rotation, which in turn is implied by the wide duty cycle of the integrated profiles.

RVM predictions for 1E 1547.0–5408 are described in Camilo et al. (2008). They carried

out polarimetric studies with several different receivers at the Parkes telescope at five different observing frequencies ranging from 1.4 to 8.4 GHz and at the Australia Telescope Compact Array (ATCA) at frequency bands centered at 18 and 44 GHz. They report on a slow PA sweep that has an absolute value identical at all observed frequencies, and their RVM fit suggests nearly aligned rotation and magnetic axes. At the time, this result was strengthened by a low pulsed fraction in the X-ray ($\sim 7\%$) measured as the source was in quiescence, shortly before the 2007 outburst (Halpern et al. 2008). It has subsequently been suggested that the low pulsed fraction may be due to a dust scattering halo around the magnetar (Tiengo et al. 2010, Olausen et al. 2011). Observations of the magnetar at the time of the 2008 October outburst showed much higher pulsed fraction values ($\sim 20\%$) which increased to $\sim 50\%$ during the following few weeks (Israel et al. 2010). The anti-correlation between the flux and the pulsed fraction that has been observed for 1E 1547.0–5408 (Israel et al. 2010, Bernardini et al. 2011, Scholz & Kaspi 2011) together with the highly variable pulse profiles as a function of time, may suggest that the magnetospheric geometry is variable during the initial phases after an outburst and may not be easily related to the geometry in quiescence (Israel et al. 2010). Hence, even though the higher pulsed fraction measured for 1E 1547.0–5408 in more recent observations conflict with the aligned geometry derived from the radio data, we do not see these results as strong enough to completely rule out an aligned geometry.

Analyses of XTE J1810–197 also result in different geometries for different research groups and wavelengths. Camilo et al. (2007d) analysed radio polarisation observations of XTE J1810–197 collected with the Parkes Telescope at three observing frequencies (1.4, 3.2 and 8.4 GHz). Their analysis shows a shallow swing of the position angle of the linear polarisation, with values that yield two possible solutions for the geometry of the magnetar. Either the magnetic and rotation axes are nearly aligned, or the emission originates high above the surface of the star. Using X-ray data, Perna & Gotthelf (2008) also estimated the viewing geometry of XTE J1810–197. They determine the allowed minimum and maximum angles between the line of sight and the emission hot spot, and find that the range of the minimum value is compatible with very small angles (including zero) while the maximum is always large ($\gtrsim 60^\circ$). It has been shown that the peaks of the radio and X-ray pulses from XTE J1810–197 are well matched (Camilo et al. 2007a), which suggests that the radio emission axis and the hot spot axis are very close to aligned. Perna & Gotthelf (2008) find that the high emission height solution from Camilo et al. (2007d) is well compatible with their results and that an aligned geometry is unlikely. However, they were not able to make a formal statistical comparison with the results from

Camilo et al. (2007d). Concurrently Kramer et al. (2007) also published results from radio polarisation observations of the same magnetar. Their simultaneous multifrequency observations (at 1.4, 4.9 and 8.4 GHz) were done with three European telescopes: the 76-m Lovell radio telescope in the UK, the 94-m equivalent Westerbork Synthesis Telescope in the Netherlands, and the 100-m radio telescope at Effelsberg in Germany. The main difference in their results compared to Camilo et al. (2007d) is that Kramer et al. (2007) include studies of the single pulse emission and identify an inter-pulse in addition to the main pulse during some of their observations and at some frequencies, that was not visible in the Parkes data. The PA values in the inter-pulse are observed to vary with time, which complicates the geometry analysis. Instead of fitting a RVM to the entire pulse profile the authors analysed the main pulse and the inter-pulse separately, with a geometry where two emission cones must be present in the neutron star magnetic field as result. This is interpreted as either an offset dipole or a non-dipolar field configuration.

The many different geometry analyses that have been carried out for the three radio magnetars make a comparison between them complicated. It is still a bit unclear but we can not completely rule out that the three sources are all aligned, as hinted by the RVM. We find this solution very tempting, as it could prove insight in the radio behavior of the magnetars. Since the probability of observing a pulsar is lower for a smaller α , aligned geometries of the radio magnetars could explain why only three of the 23 currently known magnetars and magnetar candidates have observed radio pulsations. So far no X-ray pulsations have been observed from PSR J1622–4950. Detection of pulsations in the X-ray might provide additional constraints on the geometry of PSR J1622–4950 and would help us to investigate this question further.

5.5.3 Pulse Profile Alignment

At 3.1 GHz the amount of linear polarisation is in general very large. All of our observations at this frequency band belong to category I or category IV in the classification above. Even though the amount of linear polarisation seems fairly constant, the integrated pulse profile still has a varying shape. The problem with aligning profiles of different pulse shapes was dealt with in the timing case by making a model of von Mises functions (see Section 5.4 and Fig 5.2). Seeing that the PA is often similar for all 3.1 GHz observations, we have also aligned the profiles by using the value of ϕ_0 that was estimated from the RVM model. The result is shown in Fig 5.4. Comparing the two alignment methods, it again becomes obvious that the polarisation from the magnetar is changing with time. At first glance it might seem like the aligning after the total intensity profile (the bottom plot of Fig. 5.4)

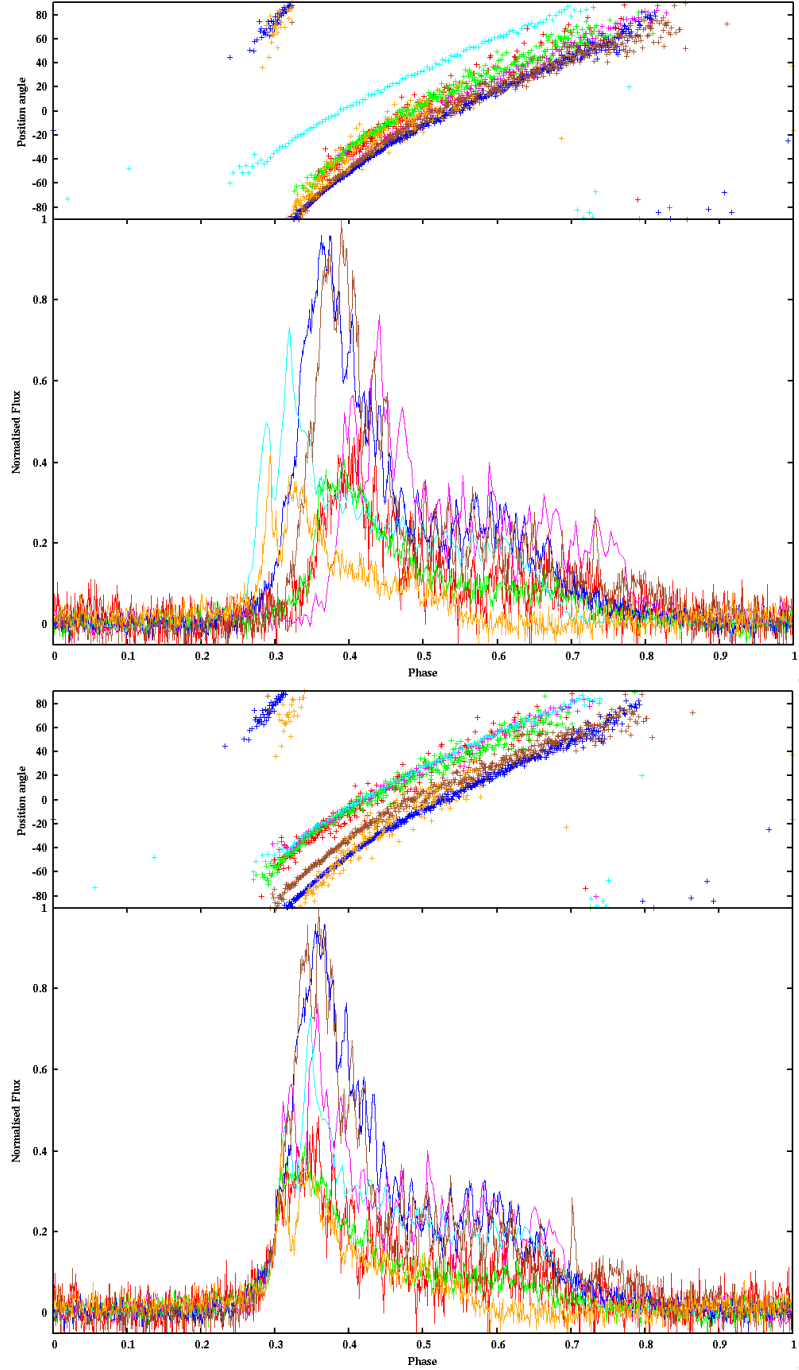


Figure 5.4 Pulse profiles and PAs for 3.1 GHz observations without orthogonal PA jumps. The flux density in the lower panels of the two plots are normalised after the maximum flux density of the brightest observation. The profiles of the same color refer to the same observation for both alignments. *Top:* The PAs are aligned after the value of ϕ_0 from the fit to the RVM model. Hence the maximum value of $\delta\psi/\delta\phi$ for each observation is centered at phase 0.3. *Bottom:* The profiles are aligned after the total intensity by centering the leading edge of each profile at phase 0.3.

is the one that should be preferred. However, a closer look at the PAs shows not only a shift in absolute value of the PAs but also that the PA curve for some of the observations have different slopes. For example, this can be seen by comparing the brown crosses with the dark blue ones in the upper panel of the bottom plot in Fig 5.4. Both PAs have similar slope in the leading edge of the pulse, but towards the trailing end the brown PA curve flattens out much faster than the dark blue one. The same slope difference is of course also present when we align the profiles after the value of ϕ_0 , but by looking at the top plot of Fig 5.4 (and disregarding from the light blue curve, which is offset from the others) even with the different slopes we find that the PAs align fairly well for the different observations. The profiles however do not.

If the rotation measure (RM) of the interstellar medium would change with time between observations, that could explain the offset in absolute value of the PAs in the bottom panel of Fig. 5.4. However, by estimating the RM value for two of the observations where the offset is large (e.g. for the dark blue and the green curves) we do not see a large enough change between our observations.

It is hard to say which (if any) of the two alignment methods describes the true magnetar emission. One way to get a better handle on this would be to use the polarisation information in the timing of the pulsar by calculating TOAs using the ϕ_0 values from each observation. The errors from this timing analysis could then be compared to the errors from the timing model described in Sec. 5.4. Such an analysis would only be possible to do with 3.1 GHz (or higher frequency) data, since part of the linear polarisation emission at 1.4 GHz is affected by interstellar scattering (see Section 5.5.4), which causes the degree of linear polarisation for many of the 1.4 GHz observations to be too small or the PA swing to be flattened, preventing a reliable RVM fit. The integrated magnetar emission also seems to be more stable at 3.1 GHz than it does at 1.4 GHz, which would help in the timing for both timing methods. Unfortunately the number of 3.1 GHz observations carried out at this point is not large enough and the observations that exist are not sampled densely enough to allow for such an analysis at the present time.

5.5.4 Depolarisation

In general, we observe a lower degree of linear polarisation at 1.4 GHz than at the higher observing frequencies. A similar trend is seen in 1E 1547.0–5408 by Camilo et al. (2008). This magnetar is at a similar DM as PSR J1622–4950 and they are both positioned close to the Galactic disk, which implies that both pulsars have a fairly high scattering timescale as predicted by the NE2001 model (Cordes & Lazio 2002): 1E 1547.0-5408 has $DM = 830 \pm$

$50 \text{ cm}^{-3}\text{pc}$ and $(l,b) = (327.23, -0.13)$ (Camilo et al. 2007b) which gives a scattering time scale of ~ 70 ms at 1 GHz compared to $\text{DM} = 820 \pm 30 \text{ cm}^{-3}\text{pc}$ at $(l,b) = (333.85, -0.10)$ for PSR J1622–4950 (Levin et al. 2010) which results in ~ 95 ms at the same frequency. Camilo et al. (2008) explain this depolarisation in 1E 1547.0–5408 at lower observing frequencies partly as an effect of the interstellar scattering of the pulse profile at these frequencies. This causes the PA to rotate through the different phases of the pulse, which will be mixed at the observer and will thus reduce the apparent linear polarisation. They also give deviations in rotation measure (RM) over different paths taken by the scattered rays as a further possible reduction effect. They conclude that scattering effects can only be responsible for part of the depolarisation. Hence, even though some of the depolarisation at lower frequencies for PSR J1622–4950 could be intrinsic to the source, it is likely that scattering effects are also responsible for some depolarisation in our case. In addition, we do observe a large amount of scattering in the single pulses at 1.4 GHz (see Sec. 5.6.1), which further justifies this hypothesis. Unfortunately, due to issues with the observing system at the time of collection of the 1.4 GHz single pulse data, we are not able to polarisation calibrate this data, and hence will not be able to analyse which effect the depolarisation has on the 1.4 GHz single pulses. The single pulse data collected at an observing frequency of 3.1 GHz is almost 100% linearly polarised, which is discussed in Sec. 5.6.2 below.

5.6 Single Pulses

Single pulse analyses have been carried out at three observing frequencies, with bands centered at 1.4, 3.1 and 17 GHz collected using the APSR backend at Parkes. Due to the large scattering effects at 1.4 GHz (discussed in Sec. 5.6.1 below) and the poor time resolution obtained at 17 GHz (1024 bins over the pulse profile), most of the single pulse analysis carried out for this paper has focused on 3.1 GHz data. In addition, one archival observation, collected within the frame work of the Methanol Multibeam Survey (Bates et al. 2011b) at Parkes using the Analogue Filterbank at a frequency band centered at 6.6 GHz has been analysed.

5.6.1 Scattering

Due to the high DM of PSR J1622–4950, the single pulses are likely broadened enough by interstellar scattering at 1.4 GHz that it will affect the pulse width at our time resolution. The pulse broadening due to scattering at the pulsar position and distance is ~ 17 ms at

1.4 GHz according to the NE2001 model (Cordes & Lazio 2002), assuming Kolmogorov scalings from 1.0 GHz, but the large uncertainties in the model indicate that this value could deviate by up to a factor of ten (as has been shown by e.g. Bhat et al. 2004). To better estimate the total scattering we analysed the widths of bright single pulses in the 3.1 GHz data by dividing the observed frequency band up in parts and calculating the pulse broadening over the bandwidth for that observation. This resulted in ~ 8.7 ms smearing over a 768 MHz band centered at 3.1 GHz. Again by assuming Kolmogorov scaling ($\tau_{\text{scatter}} \propto \nu^{-\alpha}$, using scaling index $\alpha \approx 4.0$ as an estimation for high DM pulsars (Löhmer et al. 2001, Bhat et al. 2004)) we calculate a scattering of ~ 200 ms at a band centered at 1.4 GHz, which is of the same order of magnitude as the measured value of the single pulse widths at that observing frequency (see Sec. 5.6.3 and Tab. 5.2). This implies that single pulses at 1.4 GHz will be highly dominated by scattering effects and hence we will not include the 1.4 GHz data in the single pulse analysis. The same analysis results in 0.41 ms of smearing at 6.6 GHz and $9.3\mu\text{s}$ at 17 GHz.

5.6.2 Single Pulse Characteristics

Although the integrated pulse profile for PSR J1622–4950 is often very wide (with a $\sim 50\%$ duty cycle), when analysing each rotation of the pulsar separately, it is clear that the profiles are built up by the collection of much narrower pulses (see Fig. 5.5 and Tab 5.2). Each pulse consists of one or a few narrow spikes, at all observed frequency bands.

The top right panel of Fig. 5.5 shows one of the brighter single pulses observed at 3.1 GHz and the bottom right panel is a zoom-in on the two brightest components of that particular rotation. From this plot we can see how each spike is almost 100% linearly polarised with no or very little circular polarisation. The position angle of linear polarisation of the separate components are well resolved and seem to be fairly flat across the spike. Looking at the combined PAs for the rotation in the top right panel, it is clear that they follow the PA swing of the total integrated profile. When we look at the single spike PAs in more detail, we find they are often in agreement with the total PA swing, but there are also occasions when the single PAs are much steeper than the integrated PA. This results in that we sometimes see small ‘wiggles’ in the PA swing that often correspond to emission peaks in the total intensity of the integrated profile. Similar wiggles in the PA swing are also seen in some observations of XTE J1810–197 (Kramer et al. 2007).

At 3.1 GHz a histogram of the phases of the single pulses matches the total intensity profile well (see Fig 5.6). When only the brightest 10% of the spikes are taken into account, we get the blue distribution in Fig. 5.6. These spikes seem to be spread out over almost

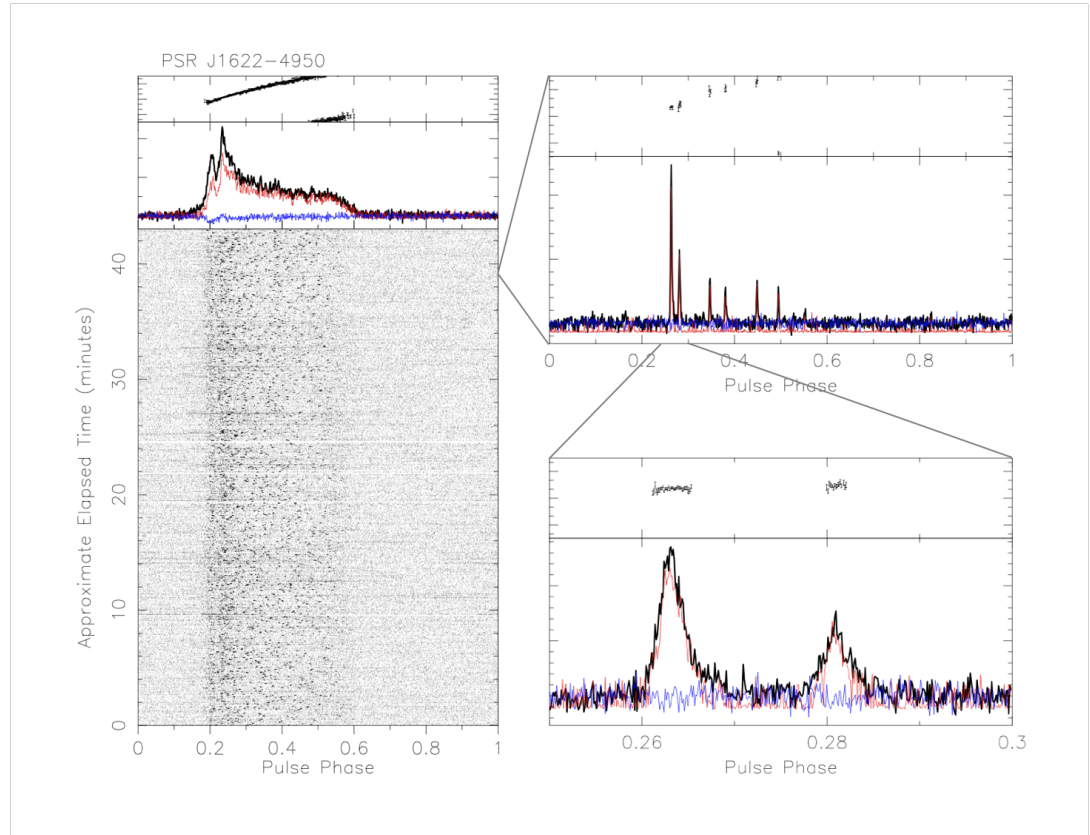


Figure 5.5 *Left:* 3.1 GHz single pulse stack with the corresponding integrated profile on top. Linear polarisation is shown in red, circular polarisation in blue and the total intensity in black. *Top right:* Pulse profile of one of the brighter single pulses showing the very narrow spikes of emission. *Bottom right:* Zoom in on the two brightest spikes of emission in the rotation above.

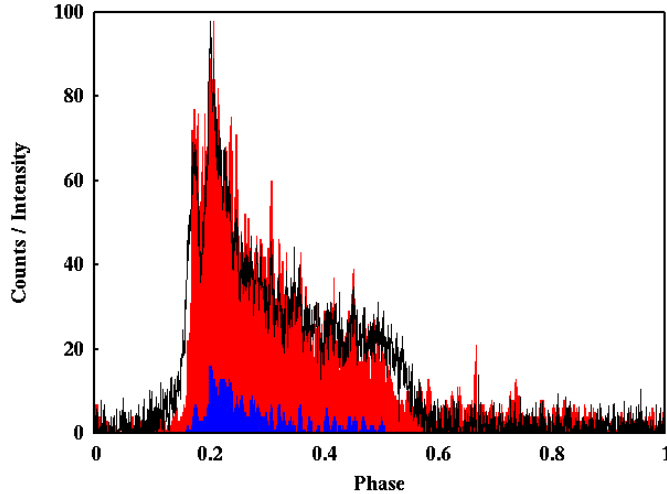


Figure 5.6 3.1 GHz pulse phase histogram. The red boxes show all pulses, while the blue boxes only account for the brightest 10% of the spikes. The black line is the total intensity profile averaged to match the top value of the histogram.

the entire pulse profile, but with a preference for certain phase bins. Each rotation consists of up to 15 spikes of emission, with 2 or 3 spikes per rotation being most frequent. The separation between emission spikes varies up to the full integrated pulse width, but with a preferred value of ~ 170 ms.

5.6.3 Width of Single Emission Spikes

The width of the total integrated pulse profiles scales with observing frequency in ordinary pulsars. This phenomenon is usually thought to be due to radius-to-frequency mapping, which suggests that the emission at different frequencies originates from different altitudes above the polar cap (Cordes 1978). A study of the integrated profile width is not as useful for PSR J1622–4950 unless simultaneous multifrequency observations are considered, as the widths of the profiles are changing with time when the profiles vary. However, in a similar way to the integrated profiles, we expect to see a decrease in the width of single emission spikes if the emission at different frequencies are emitted at different altitudes. Indeed, there have been indications that the pulse width is scaling down with increasing observing frequency in previous pulsar work (see e.g. Kramer et al. (2002) and references therein). This is even more clearly demonstrated in PSR J1622–4950, see Tab. 5.2. By comparing the average widths of the single pulse spikes at the three highest observed frequencies (3.1, 6.6 and 17 GHz) and correcting for the broadening due to scattering, we calculate a frequency dependence for the width of the single emission spikes for this source

Table 5.2 Widths of single pulse spikes at different observing frequencies. The upper limit given for the 17.0 GHz pulse width is the value of two phase bins. The scatter broadening is measured at 3.1 GHz and scaled using Kolmogorov scaling, with index $\alpha = 4.0$, to estimate the values at the other frequency bands.

Observing frequency [GHz]	Average width of single pulses [ms]	Scatter broadening of single pulses [ms]	Width of integrated profiles [ms]
1.4	215	200	2163
3.1	26	8.4	1946
6.6	13	0.41	1298
17.0	≤ 8.44	0.0093	1730

as $\tau \propto \nu^{-0.62 \pm 0.12}$. Kramer et al. (2002) carried out a similar analysis for the width of the micro-structure in PSR B1133+16 and found a much flatter dependence: $\tau_\mu \propto \nu^{-0.06 \pm 0.10}$.

Kramer et al. (2002) also confirmed a relationship between micro-structure width and pulse period first suggested by Cordes (1979) as a linear dependence. The single emission spike widths for PSR J1622–4950 at similar observing frequencies do not fit this relation, but the width at 17 GHz (≤ 8.44 ms, an upper limit estimated to two time bins) is closer to the predicted value of 3.0 ms. This may suggest that the scattering at the lower observing frequencies is underestimated, and that the 17 GHz width is the true width of the single emission spikes. However, since the scattering at 3.1 GHz is the measured value, we find it more likely that the width scaling with observing frequency is intrinsic, which indicates that perhaps separate relations are required for different frequency bands. Other reasons to why the emission from PSR J1622–4950 does not fit the relation could be that the pulse structure that we observe in PSR J1622–4950 is not of the same origin as micro-structure, or that magnetars follow a different relation than ordinary pulsars. The single pulse widths for the other two radio-emitting magnetars are in the same order of magnitude as for PSR J1622–4950, and with the discovery of more sources it will be possible to investigate if a similar dependence for magnetars is valid.

5.6.4 Pulse-Flux Distribution

By looking at the flux density of single spikes of emission we have calculated a pulse flux distribution for the single pulse spikes at 3.1 GHz. A conventional energy distribution calculation often only records the peak flux density in the on-pulse region for each rotation and compares the resulting histogram to a histogram of the peak flux density in the off-pulse region. To account for the frequent occurrence of multiple emission spikes in a single rotation of PSR J1622–4950 we have approached this analysis differently. The on-pulse

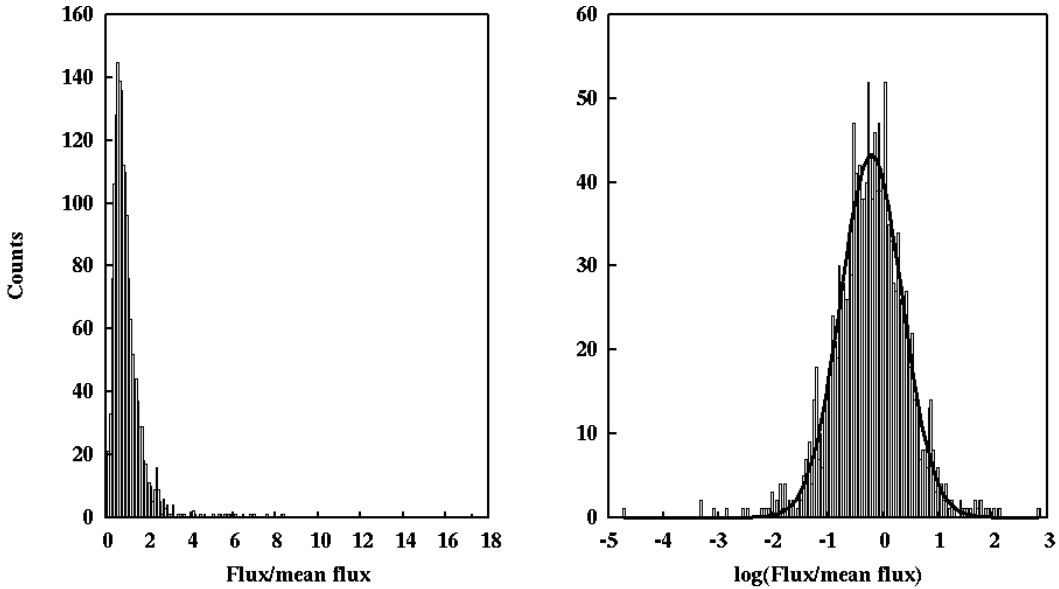


Figure 5.7 Pulse-flux distribution at 3.1 GHz. *Left:* Histogram of flux/mean flux of the single pulse spikes. *Right:* Histogram of the logarithm for the same data. The solid line shows the best fit of a Gaussian to the histogram, displaying the lognormal distribution of the flux density.

phases were chosen as all spikes that consisted of at least 3 consecutive phase bins with a signal stronger than 3 sigma, and the corresponding flux value for each spike was added to the histogram. The histogram in Fig. 5.7 was created after adding the phase bins to a total of 512 bins over the profile. The left panel shows the flux distribution and the right panel shows the 10 base logarithm of the flux. From this it is clear that the flux distribution from the magnetar is closer to a log-normal rather than Gaussian distributed. It is also evident from these plots that most spikes are of similar flux density and that there were no giant pulses observed from the magnetar. These properties are similar to the general ordinary pulsar population, for which a large fraction of the measured flux density distributions are close to log-normal and most do not emit giant pulses (e.g. Cairns et al. 2004, Burke-Spolaor et al. 2012).

5.6.5 Pulse Modulation

To get an overview of to which extent the pulses are varying over the pulse phase, we have calculated two values for each bin in the pulse profile: the modulation index and the R parameter. We define the modulation index as $m_i = \sigma_i/\mu_i$, where σ_i is the mean intensity in bin i and μ_i is the standard deviation in the i th bin after integrating over the

entire observation. While the modulation index is a good indicator of whether there are persistent oscillations within the pulsed emission (such as e.g. drifting sub-pulses), it is not very sensitive to infrequent bursts of emission. In addition, it is hard to measure in observations with a low signal to noise value. To account also for non-persistent signal variation, we have calculated the R-parameter, $R_i = (\text{MAX}_i - \mu_i)/\sigma_i$, (where MAX_i is the maximum intensity in the i th bin) as is described in Johnston et al. (2001). R_i indicates the presence of very bright, infrequent spikes of emission in the separate pulse bins. The off-pulse value for the R-parameter will increase with the number of rotations of the pulsar due to Gaussian noise statistics, while the modulation index is undefined in the off-pulse region.

Fig. 5.8 shows how the modulation index and the R-parameter is varying over the pulse profile for the 3.1 GHz single pulse observation. The minimum and maximum values of the modulation index for bins which are clearly within the on-pulse region are $m_{min} = 1.7$ and $m_{max} = 4.5$. These values are in the upper range of values for ordinary pulsars (Weltevrede et al. 2006a, Burke-Spolaor et al. 2012). From the R-parameter we can clearly see that the burst modulation is greater in the leading and the trailing edge of the on pulse region than it is in the middle of the pulse. Overall the R-parameter is high for this source, as well being among the upper range of measured values for a larger pulsar sample (Burke-Spolaor et al. 2012). This further demonstrates the irregular spikiness of the emission at each rotation. Also in the case of XTE J1810–197 the integrated pulse profile consists of strong spiky sub-pulses (Serylak et al. 2009). However, some of the sub-pulses for XTE J1810–197 could be considered giant pulses, but with broader pulse widths. Serylak et al. (2009) also report on a modulation index for the single pulses that is high on average and that increases with increasing observing frequency but varies between components also within the same observing frequency. Similar spiky emission has been observed also in ordinary pulsars, such as B0656+14 (Weltevrede et al. 2006b). Again in contrast to PSR J1622–4950, also this source also emits giant pulses and here the stronger pulses appear spikier than the weaker ones.

5.7 Conclusions

The peak flux density of PSR J1622–4950 has decreased by a factor of ~ 2 since the discovery, and analyses of non-pulsed observations confirm this trend (Anderson et al. 2012). The timing analysis of the source implies large variations in the rate of spin-down. We find a correlation between flux density decrease and spin-down decrease, but are cautious not to over-interpret this result.

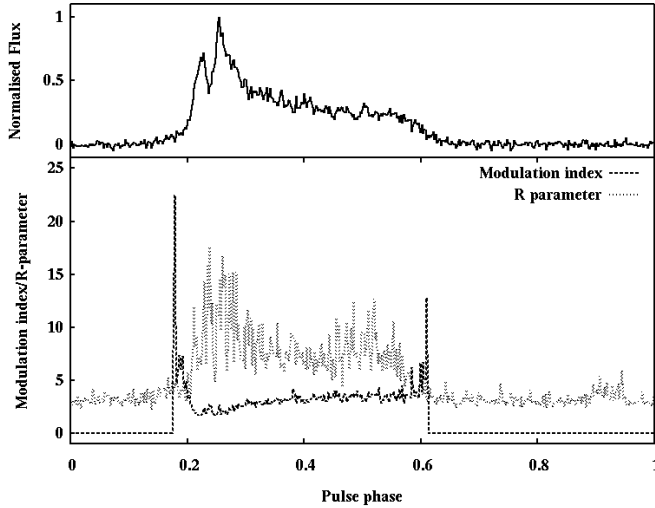


Figure 5.8 The bottom plot shows the modulation index (dashed line) and the R-parameter (dotted line). For reference, the integrated pulse profile is plotted in the top panel.

The polarisation is changing greatly between observations, but in general we observe a high degree of linear polarisation and low circular polarisation at frequencies higher than 1.4 GHz. The observations at 1.4 GHz are highly affected by interstellar scattering, which causes depolarisation in the linear component, but not all changes in the linear polarisation at this frequency can be due to propagation effects. We also see orthogonal phase jumps, flat PAs and changed handedness in the circular polarisation in some of the observations at 1.4 GHz and also at higher observing frequencies. RVM fits imply that the geometry of PSR J1622–4950 is nearly aligned, with the line of sight remaining within the emission beam for large parts of the rotation. If this proves to be a general property for magnetars, it could provide insight into why so few of the magnetars have observed radio pulsations.

The single pulses from the magnetar are very narrow in comparison to the width of the total integrated profile. The emission from each rotation consists of a few narrow spikes, that vary in longitude and separation between pulses. The widths of the single emission spikes appear to scale inversely with observed frequency, by getting narrower as the frequency gets higher. This could demonstrate that the emission spikes observed at different frequencies are emitted at different altitudes above the polar cap in the neutron star. The pulse flux distribution points towards a log-normal flux distribution of the spikes, without any signs of giant pulses from the magnetar. The spikiness in the emission results in a very high R-parameter across the pulse profile and a modulation index that is slowly increasing with pulse longitude and is higher in the pulse edges.

In all, PSR J1622–4950 has many properties that are very similar to the other radio magnetars, but also some things that differ, such as variations in linear polarisation and PA swing on short time scales and a non-smooth frequency derivative evolution. We stress the importance of regular monitoring of these sources as the known sample is very small and the only chance to understand their emission and their connection to other neutron stars is by continuing to observe their various properties. In particular, it is important to establish whether the overall flux density is the only property that is changing on longer time scales, or if also other emission properties are varying. In order to discover more radio magnetars we need to understand the time scales of their on and off periods, and depending on their special features, we may need to re-evaluate the way searches for these sources should be performed.

6

Millisecond Pulsar Population Study

The large number of pulsars detected in the HTRU medlat survey provides an ideal data set as the basis for population studies of pulsars in the Galaxy. We have used the MSPs from the medlat survey area to simulate the distribution and total population of MSPs in the Galaxy, via the scale factor method. Each detected pulsar has a scale factor that is a function of the pulsar's spin period, pulse width and luminosity, and hence the accuracy of these values for the input pulsars is crucial for the accuracy of the modelling. In turn, the luminosity of a pulsar is a function of its assumed distance and its flux density. Through the course of this analysis we found that some of the published flux densities for the pulsars in our sample do not agree with the observed flux densities from our data set. To better estimate the flux density values we have calculated average flux densities for these MSPs from archival data from the Parkes Radio Telescope. Using the NE2001 model (Cordes & Lazio 2002) to calculate distances to the pulsars from their DM values, together with the new average flux densities, we calculate average luminosity values for each pulsar and use these as input parameters in the simulation.

A comparison between simulated detections at five different scale heights and the z-values of the real detections results in a best fit scale height of $z = 500$ pc. Using this value for the z-height and omitting beaming fractions, we find an underlying population of MSPs of $\sim 150,000$ sources down to a limiting luminosity of $L_{1400} = 0.07$ mJy kpc². However, at the low end of the luminosity distribution, the uncertainties introduced by small number statistic are large. By omitting very low luminosity pulsars, we find a Galactic population above $L_{1400} = 0.1$ mJy kpc² of only $\sim 45,000$ MSPs and a luminosity distribution with a steep slope of $d \log N / d \log L = -1.75$.

From the flux density calculation we also find that 7 of the MSPs discovered in the HTRU medlat survey would not have been detected in this survey at their average flux density values. One possible reason to the higher flux density at the time of the discovery

could be if the pulsars were scintillating during the observations. This highlights the importance of including scintillation effects in future MSP population studies.

6.1 Introduction

To date pulsar astronomers have discovered over 2000 pulsars in the Galaxy and globular clusters, including over 170 MSPs (with period $P < 70$ ms and spin down $\dot{P} < 10^{-17}$), and the known population continues to grow with the results from each new successful pulsar survey. However, the distribution of the observed sample implies that we only know of a small fraction of the total Galactic pulsar population. With the help of computer simulations we can use the properties of the known sample to estimate the true population.

6.1.1 Previous Studies

Studies of the MSP population in the Galaxy were for a long time severely affected by small-number statistics. To some degree that is still true today, however with the new large scale surveys increasing the total numbers of known MSPs, we are quickly getting closer to being able to perform full population synthesis studies of MSPs with good accuracy.

The first attempt to estimate the number of MSPs in the Galaxy was made by Kulkarni & Narayan (1988), who examined the hypothesis that the birthrates of low-mass binary pulsars (LMBP) and low-mass X-ray binaries (LMXB) should be equal. This hypothesis is derived from the model of formation of MSPs through recycling (Alpar et al. 1982, Fabian et al. 1983, van den Heuvel et al. 1986), where MSPs are ordinary pulsars spun-up by the accretion of matter from a companion. During the spin-up phase, the binary system is visible as an LMXB. Kulkarni & Narayan (1988) argued that the birthrates of these two groups are in fact not equal, but that the birthrate of short orbital period LMBPs is exceeding the birthrate of LMXBs by a factor of ~ 10 . As part of their analysis they used 2 MSPs and estimated a total of $> 100,000$ MSPs in the Galaxy. However, their analysis was dominated by one of these MSPs: PSR B1855+09. The number of pulsars inferred in their analysis was later revised and limited to a smaller number after the results from subsequent surveys by Narayan et al. (1990), but the conclusion that the birthrate of MSPs is more than 10 times that of LMXBs was still present. This issue is sometimes referred to as the birthrate problem, and the question whether all MSPs are produced in LMXB systems is still discussed today (e.g. Hurley et al. 2010). This thesis chapter will however only concern the current MSP population.

In the early 1990s Johnston & Bailes (1991) used five MSPs, including PSR B1855+09,

and non-detections from two high-frequency surveys of the Galactic plane to estimate the disc population of MSPs. By using a revised distance scale, which increased the distance to PSR B1855+09, they attained a higher luminosity of the pulsar and hence derived a lower number of PSR B1855+09-like pulsars in the Galaxy. They estimated a total of $\sim 2 \times 10^5$ MSPs over a limiting radio luminosity of $L_{\min, 1500\text{MHz}} = 0.3 \text{ mJy kpc}^2$ in the Galaxy. However, this result had a large uncertainty due to the small number of MSPs known at the time, and in addition, the result was dominated by one pulsar: B1257+12.

One important result from the study by Johnston & Bailes (1991) was their prediction that, in contrast to slow pulsars, the spacial distribution of MSPs would not be concentrated on the Galactic plane but evenly distributed over the sky. This understanding together with the first discoveries of MSPs at high galactic latitudes (Wolszczan 1991) encouraged large-scale (nearly) all-sky surveys for MSPs to be undertaken at various radio telescopes (Thorsett et al. 1993, Manchester et al. 1996, Sayer et al. 1997).

One of these surveys, the Parkes Southern Pulsar Survey (Manchester et al. 1996), discovered 17 MSPs and almost doubled the known sample resulting in 35 known MSPs at the time. Using these 17 discoveries together with the parameters for another 4 previously known MSPs, Lyne et al. (1998) estimated the local surface density of MSPs to be 1110 ± 600 sources within a 1.5-kpc cylindrical radius of the Sun. This number corresponds to a local surface density of MSPs of $157 \pm 85 \text{ kpc}^{-2}$ for $L_{436} > 0.3 \text{ mJy kpc}^2$.

A more recent study of the MSP population was reported by Story et al. (2007), who used 56 radio-loud MSPs from 10 different pulsar surveys to predict the number of radio-loud and radio-quiet MSPs that are detectable as γ -ray pulsars. By assuming that ordinary and millisecond pulsars all can be described with a common radio luminosity model, their extensive study results in a Galactic birth rate of MSPs of $4 - 5 \times 10^{-4}$ per century, which corresponds to a total Galactic population of $4.8 - 6.0 \times 10^4$ MSPs.

6.1.2 Selection Effects in Pulsar Surveys

The known pulsar population for both ordinary pulsars and MSPs is strongly biased towards bright sources at small distances from the Earth. This is due to the inverse square law. Pulsar astronomers define the intrinsic luminosity of a source at the observing frequency ν as $L_\nu \equiv S_\nu d^2$, where S_ν is the mean flux density at ν and d is the distance to the pulsar (usually derived from the DM). This leads to the known sample being dominated by nearby and/or high luminosity sources. Other selection effects of pulsar surveys that affect the observed population are interstellar dispersion and scattering of pulses. To estimate the underlying population of pulsars it is important to keep these biases in mind

and take them into account in any population modelling.

The detection threshold of the apparent flux density for pulsar surveys is calculated with the radiometer equation (also noted in eq 2.1) by:

$$S_{\min} = \frac{S/N_{\min}(T_{\text{rec}} + T_{\text{sky}})}{G\eta\sqrt{n_{\text{pol}}t_{\text{int}}\Delta\nu}} \sqrt{\frac{W}{P-W}} \quad \text{mJy} \quad (6.1)$$

where S/N_{\min} is the threshold signal-to-noise ratio, T_{rec} and T_{sky} are the receiver and sky noise temperatures (measured in K), G is the telescope antenna gain (K/Jy), η is a survey dependent constant (≤ 1) which accounts for losses in sensitivity due to e.g. sampling and digitization noise, n_{pol} is the number of polarizations recorded, t_{int} is the integration time (seconds), $\Delta\nu$ is the observing bandwidth (MHz), W is the observed pulse width and P is the pulse period. From eq 6.1 we can see that the minimum detectable flux density increases as W increases, hence it is harder to detect pulsars with broad pulse profiles than those with narrower profiles. Dispersion smearing and multi-path scattering by the free electrons in the interstellar medium, as explained in Sec 1.1.3, cause the detected pulse width to be broader than the intrinsic pulse value. Since the density of free electrons is higher closer to the Galactic plane, these effects are more severe for distant pulsars in the inner Galaxy. These effects are also highly dependent on observing frequency and are a lot less severe at higher observing frequencies (≥ 1.4 GHz) than at frequencies around 400 MHz. The sky temperature scales with observing frequency (approximately as $\nu^{-2.8}$; Lawson et al. 1987) and makes higher observing frequencies attractive. On the other hand, pulsar flux densities in general possess a steep negative spectral index which causes the flux density to be roughly an order of magnitude lower at 1.4 GHz compared to at 400 MHz. This issue can be partly compensated for by increasing the receiver bandwidth at higher radio frequencies.

6.2 Millisecond Pulsar Data Set

For this analysis we have used known recycled pulsars in the HTRU medlat survey area not associated with globular clusters. We define recycled pulsars as having a period $P < 0.070$ s and a spin down $\dot{P} < 10^{-17}$. All pulsars in our sample are listed in Table 6.1 together with some of their properties and a note of in which 20-cm pulsar surveys they have been detected. Three of the newly discovered pulsars from the HTRU medlat survey were confirmed only shortly before this work started. Timing observations of these pulsars are carried out at Jodrell Bank Observatory and due to a lack of data from the Parkes Telescope at the time, these pulsars are not included in this analysis.

To make sure the numbers of detected pulsars in each survey was correct, archival data from the Parkes Multibeam survey (PM) and the Swinburne Intermediate Latitude survey (SIL) were searched for the sample pulsars. This was done by finding the observation in each survey closest on the sky to each of the pulsars. The data files were then de-dispersed at the DM of the known pulsar and searched for periodicities close to the known pulsar period by performing an FFT with the program *seek* (see Sec 2.3 for further processing details). If a periodicity within $\pm 1\mu\text{s}$ of the known pulsar period was found, the data were folded using this periodicity and the known pulsar DM. The resulting folded archives were then inspected by eye to determine if the pulsar was detected in the data or not. The analysis resulted in an additional five MSP detections in the PM survey and three MSP detections in the SIL survey, compared to published values. All the new detections were of pulsars originally discovered in the HTRU medlat survey. The total numbers of pulsars from our sample detected in each survey are 19 pulsars in the PM survey, 15 in the SIL survey and 48 in the HTRU medlat survey.

6.2.1 Pulsar Flux Densities

Through the course of this analysis it became clear that the published flux densities for some of the pulsars as stated in the pulsar catalogue¹ do not agree with the values obtained in the observations in the HTRU medlat survey. In particular the values from four pulsars stood out as being a lot higher than the published flux. The most obvious reason for this discrepancy would be if the pulsar signal was scintillated up in our observation, and would then appear to be brighter than its average state. Since the luminosity of a pulsar is proportional to its flux density, it is very important to get the flux density values right before using the luminosity to derive the underlying pulsar sample.

In an effort to better understand these differences between our data and the published flux density values, we have analysed a large number of historical observations collected with Parkes of the MSPs in our sample². By collecting data from each pulsar in our sample we have made histograms of their S/N, scaled to the HTRU medlat integration time, and noted the average S/N from these observations as well as the theoretical S/N calculated from the catalogue flux density and eq 6.1. These histograms are shown in Fig 6.1. In some cases it is obvious that the theoretical S/N value differs significantly from the observed values and cannot refer to the true flux density, even if scintillation is taken into account. Some of the pulsars have a lot higher S/N values than indicated by catalogue values. See

¹<http://www.atnf.csiro.au/research/pulsar/psrcat/>

²Most of these observations are available via the CSIRO Data Access Portal: <https://data.csiro.au/dap/>

Table 6.1 Millisecond pulsar parameters used as input numbers in the scale factor simulation. The pulse width is given at 50% of the pulse amplitude in parts of pulse period. The surveys used are the PM (p), the SIL (s) and the HTRU medlat (m) surveys.

Pulsar	Period [ms]	Width	L_{1400} [mJy kpc 2]	Survey
J0900–3144	11.1	0.07	0.4(1)	m
J1017–7156	2.3	0.03	5.4(21)	m
J1045–4509	7.5	0.11	4.9(15)	s,m
J1056–7118	26.3	0.33	4.2(15)	m
J1125–5825	3.1	0.09	3.2(12)	m
J1125–6014	2.6	0.08	0.8(3)	p,m
J1157–5112	43.6	0.04	0.4(4)	s
J1216–6410	3.5	0.07	0.5(1)	p,m
J1226–6202	34.5	0.04	9.8(41)	p,m
J1337–6423	9.4	0.06	4.0(12)	m
J1406–4656	7.6	0.16	0.07(9)	m
J1420–5625	34.1	0.04	0.3(1)	p,m
J1431–4717	2.0	0.07	0.3(1)	m
J1431–5736	4.1	0.02	0.5(2)	m
J1435–6100	9.3	0.03	0.8(3)	p,m
J1439–5501	28.6	0.03	0.08(8)	p,m
J1446–4701	2.2	0.04	0.3(1)	m
J1454–5846	45.2	0.04	0.5(1)	p
J1502–6752	26.7	0.11	6.2(20)	m
J1525–5544	11.4	0.05	1.4(1)	p,m
J1528–3835	8.5	0.14	0.5(3)	m
J1543–5149	2.1	0.11	1.9(10)	m
J1546–4552	3.6	0.02	1.4(4)	s,m
J1603–7202	14.8	0.09	3.2(21)	s,m
J1618–39	12.0	0.13	3.3(10)	s,m
J1622–6617	23.6	0.03	1.0(5)	s,m
J1629–6902	6.0	0.04	0.5(2)	s,m
J1708–3506	4.5	0.17	4.7(25)	p,m
J1719–1438	5.8	0.06	0.3(2)	s,m
J1721–2457	3.5	0.26	1.1(2)	s,m
J1729–2121	66.3	0.03	0.08(5)	m
J1730–2304	8.1	0.13	0.7(3)	p,s,m
J1731–1847	2.3	0.03	0.9(6)	m
J1732–5049	5.3	0.06	1.0(3)	s,m
J1744–1134	4.1	0.04	0.3(3)	s,m
J1745–0952	19.4	0.08	1.2(7)	s,m
J1751–2857	3.9	0.04	0.24(9)	p,m
J1755–3715	12.8	0.29	8.6(24)	m
J1756–2251	28.5	0.03	2.1(10)	p,m
J1757–5322	8.9	0.05	0.3(1)	s,m
J1801–1417	3.6	0.12	2.4(12)	p,m
J1801–3210	7.5	0.07	3.0(8)	p,m
J1802–2124	12.6	0.03	3.7(10)	p,m
J1804–2717	9.3	0.17	0.49(2)	p,m
J1810–2005	32.8	0.22	14.0(46)	p,m
J1811–2405	2.7	0.04	0.5(2)	p,m
J1825–0322	4.6	0.04	0.6(4)	m
J1843–1113	1.8	0.05	1.0(9)	p,m
J1911–1114	3.6	0.10	0.7(1)	m
J1918–0642	7.6	0.06	0.7(5)	s,m

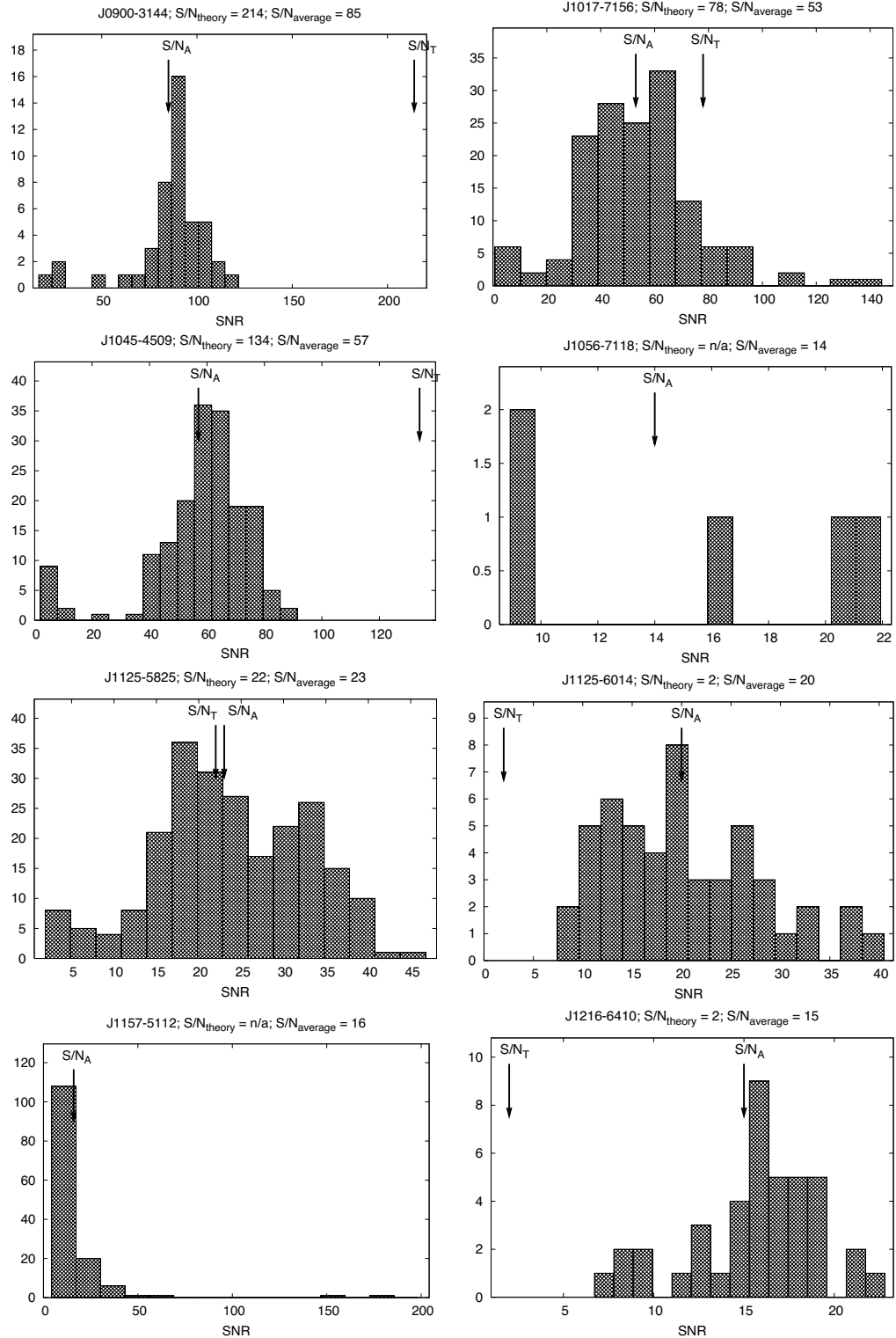


Figure 6.1 S/N histograms for MSPs in the sample. The arrows marked S/N_A and S/N_T point to the values for the average S/N from the data set and the theoretical S/N derived from the published 20-cm flux density respectively.

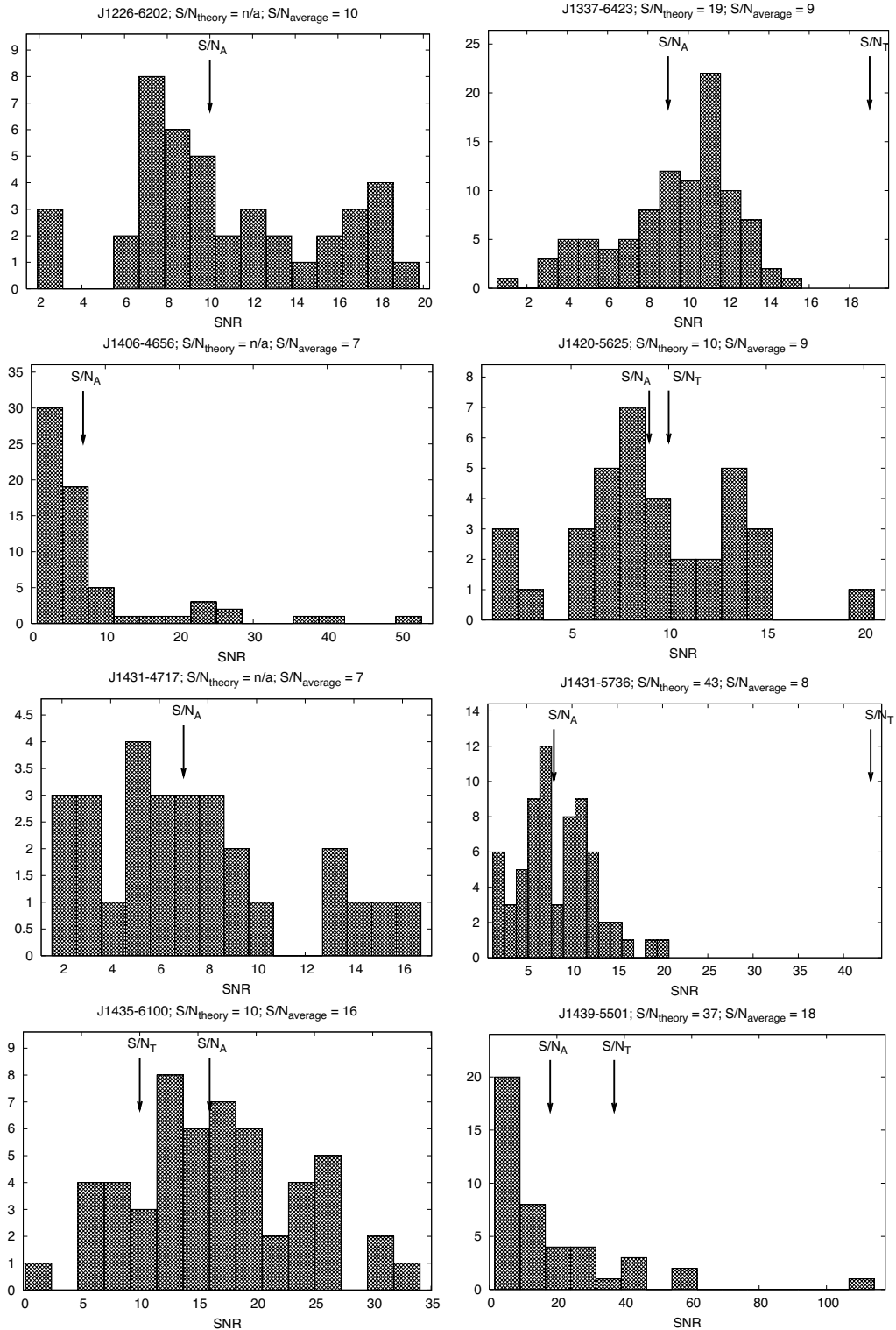


Figure 6.1 S/N histograms continued

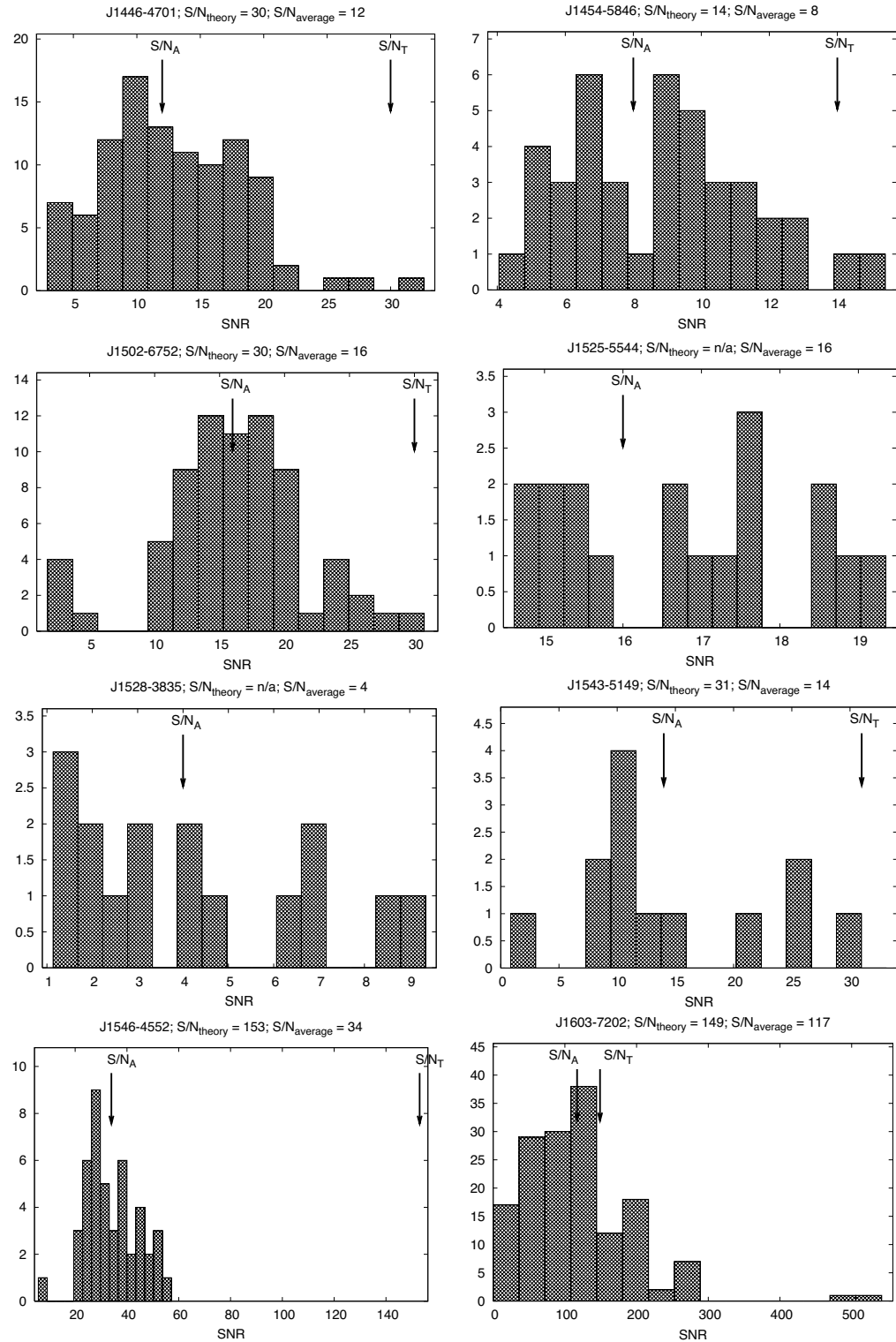


Figure 6.1 S/N histograms continued

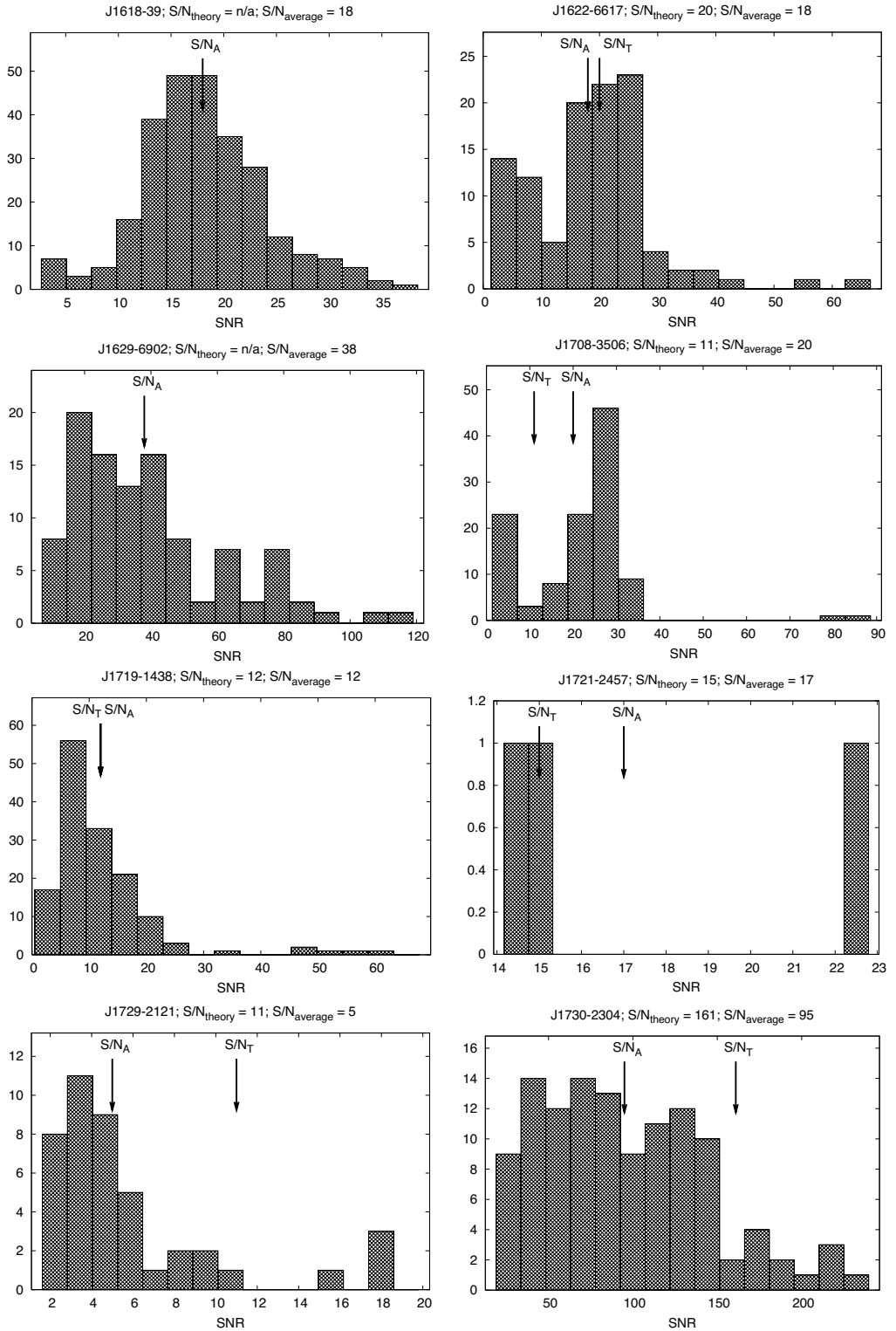


Figure 6.1 S/N histograms continued

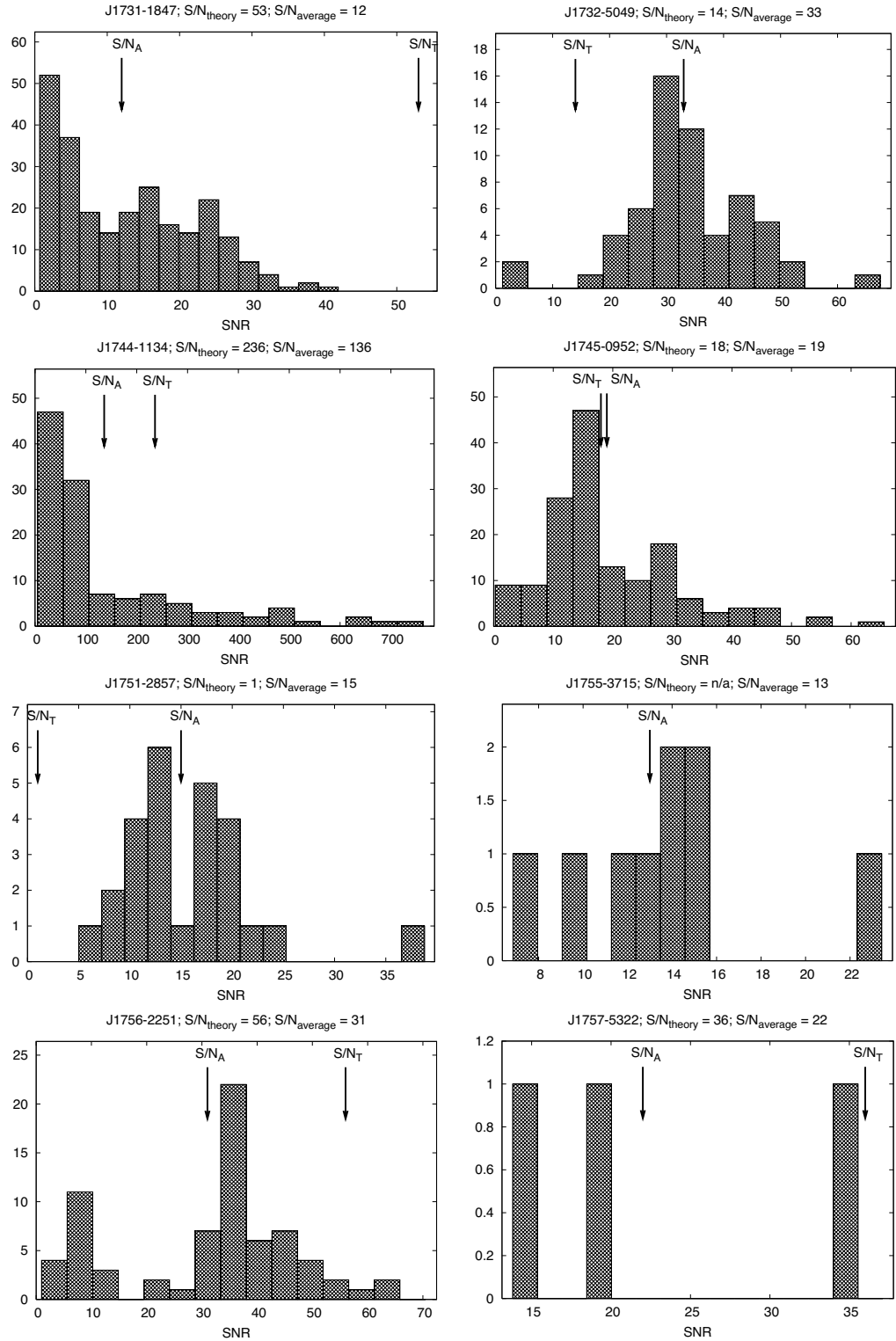


Figure 6.1 S/N histograms continued

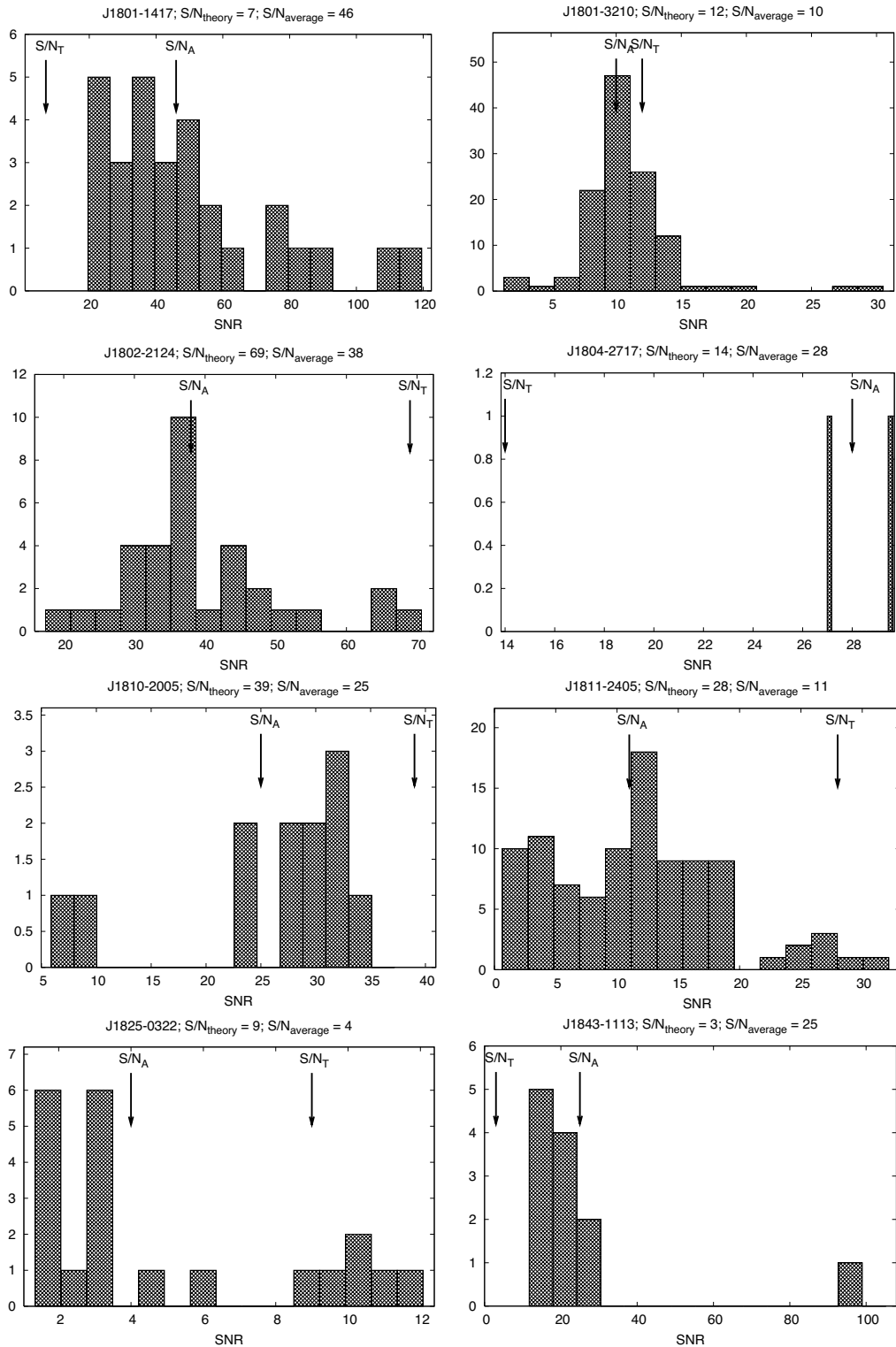


Figure 6.1 S/N histograms continued

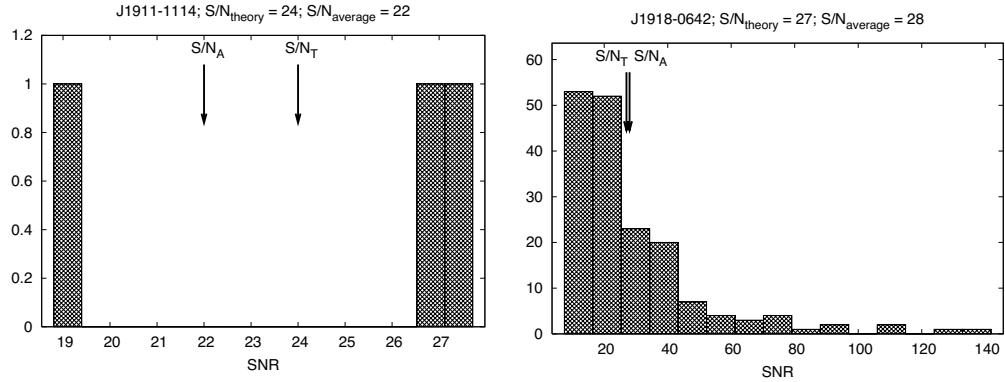


Figure 6.1 S/N histograms continued

e.g. PSR J1125–6014, which has a theoretical S/N of only 2 but the lowest S/N of the archival data is ~ 7 and the average number is 20. Similar statements can be made for e.g. PSR J1216–6410, PSR J1751–2857 and PSR J1843–1113. There are also cases where the opposite is true, and the theoretical S/N is a lot larger than the average and even top values of the archival observations, e.g. for PSR J0900–3144, PSR J1045–4509 and PSR J1546–4552.

To calculate luminosities of the sample MSPs, we have chosen to use the average values of the S/N from the archival observations, in combination with the periods and widths of the pulsars to calculate flux densities. In turn, these flux values were then used together with the DM derived distances to the pulsars to calculate their radio luminosities at an observing frequency band centered at 1.4 GHz. The values for this calculation are listed in Table 6.2. For some of the pulsars only a few archival observations were found, not enough to get a statistically significant average value. However, in order to be consistent in our analysis we have still used our derived average values rather than the catalogue values.

The luminosities for the pulsars in our sample are plotted against their periods together with other known pulsars in Fig 6.2. The top panel includes all non-globular-cluster pulsars from the pulsar catalogue and bottom panel shows only the recycled pulsars. The ordinary slow pulsars in the top panel ($P \gtrsim 0.1$ s) are collected in a distinct cluster centered around $P \sim 0.5$ s and $L \sim 50$ mJy kpc². In contrast, the sample pulsars from this analysis (represented by blue circles) show no trends of correlation between luminosity and period, neither when combined with other known MSPs (represented by red crosses) nor by themselves.

Table 6.2 Values used to calculate the luminosity for each MSP in the simulation. The distance is calculated from the DM with the NE2001 model (Cordes & Lazio 2002).

Pulsar	DM [pc cm ⁻³]	S/N _{ave}	S ₁₄₀₀ [mJy]	Distance [kpc]	L ₁₄₀₀ [mJy kpc ²]
J0900–3144	75.7	85(19)	1.5(3)	0.5	0.4(1)
J1017–7156	94.3	53(20)	0.6(2)	3.0	5.4(21)
J1045–4509	58.1	57(17)	1.3(3)	2.0	4.9(15)
J1056–7118	92.8	14(5)	0.6(2)	2.6	4.2(15)
J1125–5825	124.8	23(8)	0.5(1)	2.6	3.2(12)
J1125–6014	53.0	20(7)	0.4(1)	1.5	0.8(3)
J1157–5112	39.7	16(20)	0.2(2)	1.3	0.4(4)
J1216–6410	47.4	15(3)	0.27(6)	1.3	0.5(1)
J1226–6202	362.6	10(4)	0.14(6)	8.3	9.8(41)
J1337–6423	260.3	9(2)	0.16(4)	5.1	4.0(12)
J1406–4656	13.7	7(9)	0.2(2)	0.6	0.07(9)
J1420–5625	64.6	9(4)	0.11(5)	1.5	0.3(1)
J1431–4717	59.4	7(3)	0.13(6)	1.6	0.3(1)
J1431–5736	131.2	8(4)	0.08(3)	2.5	0.5(2)
J1435–6100	113.7	16(6)	0.17(7)	2.2	0.8(3)
J1439–5501	14.6	18(19)	0.2(2)	0.6	0.08(8)
J1446–4701	55.8	12(5)	0.16(6)	1.5	0.3(1)
J1454–5846	116.0	8(2)	0.11(3)	2.2	0.5(1)
J1502–6752	151.8	16(5)	0.4(1)	4.2	6.2(20)
J1525–5544	126.8	16(1)	0.25(2)	2.4	1.4(1)
J1528–3835	73.6	4(2)	0.11(6)	2.2	0.5(3)
J1543–5149	50.9	14(8)	0.3(1)	2.4	1.9(10)
J1546–4552	68.4	34(10)	0.31(9)	2.1	1.4(4)
J1603–7202	38.0	117(78)	2.4(15)	1.2	3.2(21)
J1618–39	117.5	18(5)	0.4(1)	2.7	3.3(10)
J1622–6617	87.9	18(10)	0.2(1)	2.2	1.0(5)
J1629–6902	29.5	38(22)	0.5(2)	1.0	0.5(2)
J1708–3506	146.8	20(11)	0.6(3)	2.8	4.7(25)
J1719–1438	36.8	12(9)	0.2(1)	1.2	0.3(2)
J1721–2457	47.8	17(3)	0.7(1)	1.3	1.1(2)
J1729–2121	35.0	5(4)	0.07(5)	1.1	0.08(5)
J1730–2304	9.6	95(48)	2.4(11)	0.5	0.7(3)
J1731–1847	106.5	12(9)	0.1(1)	2.6	0.9(6)
J1732–5049	56.8	33(10)	0.5(1)	1.4	1.0(3)
J1744–1134	3.1	136(152)	1.7(19)	0.4	0.3(3)
J1745–0952	64.5	19(11)	0.4(2)	1.8	1.2(7)
J1751–2857	42.8	15(6)	0.20(7)	1.1	0.24(9)
J1755–3715	167.4	13(3)	0.6(1)	3.9	8.6(24)
J1756–2251	121.2	31(15)	0.3(1)	2.5	2.1(10)
J1757–5322	30.8	22(9)	0.3(1)	1.0	0.3(1)
J1801–1417	57.2	46(22)	1.1(5)	1.5	2.4(12)
J1801–3210	177.7	10(3)	0.18(5)	4.0	3.0(8)
J1802–2124	149.6	38(10)	0.4(1)	2.9	3.7(10)
J1804–2717	24.7	28(1)	0.80(3)	0.8	0.49(2)
J1810–2005	241.0	25(8)	0.9(2)	4.0	14.0(46)
J1811–2405	60.6	11(6)	0.15(8)	1.8	0.5(2)
J1825–0322	119.5	4(3)	0.06(4)	3.1	0.6(4)
J1843–1113	60.0	25(22)	0.4(3)	1.7	1.0(9)
J1911–1114	31.0	22(4)	0.48(8)	1.2	0.7(1)
J1918–0642	26.6	28(20)	0.5(3)	1.2	0.7(5)

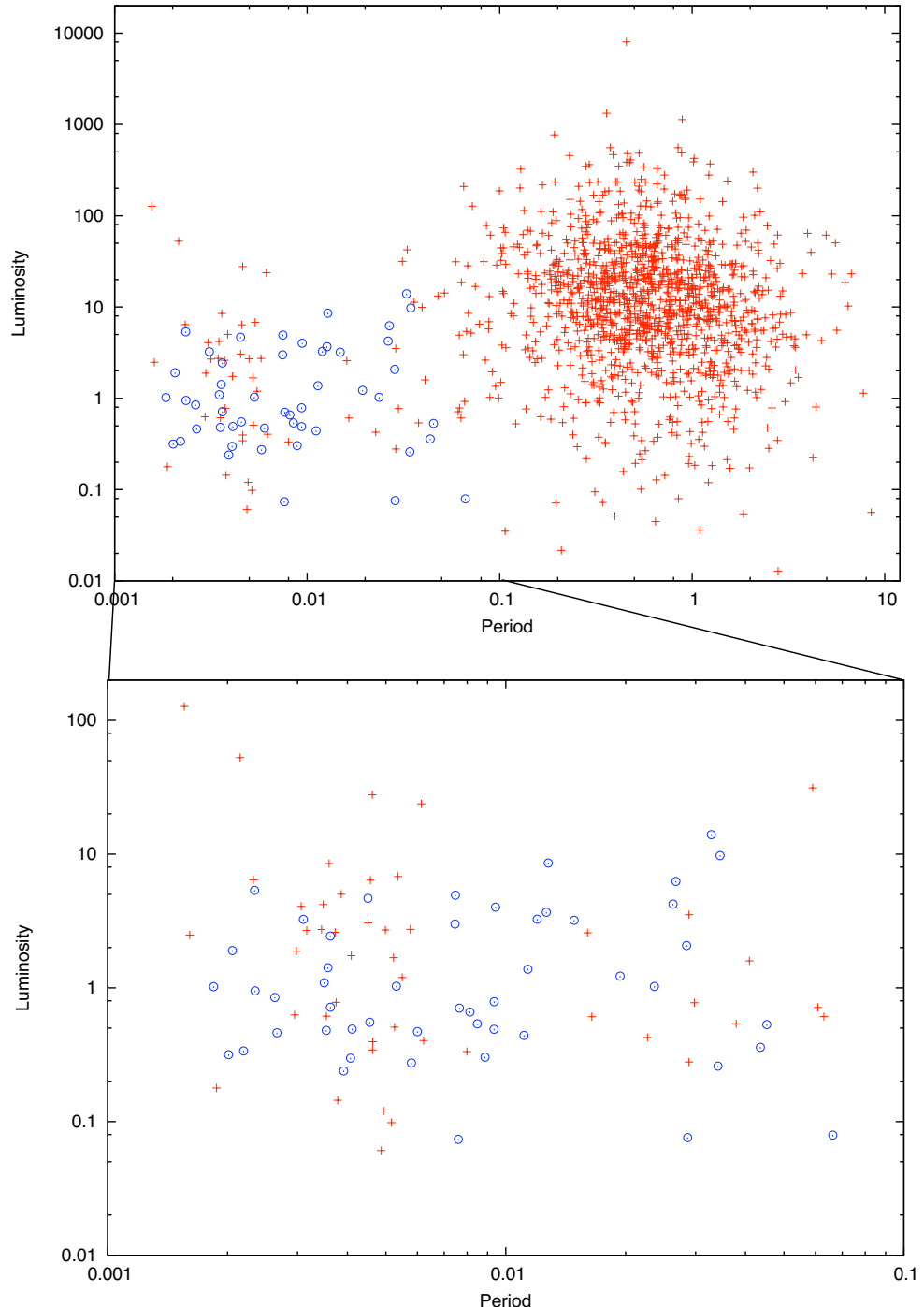


Figure 6.2 The upper panel shows the luminosity - period distribution for all pulsars in the pulsar catalogue. The lower panel shows only the known recycled pulsars. In both panels, the red crosses represent known pulsars with values from the pulsar catalogue and the blue circles represent pulsars used in this analysis with luminosity values calculated from archival data.

6.3 Model

In this analysis we are using a simple approach to make an estimate of the Galactic MSP population. We use the so-called scale factor method and only consider the pulsars discovered and detected in the southern HTRU medlat survey. By ignoring pulsars from other surveys we will only get a lower limit on the population above a certain luminosity threshold. The 50 pulsars that are considered in this analysis are listed in Table 6.1.

6.3.1 The Scale Factor Method

One way of trying to determine the total numbers of the Galactic MSP population is by defining a scaling factor as the ratio of the entire weighted volume of the Galaxy to the local volume around a pulsar in which it is detectable. That is, the scaling factor is defined as

$$\xi(P, L) = \frac{\int \int_G \sum(R, z) R dR dz}{\int \int_{P, L} \sum(R, z) R dR dz} \quad (6.2)$$

where the assumed pulsar space density distribution $\sum(R, z)$ depends on the galactocentric radius R and the height above the Galactic plane z (Vivekanand & Narayan 1981, Lorimer 2008), and is uniform in Galactic azimuth position. The scale factor is a function of pulsar period P and luminosity L and will return a higher value for pulsars with short period and/or low luminosity, which have smaller detectable volumes. The model also assumes that P, L, R and z are independent of each other. Except for a very weak correlation between P and z no significant dependence exist between these quantities (Lorimer 2009), and we disregard from the $P - z$ correlation in this work.

In this method, a separate Monte Carlo simulation is run for each known pulsar to calculate ξ for that particular pulsar. In practice, that means creating a large number of pulsars identical to the known pulsar and placing them in the Galaxy with a reasonable distribution. After taking the inverse square law and pulse broadening into account, the number of detectable pulsars for different surveys is recorded and the scale factor is set to be the number of simulated pulsars divided by the number of detections.

The true total number of pulsars in the Galaxy (N_G) depends not only on the scale factors but also on the pulsar beaming fraction (f) as

$$N_G = \sum_{i=1}^{N_{\text{known}}} \frac{\xi_i}{f_i} \quad (6.3)$$

where N_{known} is the number of observed pulsars used in the analysis. This gives us the

total number of pulsars in the Galaxy over a limiting luminosity L_{\min} , since this model is ignorant of sources below the weakest pulsar used as input.

The beaming fraction correction in this equation originates from the finite size of the pulsar beam in the pulsar emission model (see Sec 1.1.1) and is the fraction of 4π steradians that is covered by the radiation beam during one rotation. In other words, f is the probability that the pulsar beam sweeps past an arbitrary observer and is given by

$$f = (1 - \cos \theta) + \left(\frac{\pi}{2} - \theta\right) \sin \theta \quad (6.4)$$

where θ is the half-angle of the emission cone (Emmering & Chevalier 1989). Assuming a circular beam with a width of $\sim 10^\circ$ and a randomly distributed inclination angle between the spin and magnetic axes, b would be approximately 20% (Taylor & Manchester 1977). However, we know from observations that shorter period pulsars in general have larger beams and hence larger beaming fractions than slower pulsars (see e.g. Narayan & Vivekanand 1983, Tauris & Manchester 1998). For millisecond pulsars the beaming fraction is believed to be between $0.4 < f < 1.0$ (Kramer et al. 1998, Camilo et al. 2000) and likely in the upper range, closer to unity (Heinke et al. 2005). Throughout this analysis we will assume a beaming fraction of 1.

For small samples, the detected pulsars are likely to be biased towards brighter sources, and in that case this analysis will underestimate the true underlying population. However, as long as N_{known} is large enough ($N_{\text{known}} \gtrsim 10$), the scale factor model has proven to give reliable predictions (Lorimer et al. 1993).

6.3.2 Analysis

We have used the program *psrevolve*³ to generate pulsars randomly spread out in the Galaxy and check if they are detectable in a number of radio pulsar surveys. To start with, we simulated 150,000 pulsars with periods, pulse widths and luminosities identical to each of the input pulsars in Tab 6.1. These were spread out in the Galaxy assuming a Gaussian radial distribution with radial scale length $r = 4.5$ kpc and z-values from a Gaussian distribution with a root mean square height $z = 500$ pc. The scale height was later varied to investigate the z-height of the underlying population.

A snapshot approach was used, in which it is checked whether a pulsar is detectable by different pulsar surveys directly where it is placed by the simulation. For each of the surveys used in this analysis, we have created a database of the coordinates for each

³Developed by Dr. F Donea and Prof. M Bailes, originally based on work by Prof. D Lorimer. <http://astronomy.swin.edu.au/~fdonea/psrevolve.html>

observation. We then define the survey region for each survey to be the area of the sky that is covered by at least one of the survey beams. This makes the analysis more accurate than simply defining the survey region as the approximate areas limited by l and b that are often given as survey parameters. It also gives us the advantage of knowing in which of the beams in the Multibeam receiver a pulsar was detected, as well as the exact offset of the pulsar's position to the centre of the beam. Since the telescope beams are not uniformly sensitive, neither in comparison to each other nor over the beam field of view (see Table 2.1 for details), we use this information when calculating the sensitivity for the different surveys.

To decide if a pulsar is detected or not, the program checks a few different conditions for each survey. The first of these conditions is the location of the pulsar. If the pulsar's position on the sky is outside of the survey region, the pulsar is marked as undetected.

If the pulsar instead is inside the survey region we continue to check the second condition: the broadening of the pulse width due to propagation through the interstellar medium. This is done by calculating the effective pulse width for each pulsar and survey as a function of the pulsar's intrinsic pulse width and DM as well as the survey sampling time. The effective pulse width at the observer is given by:

$$W_e = \sqrt{W_i^2 + \left(1 + \frac{DM^2}{DM_0^2}\right) t_{\text{samp}}^2 + t_{\text{scatter}}^2} \quad (6.5)$$

where W_i is the intrinsic pulse width, t_{samp} is the survey sampling time and t_{scatter} is the scattering time scale given by:

$$t_{\text{scatter}} = 10^{-4.62+1.14 \log(DM)} + 10^{-9.22+4.46 \log(DM)} \quad \text{ms} \quad (6.6)$$

first modelled by Bhattacharya et al. (1992) at 400 MHz and scaled to the appropriate frequency for each survey after a $\nu^{-4.4}$ scaling law (Romani et al. 1986). The dispersion smearing due to the finite sampling time and channel bandwidth in each survey, such that the smearing of the pulse in one channel is equal to the sampling time, is given by DM_0 . If the pulse width at the observer is larger than the pulse period, the pulsar is marked as undetected, and otherwise a third condition is checked.

The third and last condition is that the flux density of the pulsar must be larger than the lower flux density limit of the survey, S_{\min} , as calculated by eq 6.1 assuming the minimum detectable signal to noise is $S/N_{\min} = 10$. If a simulated pulsar has passed all of these tests, it is marked as detected in that particular survey.

When all of the 150,000 simulated pulsars have gone through the detection tests, we

check how many of the pulsars would be detected by the HTRU medlat survey. To estimate the scale factor for each pulsar, the number of simulated pulsars is divided by the number of HTRU medlat detections. Also the detections for each of the Parkes 20-cm surveys are noted and scaled after the number of HTRU medlat detections. This entire process is run 10 times for each of 5 different z-heights: $z = 100, 250, 500, 750$ and 1000 pc.

In addition, we have simulated pulsars with periods shorter than any currently known pulsar, to see if we would be able to detect these pulsars if they exist in the Galaxy. By creating pulsars of different periods ($P = 1.5, 1.0, 0.5$ ms) and luminosities ($L = 0.1, 1.0, 10.0$ mJy kpc 2), and with a pulse width of $0.10P$, we can put limits on how many pulsars of each of these different kinds could exist in our Galaxy before we would detect one. In this analysis we started with simulating 150,000 of each hypothetical short period pulsar and after the simulation was finished we checked how many of these pulsars the HTRU medlat survey would have found. We then rescaled the input numbers and reran the simulation until exactly one pulsar was found. This is our upper limit on the population of pulsars with these particular properties. This process is then run 20 times to get average values on the population numbers.

6.4 Results

The resulting scale factors for each of the sample pulsars are shown in Table 6.3, together with the total numbers of the Galactic population of millisecond pulsars for each of the z-heights. One of the pulsars, PSR J1406–4656, contributes to up to more than half of the total population. This is the weakest pulsar in our sample, with a luminosity of only $L_{1400} = 0.07$ mJy kpc 2 , and as such puts the limit on the minimum luminosity we can consider in this study. For $z = 500$ pc (which is a more likely value of the real z-height, see Sec 6.5.2 for discussion) the fraction of J1406–4656-like pulsars to the Galactic population is about 50%.

From the 10 simulation runs of each scale height we can calculate average numbers of detections for each of the surveys that we are considering. These numbers are shown in Table 6.4. The difference in the *psrcat* values and the *real number* values comes from the extra search we have made of the medlat discoveries in the PM and SIL surveys, explained in Sec 6.2. The simulated detections are scaled to return the right number of HTRU medlat detections.

Average scale factors from the analysis of pulsars with periods $P \lesssim 1.5$ ms are shown in Table 6.5. These values are calculated as averages over 20 runs of the simulation. Here we used a z-height of 500 pc.

Table 6.3 Scale factors for different z-heights of all pulsars used in the simulation. Periods (P) are given in ms, luminosities (L) in mJy kpc 2 and z-heights (z) in pc.

Pulsar	P	L	$z=100$	$z=250$	$z=500$	$z=750$	$z=1000$
J0900–3144	11.1	0.4(1)	683	1005	1758	2763	3552
J1017–7156	2.3	5.4(21)	42	41	44	51	62
J1045–4509	7.5	4.9(15)	43	44	51	64	79
J1056–7118	26.3	4.2(15)	128	144	197	276	348
J1125–5825	3.1	3.2(12)	75	79	99	128	160
J1125–6014	2.6	0.8(3)	362	462	751	1074	1492
J1157–5112	43.6	0.4(4)	631	902	1555	2227	2980
J1216–6410	3.5	0.5(1)	634	893	1554	2308	3216
J1226–6202	34.5	9.8(41)	10	8	7	7	8
J1337–6423	9.4	4.0(12)	39	40	46	56	69
J1406–4656	7.6	0.07(9)	17078	37301	77812	71388	103571
J1420–5625	34.1	0.3(1)	879	1325	2495	3724	5189
J1431–4717	2.0	0.3(1)	1203	2018	3547	5390	6828
J1431–5736	4.1	0.5(2)	374	486	788	1124	1443
J1435–6100	9.3	0.8(3)	189	220	329	439	593
J1439–5501	28.6	0.08(8)	3442	7446	12052	26798	48500
J1446–4701	2.2	0.3(1)	824	1223	2311	3306	3789
J1454–5846	45.2	0.5(1)	357	464	793	1108	1460
J1502–6752	26.7	6.2(20)	29	30	33	40	49
J1525–5544	11.4	1.4(1)	134	150	211	290	372
J1528–3835	8.5	0.5(3)	893	1249	2435	3812	4726
J1543–5149	2.1	1.9(10)	170	192	280	395	495
J1546–4552	3.6	1.4(4)	128	142	189	257	330
J1603–7202	14.8	3.2(21)	65	69	85	111	140
J1618–39	12.0	3.3(10)	81	88	115	148	188
J1622–6617	23.6	1.0(5)	133	147	210	283	359
J1629–6902	6.0	0.5(2)	462	627	1123	1679	1939
J1708–3506	4.5	4.7(25)	64	68	84	109	137
J1719–1438	5.8	0.3(2)	1130	1742	3397	4461	6592
J1721–2457	3.5	1.1(2)	588	803	1488	2332	2772
J1729–2121	66.3	0.08(5)	3097	6334	13086	27547	25548
J1730–2304	8.1	0.7(3)	627	909	1520	2259	3133
J1731–1847	2.3	0.9(6)	249	292	439	621	842
J1732–5049	5.3	1.0(3)	218	268	381	537	712
J1744–1134	4.1	0.3(3)	809	1306	2277	3312	4700
J1745–0952	19.4	1.2(7)	214	257	368	546	692
J1751–2857	3.9	0.24(9)	1103	1590	3096	4843	6135
J1755–3715	12.8	8.6(24)	43	45	53	67	83
J1756–2251	28.5	2.1(10)	51	52	63	80	100
J1757–5322	8.9	0.3(1)	838	1282	2317	3435	5130
J1801–1417	3.6	2.4(12)	119	132	177	241	317
J1801–3210	7.5	3.0(8)	63	65	80	103	127
J1802–2124	12.6	3.7(10)	30	29	31	36	43
J1804–2717	9.3	0.49(2)	1094	1695	3361	5244	5780
J1810–2005	32.8	14.0(46)	16	16	17	19	22
J1811–2405	2.7	0.5(2)	533	785	1276	1876	2620
J1825–0322	4.6	0.6(4)	376	510	839	1200	1620
J1843–1113	1.8	1.0(9)	273	328	508	693	977
J1911–1114	3.6	0.7(1)	480	669	1071	1539	2066
J1918–0642	7.6	0.7(5)	354	461	739	1045	1392
TOTAL:			41457	76433	147538	191391	263477

Table 6.4 Average numbers of detected pulsars over 10 simulation runs, scaled after the number of medlat detections. The detection values are given for two archival surveys (PM and SIL) and for the three sub-surveys of the southern HTRU survey (medlat, deep and hilat).

z-height [pc]	PM	SIL	Medlat	Deep	Hilat
100	42	7	48	114	12
250	29	9	48	85	27
500	24	9	48	67	50
750	22	9	48	63	66
1000	22	9	48	61	77
psrcat	14	12	48	—	—
real number	19	15	48	—	—

Table 6.5 Scale factors for simulated pulsars with $P \lesssim 1.5$ ms over 20 runs. A z-height of 500 pc was used.

Period [ms]		Luminosity [mJy kpc ²]		
		0.1	1.0	10.0
1.5	28000(19000)	800(540)	30(20)	
1.0	25000(17000)	900(610)	34(23)	
0.75	35000(24000)	1200(780)	56(38)	
0.5	38000(26000)	1100(760)	61(41)	

6.5 Discussion

6.5.1 S/N Variations

Scintillation effects could result in varying values of the S/N of pulsar observations, in particular for sources with low values of DM. However, the large variations of S/N in many of the histograms in Fig 6.1, for both high and low DM pulsars, are surprising. Some of this variation could be due to scintillation, but it could also mean that the observing system noise fluctuates more than expected or that very thorough RFI removal is more important than assumed here.

When creating the S/N histograms, the discovery observations for the HTRU medlat pulsars were omitted. A comparison between the discovery S/N and the calculated average S/N is shown in Fig 6.3. The dashed line represent the equality of the two S/N values, and the arrow points to one pulsar (PSR J1406–4656) outside of the plot with a much higher discovery S/N than average S/N.

The pulsars that end up above the line were possibly scintillating during the discovery observation and would then appear brighter than they are on average. Looking at the lower end of the S/Ns, it is clear that some of the MSPs would not have been discovered in the medlat survey without this variation. No MSP with $S/N < 10$ has been discovered in the survey, but 7 of the pulsars have average S/N below this limit. This opens the question of how many pulsars exist in the Galaxy that we would detect if they were scintillating up at the time of the observation. The modelling used in this analysis does not take scintillation into account, and this result highlights the importance of including scintillation effects in future MSP population modelling.

The pulsars that end up below the line in Fig 6.3 might be explained by a combination of scintillation effects and offsets in the discovery position to the true position of the pulsar. In addition, the gain of the beams in the multibeam receiver varies between beams (as shown in Table 2.1) and would affect the discovery S/N of the pulsars more than the average S/N since timing observations usually are performed with the centre beam.

6.5.2 Choice of Scale Height

In general, the scale height of the observed MSP population is larger than the scale height of the slow pulsars, which are observed to be more tightly clustered around the Galactic plane. In addition, it is harder to find low-luminosity pulsars at higher z-heights, because of the large distances to those pulsars, and hence the known sample is biased towards MSPs at lower z-heights. This implies that the underlying Galactic population of MSPs

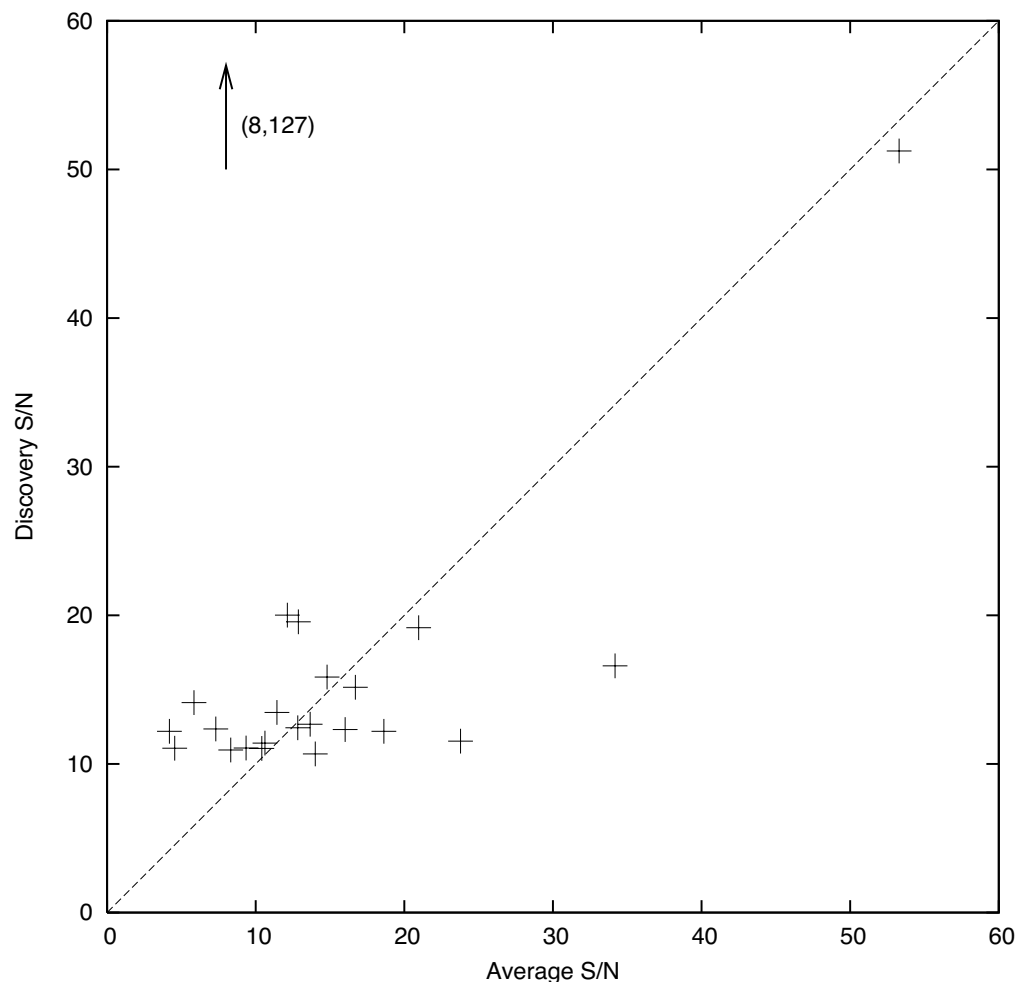


Figure 6.3 Comparison of the discovery S/N to the average S/N of the HTRU medlat discoveries in the sample. The dashed line, $y=x$, is plotted for reference. The arrow points to a pulsar, PSR J1406–4656, that was discovered with S/N = 127 and end up outside of this plot.

have a larger scale height than the currently known sample, and therefore we cannot use the known z-heights of the pulsars directly in the simulation. Instead we have chosen to give each simulated pulsar a z-value from a Gaussian distribution with a root mean square height, z , and run the simulation for 5 different values of z (100, 250, 500, 750 and 1000 pc). We can compare the z-heights for the simulated pulsar detections from these runs to the z-heights of the input pulsars to determine the most likely underlying scale height. This analysis is however only as accurate as the assumptions made on the other parameters of the simulation. In an attempt to avoid the bias of small number statistics at low luminosities, we have chosen to only include pulsars with $L_{1400} > 0.5 \text{ mJy } \text{kc}^2$ in this analysis. By randomly choosing 10 medlat detections of each simulated pulsar we have plotted cumulative histograms for each z-height together with the z-values for the real medlat detections, as shown in Fig 6.4. From this plot it seems like $z = 500 \text{ pc}$ best describes the real population. This result is confirmed by a Kolmogorov-Smirnov (K-S) test, which calculates the probability that the real and simulated pulsars are drawn from the same distribution. In the case of $z = 500 \text{ pc}$ the K-S test returns a probability of $\sim 60\%$, while for $z = 250 \text{ pc}$ and $z = 750 \text{ pc}$ it returns $\sim 15\%$ and $\sim 40\%$ respectively. Hence we have chosen to use a z-height of $z = 500 \text{ pc}$ for the main part of this chapter.

6.5.3 Luminosity Distribution

By using the scale factors in Table 6.3 and the luminosity for each of the pulsars, we can create a luminosity histogram for the simulated population. This can give us an idea of the underlying luminosity distribution. In Fig. 6.5 we have plotted these numbers assuming a z-height of $z = 500 \text{ pc}$. The red bars in this histogram show the simulated population and the blue bars show the numbers of real pulsars in each bin.

Using the values for $L > 0.1 \text{ mJy kpc}^2$ (to avoid the small number statistics issues introduced by the low luminosity pulsars), a fit of a straight line to the logarithm of the luminosity distribution results in a slope ($d \log N / d \log L$) of -1.75 and gives a luminosity dependence

$$N = aL^b \approx 4000L^{-1.75} \quad (6.7)$$

for our data. Similar values calculated for slow pulsars in a snapshot model results in a slope of ~ -1 (Lorimer et al. 1993), and hence the MSP luminosity distribution seem to possess a steeper slope than the slow pulsars. Since our simulation is based directly on the luminosities of the known pulsars and we have not made any assumptions on the luminosity distribution of the MSPs in the Galaxy, this analysis can not tell us anything about the luminosity distribution below the luminosity value for the weakest pulsar in our

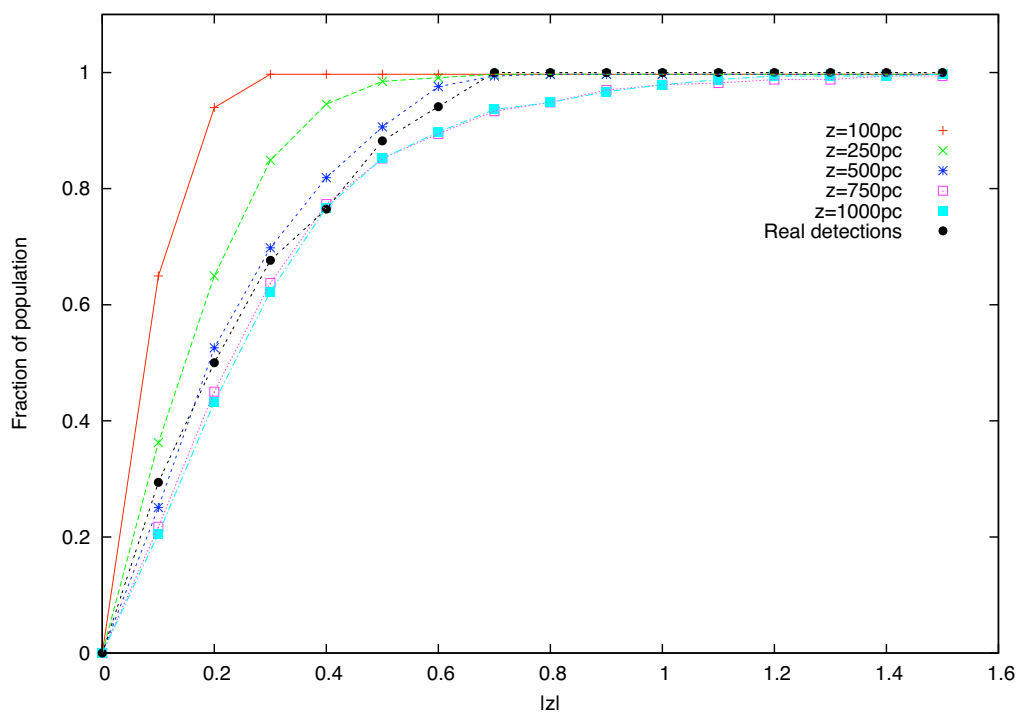


Figure 6.4 Cumulative histogram of z-heights of simulated medlat detections together with the real medlat detections.

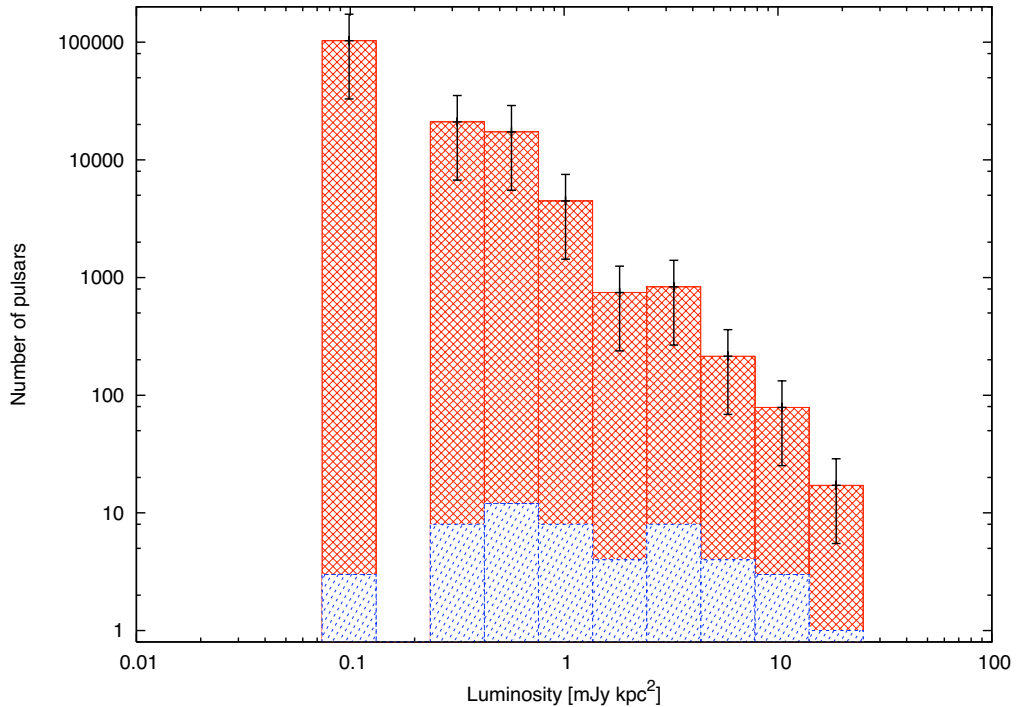


Figure 6.5 Luminosity histogram for the simulated Galactic population of MSPs over a limiting luminosity of $L_{1400} = 0.075 \text{ mJy kpc}^2$, assuming a z-height of $z = 500 \text{ pc}$. The red bars in this histogram show the simulated population and the blue bars show the numbers of real pulsars in each bin.

sample.

6.5.4 DM Distance Errors

The validity of the scale factors calculated in this analysis is highly dependent on the estimated distance to the real and simulated pulsars. In this entire analysis we have used the NE2001 model (Cordes & Lazio 2002) to estimate distances to the pulsars from their DM and Galactic coordinates.

Since the luminosity of a pulsar is proportional to the square of the distance (as $L = Sd^2$) a variation in distance of 30% translates to a variation in luminosity of 60%. We have analysed which effect the distance has on the scale factors by assuming distances to the pulsars that are 30% higher and 30% lower than the DM derived value and run the simulation using the new corresponding luminosities. This resulted in an average change in the Galactic population of a factor of 3, similar to what has been shown before by Lorimer et al. (1995a). This verifies the importance of an accurate distance model.

The NE2001 model is a model of the structure of the ionised gas in the Galaxy (Cordes & Lazio 2002). It consists of a thin disk of scale height 140 pc associated with low-latitude HII-regions and a thicker layer of a warm ionised medium up to a scale height 950 pc, as well as large-scale structure of spiral arms and other known features in the interstellar medium. This model is based partly on DMs and distances to known pulsars, and can be improved by the addition of new measurements of DMs and independent distance estimates. It has been shown that the NE2001 model sometimes is unsuccessful in predicting DMs, in particular at higher galactic latitudes, a fact which is also acknowledged by Cordes & Lazio (2002). This has led to suggestions and attempts to improve the NE2001 model (see e.g. Berkhuijsen et al. 2006, Sun et al. 2008, Gaensler et al. 2008). A future implementation of an improved distance model, e.g. by using the modification proposed to the scale height by Gaensler et al. (2008), into our simulations might result in more accurate values for the Galactic population of pulsars.

6.5.5 Pulsars with $P \lesssim 1.5$ ms

The fastest spinning currently known pulsar is PSR J1748–2446ad with a period $P = 1.396$ ms (Hessels et al. 2006), located in the globular cluster Terzan 5. Outside of globular clusters the shortest period pulsar is PSR J1939+2134 with a period $P = 1.558$ ms (Backer et al. 1982). This was the first MSP ever discovered and it held the record as the fastest spinning pulsar from its discovery in 1982 until 2006 when PSR J1748–2446ad was found. The maximum spin period of a pulsar is determined by the equation of state (the relationship between the density and the pressure) of the internal structure of the neutron star. By requiring that the neutron star is stable against break-up due to centrifugal forces, we can get an upper limit on the spin frequency of a neutron star with a given mass, M , and radius, R , by

$$M = \frac{4\pi^2\nu_k^2}{G} R^3 \quad (6.8)$$

where G is the gravitational constant and ν_k is the Kepler or mass-shedding frequency (Lorimer & Kramer 2005, Friedman et al. 1989). ν_k is the highest possible frequency for a star before it starts to shed mass at the equator, and hence the maximum spin frequency of a pulsar. This gives a theoretical limit of the maximum spin frequency of $\nu = 2170$ Hz for a typical neutron star of mass $M = 1.4 M_\odot$ and radius $R = 10$ km. Recent work discussing different neutron star equations of state and rapidly rotating pulsars can be found in e.g. Krastev et al. (2008), Haensel et al. (2008).

The fastest spinning pulsar in our sample is PSR J1843–1143, $P = 1.85$ ms. In an

attempt to estimate how many faster pulsars could exist in the Galaxy we have simulated pulsars with four different periods and three different luminosities. The scale factors for these twelve hypothetical pulsars can be found in Table 6.5. From this analysis it is clear that at a luminosity of $L = 10 \text{ mJy kpc}^2$, only a very small population (<181 sources) of short period pulsars could exist in the Galaxy before we would detect one, even for periods as small as $P = 0.5 \text{ ms}$.

Looking at the scale factors for pulsars with the same pulse period in Table 6.5, the scale factors change with a factor of ~ 30 when the luminosity is increased by a factor of 10. This can be understood by looking at the definition of pulsar luminosity and the volume of space that the pulsar would be detectable in. The luminosity is defined as $L = Sd^2$, where S is the flux density and d is the distance from the pulsar to the observer. If we assume a pulsar with a constant S and vary its luminosity with a factor of 10, i.e. $L_1/L_2 = 10$, we can write the distance as

$$\frac{L_1}{d_1^2} = \frac{L_2}{d_2^2} \Rightarrow d_1 = \sqrt{\frac{L_1}{L_2}} d_2 = \sqrt{10} d_2. \quad (6.9)$$

If we also assume that the pulsar can be detected in a uniform sphere around the Earth, we can use the equation for the volume of a sphere,

$$V = \frac{4\pi}{3} d^3 \quad (6.10)$$

to calculate the difference in detectable volume for the two distances, and hence luminosities, as

$$\frac{V_1}{d_1^3} = \frac{V_2}{d_2^3} \Rightarrow V_1 = 10^{\frac{3}{2}} V_2 \approx 31.6 V_2. \quad (6.11)$$

This value is only a rough estimate of the change in detection volume and the real value will depend on the chosen distribution of pulsars in the Galaxy, and hence in our case on the values of the radial scale length, r , and the z-height, z .

6.5.6 Estimation of Detections for the Other HTRU Sub-surveys

In addition to the archival Parkes 20-cm surveys and the finished HTRU medlat survey, we have included the positions of finished and future observations of the HTRU hilat and HTRU deep surveys in the simulation. This provides us with estimates of how many MSPs we should anticipate detecting in these surveys.

The deep survey covers part of the same region of the sky as the medlat survey, limited by $|b| < 3.5^\circ$ and $-80^\circ < l < 30^\circ$, but with an eight times longer integration time of 4300 s.

At our preferred z-height of 500 pc we estimate that this survey will detect ~ 67 MSPs, including ~ 51 new discoveries.

At the same z-height we expect the hilat survey to detect 50 MSPs, including ~ 33 discoveries. The hilat survey covers all the sky south of a declination of $+10^\circ$, not included in the medlat survey (which has limits $|b| < 15^\circ$, $-120^\circ < l < 30^\circ$). Each pointing in the hilat survey is integrated for 270 s, which is half the integration time of the medlat survey observations.

In the first survey paper of the HTRU survey, Keith et al. (2010) simulated the estimated detection and discovery numbers for each of sub-surveys, using the pulsar population model described by Lorimer et al. (2006) and the PSRPOP⁴ software. The main difference between that simulation and the analysis described in this thesis is that Keith et al. assumed a luminosity distribution as a power law with index -0.59 and minimum luminosity $L_{\min} = 0.1$ mJy kpc 2 . The Keith et al. simulation returned a similar number of medlat detections with 48 detections (and 28 discoveries) compared to the actual numbers of MSPs detected in the survey (51 detections, 26 discoveries). For the other two sub-surveys the corresponding values of MSPs from Keith et al. were 51 detections, 33 discoveries for the deep survey and 65 detections, 13 discoveries for the hilat survey. Hence, the simulation presented here predicts a larger total number of MSP detections and discoveries for the combined HTRU survey.

When all the HTRU sub-surveys are finished, using the numbers of new discoveries from the simulation, we estimate the total known sample of MSPs in the southern sky to ~ 190 sources, which corresponds to ~ 235 MSPs the Galaxy in total. These numbers include the MSPs recently discovered by the Fermi collaboration, which at the time of writing is 43 MSPs (Ray et al. 2012), but not MSPs in globular clusters. (It is worth noting that the numbers of discoveries predicted for the hilat and deep HTRU surveys have not taken the newly discovered Fermi pulsars into account, and hence the actual numbers of discoveries might be lower. The predicted number of detected pulsars, however, should be the same.) At the stage, more accurate population studies of the MSPs in the Galaxy can be performed. With such a large number of MSPs known, we would gain a better understanding of the MSP luminosity function and might be able to perform a full population synthesis study with dynamical modeling of the MSPs in the Galaxy.

⁴<http://psrpop.sourceforge.net>

6.6 Conclusions

We have performed a first-order pulsar population study, by using a snapshot model to simulate the distribution of MSPs in the Galaxy. Since many of the published luminosity values for the MSPs in our sample were found to differ from the values calculated from the S/N measured in archival observations, we calculated average luminosities for these pulsars to use as input parameters in the simulation.

The average luminosities for the sample pulsars show no correlation with spin period, neither by themselves nor when combined with the remaining known MSP population. This is at odds with the slow pulsars, which are collected in a distinct cluster in luminosity-period space. The S/N values for many of the pulsars differ greatly between the average value and that at the time of discovery. We have chosen to use the average values in this work, but since pulsar surveys are flux limited it is arguable if the discovery S/N should be an input parameter to the model as well as the average S/N. To attempt to account for this discrepancy, we stress the importance of including scintillation effects in future pulsar population studies.

The scale factors for the 50 sample pulsars have been simulated using 5 different values of the scale height ($z = 100, 250, 500, 750$ and 1000 pc). A K-S test between real and simulated detections results in a best fitted scale height of $z = 500$ pc. By omitting beaming fractions, we find a total population of $\sim 150,000$ MSPs in the Galaxy at $z = 500$ pc, down to a limiting luminosity of $L_{1400} = 0.07$ mJy kpc 2 . However, at the low end of the luminosity distribution, the uncertainties introduced by small number statistics are large. By omitting very low luminosity pulsars, we find a Galactic population above $L_{1400} = 0.1$ mJy kpc 2 of only $\sim 45,000$ MSPs and a luminosity distribution with a steep slope of $d \log N / d \log L = -1.75$. Using the same z-height, $z = 500$ pc, we estimate the maximum number of sub-MSPs in the Galaxy to be $\sim 35,000$ at $L_{1400} = 0.1$ mJy kpc 2 .

Finally, we predict that the HTRU deep and hilat surveys will detect 67 and 50 MSPs respectively, including a total of 84 new MSP discoveries. With the large number of MSPs detected at the time of completion of the entire HTRU survey, it will be possible to perform a complete population synthesis study and extend it with dynamical modelling of the MSPs in the Galaxy.

7

Conclusions and Future Work

The research carried out as part of this thesis included a search for pulsars at intermediate Galactic latitudes, individual details on some of the discoveries and on the pulsars detected as a whole, as well as a population study of millisecond pulsars in the Galaxy. Some focus was also directed at one of the pulsars discovered in the survey: the radio magnetar PSR J1622–4950. This chapter will summarise the major findings of the work presented in this thesis and give suggestions of future research possible as an extension to this work.

The structure of this chapter will deviate slightly from the main structure of the thesis and is arranged as follows: Firstly we will summarise the research and major findings of the HTRU medlat survey (Chapters 2 and 3), focusing on the part of the work carried out leading to the completion of this thesis. We will then give a status update on other research connected to the southern HTRU survey led by other members of the survey team, to provide a more complete picture of the survey as a whole. Then we will summarise the results from the MSP population study that has been performed using the results from the HTRU medlat suvery (Chapter 6), and give some examples of future research possible as an extension to this work. Finally we will summarise the research carried out in this thesis on the radio magnetar PSR J1622–4950 (Chapters 4 and 5) and discuss possible future research projects in connection to this source and to the radio magnetars in general.

7.1 The High Time Resolution Universe Survey

The southern HTRU survey commenced in November 2008 and is still ongoing at the Parkes 64-m Radio Telescope in Australia. It is divided into three sub-surveys, that have different integration times and are focused on different parts of the Galaxy. The observations for the intermediate latitude sub-survey (medlat) have been completed and searched for pulsars as part of this thesis. In total, the medlat survey discovered 104

pulsars with another ~ 10 promising pulsar candidates still awaiting confirmation at the telescope. A large fraction of the new pulsars are MSPs, 26 of 104 sources. In addition, the medlat survey pipeline has detected 725 previously known pulsars and another 96 known pulsars have been detected in the data by folding with the known ephemeris.

In general, the MSPs discovered in the medlat survey have large DMs compared to the known sample. This is a result of the back-end design of the HTRU survey, and its higher time and frequency resolution compared to previous surveys carried out at Parkes. By comparing the S/N of previously known pulsars in the HTRU medlat data set to the theoretical S/N for those pulsars calculated from published values of their respective flux densities and pulse widths, we concluded that the sensitivity of the medlat survey was within the expectations prior to the commencement of the survey.

The candidate viewing system adopted in this thesis has been very successful and resulted in the original discovery of 70 of the 104 discovered pulsars (including 18 of the 26 MSPs) in the medlat survey. However, this candidate sifting system is highly time consuming and, with the 9.5 million candidates generated in this part of the survey, on the limit of what is possible to fit into a PhD project. Future pulsar surveys with upcoming radio telescopes like ASKAP, MeerKAT and the SKA will collect a considerably larger number of synthesised survey pointings and return too many pulsar candidates for this methodology to be feasible. The development of automatic candidate sifting systems, e.g. systems that make use of artificial neural networks (Eatough et al. 2010, Bates et al. 2012), will be essential for these future large-scale surveys.

The HTRU survey is still underway and below we outline some of the currently ongoing research as well as planned future research within the framework of the survey. In addition to these, we are also conducting a large amount of follow-up work on sources presented in earlier chapters of this thesis.

- *The HTRU hilat survey*

The high latitude part of the HTRU survey covers all the sky south of an equatorial declination of $+10^\circ$, not included in the other HTRU sub-surveys, with an integration time of 270 s. To date (June 15, 2012) we have observed $\sim 45\%$ of the 36583 pointings planned for this sub-survey and $\sim 13\%$ of the total pointings have been searched for pulsars. Most of the work on the hilat survey has been carried out at the University of Manchester. To date this survey has discovered 3 slow pulsars and 1 millisecond pulsar.

- *The HTRU deep survey*

The deep survey covers the low latitude parts of the Galaxy, with $|b| < 3.5^\circ$ and

$-80^\circ < l < 30^\circ$. It has an integration time of 4300 s and hence will search for pulsars deep into the Galactic plane. About 70% of the 1230 pointings have been observed so far, and $\sim 13\%$ of the pointings have been searched. In this data set we have discovered 10 previously unknown ordinary pulsars and another ~ 13 promising candidates are awaiting confirmation at the telescope. The main part of the research for the deep survey is conducted at the Max Planck Institute for Radio Astronomy in Bonn.

- *Acceleration search of the HTRU medlat survey*

The work in this thesis has focused on finding pulsars with a standard periodicity search pipeline. Depending on the pulsar parameters, it can be very hard or even impossible to discover some pulsars in close binary systems with this method. Due to the changing doppler shift of the pulse period caused by binary motion, the periodicity from short period binary pulsars can get smeared out, and a search method that accounts for this is required to discover these pulsars. This kind of search methodology is usually referred to as *acceleration search* and a pipeline to search for accelerated pulsars is currently being implemented at Swinburne University. Acceleration searching is a very computing intensive task that adds a huge amount of processing time to the standard search.

A small fraction ($\sim 3\%$) of the medlat survey data has gone through an acceleration search pipeline using CPUs (Central Processing Unit) at Sardinia Observatory. This work has been published in the PhD thesis of Sabrina Milia (Milia 2011). To get around the processing time issue of acceleration searching and make such a search process feasible, the survey team is developing new search code, including a new dedispersion code (Barsdell et al. 2012), to run on GPUs (Graphical Processing Unit), which will speed up the total processing time by at least a factor of ~ 4 . This pipeline is planned to run on the newly installed computer cluster gSTAR (the GPU Supercomputer for Theoretical Astrophysics Research) located at Swinburne. gSTAR is a hybrid of traditional processing cores (CPUs) and GPUs, currently consisting of 50 standard SGI C3108-TY11 nodes that each contain 2 six-core Westmere processors and 2 NVIDIA Tesla C2070 GPUs, and will be expanded in the near future.

- *Single pulse searches*

In addition to searching for periodic signals in the data, the survey team has also been searching for single pulses of radio emission. This kind of searches have become

more common during the last decade and resulted not only in the discovery of RRATs (McLaughlin et al. 2006), but also in detections of single pulses from neutron stars in other galaxies than our own (Johnston & Romani 2003, Rubio Herrera 2010).

A single pulse search pipeline has been implemented at Swinburne and is partly run together with the periodicity search, to optimise the processing time. The single pulse pipeline is described in Burke-Spolaor et al. (2011) together with 11 discoveries from the first $\sim 25\%$ of the medlat survey and a very small fraction of the hilat survey $<1\%$.

A real-time processing pipeline for transient detection is currently being developed and is planned to run simultaneously with survey pointing observations on a newly installed GPU cluster at the Parkes Telescope. This pipeline will enable the possibility of recording high-resolution base-band data of interesting events as they happen. The search procedure and pipeline are described in (Barsdell et al. 2011).

- *High precision timing*

As part of the follow-up work the survey team will continue to collect timing observations of the MSPs discovered in the survey. For high precision timing, it is necessary to make use of coherent dedispersion to eliminate the undesirable effects of interstellar dispersion. Ultimately, high precision timing will result in improved accuracy in the pulsar parameters and for some of the pulsars might lead to measurements of their proper motions.

7.2 Millisecond Pulsar Population Studies

Pulsar population studies make use of the observed properties of the known pulsar sample to derive the distribution of the underlying Galactic population. The uncertainties of these models decrease as more pulsars are discovered and as our knowledge of possible biases in our sample improves. In the case of MSPs, most previous surveys have either not been sensitive enough or not covered enough area of the sky to detect a large enough number of MSPs to accurately model the underlying population. Hence it has been necessary to include pulsars from a number of different pulsar surveys and possibly introduce unknown biases from each of these surveys.

We have performed a first order population study with the scale factor method, using 50 MSPs in the HTRU medlat survey region. If a scale height of $z = 500$ pc is assumed, the simulation estimates the underlying population of MSPs to be $\sim 147,000$ sources with luminosities above a minimum of $L_{1400} = 0.075$ mJy kpc 2 . In addition, a population of

sub-MSPs of up to $\sim 35,000$ sources at luminosities $L_{1400} \geq 0.1 \text{ mJy kpc}^2$ could exist in the Galaxy before the medlat survey would discover one. For the ongoing HTRU sub-surveys, we predict that the deep survey will detect 67 MSPs including ~ 50 new discoveries, and the hilat survey will detect 50 MSPs, including ~ 30 discoveries. With the large number of MSPs known in the Galaxy at the time of completion of the entire HTRU survey, modeling with higher accuracy will be possible. Improvements to the modeling presented in this thesis and future research possible as an extension of this work are outlined below:

- *Implement improved distance models*

As discussed in Sec 6.5.4, the validity of the results from our modeling is highly dependent on the accuracy of the pulsar distances used. In this thesis we have used the NE2001 model (Cordes & Lazio 2002) to derive distances to the pulsars from their observed DM value. It is known that this model is less accurate at higher Galactic latitudes than at lower latitudes. One way to improve the results of our simulation is to implement a more recent and improved model of the free electrons in the Galaxy (e.g. by including the modifications to the scale height proposed by Gaensler et al. 2008), and use that model to derive the distances in the simulation.

- *Full population study with dynamical modeling*

A different approach to the snapshot model used in this thesis, would be to implement a full dynamical model to simulate the MSP population in the Galaxy. A study of both these models were not possible within the timeframe of this thesis, but would be a natural continuation of this work. In the dynamical model, a galaxy of simulated pulsars is created where the pulsars are given an initial starting point from a distribution of birth locations and initial rotational parameters. The pulsars are then evolved for a given time, both kinematically using models of Galactic gravitational potential and rotationally using models for the pulsar spin-down. After that, the pulsars can be checked for detectability in different surveys in the same way as was done in the snapshot model, and the result can be compared to the known pulsar sample.

Compared to the snapshot model, the dynamical model requires more assumptions to be made, such as the motion and rotational evolution of the pulsars. As input to a dynamical model we would need to assume initial period and magnetic field distributions to simulate the pulsars, which is not necessary in the snapshot model. On the other hand, the dynamical model has the advantage of being able to predict details of the progenitor population. For example, using a dynamical approach

we will be able to discuss the period and spin-down distributions of the pulsar population.

With a larger number of Galactic MSPs known, we would gain a better understanding of the period and luminosity distributions of the pulsar population as well as the spatial distribution in the Galaxy. With that knowledge the dynamical approach becomes a feasible alternative to the snapshot model.

In addition, these future simulations should attempt to model scintillation effects to account for the variations in flux density observed in many pulsars.

7.3 PSR J1622–4950 and Radio Magnetars

Magnetars are slowly rotating neutron stars with extremely large surface magnetic field strengths, that occasionally undergo large bursts and outbursts of X-ray and γ -ray radiation. The magnetar group is still a small group of pulsars, but it is growing with the discovery of new sources. Currently 23 magnetars and magnetar candidates are known¹, but only three of those have observed radio pulsations. The latest addition to the radio magnetar group, PSR J1622–4950, is the only magnetar so far discovered through its radio emission. The radio magnetars differ from ordinary rotation-powered pulsars e.g. by their long pulse periods and high surface magnetic field strengths as well as their highly variable flux densities, changing pulse profiles and flat radio spectrum. At least two of the radio magnetars are so-called transient magnetars, that occasionally undergo large outbursts of X-ray emission.

In this thesis we have described the discovery and detailed analysis of the radio magnetar PSR J1622–4950. This source shares many of the properties of the other radio magnetars, such as a highly variable pulse profile and flux density on time scales of days, highly polarised emission and a flat or possibly even inverted radio spectrum. The peak flux density of PSR J1622–4950 has decreased by a factor of ~ 2 over 700 days since the discovery, and the flux density decrease might be correlated with the spin-down decrease over the same period. The overall highly polarised emission changes greatly between observations and orthogonal phase jumps, flat position angles and changed handedness in the circular polarisation are observed. Fits to the rotating vector model imply that the geometry of PSR J1622–4950 is close to aligned. Finally, the single pulses from the pulsar are very narrow in comparison to the total width of the integrated pulse profile. The

¹See the McGill SGR/AXP Online Catalog for details:
<http://www.physics.mcgill.ca/~pulsar/magnetar/main.html>

single pulse widths appear to scale inversely with observing frequency, which could be a sign of emission spikes at different frequencies being emitted at different altitudes above the polar cap in the neutron star.

Many questions regarding magnetars are yet to be answered, such as why some of the sources emit radio pulsations while others do not; why do some stars turn into bursting magnetars as they are born as pulsars while others become regular rotation-powered pulsars; where is the limit between the ordinary pulsars and the magnetars in the $P - \dot{P}$ diagram, etc. Described below are some examples of possible future research of magnetars in general, and PSR J1622–4950 in particular. Each of these projects is interesting in its own right, but will ultimately contribute to a more complete understanding of the magnetar sources.

- *Continued monitoring of PSR J1622–4950 to see when/if it turns off.*

PSR J1622–4950 is transient in the radio and an on-going observing effort at Parkes (described in Sec 5.3) suggests that its flux density is currently decreasing with time. To analyse the time-scale of the on-off periods of the emission, it is important to keep monitoring the source at regular intervals. This can easily be done as part of other pulsar timing proposals at Parkes. However, timing analyses of magnetars show great amounts of timing noise at shorter time scales than our current sampling. To improve the current timing solution, a more detailed timing analysis of PSR J1622–4950 is required, using more frequent and regular observations. Due to severe scattering effects, the timing observations would preferably be carried out at higher radio frequencies than were used previously, e.g. at 3.1 GHz with Parkes.

- *Explore the radio spectrum*

The radio magnetars have an usually flat radio spectrum when compared to the ordinary pulsar population. One of them, XTE J1810-197, holds the record of the highest radio frequency detection of a pulsar – it has been observed at various radio frequencies up to 144 GHz (Camilo et al. 2007c). PSR J1622–4950 has so far been observed at frequencies up to 27 GHz with Parkes and the Australia Telescope Compact Array (ATCA), with flux densities suggesting a flat spectrum for this source (Keith et al. 2011a, Levin et al. 2010). By extending the observed radio frequencies up to \sim 100 GHz we could reveal the extent of the radio emission. In addition, the spectral index of PSR J1622–4950 seems to be varying with time (Anderson et al. 2012). Simultaneous multi-frequency observations (e.g. with ATCA) would enable a more detailed analysis of this phenomenon.

- *A search for X-ray pulsations*

So far only integrated X-ray emission has been observed for PSR J1622–4950, but since all other magnetars are primarily X-ray sources and emit pulsations in the X-ray band, it is expected that this source also is an X-ray pulsar. If X-ray pulsations from PSR J1622–4950 are detected, the next step could be simultaneous radio and X-ray observations to analyse the relationship between the emission at the two wavelengths.

- *Measurement of the proper motion*

Magnetars have a low inferred characteristic age and a few of them have been associated with supernova remnants (SNR). Motivated by cases with large offsets between the magnetar and the centre of the proposed SNR, it was argued that the magnetars would have very high space velocities of $\sim 10^3 \text{ km/s}$ (e.g. Rothschild et al. 1994). Later on, more magnetars were found much closer to the SNR centre (Gaensler et al. 2001) and the connection with high velocity sources was questioned. The first direct measurement of a proper motion of a magnetar was reported on by Helfand et al. (2007). Their observations of XTE J1810-197 with the VLBA showed a velocity somewhat below the average for ordinary young pulsars. Subsequently also the proper motion for 1E 1547.0–5408 have been measured (Deller et al. 2012) showing that also this magnetar has a lower space velocity ($\sim 280 \text{ km s}^{-1}$). Together these two results suggest that the mechanisms of magnetar birth does not necessarily lead to high neutron star velocities. More measurements of this kind would provide insight in the magnetar birth process and would assist in the identification or rejection of possible associations with SNRs.

For PSR J1622–4950, with a flux density of $\sim 15 \text{ mJy}$ at 8 GHz, detection with the VLBI network would be straightforward, unless the flux density decreases significantly. However, the distance of $\sim 10 \text{ kpc}$ means that a velocity of 100 km s^{-1} would only give rise to a proper motion of $\sim 2 \text{ mas yr}^{-1}$.

- *How many radio magnetars exist in the Galaxy*

By taking into account all information on previous radio surveys for pulsars as well as the magnetar properties and the observed on/off periods for the magnetar emission, it is theoretically possible to model how many radio magnetars should exist in our Galaxy. The models would obviously be severely affected by small number statistics and would only provide a very approximate first order estimate. However, it is an important part in the search for previously unknown magnetars. If the models predict a much larger number of sources than are currently known, it may

be necessary to develop new search methods for this kind of objects.

In its discovery observation, PSR J1622–4950 was bright enough to be easily detected in a ~ 10 s pointing. One way to search for sources with varying flux densities occasionally reaching such high values, is to frequently do a quick survey of the Galactic plane. For example, to scan the 900 square degree region limited by $|b| < 6^\circ$, $-120^\circ < l < 30^\circ$ with 10 s pointings would only take ~ 5 hours with the multibeam receiver at Parkes. Such a quick survey could be completed once every year to search for previously unknown radio magnetars.

- *Conduct a radio spectrum survey of high B-field pulsars*

Another approach towards understanding the connection between the magnetars and the ordinary pulsars is to study different aspects of rotation powered pulsars that have some properties similar to magnetars. One of the most unusual properties of the radio magnetars is their flat radio spectra. Investigating a possible trend towards flatter spectra in the high magnetic field ordinary pulsar population might shed some light on the relation between these two groups of pulsars. Many of the high B-field pulsars do not have published spectral indices and by selecting suitable high B-field pulsars, a mini-survey of their radio spectra could be performed to analyse how their emission compares with the magnetars and the remaining pulsar population.

Bibliography

- Abdo, A. A., Ackermann, M., Ajello, M., Atwood, W. B., Axelsson, M., Baldini, L., Ballet, J., Barbiellini, G., Baring, M. G., Bastieri, D., & et al., *ApJS*, 187, 460–494, 2010.
- Alpar, M. A., Cheng, A. F., Ruderman, M. A., & Shaham, J., *Nature*, 300, 728–730, 1982.
- Anderson, G. E., Gaensler, B. M., Kaplan, D. L., Posselt, B., Slane, P. O., Murray, S. S., Mauerhan, J. C., Benjamin, R. A., Brogan, C. L., Chakrabarty, D., Drake, J. J., Drew, J. E., Grindlay, J. E., Hong, J., Lazio, T. J. W., Lee, J. C., Steeghs, D. T. H., & van Kerkwijk, M. H., *ApJ*, 727:105, 2011.
- Anderson, G. E., Gaensler, B. M., Slane, P. O., Rea, N., Kaplan, D. L., Posselt, B., Levin, L., Johnston, S., Murray, S. S., Brogan, C. L., Bailes, M., Bates, S., Benjamin, R. A., Bhat, N. D. R., Burgay, M., Burke-Spolaor, S., Chakrabarty, D., D’Amico, N., Drake, J. J., Esposito, P., Grindlay, J. E., Hong, J., Israel1, G. L., Keith, M. J., Kramer, M., Lazio, T. J. W., Lee, J. C., Mauerhan, J. C., Milia, S., Possenti, A., Stappers, B., & Steeghs, D. T. H., *ArXiv e-prints*, 2012.
- Arzoumanian, Z., Nice, D. J., Taylor, J. H., & Thorsett, S. E., *ApJ*, 422, 671–680, 1994.
- Backer, D. C. & Rankin, J. M., *ApJS*, 42, 143–173, 1980.
- Backer, D. C., Kulkarni, S. R., Heiles, C., Davis, M. M., & Goss, W. M., *Nature*, 300, 615–618, 1982.
- Bailes, M., *ApJ*, 342, 917–927, 1989.
- Bailes, M., Bates, S. D., Bhalerao, V., Bhat, N. D. R., Burgay, M., Burke-Spolaor, S., D’Amico, N., Johnston, S., Keith, M. J., Kramer, M., Kulkarni, S. R., Levin, L., Lyne, A. G., Milia, S., Possenti, A., Spitler, L., Stappers, B., & van Straten, W., *Science*, 333, 1717–, 2011.
- Barsdell, B. R., Bailes, M., Barnes, D. G., & Fluke, C. J., *ArXiv e-prints*, 2011.
- Barsdell, B. R., Bailes, M., Barnes, D. G., & Fluke, C. J., *MNRAS*, 422, 379–392, 2012.
- Bates, S. D., Bailes, M., Bhat, N. D. R., Burgay, M., Burke-Spolaor, S., D’Amico, N., Jameson, A., Johnston, S., Keith, M. J., Kramer, M., Levin, L., Lyne, A., Milia, S., Possenti, A., Stappers, B., & van Straten, W., *MNRAS*, 416, 2455–2464, 2011a.
- Bates, S. D., Johnston, S., Lorimer, D. R., Kramer, M., Possenti, A., Burgay, M., Stappers, B., Keith, M. J., Lyne, A., Bailes, M., McLaughlin, M. A., O’Brien, J. T., & Hobbs, G., *MNRAS*, 411, 1575–1584, 2011b.

- Bates, S. D., Bailes, M., Bhat, N. D. R., Burgay, M., Burke-Spolaor, S., D'Amico, N., Jameson, A., Johnston, S., Keith, M. J., Kramer, M., Levin, L., Lyne, A., Milia, S., Possenti, A., Stappers, B., & van Straten, W., *MNRAS*- submitted, 2012.
- Becker, W. & Truemper, J., *A&A*, 326, 682–691, 1997.
- Beloborodov, A. M., *ApJ*, 703, 1044–1060, 2009.
- Berkhuijsen, E. M., Mitra, D., & Mueller, P., *Astronomische Nachrichten*, 327, 82–96, 2006.
- Bernardini, F., Israel, G. L., Stella, L., Turolla, R., Esposito, P., Rea, N., Zane, S., Tiengo, A., Campana, S., Götz, D., Mereghetti, S., & Romano, P., *A&A*, 529:A19, 2011.
- Bhat, N. D. R., Cordes, J. M., Camilo, F., Nice, D. J., & Lorimer, D. R., *ApJ*, 605, 759–783, 2004.
- Bhat, N. D. R., Bailes, M., & Verbiest, J. P. W., *Phys. Rev. D*, 77(12):124017, 2008.
- Bhattacharya, D. & van den Heuvel, E. P. J., *Phys. Rep.*, 203, 1–124, 1991.
- Bhattacharya, D., Wijers, R. A. M. J., Hartman, J. W., & Verbunt, F., *A&A*, 254, 198–212, 1992.
- Blandford, R. D. & Romani, R. W., *MNRAS*, 234, 57P–60P, 1988.
- Boyles, J., Lorimer, D. R., McLaughlin, M. A., Ransom, S. M., Lynch, R., Kaspi, V. M., Archibald, A. M., Stairs, I. H., McPhee, C. A., Roberts, M. S. E., Kondratiev, V. I., Hessels, J. W. T., van Leeuwen, J., Champion, D. J., Deller, A., & Dunlap, B. H. *New Discoveries from the GBT 350-MHz Drift-Scan Survey*. In M. Burgay, N. D'Amico, P. Esposito, A. Pellizzoni, & A. Possenti , editor, *American Institute of Physics Conference Series*, volume 1357 of *American Institute of Physics Conference Series*, pages 32–35, 2011.
- Boyles, J. e. a. *Initial Findings of the GBT 350-MHz Drift Scan Pulsar Survey*. In *American Astronomical Society Meeting Abstracts #212*, volume 40 of *Bulletin of the American Astronomical Society*, page 208, 2008.
- Burgay, M., D'Amico, N., Possenti, A., Manchester, R. N., Lyne, A. G., Joshi, B. C., McLaughlin, M. A., Kramer, M., Sarkissian, J. M., Camilo, F., Kalogera, V., Kim, C., & Lorimer, D. R., *Nature*, 426, 531–533, 2003.

- Burgay, M., Rea, N., Israel, G. L., Possenti, A., Burderi, L., di Salvo, T., D'Amico, N., & Stella, L., *MNRAS*, 372, 410–416, 2006.
- Burgay, M., Bailes, M., Bates, S. D., Bhat, N. D. R., Burke-Spolaoor, S., D'Amico, N., Jameson, A., Johnston, S., Keith, M. J., Kramer, M., Levin, L., Lyne, A., Milia, S., Possenti, A., Stappers, B., & van Straten, W., *MNRAS- in prep.*, 2012.
- Burke-Spolaoor, S. & Bailes, M., *MNRAS*, 402, 855–866, 2010.
- Burke-Spolaoor, S., Bailes, M., Johnston, S., Bates, S. D., Bhat, N. D. R., Burgay, M., D'Amico, N., Jameson, A., Keith, M. J., Kramer, M., Levin, L., Milia, S., Possenti, A., Stappers, B., & van Straten, W., *MNRAS*, 416, 2465–2476, 2011.
- Burke-Spolaoor, S., Johnston, S., Bailes, M., Bates, S. D., Bhat, N. D. R., Burgay, M., Champion, D. J., D'Amico, N., Keith, M. J., Kramer, M., Levin, L., Possenti, S. M. A., Stappers, B., & van Straten, W., *ArXiv e-prints*, 2012.
- Cairns, I. H., Johnston, S., & Das, P., *MNRAS*, 353, 270–286, 2004.
- Camilo, F., Lorimer, D. R., Freire, P., Lyne, A. G., & Manchester, R. N., *ApJ*, 535, 975–990, 2000.
- Camilo, F., Ransom, S. M., Halpern, J. P., Reynolds, J., Helfand, D. J., Zimmerman, N., & Sarkissian, J., *Nature*, 442, 892–895, 2006.
- Camilo, F., Cognard, I., Ransom, S. M., Halpern, J. P., Reynolds, J., Zimmerman, N., Gotthelf, E. V., Helfand, D. J., Demorest, P., Theureau, G., & Backer, D. C., *ApJ*, 663, 497–504, 2007a.
- Camilo, F., Ransom, S. M., Halpern, J. P., & Reynolds, J., *ApJ*, 666, L93–L96, 2007b.
- Camilo, F., Ransom, S. M., Peñalver, J., Karastergiou, A., van Kerkwijk, M. H., Durant, M., Halpern, J. P., Reynolds, J., Thum, C., Helfand, D. J., Zimmerman, N., & Cognard, I., *ApJ*, 669, 561–569, 2007c.
- Camilo, F., Reynolds, J., Johnston, S., Halpern, J. P., Ransom, S. M., & van Straten, W., *ApJ*, 659, L37–L40, 2007d.
- Camilo, F., Reynolds, J., Johnston, S., Halpern, J. P., & Ransom, S. M., *ApJ*, 679, 681–686, 2008.

- Camilo, F., Ray, P. S., Ransom, S. M., Burgay, M., Johnson, T. J., Kerr, M., Gotthelf, E. V., Halpern, J. P., Reynolds, J., Romani, R. W., Demorest, P., Johnston, S., van Straten, W., Saz Parkinson, P. M., Ziegler, M., Dormody, M., Thompson, D. J., Smith, D. A., Harding, A. K., Abdo, A. A., Crawford, F., Freire, P. C. C., Keith, M., Kramer, M., Roberts, M. S. E., Weltevrede, P., & Wood, K. S., *ApJ*, 705, 1–13, 2009.
- Cordes, J. M., *ApJ*, 222, 1006–1011, 1978.
- Cordes, J. M., *Australian Journal of Physics*, 32, 9–24, 1979.
- Cordes, J. M. & Lazio, T. J. W., *ArXiv Astrophysics e-prints*, 2002.
- Cordes, J. M. & Rickett, B. J., *ApJ*, 507, 846–860, 1998.
- Cordes, J. M., Rankin, J., & Backer, D. C., *ApJ*, 223, 961–972, 1978.
- Cordes, J. M., Rickett, B. J., Stinebring, D. R., & Coles, W. A., *ApJ*, 637, 346–365, 2006.
- Deller, A. T., Bailes, M., & Tingay, S. J., *Science*, 323, 1327–, 2009.
- Deller, A. T., Camilo, F., Reynolds, J. E., & Halpern, J. P., *ApJ*, 748:L1, 2012.
- Dib, R., Kaspi, V. M., & Gavriil, F. P., *ApJ*, 673, 1044–1061, 2008.
- Dickey, J. M. & Lockman, F. J., *ARA&A*, 28, 215–261, 1990.
- Duncan, R. C. & Thompson, C., *ApJ*, 392, L9–L13, 1992.
- Dyks, J., *MNRAS*, 391, 859–868, 2008.
- Dyks, J. & Harding, A. K., *ApJ*, 614, 869–880, 2004.
- Eatough, R. P., Molkenthin, N., Kramer, M., Noutsos, A., Keith, M. J., Stappers, B. W., & Lyne, A. G., *MNRAS*, 407, 2443–2450, 2010.
- Edwards, R. T. & Stappers, B. W., *A&A*, 421, 681–691, 2004.
- Edwards, R. T., Bailes, M., van Straten, W., & Britton, M. C., *MNRAS*, 326, 358–374, 2001.
- Emmering, R. T. & Chevalier, R. A., *ApJ*, 345, 931–938, 1989.
- Espinoza, C. M., Lyne, A. G., Stappers, B. W., & Kramer, M., *MNRAS*, 414, 1679–1704, 2011.

- Fabian, A. C., Pringle, J. E., Verbunt, F., & Wade, R. A., *Nature*, 301, 222, 1983.
- Faucher-Giguère, C.-A. & Kaspi, V. M., *ApJ*, 643, 332–355, 2006.
- Friedman, J. L., Parker, L., & Ipser, J. R., *Physical Review Letters*, 62, 3015–3019, 1989.
- Gaensler, B. M., Slane, P. O., Gotthelf, E. V., & Vasisht, G., *ApJ*, 559, 963–972, 2001.
- Gaensler, B. M., Madsen, G. J., Chatterjee, S., & Mao, S. A., *PASA*, 25, 184–200, 2008.
- Gavriil, F. P., Kaspi, V. M., & Woods, P. M., *Nature*, 419, 142–144, 2002.
- Gavriil, F. P., Gonzalez, M. E., Gotthelf, E. V., Kaspi, V. M., Livingstone, M. A., & Woods, P. M., *Science*, 319, 1802–, 2008.
- Gould, D. M. & Lyne, A. G., *MNRAS*, 301, 235–260, 1998.
- Haensel, P., Zdunik, J. L., & Bejger, M., "New Astronomy Reviews", 51, 785–790, 2008.
- Halpern, J. P., Gotthelf, E. V., Becker, R. H., Helfand, D. J., & White, R. L., *ApJ*, 632, L29–L32, 2005.
- Halpern, J. P., Gotthelf, E. V., Reynolds, J., Ransom, S. M., & Camilo, F., *ApJ*, 676, 1178–1183, 2008.
- Heinke, C. O., Grindlay, J. E., Edmonds, P. D., Cohn, H. N., Lugger, P. M., Camilo, F., Bogdanov, S., & Freire, P. C., *ApJ*, 625, 796–824, 2005.
- Helfand, D. J., Chatterjee, S., Brisken, W. F., Camilo, F., Reynolds, J., van Kerkwijk, M. H., Halpern, J. P., & Ransom, S. M., *ApJ*, 662, 1198–1203, 2007.
- Hessels, J. W. T., Ransom, S. M., Stairs, I. H., Freire, P. C. C., Kaspi, V. M., & Camilo, F., *Science*, 311, 1901–1904, 2006.
- Hewish, A., Bell, S. J., Pilkington, J. D. H., Scott, P. F., & Collins, R. A., *Nature*, 217, 709–713, 1968.
- Hobbs, G., Lorimer, D. R., Lyne, A. G., & Kramer, M., *MNRAS*, 360, 974–992, 2005.
- Hobbs, G. B., Bailes, M., Bhat, N. D. R., Burke-Spolaor, S., Champion, D. J., Coles, W., Hotan, A., Jenet, F., Kedziora-Chudczer, L., Khoo, J., Lee, K. J., Lommen, A., Manchester, R. N., Reynolds, J., Sarkissian, J., van Straten, W., To, S., Verbiest, J. P. W., Yardley, D., & You, X. P., *PASA*, 26, 103–109, 2009.

- Hotan, A. W., van Straten, W., & Manchester, R. N., *PASA*, 21, 302–309, 2004.
- Hulse, R. A. & Taylor, J. H., *ApJ*, 195, L51–L53, 1975.
- Hurley, J. R., Tout, C. A., Wickramasinghe, D. T., Ferrario, L., & Kiel, P. D., *MNRAS*, 402, 1437–1448, 2010.
- Israel, G. L., Esposito, P., Rea, N., Dall’Osso, S., Senziani, F., Romano, P., Mangano, V., Götz, D., Zane, S., Tiengo, A., Palmer, D. M., Krimm, H., Gehrels, N., Mereghetti, S., Stella, L., Turolla, R., Campana, S., Perna, R., Angelini, L., & de Luca, A., *MNRAS*, 408, 1387–1395, 2010.
- Johnston, S. & Bailes, M., *MNRAS*, 252, 277–281, 1991.
- Johnston, S. & Romani, R. W., *ApJ*, 590, L95–L98, 2003.
- Johnston, S., van Straten, W., Kramer, M., & Bailes, M., *ApJ*, 549, L101–L104, 2001.
- Kaplan, D. L. & van Kerkwijk, M. H., *ApJ*, 705, 798–808, 2009.
- Kaplan, D. L. A. *Recent Results from Timing Nearby Isolated Neutron Stars*. In *American Astronomical Society Meeting Abstracts 211*, volume 211 of *American Astronomical Society Meeting Abstracts*, page 161.04, 2008.
- Kaspi, V. M. & Helfand, D. J. *Constraining the Birth Events of Neutron Stars*. In P. O. Slane & B. M. Gaensler, editor, *Neutron Stars in Supernova Remnants*, volume 271 of *Astronomical Society of the Pacific Conference Series*, page 3, 2002.
- Keane, E. F. & McLaughlin, M. A., *Bulletin of the Astronomical Society of India*, 39, 333–352, 2011.
- Keane, E. F., Kramer, M., Lyne, A. G., Stappers, B. W., & McLaughlin, M. A., *MNRAS*, 415, 3065–3080, 2011.
- Keith, M. J., Jameson, A., van Straten, W., Bailes, M., Johnston, S., Kramer, M., Possenti, A., Bates, S. D., Bhat, N. D. R., Burgay, M., Burke-Spolaor, S., D’Amico, N., Levin, L., McMahon, P. L., Milia, S., & Stappers, B. W., *MNRAS*, 409, 619–627, 2010.
- Keith, M. J., Johnston, S., Levin, L., & Bailes, M., *MNRAS*, 416, 346–354, 2011a.
- Keith, M. J., Johnston, S., Ray, P. S., Ferrara, E. C., Saz Parkinson, P. M., Çelik, Ö., Belfiore, A., Donato, D., Cheung, C. C., Abdo, A. A., Camilo, F., Freire, P. C. C., Guillemot, L., Harding, A. K., Kramer, M., Michelson, P. F., Ransom, S. M., Romani,

- R. W., Smith, D. A., Thompson, D. J., Weltevrede, P., & Wood, K. S., *MNRAS*, 414, 1292–1300, 2011b.
- Keith, M. J., Johnston, S., Bailes, M., Bates, S. D., Bhat, N. D. R., Burgay, M., Burke-Spoloar, S., D’Amico, N., Jameson, A., Kramer, M., Levin, L., Milia, S., Possenti, A., Stappers, B. W., van Straten, W., & Parent, D., *MNRAS*, 419, 1752–1765, 2012.
- Kondratiev, V. I., McLaughlin, M. A., Lorimer, D. R., Burgay, M., Possenti, A., Turolla, R., Popov, S. B., & Zane, S., *ApJ*, 702, 692–706, 2009.
- Kramer, M., Xilouris, K. M., Lorimer, D. R., Doroshenko, O., Jessner, A., Wielebinski, R., Wolszczan, A., & Camilo, F., *ApJ*, 501, 270, 1998.
- Kramer, M., Johnston, S., & van Straten, W., *MNRAS*, 334, 523–532, 2002.
- Kramer, M., Stairs, I. H., Manchester, R. N., McLaughlin, M. A., Lyne, A. G., Ferdman, R. D., Burgay, M., Lorimer, D. R., Possenti, A., D’Amico, N., Sarkissian, J. M., Hobbs, G. B., Reynolds, J. E., Freire, P. C. C., & Camilo, F., *Science*, 314, 97–102, 2006.
- Kramer, M., Stappers, B. W., Jessner, A., Lyne, A. G., & Jordan, C. A., *MNRAS*, 377, 107–119, 2007.
- Krastev, P. G., Li, B.-A., & Worley, A., *ApJ*, 676, 1170–1177, 2008.
- Kriss, G. A., Becker, R. H., Helfand, D. J., & Canizares, C. R., *ApJ*, 288, 703–706, 1985.
- Kulkarni, S. R. & Narayan, R., *ApJ*, 335, 755–768, 1988.
- Laros, J. G., Fenimore, E. E., Fikani, M. M., Klebesadel, R. W., & Barat, C., *Nature*, 322, 152, 1986.
- Lawson, K. D., Mayer, C. J., Osborne, J. L., & Parkinson, M. L., *MNRAS*, 225, 307, 1987.
- Lazaridis, K., Jessner, A., Kramer, M., Stappers, B. W., Lyne, A. G., Jordan, C. A., Serylak, M., & Zensus, J. A., *MNRAS*, 390, 839–846, 2008.
- Levin, L., Bailes, M., Bates, S., Bhat, N. D. R., Burgay, M., Burke-Spoloar, S., D’Amico, N., Johnston, S., Keith, M., Kramer, M., Milia, S., Possenti, A., Rea, N., Stappers, B., & van Straten, W., *ApJ*, 721, L33–L37, 2010.
- Levin, L., Bailes, M., Bates, S. D., Bhat, N. D. R., Burgay, M., Burke-Spoloar, S., D’Amico, N., Johnston, S., Keith, M. J., Kramer, M., Milia, S., Possenti, A., Stappers, B., & van Straten, W., *MNRAS*, 422, 2489–2500, 2012.

- Löhmer, O., Kramer, M., Mitra, D., Lorimer, D. R., & Lyne, A. G., *ApJ*, 562, L157–L161, 2001.
- Lorimer, D. R., *Living Reviews in Relativity*, 11, 8, 2008.
- Lorimer, D. R. *Radio Pulsar Statistics*. In Becker, W., editor, *Astrophysics and Space Science Library*, volume 357 of *Astrophysics and Space Science Library*, page 1, 2009.
- Lorimer, D. R. & Kramer, M. *Handbook of Pulsar Astronomy*. 2005.
- Lorimer, D. R., Bailes, M., Dewey, R. J., & Harrison, P. A., *MNRAS*, 263, 403, 1993.
- Lorimer, D. R., Nicastro, L., Lyne, A. G., Bailes, M., Manchester, R. N., Johnston, S., Bell, J. F., D'Amico, N., & Harrison, P. A., *ApJ*, 439, 933–938, 1995a.
- Lorimer, D. R., Yates, J. A., Lyne, A. G., & Gould, D. M., *MNRAS*, 273, 411–421, 1995b.
- Lorimer, D. R., Faulkner, A. J., Lyne, A. G., Manchester, R. N., Kramer, M., McLaughlin, M. A., Hobbs, G., Possenti, A., Stairs, I. H., Camilo, F., Burgay, M., D'Amico, N., Corongiu, A., & Crawford, F., *MNRAS*, 372, 777–800, 2006.
- Lyne, A. G. & Rickett, B. J., *Nature*, 219, 1339–1342, 1968.
- Lyne, A. G., Manchester, R. N., Lorimer, D. R., Bailes, M., D'Amico, N., Tauris, T. M., Johnston, S., Bell, J. F., & Nicastro, L., *MNRAS*, 295, 743–755, 1998.
- Lyne, A. G., Burgay, M., Kramer, M., Possenti, A., Manchester, R. N., Camilo, F., McLaughlin, M. A., Lorimer, D. R., D'Amico, N., Joshi, B. C., Reynolds, J., & Freire, P. C. C., *Science*, 303, 1153–1157, 2004.
- Lyne, A. G., McLaughlin, M. A., Keane, E. F., Kramer, M., Espinoza, C. M., Stappers, B. W., Palliyaguru, N. T., & Miller, J., *MNRAS*, 400, 1439–1444, 2009.
- Manchester, R. N., Newton, L. M., & Durdin, J. M., *Nature*, 313, 374–376, 1985.
- Manchester, R. N., Lyne, A. G., Robinson, C., Bailes, M., & D'Amico, N., *Nature*, 352, 219–221, 1991.
- Manchester, R. N., Lyne, A. G., D'Amico, N., Bailes, M., Johnston, S., Lorimer, D. R., Harrison, P. A., Nicastro, L., & Bell, J. F., *MNRAS*, 279, 1235–1250, 1996.
- Manchester, R. N., Lyne, A. G., Camilo, F., Bell, J. F., Kaspi, V. M., D'Amico, N., McKay, N. P. F., Crawford, F., Stairs, I. H., Possenti, A., Kramer, M., & Sheppard, D. C., *MNRAS*, 328, 17–35, 2001.

- Mazets, E. P., Golentskii, S. V., Ilinskii, V. N., Aptekar, R. L., & Guryan, I. A., *Nature*, 282, 587–589, 1979.
- McKinnon, M. M., *ApJ*, 590, 1026–1034, 2003.
- McLaughlin, M. A., Lyne, A. G., Lorimer, D. R., Kramer, M., Faulkner, A. J., Manchester, R. N., Cordes, J. M., Camilo, F., Possenti, A., Stairs, I. H., Hobbs, G., D’Amico, N., Burgay, M., & O’Brien, J. T., *Nature*, 439, 817–820, 2006.
- McMahon, P., *Master’s Thesis, Univ. Cape Town*, 2008.
- Mereghetti, S., *A&A Rev.*, 15, 225–287, 2008.
- Mereghetti, S., Tiengo, A., Esposito, P., Vianello, G., De Luca, A., Gotz, D., Weidens-pointner, G., von Kienlin, A., Israel, G. L., Stella, L., Rea, N., Turolla, R., & Zane, S., *ArXiv e-prints*, 2009.
- Milia, S. *Search for Millisecond Pulsars for the Pulsar Timing Array project*. PhD thesis, Universita Degli Studi Di Cagliari, 2011.
- Narayan, R. & Vivekanand, M., *A&A*, 122, 45–53, 1983.
- Narayan, R., Fruchter, A. S., Kulkarni, S. R., & Romani, R. W. *Are LMXRBs the progenitors of low mass binary pulsars?* In Mauche, C. W., editor, *Accretion-Powered Compact Binaries*, pages 451–455, 1990.
- O’Brien, J. T., Kramer, M., Lyne, A. G., Lorimer, D. R., & Jordan, C. A., *Chinese Journal of Astronomy and Astrophysics Supplement*, 6(2), 020000–7, 2006.
- Olausen, S. A., Kaspi, V. M., Ng, C.-Y., Zhu, W. W., Dib, R., Gavriil, F. P., & Woods, P. M., *ApJ*, 742:4, 2011.
- Perna, R. & Gotthelf, E. V., *ApJ*, 681, 522–529, 2008.
- Petrova, S. A., *MNRAS*, 368, 1764–1772, 2006.
- Radhakrishnan, V. & Cooke, D. J., *Astrophys. Lett.*, 3, 225, 1969.
- Ransom, S. M., Hessels, J. W. T., Stairs, I. H., Freire, P. C. C., Camilo, F., Kaspi, V. M., & Kaplan, D. L., *Science*, 307, 892–896, 2005.
- Ransom, S. M., Ray, P. S., Camilo, F., Roberts, M. S. E., Çelik, Ö., Wolff, M. T., Cheung, C. C., Kerr, M., Pennucci, T., DeCesar, M. E., Cognard, I., Lyne, A. G., Stappers,

- B. W., Freire, P. C. C., Grove, J. E., Abdo, A. A., Desvignes, G., Donato, D., Ferrara, E. C., Gehrels, N., Guillemot, L., Gwon, C., Harding, A. K., Johnston, S., Keith, M., Kramer, M., Michelson, P. F., Parent, D., Saz Parkinson, P. M., Romani, R. W., Smith, D. A., Theureau, G., Thompson, D. J., Weltevrede, P., Wood, K. S., & Ziegler, M., *ApJ*, 727:L16, 2011.
- Ray, P. S., Abdo, A. A., Parent, D., Bhattacharya, D., Bhattacharyya, B., Camilo, F., Cognard, I., Theureau, G., Ferrara, E. C., Harding, A. K., Thompson, D. J., Freire, P. C. C., Guillemot, L., Gupta, Y., Roy, J., Hessels, J. W. T., Johnston, S., Keith, M., Shannon, R., Kerr, M., Michelson, P. F., Romani, R. W., Kramer, M., McLaughlin, M. A., Ransom, S. M., Roberts, M. S. E., Saz Parkinson, P. M., Ziegler, M., Smith, D. A., Stappers, B. W., Weltevrede, P., & Wood, K. S., *ArXiv e-prints*, 2012.
- Rea, N. & Esposito, P. *Magnetar outbursts: an observational review*. In D. F. Torres & N. Rea, editor, *High-Energy Emission from Pulsars and their Systems*, page 247, 2011.
- Rea, N., Israel, G. L., Turolla, R., Esposito, P., Mereghetti, S., Götz, D., Zane, S., Tiengo, A., Hurley, K., Feroci, M., Still, M., Yershov, V., Winkler, C., Perna, R., Bernardini, F., Ubertini, P., Stella, L., Campana, S., van der Klis, M., & Woods, P., *MNRAS*, 396, 2419–2432, 2009.
- Rea, N., Esposito, P., Turolla, R., Israel, G. L., Zane, S., Stella, L., Mereghetti, S., Tiengo, A., Götz, D., Göğüş, E., & Kouveliotou, C., *Science*, 330, 944–, 2010.
- Rickett, B. J., Coles, W. A., & Bourgois, G., *A&A*, 134, 390–395, 1984.
- Ridley, J. P. & Lorimer, D. R., *MNRAS*, 404, 1081–1088, 2010.
- Roberts, M. S. E. *New Black Widows and Redbacks in the Galactic Field*. In M. Burgay, N. D’Amico, P. Esposito, A. Pellizzoni, & A. Possenti , editor, *American Institute of Physics Conference Series*, volume 1357 of *American Institute of Physics Conference Series*, pages 127–130, 2011.
- Romani, R. W., Narayan, R., & Blandford, R., *MNRAS*, 220, 19–49, 1986.
- Rothschild, R. E., Kulkarni, S. R., & Lingenfelter, R. E., *Nature*, 368, 432–434, 1994.
- Rubio Herrera, E. A. *Galactic and extragalactic searches for pulsars and radio transients*. PhD thesis, University of Amsterdam, 2010.
- Ruderman, M., Shaham, J., Tavani, M., & Eichler, D., *ApJ*, 343, 292–312, 1989.

- Sayer, R. W., Nice, D. J., & Taylor, J. H., *ApJ*, 474, 426, 1997.
- Scheuer, P. A. G., *Nature*, 218, 920–922, 1968.
- Scholz, P. & Kaspi, V. M., *ApJ*, 739:94, 2011.
- Serylak, M., Stappers, B. W., Weltevrede, P., Kramer, M., Jessner, A., Lyne, A. G., Jordan, C. A., Lazaridis, K., & Zensus, J. A., *MNRAS*, 394, 295–308, 2009.
- Sieber, W., *A&A*, 113, 311–313, 1982.
- Staveley-Smith, L., Wilson, W. E., Bird, T. S., Disney, M. J., Ekers, R. D., Freeman, K. C., Haynes, R. F., Sinclair, M. W., Vaile, R. A., Webster, R. L., & Wright, A. E., *PASA*, 13, 243–248, 1996.
- Stinebring, D. R., Smirnova, T. V., Hankins, T. H., Hovis, J. S., Kaspi, V. M., Kempner, J. C., Myers, E., & Nice, D. J., *ApJ*, 539, 300–316, 2000.
- Story, S. A., Gonthier, P. L., & Harding, A. K., *ApJ*, 671, 713–726, 2007.
- Sun, X. H., Reich, W., Waelkens, A., & Enßlin, T. A., *A&A*, 477, 573–592, 2008.
- Tauris, T. M. & Manchester, R. N., *MNRAS*, 298, 625–636, 1998.
- Taylor, J. H. & Manchester, R. N., *ApJ*, 215, 885–896, 1977.
- Thompson, C., Lyutikov, M., & Kulkarni, S. R., *ApJ*, 574, 332–355, 2002.
- Thornton, D., Bailes, M., Bates, S. D., Bhat, N. D. R., Burgay, M., Burke-Spolaor, S., D’Amico, N., Jameson, A., Johnston, S., Keith, M. J., Kramer, M., Levin, L., Lyne, A., Milia, S., Possenti, A., Stappers, B., & van Straten, W., *MNRAS- in prep.*, 2012.
- Thorsett, S. E., Deich, W. T. S., Kulkarni, S. R., Navarro, J., & Vasisht, G., *ApJ*, 416, 182, 1993.
- Tiengo, A., Vianello, G., Esposito, P., Mereghetti, S., Giuliani, A., Costantini, E., Israel, G. L., Stella, L., Turolla, R., Zane, S., Rea, N., Götz, D., Bernardini, F., Moretti, A., Romano, P., Ehle, M., & Gehrels, N., *ApJ*, 710, 227–235, 2010.
- Turolla, R., Zane, S., Pons, J. A., Esposito, P., & Rea, N., *ApJ*, 740:105, 2011.
- van den Heuvel, E. P., van Paradijs, J. A., & Taam, R. E., *Nature*, 322, 153–155, 1986.

- van Haasteren, R., Levin, Y., Janssen, G. H., Lazaridis, K., Kramer, M., Stappers, B. W., Desvignes, G., Purver, M. B., Lyne, A. G., Ferdman, R. D., Jessner, A., Cognard, I., Theureau, G., D'Amico, N., Possenti, A., Burgay, M., Corongiu, A., Hessels, J. W. T., Smits, R., & Verbiest, J. P. W., *MNRAS*, 414, 3117–3128, 2011.
- van Straten, W. & Bailes, M., *PASA*, 28, 1–14, 2011.
- Vivekanand, M. & Narayan, R., *Journal of Astrophysics and Astronomy*, 2, 315–337, 1981.
- von Mises, R., *Phys. Z.*, 19, 490, 1918.
- Weltevrede, P., Edwards, R. T., & Stappers, B. W., *A&A*, 445, 243–272, 2006a.
- Weltevrede, P., Stappers, B. W., Rankin, J. M., & Wright, G. A. E., *ApJ*, 645, L149–L152, 2006b.
- Wolszczan, A., *IAU Circ.*, 5073, 1, 1990.
- Wolszczan, A., *Nature*, 350, 688–690, 1991.
- Wolszczan, A. & Frail, D. A., *Nature*, 355, 145–147, 1992.
- Xilouris, K. M., Kramer, M., Jessner, A., von Hoensbroech, A., Lorimer, D., Wielebinski, R., Wolszczan, A., & Camilo, F., *ApJ*, 501, 286, 1998.
- Yardley, D. R. B., Coles, W. A., Hobbs, G. B., Verbiest, J. P. W., Manchester, R. N., van Straten, W., Jenet, F. A., Bailes, M., Bhat, N. D. R., Burke-Spolaor, S., Champion, D. J., Hotan, A. W., Oslowski, S., Reynolds, J. E., & Sarkissian, J. M., *MNRAS*, 414, 1777–1787, 2011.
- Young, M. D., Manchester, R. N., & Johnston, S., *Nature*, 400, 848–849, 1999.

A

Appendix: Previously Known Pulsars

Table A.1: Known pulsars detected in the pipeline. The columns of the table are: pulsar name based on J2000 coordinates, pulsar spin period (P), dispersion measure (DM), flux density at an observing frequency of 1400 MHz (S_{1400}), theoretical S/N (Theory), spectral S/N (FFT), pipeline folded S/N (Fold) and folded S/N when using published values (Dir).

Pulsar	P	DM	S_{1400}	Theory	FFT	Fold	Dir
J0737-3039A	0.022699	48.92	1.60	9.2	10.3	12.2	28.0
J0738-4042	0.374920	160.80	80.00	2535.3	321.1	2805.6	2584.6
J0742-2822	0.166762	73.78	15.00	821.0	524.5	1210.9	1247.3
J0745-5353	0.214836	122.30	—	—	207.2	166.5	155.1
J0749-4247	1.095452	104.59	0.60	29.0	11.8	17.6	15.5
J0809-4753	0.547199	228.30	3.00	127.8	122.6	105.1	96.3
J0818-3232	2.161259	131.80	0.50	64.3	44.9	50.0	65.0
J0820-3921	1.073567	179.40	0.20	12.8	7.4	13.2	15.8
J0820-4114	0.545446	113.40	5.20	73.0	74.8	109.6	98.9
J0821-4221	0.396728	270.60	0.20	10.6	23.4	24.9	23.5
J0831-4406	0.311674	254.00	0.43	20.3	29.6	27.7	28.0
J0834-4159	0.121116	240.50	0.19	7.9	7.9	12.4	11.3
J0835-3707	0.541404	112.30	0.28	21.0	22.6	27.1	32.1
J0835-4510	0.089328	67.99	1100.00	75725.9	712.8	15571.4	11797.1
J0837-4135	0.751624	147.29	16.00	1154.7	380.7	1645.9	1588.4
J0838-2621	0.308581	116.90	0.20	15.2	8.9	13.2	13.6
J0840-5332	0.720612	156.50	2.00	91.8	74.2	68.1	61.1
J0842-4851	0.644354	196.85	0.62	37.3	23.7	25.4	27.3
J0843-5022	0.208956	178.47	0.31	15.9	13.1	15.3	15.6
J0846-3533	1.116097	94.16	2.70	241.1	170.7	133.2	155.3
J0849-6322	0.367953	91.29	—	—	28.8	26.1	23.2
J0855-3331	1.267536	86.64	0.60	44.2	57.8	56.7	68.0
J0855-4644	0.064686	238.20	0.20	6.1	8.8	10.1	9.5
J0855-4658	0.575072	472.70	0.23	17.3	13.8	19.2	17.7
J0856-6137	0.962509	95.00	—	—	48.6	78.8	73.0
J0857-4424	0.326774	184.43	0.88	53.4	51.0	42.5	50.3

Table A.1 – Continued

Pulsar	P	DM	S ₁₄₀₀	Theory	FFT	Fold	Dir
J0900-3144	0.011110	75.70	3.80	102.6	40.4	41.2	48.2
J0902-6325	0.660313	76.00	—	—	37.4	38.1	35.1
J0905-4536	0.988281	116.80	0.83	41.8	23.2	23.7	27.3
J0905-5127	0.346287	196.43	1.10	43.8	38.3	38.0	32.1
J0907-5157	0.253556	103.72	9.30	307.4	431.0	431.0	429.2
J0908-4913	0.106755	180.37	10.00	617.9	613.1	484.6	502.6
J0922-4949	0.950289	237.10	0.52	43.8	19.9	20.6	23.5
J0924-5302	0.746295	152.90	1.10	85.2	54.3	50.2	58.6
J0924-5814	0.739501	57.40	4.30	131.8	88.6	79.6	49.5
J0932-3217	1.931627	102.10	—	—	30.2	33.8	30.4
J0932-5327	4.392159	122.00	0.15	13.0	8.7	11.0	11.6
J0934-5249	1.444773	100.00	1.20	106.1	183.5	227.4	199.5
J0941-39	0.586778	78.20	—	—	37.4	38.6	35.4
J0941-5244	0.658558	157.94	0.28	18.7	17.4	21.3	18.3
J0942-5552	0.664367	180.20	10.00	795.4	187.0	306.4	305.5
J0942-5657	0.808127	159.74	0.72	94.8	97.1	108.6	102.2
J0945-4833	0.331586	98.10	0.39	23.7	28.1	30.9	27.7
J0952-3839	1.373815	167.00	—	—	24.4	24.7	22.0
J0954-5430	0.472834	200.30	0.36	24.8	19.2	19.4	22.6
J0955-5304	0.862118	156.90	0.94	71.2	41.0	41.1	37.8
J0959-4809	0.670086	92.70	—	—	27.7	31.8	30.1
J1000-5149	0.255677	72.80	0.26	15.9	38.6	41.2	39.8
J1001-5507	1.436583	130.32	6.30	417.8	229.0	339.6	399.4
J1001-5559	1.661177	159.30	0.64	47.7	20.1	27.1	31.8
J1001-5939	7.733640	113.00	0.15	25.9	13.4	8.5	16.2
J1003-4747	0.307072	98.10	—	—	53.9	48.6	39.1
J1012-5857	0.819911	383.90	1.70	165.5	103.4	108.7	95.8
J1013-5934	0.442901	379.78	1.90	117.9	87.8	69.4	81.4
J1015-5719	0.139882	278.70	0.90	11.3	43.6	38.6	38.7
J1016-5345	0.769584	66.80	0.82	48.9	64.9	72.0	65.5
J1016-5819	0.087834	252.10	0.31	14.5	18.4	19.0	18.3
J1016-5857	0.107386	394.20	0.46	13.4	16.4	16.1	16.0
J1017-5621	0.503459	439.10	2.90	146.7	72.2	81.8	65.9
J1019-5749	0.162499	1039.40	0.80	10.8	19.1	27.6	33.7
J1020-5921	1.238305	80.00	0.45	29.9	14.5	19.6	23.7
J1020-6026	0.140480	445.00	0.14	4.0	8.2	11.2	10.7
J1032-5206	2.407622	139.00	0.19	27.6	18.4	21.2	21.3
J1032-5911	0.464208	418.20	0.93	70.8	50.2	44.0	51.6
J1035-6345	0.579577	189.70	0.24	20.2	9.7	12.1	12.4
J1036-4926	0.510368	136.53	—	—	90.4	79.4	65.8
J1038-5831	0.661992	72.74	0.79	25.4	26.6	29.5	33.1
J1042-5521	1.170859	306.50	0.62	26.4	79.0	79.1	59.9
J1043-6116	0.288602	449.20	0.91	42.5	39.9	42.3	38.0
J1045-4509	0.007474	58.17	3.00	104.6	38.9	64.7	62.8

Table A.1 – Continued

Pulsar	P	DM	S ₁₄₀₀	Theory	FFT	Fold	Dir
J1046-5813	0.369427	240.20	1.10	49.2	74.0	65.6	60.0
J1047-6709	0.198451	116.16	4.00	137.8	56.5	76.4	68.9
J1048-5832	0.123671	129.10	6.50	193.7	71.9	351.1	293.8
J1049-5833	2.202325	446.80	0.72	41.2	18.2	40.3	39.0
J1054-5943	0.346909	330.70	0.31	20.2	17.4	24.1	21.7
J1054-6452	1.840004	234.00	0.25	24.8	13.7	21.8	19.2
J1055-6028	0.099661	635.90	0.78	18.4	50.5	46.7	45.8
J1055-6905	2.919397	142.80	–	–	18.4	28.8	30.5
J1056-6258	0.422447	320.30	21.00	1202.1	387.5	920.3	889.1
J1057-4754	0.628306	60.00	–	–	23.7	22.7	19.6
J1057-5226	0.197108	30.10	–	–	93.7	82.2	71.6
J1058-5957	0.616270	334.00	0.51	19.8	17.8	18.6	17.5
J1059-5742	1.184999	108.70	1.20	75.8	45.9	77.4	69.0
J1103-6025	0.396587	275.90	0.17	11.2	14.0	20.0	18.2
J1104-6103	0.280905	78.51	0.24	12.6	15.2	17.7	17.7
J1105-6107	0.063193	271.01	0.75	14.7	14.9	17.7	15.6
J1106-6438	2.717934	203.00	0.19	22.3	10.6	15.4	16.3
J1107-5947	1.516531	158.40	0.43	18.6	13.9	19.3	14.3
J1107-6143	1.799396	406.00	0.38	28.2	25.0	29.2	33.7
J1110-5637	0.558253	262.56	1.80	86.2	165.5	143.9	164.4
J1112-6103	0.064962	599.10	1.40	23.9	26.4	28.1	27.0
J1112-6613	0.334213	249.30	2.60	154.3	108.5	96.0	89.3
J1112-6926	0.820484	148.40	–	–	72.2	63.4	61.3
J1114-6100	0.880820	677.00	2.00	61.0	98.0	99.8	116.8
J1117-6154	0.505097	493.60	0.68	43.2	35.9	35.9	34.4
J1119-6127	0.407963	707.40	0.80	37.4	37.9	34.3	27.5
J1121-5444	0.535783	204.70	1.30	68.5	48.3	58.6	54.6
J1123-4844	0.244838	92.92	–	–	98.9	98.2	90.1
J1123-6102	0.640234	439.40	0.53	43.2	53.9	54.3	50.2
J1123-6259	0.271434	223.26	0.56	27.0	24.3	26.7	24.4
J1123-6651	0.232976	111.20	0.36	17.5	17.8	18.9	17.3
J1124-5638	0.185560	289.50	0.31	11.7	17.3	16.6	20.0
J1124-6421	0.479099	298.00	0.19	13.0	8.6	11.6	10.8
J1125-6014	0.002630	52.95	0.05	2.1	38.4	35.1	35.4
J1126-6054	0.202737	280.27	1.00	70.5	79.5	69.2	68.3
J1126-6942	0.579416	55.33	–	–	15.7	16.6	13.2
J1128-6219	0.515984	675.00	0.27	5.8	9.2	10.9	10.3
J1130-6807	0.256353	148.73	–	–	13.7	12.1	11.1
J1132-5627	0.175166	305.70	0.09	5.4	7.0	11.1	13.5
J1133-6250	1.022875	567.80	2.90	50.7	69.1	104.3	120.6
J1136-5525	0.364706	85.50	4.00	174.9	153.0	119.0	138.5
J1137-6700	0.556216	228.04	1.20	27.5	22.6	23.9	21.5
J1138-6207	0.117564	519.80	0.49	10.3	13.0	15.0	13.7

Table A.1 – Continued

Pulsar	P	DM	S ₁₄₀₀	Theory	FFT	Fold	Dir
J1141-6545	0.393899	116.08	3.30	223.3	59.2	55.1	29.6
J1142-6230	0.558383	343.80	0.26	9.6	6.8	10.1	8.6
J1143-5158	0.675646	159.03	0.30	25.2	21.5	24.3	28.6
J1144-6146	0.987783	78.70	0.45	28.1	10.3	15.3	11.2
J1146-6030	0.273372	111.68	3.60	121.8	57.4	102.0	92.8
J1152-6012	0.376570	74.00	0.17	9.9	25.7	26.9	24.9
J1157-6224	0.400522	325.20	5.90	149.1	138.7	184.0	214.6
J1202-5820	0.452801	145.41	2.00	155.7	183.7	165.0	149.5
J1204-6843	0.308861	133.93	—	—	22.0	23.3	20.8
J1210-5559	0.279767	174.35	2.10	80.0	22.4	26.7	25.0
J1211-6324	0.433084	333.80	0.45	22.4	19.2	18.4	18.8
J1214-5830	0.909823	141.10	0.14	11.0	7.6	10.8	12.4
J1215-5328	0.636414	163.00	—	—	21.2	21.2	22.4
J1216-6410	0.003539	47.40	0.05	1.5	19.9	19.2	19.4
J1220-6318	0.789212	347.00	0.68	15.8	7.1	9.2	9.3
J1224-6208	0.585761	454.20	0.23	11.3	14.3	13.5	14.1
J1224-6407	0.216476	97.47	3.90	153.1	358.6	390.2	461.0
J1225-5556	1.018453	125.83	0.40	25.5	7.7	13.9	13.7
J1225-6035	0.626324	176.10	0.26	32.7	17.8	21.8	14.9
J1225-6408	0.419618	415.10	0.38	26.0	80.6	65.5	76.2
J1231-6303	1.351236	301.00	1.50	33.2	38.0	48.7	48.1
J1232-4742	1.872994	26.00	—	—	43.8	97.8	93.4
J1232-6501	0.088282	239.40	0.34	5.4	9.2	10.3	10.2
J1233-6312	0.564759	414.00	0.25	7.6	8.7	10.6	12.3
J1236-5033	0.294760	105.02	—	—	12.2	12.2	13.4
J1237-6725	2.110974	179.00	0.36	20.7	8.9	10.9	15.5
J1239-6832	1.301908	94.30	0.96	68.0	34.5	37.7	33.6
J1243-6423	0.388481	297.25	13.00	1138.4	356.3	1311.0	1739.7
J1244-5053	0.275207	109.95	—	—	10.6	14.0	13.4
J1252-6314	0.823339	278.40	0.66	31.1	21.2	23.1	25.0
J1253-5820	0.255496	100.58	3.50	334.6	65.2	170.9	158.4
J1259-6741	0.663329	94.70	1.30	110.4	85.8	83.1	75.4
J1302-6350	0.047763	146.72	1.70	12.6	42.2	38.9	32.3
J1303-6305	2.306642	343.00	0.36	19.6	11.7	17.9	18.3
J1305-6203	0.427762	470.00	0.62	17.8	10.7	14.8	11.8
J1305-6256	0.478231	967.00	0.32	16.2	10.9	12.8	15.1
J1305-6455	0.571647	505.00	1.60	51.3	57.6	47.5	57.1
J1306-6617	0.473026	436.90	2.50	97.8	139.8	156.0	144.9
J1307-6318	4.962427	374.00	1.40	38.8	11.2	23.0	19.7
J1308-5844	0.464700	205.60	0.21	21.3	26.4	18.1	26.7
J1309-6415	0.619454	574.00	0.21	6.3	6.8	6.8	10.0
J1312-5516	0.849236	134.10	—	—	49.8	44.6	51.7
J1314-6101	2.948390	309.00	0.41	21.4	10.8	19.0	15.7
J1316-6232	0.342825	983.30	0.74	7.6	19.4	19.2	19.2

Table A.1 – Continued

Pulsar	P	DM	S ₁₄₀₀	Theory	FFT	Fold	Dir
J1317-6302	0.261271	678.10	0.99	27.6	29.1	28.7	28.2
J1319-6056	0.284351	400.94	1.20	68.0	53.7	53.4	51.5
J1319-6105	0.421118	442.20	0.84	35.1	37.3	37.5	36.0
J1320-5359	0.279729	97.60	–	–	96.8	81.2	65.6
J1322-6241	0.506058	618.80	0.37	19.0	7.6	13.7	15.7
J1324-6146	0.844109	828.00	0.73	17.2	20.6	19.4	19.2
J1324-6302	2.483804	497.00	0.23	16.9	8.0	12.1	13.8
J1326-5859	0.477991	287.30	9.90	727.8	283.3	637.9	899.9
J1326-6408	0.792670	502.70	1.40	141.3	85.6	79.3	93.5
J1326-6700	0.543009	209.60	11.00	423.8	131.1	411.4	373.0
J1327-6222	0.529913	318.80	16.00	1127.9	294.2	364.8	1441.5
J1327-6301	0.196479	294.91	3.20	143.0	127.5	113.3	131.8
J1327-6400	0.280678	680.90	0.36	17.0	7.2	11.0	10.2
J1328-4921	1.478721	118.00	–	–	29.3	30.0	24.7
J1329-6158	1.565218	514.00	0.22	11.1	6.0	10.0	11.3
J1334-5839	0.107718	119.30	0.62	26.6	22.6	24.8	16.3
J1338-6204	1.238990	640.30	3.80	74.0	121.4	109.2	127.3
J1339-4712	0.137055	39.90	–	–	27.9	26.5	24.2
J1339-6618	0.558179	241.00	0.23	8.0	6.0	8.5	7.3
J1340-6456	0.378622	76.99	1.10	64.9	63.3	50.6	60.5
J1341-6023	0.627285	364.60	0.63	40.6	31.3	36.4	37.7
J1341-6220	0.193340	717.30	1.90	39.5	31.9	29.9	28.3
J1345-6115	1.253085	278.10	0.59	19.2	34.7	37.9	30.3
J1347-5947	0.609962	293.40	0.67	52.3	34.6	37.3	44.6
J1348-6307	0.927772	597.00	0.51	15.8	22.1	21.0	25.1
J1349-6130	0.259363	284.60	0.58	24.3	21.2	24.0	24.3
J1350-5115	0.295699	90.39	–	–	29.0	31.3	27.8
J1352-6803	0.628903	214.60	1.10	32.4	26.5	44.5	32.3
J1355-5153	0.644301	112.10	–	–	71.9	82.1	76.5
J1355-5747	2.038674	229.00	0.36	26.7	9.4	15.5	13.8
J1355-5925	1.213381	354.80	0.55	23.3	14.7	17.9	16.2
J1355-6206	0.276603	547.00	0.54	20.7	24.4	21.2	24.6
J1356-5521	0.507380	174.17	1.50	102.1	23.6	23.4	27.4
J1357-62	0.455761	416.80	8.70	212.4	272.1	234.3	191.6
J1357-6429	0.166108	128.50	0.44	12.3	17.8	16.3	16.4
J1359-6038	0.127501	293.71	7.60	358.2	486.7	557.8	515.1
J1401-6357	0.842790	98.00	6.20	625.8	246.2	454.7	598.8
J1403-6310	0.399170	305.00	0.65	13.8	10.4	11.8	10.2
J1405-5641	0.617575	273.00	0.10	7.6	6.2	7.6	9.4
J1406-5806	0.288349	229.00	0.84	12.3	11.5	18.7	22.1
J1407-6048	0.492344	575.20	0.20	7.4	11.6	11.7	11.9
J1407-6153	0.701615	645.00	0.36	10.8	7.5	10.4	9.4
J1410-6132	0.050052	960.00	–	–	15.2	12.7	17.7

Table A.1 – Continued

Pulsar	P	DM	S ₁₄₀₀	Theory	FFT	Fold	Dir
J1410-7404	0.278729	54.24	–	–	44.0	70.0	60.0
J1412-6111	0.529156	311.80	0.44	20.2	18.5	21.7	18.3
J1412-6145	0.315225	514.70	0.47	23.5	13.6	16.0	18.9
J1413-6141	0.285625	677.00	0.61	9.7	15.5	14.9	16.4
J1413-6222	0.292408	808.10	0.96	32.6	37.2	31.7	36.3
J1413-6307	0.394946	121.98	0.90	68.3	49.8	56.5	49.6
J1414-6802	4.630188	153.50	–	–	27.4	43.9	35.8
J1415-6621	0.392479	260.17	0.71	43.0	33.2	27.9	33.0
J1416-6037	0.295580	289.20	0.70	19.5	21.9	23.3	21.9
J1420-5416	0.935772	129.60	–	–	38.0	38.7	34.0
J1420-6048	0.068180	358.80	0.90	18.0	20.9	21.2	19.5
J1423-6953	0.333411	123.98	–	–	21.2	26.5	26.3
J1424-5556	0.770375	198.70	0.38	15.3	9.6	12.5	15.0
J1424-5822	0.366734	323.90	1.10	41.1	58.7	49.2	57.8
J1425-5723	0.353263	43.40	0.24	9.9	8.1	13.1	11.3
J1425-6210	0.501730	430.10	0.19	8.7	7.0	5.7	6.2
J1428-5530	0.570290	82.40	3.90	193.8	226.3	283.9	255.4
J1430-6623	0.785441	65.30	8.00	639.8	358.5	799.6	1223.0
J1434-6006	0.306368	332.00	0.24	14.4	7.0	7.5	9.3
J1435-5954	0.472995	44.26	3.60	127.5	35.6	36.0	29.6
J1437-6146	0.467616	200.50	0.24	8.5	12.6	14.7	15.8
J1440-6344	0.459605	124.20	0.78	39.5	80.7	61.1	71.0
J1441-6137	1.175840	166.00	0.15	8.8	12.8	15.7	18.4
J1444-5941	2.760228	177.10	0.42	25.1	9.1	14.4	17.2
J1449-5846	0.463330	216.60	0.28	11.4	6.9	9.0	10.7
J1452-5851	0.386625	262.40	0.24	7.8	8.2	12.2	11.3
J1452-6036	0.154991	349.70	1.40	71.4	62.5	56.8	64.1
J1453-6413	0.179485	71.07	14.00	676.1	343.9	572.8	880.5
J1456-6843	0.263377	8.60	80.00	2320.6	98.5	408.6	1074.8
J1457-5122	1.748301	37.00	–	–	30.2	42.1	26.5
J1457-5900	1.498637	175.00	0.24	6.8	6.9	11.9	15.0
J1502-5653	0.535504	194.00	0.39	37.1	39.6	39.4	44.6
J1502-5828	0.668105	584.00	0.50	18.7	12.0	16.2	18.4
J1502-6128	0.842104	256.50	0.56	20.8	20.1	21.6	21.4
J1504-5621	0.412985	143.00	0.24	13.7	7.2	8.5	17.4
J1507-4352	0.286757	48.70	–	–	76.0	363.2	342.1
J1507-6640	0.355655	129.80	–	–	86.8	100.4	87.6
J1509-6015	0.339038	423.60	0.17	8.8	7.4	9.6	8.9
J1510-4422	0.943871	84.00	–	–	18.5	22.3	19.3
J1511-5414	0.200384	84.76	0.75	26.0	37.4	37.0	34.3
J1511-5835	0.301511	332.00	0.50	13.9	15.6	18.4	15.6
J1512-5431	2.040532	219.00	0.38	9.6	12.6	18.1	16.1
J1512-5759	0.128694	628.70	6.00	171.2	194.6	184.8	178.3
J1513-5739	0.973458	469.70	0.77	30.7	22.8	28.3	33.8

Table A.1 – Continued

Pulsar	P	DM	S ₁₄₀₀	Theory	FFT	Fold	Dir
J1513-5908	0.150658	252.50	0.94	26.3	24.1	25.5	23.3
J1514-4834	0.454839	51.50	–	–	108.3	99.5	93.2
J1517-4356	0.650837	87.78	–	–	30.0	32.2	28.9
J1519-5734	0.518758	664.00	0.45	11.2	9.9	12.2	14.3
J1519-6106	2.154307	221.00	0.19	15.5	8.8	12.9	19.0
J1519-6308	1.254052	250.00	0.32	14.5	14.2	19.6	23.3
J1522-5525	1.389605	79.00	0.25	20.3	8.0	12.8	15.6
J1522-5829	0.395353	199.90	4.30	210.1	278.4	222.0	263.3
J1524-5625	0.078219	152.70	0.83	13.1	18.9	18.0	17.0
J1524-5706	1.116049	833.00	0.41	19.4	11.7	19.0	18.2
J1525-5417	1.011694	235.00	0.18	16.7	9.9	17.5	19.0
J1527-3931	2.417582	49.00	–	–	10.6	39.0	57.3
J1527-5552	1.048705	362.70	0.84	49.2	48.7	47.9	55.8
J1528-4109	0.526556	89.50	–	–	25.6	27.8	26.2
J1530-5327	0.278957	49.60	0.59	23.5	48.8	43.1	38.9
J1531-5610	0.084202	110.90	0.60	13.1	14.7	16.7	16.4
J1534-5334	1.368881	24.82	6.80	573.5	188.2	174.2	205.9
J1534-5405	0.289689	190.82	1.20	79.7	72.8	58.8	69.2
J1535-4114	0.432866	66.28	–	–	91.5	79.0	72.0
J1535-4415	0.468402	110.70	–	–	21.1	28.5	22.9
J1535-5848	0.307178	107.00	0.35	27.5	22.7	22.7	27.0
J1536-5433	0.881438	147.50	1.30	33.0	43.7	44.2	59.2
J1537-5645	0.430464	707.00	1.00	20.4	27.4	22.6	22.1
J1538-5519	0.395731	611.00	0.42	6.0	11.1	9.3	8.7
J1538-5551	0.104675	603.00	0.25	6.9	8.1	11.2	12.7
J1538-5638	0.843980	546.00	0.28	8.7	9.7	11.5	12.7
J1539-5626	0.243392	175.88	4.60	136.5	123.1	95.5	112.0
J1539-6322	1.630846	163.50	–	–	54.7	58.6	57.6
J1541-5535	0.295838	428.00	0.22	10.0	13.9	16.2	14.3
J1542-5034	0.599245	91.00	0.55	42.1	23.5	28.2	25.5
J1542-5133	1.783865	186.00	0.27	15.9	6.8	13.5	11.4
J1543-5459	0.377119	345.70	0.62	16.7	11.9	14.4	12.2
J1544-5308	0.178554	35.16	3.60	195.4	111.7	95.4	86.4
J1546-5302	0.580840	287.00	0.32	23.8	26.3	27.7	25.2
J1547-5839	0.242190	222.30	0.41	16.1	10.7	13.6	12.5
J1548-4821	0.145655	126.00	0.51	19.2	14.1	15.8	18.2
J1548-4927	0.602738	141.20	0.69	56.0	57.2	60.9	55.5
J1548-5607	0.170934	315.50	1.00	23.0	17.1	17.6	16.6
J1549-4848	0.288347	55.98	0.47	23.1	26.0	24.0	27.9
J1550-5242	0.749659	337.70	0.32	16.8	13.7	18.4	17.1
J1551-5310	0.453394	493.00	0.54	11.5	17.8	20.8	19.7
J1553-5456	1.081328	210.00	0.79	36.2	40.4	38.3	35.2
J1556-5358	0.994681	436.00	0.53	13.5	17.1	22.7	20.9
J1557-4258	0.329187	144.50	5.10	345.1	108.8	104.3	85.9

Table A.1 – Continued

Pulsar	P	DM	S ₁₄₀₀	Theory	FFT	Fold	Dir
J1558-5419	0.594575	657.00	0.40	13.3	10.3	11.4	11.1
J1559-4438	0.257056	56.10	40.00	2403.3	367.6	492.6	359.9
J1559-5545	0.957242	212.90	0.72	67.6	23.3	20.4	7.9
J1600-5044	0.192601	260.56	17.00	691.8	423.8	713.8	667.9
J1600-5751	0.194454	176.55	1.40	47.1	57.5	57.0	66.4
J1602-5100	0.864227	170.93	5.70	434.8	223.2	252.4	230.3
J1603-3539	0.141909	77.50	–	–	13.4	12.9	12.5
J1603-5657	0.496077	264.07	0.53	42.6	85.5	83.7	77.0
J1603-7202	0.014842	38.05	3.00	63.2	45.7	40.8	34.7
J1604-4718	0.527466	52.00	0.22	9.5	12.5	15.6	14.2
J1604-4909	0.327418	140.80	5.50	428.5	159.2	156.7	149.4
J1604-7203	0.341403	54.37	–	–	32.6	37.3	33.7
J1605-5257	0.658013	35.10	13.00	292.0	160.2	258.7	321.8
J1609-4616	0.249609	150.10	0.38	14.0	10.0	15.4	13.5
J1610-5006	0.481119	416.00	1.60	39.6	43.2	39.6	45.6
J1610-5303	0.786468	380.10	0.76	14.2	8.2	13.6	12.4
J1611-4949	0.666438	556.80	0.58	17.7	10.1	12.3	14.4
J1611-5209	0.182492	127.57	1.20	69.7	36.4	39.8	37.5
J1611-5847	0.354550	79.90	0.11	16.1	11.6	15.8	14.4
J1613-4714	0.382376	161.20	1.50	59.9	29.2	28.5	31.9
J1613-5211	0.457502	360.10	0.29	13.5	7.4	11.3	11.4
J1613-5234	0.655221	624.00	0.28	8.5	6.4	9.3	9.2
J1614-3937	0.407292	152.44	–	–	12.5	12.9	15.6
J1614-5048	0.231694	582.80	2.40	43.9	77.6	70.5	54.4
J1614-5402	0.572592	300.00	0.25	8.0	8.8	10.5	8.1
J1615-2940	2.477568	44.79	–	–	26.2	31.2	28.8
J1615-5444	0.360958	312.60	0.59	39.5	32.1	30.1	35.0
J1615-5537	0.791526	124.48	0.44	25.3	11.8	15.8	13.7
J1616-5109	1.219594	1160.00	1.20	14.7	9.7	12.1	15.0
J1617-4608	0.567080	321.50	0.15	11.1	8.7	13.9	14.0
J1618-4723	0.203553	134.70	1.00	24.2	17.1	18.0	16.4
J1621-5039	1.084020	261.00	0.36	11.0	9.0	13.4	12.3
J1621-5243	0.371924	363.00	0.27	9.2	8.8	11.4	10.7
J1622-4332	0.916938	230.68	0.53	30.4	56.4	52.8	48.1
J1622-4347	0.457681	177.00	0.18	7.6	7.1	8.2	7.8
J1622-4802	0.265072	364.30	0.92	16.6	15.8	17.2	19.6
J1622-4944	1.072968	755.00	0.52	11.1	7.2	11.9	10.7
J1623-4256	0.364590	295.00	1.30	42.8	68.8	57.5	52.9
J1623-4949	0.725732	183.30	0.36	14.2	6.8	9.7	11.6
J1624-4411	0.233164	139.40	0.48	22.5	13.5	15.1	18.0
J1624-4613	0.871243	224.20	0.39	5.0	11.9	14.2	14.0
J1625-4048	2.355278	145.00	–	–	22.0	29.7	60.2
J1626-4537	0.370141	237.00	1.10	37.8	21.2	30.4	39.5

Table A.1 – Continued

Pulsar	P	DM	S ₁₄₀₀	Theory	FFT	Fold	Dir
J1626-4807	0.293928	817.00	0.37	5.7	6.5	8.4	9.4
J1627-4845	0.612331	557.80	0.48	8.3	9.5	14.0	12.2
J1627-5547	0.352464	166.20	0.65	34.6	40.7	37.8	43.5
J1628-4804	0.865971	952.00	1.00	20.8	22.3	19.9	22.8
J1629-6902	0.006001	29.49	–	–	43.6	43.6	38.7
J1630-4719	0.559071	489.60	0.46	13.7	11.9	16.6	14.8
J1630-4733	0.575971	498.00	4.00	52.6	30.9	37.5	43.6
J1632-4621	1.709154	562.90	0.99	42.2	17.1	18.9	26.5
J1632-4757	0.228564	578.00	0.30	6.4	8.1	9.8	9.0
J1633-4453	0.436507	474.10	1.90	67.5	54.1	51.5	59.9
J1633-5015	0.352142	398.41	5.70	309.3	275.0	310.0	362.2
J1635-4513	1.594746	416.00	0.25	7.6	10.7	15.8	13.7
J1635-4944	0.671964	474.00	0.40	15.7	14.8	14.5	17.6
J1635-5954	0.529121	134.90	–	–	52.3	43.1	45.9
J1636-4803	1.204644	503.00	1.10	46.2	36.7	38.2	44.3
J1636-4933	0.430367	542.70	0.45	22.7	19.8	18.9	22.4
J1637-4450	0.252870	470.70	0.40	14.7	12.3	14.1	13.4
J1637-4553	0.118771	193.23	1.10	30.3	35.5	33.4	30.3
J1637-4642	0.154027	417.00	0.78	9.9	13.1	15.3	14.6
J1638-3815	0.698261	238.00	0.62	19.3	26.3	24.6	29.2
J1638-4608	0.278137	424.30	0.33	8.6	6.6	10.7	10.4
J1639-4359	0.587559	258.90	0.92	42.8	41.4	40.5	37.3
J1639-4604	0.264558	258.91	0.78	33.6	53.4	49.7	40.3
J1640-4715	0.517405	591.70	1.20	27.7	21.1	22.2	25.1
J1643-4550	0.717508	450.80	0.34	16.7	7.2	12.1	18.0
J1644-4559	0.455060	478.80	310.00	10311.3	468.7	7230.4	6436.5
J1646-4346	0.231603	490.40	0.98	21.0	33.5	29.5	29.4
J1646-6831	1.785611	43.00	2.00	79.5	86.2	269.7	235.6
J1647-36	0.210726	223.90	–	–	6.7	9.1	5.0
J1648-3256	0.719455	128.28	1.00	67.8	93.0	94.2	79.8
J1648-4458	0.629632	925.00	0.55	16.2	10.5	13.8	12.1
J1648-4611	0.164950	392.90	0.58	15.7	12.9	13.5	15.6
J1649-3805	0.262026	213.80	1.00	32.0	21.7	23.3	22.0
J1649-4349	0.870712	398.60	0.75	32.0	11.6	19.2	21.9
J1649-4653	0.557019	332.00	0.31	14.2	7.3	10.1	13.4
J1649-4729	0.297692	540.20	0.29	10.5	10.0	11.7	10.9
J1649-5553	0.613571	180.40	–	–	16.8	17.8	15.9
J1650-4126	0.308918	251.50	0.29	10.3	6.8	8.3	9.2
J1650-4502	0.380870	319.70	0.35	22.7	22.2	20.9	25.5
J1650-4921	0.156399	229.90	0.16	5.9	8.8	13.0	12.1
J1651-4246	0.844081	482.00	16.00	330.0	173.5	348.9	419.2
J1651-4519	0.517443	562.00	0.54	12.6	8.2	12.5	11.7
J1651-5222	0.635056	179.10	2.90	176.8	153.5	158.0	144.8
J1651-5255	0.890534	164.00	–	–	63.5	62.3	56.2

Table A.1 – Continued

Pulsar	P	DM	S ₁₄₀₀	Theory	FFT	Fold	Dir
J1652-2404	1.703739	68.41	1.10	72.1	44.3	84.9	69.9
J1653-3838	0.305037	207.20	1.30	100.6	110.8	99.0	114.3
J1653-4249	0.612558	416.10	1.30	46.6	39.4	36.0	41.2
J1653-4315	0.419280	337.00	0.53	4.5	7.8	9.7	8.6
J1653-4854	3.059510	354.00	0.18	8.2	6.6	12.4	12.0
J1654-3710	0.939165	302.00	0.22	11.2	6.7	12.7	13.1
J1654-4140	1.273945	307.00	0.71	53.4	24.3	26.6	36.5
J1655-3048	0.542936	154.30	—	—	17.5	22.8	20.9
J1656-3621	0.730134	229.00	0.29	11.1	8.0	12.1	10.9
J1658-4306	1.166449	845.00	0.80	14.7	11.7	18.8	22.0
J1658-4958	0.416874	193.40	0.87	44.0	44.2	38.6	44.7
J1659-4316	0.474381	640.90	0.21	13.0	7.1	10.9	9.6
J1659-4439	0.353293	535.00	0.42	16.4	16.5	16.8	20.2
J1700-3312	1.358307	166.97	1.20	52.5	44.6	61.5	72.1
J1700-3611	1.494091	232.70	0.51	41.3	25.7	31.5	29.6
J1701-3130	0.291341	130.73	—	—	58.8	54.8	64.8
J1701-3726	2.454609	303.40	2.90	192.6	84.6	126.1	111.2
J1701-4533	0.322909	526.00	2.50	93.7	127.5	107.4	125.0
J1702-4128	0.182136	367.10	1.10	27.8	19.6	19.7	23.8
J1702-4217	0.227565	629.00	0.50	9.3	10.8	13.9	14.1
J1702-4306	0.215507	537.00	0.27	9.6	8.6	12.8	10.8
J1702-4310	0.240524	377.00	0.72	15.7	20.2	22.5	21.3
J1703-3241	1.211785	110.31	7.60	416.8	233.6	373.2	310.6
J1703-4442	1.747293	280.20	0.21	21.6	6.8	10.5	12.4
J1705-1906	0.298987	22.91	8.00	660.5	323.5	370.5	432.1
J1705-3423	0.255426	146.36	4.10	169.9	199.2	173.4	205.8
J1705-3936	0.854482	598.00	0.33	13.4	7.7	12.1	13.9
J1705-3950	0.318941	207.10	1.50	62.5	35.2	32.9	38.6
J1705-4108	0.861067	1077.00	1.30	24.7	26.5	34.5	26.8
J1706-6118	0.361921	76.13	—	—	32.4	45.4	41.3
J1707-4053	0.581017	360.00	7.20	160.3	134.7	117.2	140.1
J1707-4341	0.890594	398.20	0.46	25.2	11.9	17.1	19.7
J1707-4729	0.266474	268.30	1.90	106.2	61.7	62.0	57.1
J1708-3426	0.692113	190.70	1.50	49.6	63.4	62.7	72.5
J1708-4522	1.297837	454.00	0.22	14.7	10.3	13.9	13.3
J1709-1640	0.653054	24.87	4.00	198.2	197.7	327.0	362.9
J1709-3626	0.447857	393.60	0.58	22.4	20.9	20.6	19.3
J1709-4342	1.735898	281.00	0.14	8.4	7.7	7.8	9.6
J1709-4429	0.102459	75.69	7.30	195.3	224.1	192.8	167.8
J1710-4148	0.286561	461.00	0.31	7.9	7.6	11.4	10.8
J1711-1509	0.868804	59.88	0.70	32.9	15.4	17.5	17.2
J1711-5350	0.899218	106.10	—	—	53.0	53.5	50.2
J1712-2715	0.255360	92.64	—	—	19.3	19.4	22.1
J1713-3844	1.600114	544.00	0.26	17.0	10.2	14.1	15.9

Table A.1 – Continued

Pulsar	P	DM	S ₁₄₀₀	Theory	FFT	Fold	Dir
J1715-3859	0.928108	817.00	0.54	13.7	7.1	8.3	11.4
J1715-3903	0.278481	313.10	0.46	17.3	9.8	12.9	15.7
J1715-4034	2.072153	254.00	1.60	40.6	37.7	45.2	45.0
J1716-3720	0.630314	682.70	0.41	17.0	10.6	14.8	13.7
J1716-4111	1.036067	245.80	0.22	20.7	9.7	13.8	12.0
J1717-3425	0.656299	587.70	3.30	109.6	104.6	91.9	84.5
J1717-3737	0.682419	525.80	0.69	21.1	19.4	21.5	25.4
J1717-3953	1.085521	466.00	0.78	6.1	14.6	15.3	17.7
J1717-4043	0.397857	452.60	0.54	12.4	16.5	16.6	15.5
J1717-40433	0.349929	539.00	0.41	9.1	7.9	7.8	9.6
J1717-5800	0.321793	125.22	–	–	10.1	12.1	12.1
J1718-3825	0.074670	247.40	1.30	29.9	33.8	27.9	32.7
J1719-4006	0.189094	386.60	1.10	36.8	35.9	35.4	39.2
J1720-1633	1.565601	44.83	1.10	85.5	8.1	15.7	13.9
J1720-2933	0.620448	42.64	2.10	101.1	21.0	27.5	32.6
J1720-3659	0.351125	381.60	0.74	33.3	33.7	32.2	37.1
J1721-1939	0.404040	103.00	–	–	6.0	11.8	15.5
J1721-2457	0.003497	47.76	0.58	6.5	27.2	27.2	23.0
J1721-3532	0.280424	496.00	11.00	281.0	177.8	203.6	237.4
J1722-3207	0.477158	126.06	3.40	228.1	250.0	278.0	257.9
J1722-3632	0.399183	416.20	1.60	28.3	39.4	34.6	40.5
J1722-3712	0.236173	99.50	3.20	214.3	244.6	225.4	202.3
J1723-3659	0.202722	254.20	1.50	40.0	41.6	35.7	41.9
J1724-3149	0.948237	409.00	0.36	13.4	9.6	12.1	11.8
J1724-3505	1.221708	875.00	0.24	10.6	8.5	11.3	10.9
J1725-3546	1.032471	744.00	0.61	17.5	9.9	14.8	17.6
J1725-4043	1.465071	203.00	0.34	16.4	15.2	17.5	20.4
J1726-4006	0.882778	277.00	0.21	12.5	12.9	17.6	16.1
J1727-2739	1.293100	147.00	1.60	47.4	56.2	84.5	78.0
J1728-4028	0.866343	231.00	0.69	10.7	14.2	18.6	24.0
J1730-2304	0.008123	9.62	4.00	68.1	81.6	68.0	52.4
J1730-3350	0.139460	259.00	3.20	98.4	102.2	79.9	79.0
J1731-4744	0.829829	123.33	12.00	607.4	292.5	613.2	1218.6
J1732-1930	0.483770	72.43	0.30	14.8	9.7	11.9	14.1
J1732-4128	0.627981	195.30	0.63	33.9	32.3	32.7	30.3
J1732-5049	0.005313	56.82	–	–	24.3	26.6	23.5
J1733-2228	0.871683	41.14	2.30	62.5	128.8	133.2	160.5
J1733-3322	1.245915	524.00	0.80	23.4	20.4	23.0	21.3
J1733-3716	0.337586	153.50	3.40	143.9	48.3	49.4	58.5
J1733-4005	0.561778	317.80	0.49	20.0	23.3	26.7	26.9
J1734-2415	0.612524	126.30	0.29	8.6	11.3	15.3	14.6
J1735-0724	0.419335	73.51	1.70	135.8	119.3	102.2	77.6
J1736-2457	2.642223	170.00	0.52	23.4	38.5	41.4	37.1

Table A.1 – Continued

Pulsar	P	DM	S ₁₄₀₀	Theory	FFT	Fold	Dir
J1736-3511	0.502803	106.00	0.18	10.4	7.4	8.9	10.8
J1737-3102	0.768672	280.00	0.60	20.0	12.8	15.7	17.5
J1737-3137	0.450432	488.20	0.80	16.3	7.9	10.7	9.9
J1737-3320	0.816273	804.00	0.35	11.0	6.8	10.2	9.1
J1737-3555	0.397585	89.41	0.74	32.3	31.1	28.9	34.1
J1738-2647	0.349591	182.20	0.44	15.1	10.7	15.1	13.1
J1738-3107	0.549498	735.00	0.26	7.6	8.4	9.2	8.4
J1738-3211	0.768499	49.59	2.80	112.9	99.2	106.8	83.4
J1739-1313	1.215698	58.20	–	–	13.1	21.7	16.6
J1739-2903	0.322882	138.56	2.00	61.9	111.2	103.6	87.3
J1739-3023	0.114368	170.00	1.00	15.4	4.6	10.5	15.3
J1739-3049	0.239317	573.20	0.50	7.0	8.8	11.7	9.9
J1739-3131	0.529441	600.10	4.90	104.6	87.1	78.4	70.8
J1739-3159	0.877561	337.00	1.00	32.2	34.7	34.7	41.4
J1740-3015	0.606887	152.15	6.40	251.0	146.2	152.6	169.9
J1740-3052	0.570310	740.90	0.70	25.3	7.3	9.9	8.7
J1740-3327	0.515001	274.10	0.30	12.4	6.3	11.7	10.4
J1741-0840	2.043082	74.90	1.40	51.8	94.7	127.0	80.4
J1741-2019	3.904506	74.90	–	–	18.7	29.1	34.3
J1741-2733	0.892959	149.20	1.10	28.7	42.0	46.9	35.9
J1741-3016	1.893749	382.00	2.30	85.5	37.1	44.2	40.0
J1741-3927	0.512211	158.50	4.70	305.6	173.0	205.1	139.3
J1742-4616	0.412401	115.96	–	–	51.8	61.9	56.6
J1743-1351	0.405337	116.30	0.50	23.5	18.8	25.4	23.6
J1743-3150	2.414576	193.05	1.90	102.2	71.5	77.1	92.2
J1743-3153	0.193105	505.70	0.50	10.8	8.4	9.9	14.4
J1743-4212	0.306167	131.94	–	–	25.4	25.7	23.6
J1744-1134	0.004075	3.14	3.00	167.0	25.0	27.5	25.1
J1744-1610	1.757206	66.67	–	–	12.9	19.4	18.7
J1744-3130	1.066061	192.90	0.70	22.3	11.8	16.6	19.9
J1745-0952	0.019376	64.47	0.38	9.6	10.1	12.3	12.2
J1745-3040	0.367429	88.37	13.00	387.8	100.7	381.1	442.2
J1747-2647	0.500254	570.00	1.54	18.1	37.4	37.0	32.8
J1748-2021A	0.288603	219.40	0.37	3.5	7.6	7.8	7.7
J1748-2444	0.442838	207.33	0.34	18.7	11.3	13.8	12.0
J1749-3002	0.609874	509.40	3.70	69.0	58.9	53.4	49.7
J1749-5605	1.332310	58.00	–	–	38.6	43.8	40.8
J1750-2438	0.712794	476.00	0.50	18.1	16.2	18.3	16.0
J1750-2444	0.899377	331.00	0.27	10.4	7.6	10.5	10.3
J1750-3157	0.910363	206.34	1.20	96.5	40.0	38.2	44.5
J1750-3503	0.684014	189.35	0.79	16.9	16.5	17.3	14.3
J1751-2857	0.003915	42.81	0.06	1.2	16.2	17.4	14.2
J1751-3323	0.548227	296.70	1.30	100.2	50.6	44.1	50.7
J1751-4657	0.742352	20.40	10.00	537.1	112.0	120.5	139.9

Table A.1 – Continued

Pulsar	P	DM	S ₁₄₀₀	Theory	FFT	Fold	Dir
J1752-2410	0.191037	508.30	0.47	21.0	16.8	18.9	17.8
J1752-2806	0.562558	50.37	18.00	767.0	358.1	484.1	1382.0
J1752-2821	0.640229	516.30	0.32	14.6	15.0	21.3	18.4
J1753-2501	0.528336	672.00	2.30	30.9	28.7	30.6	22.8
J1754-3443	0.361691	187.70	0.49	21.0	13.2	16.1	19.7
J1754-3510	0.392704	82.30	0.47	26.5	36.5	37.5	44.5
J1755-1650	0.733744	159.90	0.13	10.5	7.8	10.7	12.2
J1755-2725	0.261955	115.00	0.50	10.2	13.2	14.0	18.8
J1756-2225	0.404980	326.00	0.25	6.0	7.8	10.7	12.7
J1756-2251	0.028462	121.18	0.60	20.9	19.9	18.2	28.9
J1756-2435	0.670480	367.10	2.00	77.9	77.4	72.2	54.7
J1757-2223	0.185310	239.30	1.10	45.0	9.7	16.0	15.3
J1757-2421	0.234101	179.45	3.90	102.2	205.9	185.1	215.2
J1757-5322	0.008870	30.82	–	–	27.5	23.5	21.8
J1758-1931	0.692552	207.00	0.38	15.4	6.4	7.7	8.7
J1758-2206	0.430278	678.00	0.41	12.0	9.8	11.1	13.2
J1758-2540	2.107263	218.20	0.65	13.5	34.4	34.9	32.0
J1758-2846	0.766706	66.60	0.20	17.1	9.9	14.6	13.5
J1759-1940	0.254720	302.70	0.90	30.2	46.6	38.5	44.8
J1759-1956	2.843389	236.40	0.41	32.7	29.1	36.4	43.1
J1759-2205	0.460974	177.16	1.30	70.7	106.0	96.7	114.0
J1759-2302	0.810718	889.00	1.30	17.1	14.9	18.9	13.5
J1759-2307	0.558889	812.60	0.70	26.7	14.7	18.4	17.7
J1759-2549	0.956549	431.00	0.60	20.0	10.0	12.7	12.8
J1759-2922	0.574400	79.42	0.56	30.4	15.2	20.7	18.8
J1759-3107	1.078953	128.60	0.91	45.9	45.9	47.8	42.9
J1800-0125	0.783185	50.00	0.14	3.1	7.4	11.3	11.4
J1801-0357	0.921491	120.37	0.70	56.3	19.0	19.7	20.3
J1801-1855	2.550498	484.00	0.47	22.3	11.7	21.4	18.9
J1801-1909	1.108725	264.00	0.50	15.9	13.5	18.0	16.7
J1801-2154	0.375297	387.90	0.18	6.0	7.5	9.4	6.7
J1801-2304	0.415827	1073.90	2.20	19.4	15.6	22.0	21.8
J1801-2451	0.124924	289.00	0.85	12.1	23.2	23.6	20.2
J1801-2920	1.081908	125.61	1.80	42.1	46.2	48.6	44.9
J1802-1745	0.514671	264.20	0.21	8.4	9.1	12.8	11.9
J1802-2124	0.012648	149.63	0.77	28.5	24.6	21.4	29.4
J1802-2426	0.569007	711.00	0.60	13.5	11.9	15.2	13.8
J1803-1616	0.536596	388.10	0.16	7.8	7.9	10.6	13.0
J1803-1857	2.864338	392.00	0.40	30.1	16.8	23.0	27.9
J1803-2137	0.133667	233.99	7.60	99.2	156.8	155.7	150.8
J1803-2712	0.334415	165.50	1.00	35.0	37.5	32.9	38.4
J1804-0735	0.023101	186.32	1.00	25.2	13.2	14.6	13.9
J1805-0619	0.454651	146.22	–	–	20.9	34.5	34.7

Table A.1 – Continued

Pulsar	P	DM	S ₁₄₀₀	Theory	FFT	Fold	Dir
J1805-1504	1.181269	225.00	2.20	47.4	25.0	65.4	85.5
J1805-2037	0.357807	708.10	0.34	10.5	6.7	9.6	8.7
J1806-1154	0.522618	122.41	2.60	57.1	80.5	72.2	84.7
J1806-1618	0.668309	319.00	0.22	7.1	7.7	9.1	7.8
J1806-1920	0.879791	683.00	1.90	14.9	12.7	14.0	16.4
J1806-2125	0.481789	750.40	1.10	22.9	14.1	14.1	15.6
J1807-0847	0.163727	112.38	15.00	457.5	357.8	424.8	351.9
J1807-2459A	0.003059	134.00	1.10	26.8	22.3	19.7	17.2
J1807-2715	0.827776	312.98	0.91	49.2	61.3	56.9	52.3
J1808-0813	0.876044	151.27	1.80	83.9	51.6	55.4	49.7
J1808-1020	0.596993	225.30	0.23	17.0	17.2	17.4	20.6
J1808-2057	0.918410	606.80	2.60	56.1	99.0	108.8	98.0
J1808-3249	0.364912	147.37	—	—	32.3	35.7	32.8
J1809-1429	0.895285	411.30	0.60	33.8	22.1	27.3	25.6
J1809-1917	0.082747	197.10	2.50	31.9	36.4	29.4	34.7
J1809-2004	0.434811	867.10	0.90	17.2	9.3	10.7	12.4
J1809-2109	0.702414	381.91	0.84	36.2	30.5	33.4	41.2
J1809-3547	0.860388	193.84	—	—	7.3	10.5	10.5
J1810-1441	0.217214	304.90	0.21	6.5	7.9	9.2	8.9
J1810-1820	0.153716	452.20	0.70	9.4	7.6	9.5	7.6
J1810-2005	0.032822	241.00	1.33	24.5	35.5	33.4	32.4
J1811-0154	0.924945	148.10	—	—	30.7	34.1	31.1
J1811-1736	0.104182	476.00	1.30	13.8	7.3	7.4	13.4
J1811-1835	0.557464	761.00	0.42	15.0	8.1	10.1	12.5
J1811-2439	0.415813	172.00	0.26	11.9	31.8	27.9	25.7
J1812-1718	1.205374	255.10	1.00	35.0	17.6	22.3	20.0
J1812-1733	0.538341	518.00	3.30	37.7	52.5	45.9	53.7
J1812-2102	1.223352	547.20	1.40	57.8	52.5	48.8	57.2
J1812-2526	0.315835	361.40	0.18	2.7	6.4	11.2	10.4
J1813-2113	0.426466	462.30	0.60	18.5	13.0	14.3	14.7
J1813-2242	0.328514	333.00	0.21	6.7	7.4	9.9	8.8
J1814-1649	0.957464	782.00	1.10	56.2	44.1	42.2	38.2
J1814-1744	3.975905	792.00	0.70	18.5	12.8	25.5	20.1
J1816-0755	0.217643	116.80	0.17	11.2	36.9	33.0	27.5
J1816-1446	0.594500	629.00	0.23	8.6	8.6	11.6	11.0
J1816-1729	0.782313	525.50	1.20	50.0	64.2	52.4	61.7
J1816-2650	0.592885	128.12	1.10	26.0	54.9	50.8	58.7
J1817-1511	0.224604	970.00	0.43	9.1	11.4	12.8	12.1
J1817-3618	0.387017	94.30	2.00	99.0	54.7	121.7	112.4
J1817-3837	0.384487	102.85	—	—	52.5	85.3	76.1
J1818-1519	0.939690	845.00	2.10	22.5	26.1	26.6	24.1
J1818-1541	0.551134	690.00	1.00	17.8	7.1	9.9	10.6
J1819-0925	0.852047	378.00	0.72	21.9	22.4	27.6	24.9
J1819-1008	0.301490	404.00	0.35	14.1	9.2	12.1	11.7

Table A.1 – Continued

Pulsar	P	DM	S ₁₄₀₀	Theory	FFT	Fold	Dir
J1819-1510	0.226539	421.70	0.60	23.4	22.9	22.3	20.5
J1820-0427	0.598076	84.44	6.10	535.6	80.2	608.6	489.3
J1820-0509	0.337321	104.00	0.25	9.7	13.5	19.0	16.6
J1820-1346	0.921460	776.70	2.00	82.5	73.4	80.6	71.6
J1820-1818	0.309905	436.00	1.10	29.7	28.2	29.3	28.3
J1821-1432	1.915131	570.00	0.22	13.5	9.7	13.6	9.2
J1822-0848	0.834839	186.30	0.04	1.7	17.3	23.5	14.8
J1822-1400	0.214771	651.10	0.80	28.6	26.7	25.9	24.4
J1822-2256	1.874269	121.20	2.40	112.5	98.3	112.1	99.9
J1822-4209	0.456512	72.51	1.50	51.3	8.8	30.8	36.0
J1823-0154	0.759777	135.87	0.78	42.9	17.1	20.9	48.5
J1823-1115	0.279829	428.59	3.20	68.9	67.1	80.1	79.5
J1823-1126	1.846534	607.00	0.51	26.8	14.8	20.1	18.3
J1823-1347	0.617107	1044.00	0.41	11.9	9.4	15.2	14.7
J1823-1526	1.625405	611.00	0.47	13.2	8.8	12.4	12.0
J1823-3021A	0.005440	86.83	0.72	19.8	19.1	18.4	18.0
J1823-3021B	0.378596	86.91	0.07	5.1	6.8	10.2	30.7
J1823-3106	0.284054	50.24	2.50	192.6	269.9	338.6	438.3
J1824-1118	0.435759	603.00	1.30	28.5	37.1	31.6	36.9
J1824-1159	0.362492	463.40	0.70	21.5	12.3	14.0	15.6
J1824-1423	0.359394	428.30	0.80	35.8	36.5	35.6	32.9
J1824-1945	0.189335	224.65	4.90	285.5	75.5	397.2	370.8
J1824-2233	1.161743	156.50	0.22	13.8	12.1	17.2	17.7
J1824-2328	1.505875	185.00	0.32	18.2	17.0	33.6	30.1
J1824-2537	0.223320	158.50	–	–	12.8	15.7	16.1
J1825+0004	0.778949	56.62	0.40	2.3	5.8	9.1	7.8
J1825-0935	0.769006	19.38	12.00	720.0	134.2	319.9	335.9
J1825-1446	0.279187	357.00	2.60	98.6	79.7	105.5	123.6
J1826-1131	2.093136	320.58	0.71	15.7	70.4	60.0	69.8
J1826-1334	0.101487	231.00	2.10	39.8	24.7	22.9	22.8
J1826-1526	0.382073	530.00	0.46	15.3	8.0	9.5	9.3
J1827-0750	0.270502	381.00	1.40	55.1	40.4	52.6	44.7
J1827-0934	0.512548	259.20	0.29	8.5	9.9	12.3	11.4
J1827-0958	0.245757	430.00	1.80	23.8	31.3	30.1	25.9
J1828-0611	0.269415	363.20	1.20	64.4	65.9	54.1	46.0
J1828-1057	0.246328	245.00	0.23	3.5	8.6	9.4	8.6
J1828-1101	0.072052	607.40	2.90	60.6	38.6	39.2	45.5
J1828-1336	0.860332	494.70	0.26	5.9	11.1	12.4	14.6
J1828-2119	0.514523	268.00	0.38	13.0	16.3	19.9	19.0
J1829-0734	0.318401	316.80	0.45	26.3	15.7	18.6	16.1
J1829-1751	0.307133	217.11	7.70	202.4	285.1	279.9	328.1
J1830-0131	0.152512	95.70	0.35	7.3	12.4	18.4	15.2
J1830-1059	0.405043	161.50	1.40	111.9	47.0	47.2	43.5

Table A.1 – Continued

Pulsar	P	DM	S ₁₄₀₀	Theory	FFT	Fold	Dir
J1830-1135	6.221553	257.00	1.10	69.7	19.8	26.9	19.5
J1830-1313	0.747188	537.00	0.26	7.8	7.9	10.5	8.4
J1831-0823	0.612133	245.90	0.97	36.7	21.6	25.0	23.4
J1831-0952	0.067267	247.00	0.33	5.4	7.6	8.4	8.7
J1831-1223	2.857941	342.00	1.20	36.9	22.1	31.2	35.8
J1831-1329	2.165679	338.00	0.50	19.5	28.3	31.3	23.9
J1832-0644	0.744295	578.00	0.70	32.9	37.7	37.4	32.3
J1832-0827	0.647293	300.87	2.10	95.5	106.6	105.9	97.2
J1832-1021	0.330354	475.70	1.30	50.5	57.8	53.1	49.0
J1833-0338	0.686704	234.54	2.80	208.6	142.2	146.3	109.9
J1833-0559	0.483459	353.00	0.60	11.5	15.8	16.2	14.9
J1833-0827	0.085284	411.00	3.60	69.8	122.7	109.1	104.3
J1833-1055	0.633640	543.00	0.50	19.9	12.2	14.6	11.8
J1834-0426	0.290108	79.31	5.00	61.3	162.6	288.0	264.9
J1834-0602	0.487914	445.00	0.80	21.6	15.8	15.7	10.2
J1834-0731	0.512980	295.00	1.00	19.3	11.3	14.6	13.5
J1834-0742	0.788354	552.00	0.35	14.7	8.9	12.4	9.5
J1834-1710	0.358306	123.80	1.00	39.8	40.2	45.3	41.6
J1834-1855	1.465656	185.20	0.48	16.8	27.7	25.7	24.1
J1835-0643	0.305830	472.90	1.30	22.1	31.9	30.2	25.6
J1835-0924	0.859192	471.00	0.50	18.4	12.9	16.0	11.9
J1835-0944	0.145347	277.20	0.41	14.8	18.8	18.8	16.4
J1835-0946	0.379536	193.30	0.18	15.1	12.8	19.4	15.4
J1835-1020	0.302448	113.70	1.90	107.8	39.5	39.5	45.5
J1835-1106	0.165907	132.68	2.20	99.9	113.0	89.9	81.3
J1836-0436	0.354237	231.50	1.80	79.8	81.2	74.0	67.3
J1836-1008	0.562711	316.98	3.70	201.7	172.6	167.1	149.7
J1836-1324	0.178756	157.33	0.10	6.6	10.0	13.6	12.6
J1837-0559	0.201063	317.80	0.50	11.7	10.2	12.1	9.5
J1837-0604	0.096294	462.00	0.70	17.3	12.2	14.2	13.4
J1837-0653	1.905809	316.10	2.50	67.5	47.8	80.1	61.9
J1837-1837	0.618358	100.74	0.36	22.0	17.1	19.9	16.9
J1838-0453	0.380831	621.00	0.33	14.7	8.8	12.0	10.7
J1838-1046	1.218354	208.00	0.50	33.0	19.0	25.2	20.3
J1839-0402	0.520940	242.00	0.21	13.0	8.8	12.4	12.7
J1839-0436	0.149461	292.70	0.23	9.5	9.2	12.0	10.8
J1839-0627	0.484914	88.50	0.29	7.9	6.0	9.5	21.1
J1839-0643	0.449548	497.90	1.40	53.9	49.5	46.7	38.2
J1839-0905	0.418969	348.00	0.16	7.7	8.0	11.7	10.5
J1839-1238	1.911428	169.80	0.37	19.8	19.3	25.8	20.1
J1840-0559	0.859368	321.70	0.31	15.0	6.2	9.3	16.5
J1840-0809	0.955672	349.80	2.30	102.8	35.0	36.6	36.9
J1840-0815	1.096440	233.20	1.40	67.2	75.0	87.3	77.1
J1840-0840	5.309377	272.00	1.00	44.5	37.0	60.2	139.8

Table A.1 – Continued

Pulsar	P	DM	S ₁₄₀₀	Theory	FFT	Fold	Dir
J1840-1207	0.754470	302.30	0.22	17.7	27.5	33.3	27.3
J1841-0157	0.663321	475.00	0.81	28.9	46.8	47.1	41.9
J1841-0345	0.204068	194.32	1.40	56.9	31.7	31.7	28.4
J1841-0425	0.186149	325.49	2.60	139.8	140.1	127.3	79.5
J1842-0359	1.839944	195.98	4.40	45.8	86.8	116.8	89.9
J1842-0415	0.526682	188.00	0.35	15.0	8.5	10.8	9.2
J1842-0612	0.564475	485.00	0.54	13.7	15.2	14.1	14.6
J1842-0905	0.344643	343.30	0.81	50.3	31.6	32.2	26.7
J1843-0355	0.132314	797.60	0.80	14.3	11.1	10.8	10.8
J1843-0459	0.754963	444.10	1.70	51.8	45.8	45.1	38.1
J1843-0806	0.536414	215.80	0.36	11.5	10.0	14.1	20.3
J1843-1113	0.001846	59.96	0.10	2.1	15.4	20.2	20.0
J1843-1507	0.583550	215.50	0.17	13.2	19.3	19.3	17.6
J1844-0310	0.525049	836.10	0.53	19.7	16.4	19.1	17.6
J1844-0433	0.991027	123.16	1.10	82.4	69.1	74.4	67.7
J1844-0538	0.255699	412.80	2.20	74.9	59.9	117.7	106.8
J1845-0434	0.486751	230.80	1.60	72.6	140.0	116.6	104.0
J1845-0545	1.092348	315.90	0.47	31.5	22.6	27.1	20.1
J1845-0743	0.104695	281.00	2.70	69.3	50.2	47.5	44.0
J1845-1114	0.206220	206.70	0.52	30.4	35.8	35.2	32.6
J1846-0749	0.350110	388.30	0.35	17.9	24.9	29.4	34.1
J1847-0438	0.957991	229.00	0.50	24.4	23.4	30.7	27.1
J1847-0605	0.778164	207.90	0.80	30.7	9.0	14.3	37.1
J1848-0511	1.637129	418.00	0.40	9.5	16.3	17.8	14.7
J1848-0601	0.225004	496.60	0.24	4.7	9.7	11.4	9.6
J1848-1150	1.312218	163.40	0.21	13.4	19.0	17.1	15.7
J1848-1414	0.297770	134.47	–	–	27.6	24.4	22.1
J1848-1952	4.308190	18.23	–	–	54.6	109.6	103.0
J1849-0317	0.668408	42.90	0.70	32.8	51.2	46.9	37.3
J1852-0635	0.524151	171.00	5.90	62.0	61.0	90.7	76.8
J1852-2610	0.336337	56.81	1.40	89.6	65.6	63.3	58.5
J1854-1421	1.146595	130.40	–	–	92.4	128.0	96.4
J1855-0941	0.345401	151.99	0.48	17.2	37.9	33.9	30.6
J1856-0526	0.370483	130.50	0.40	13.8	20.3	21.4	19.3
J1857-1027	3.687219	108.90	–	–	38.6	100.5	84.5
J1900-2600	0.612209	37.99	13.00	405.1	68.5	410.6	382.5
J1901-0906	1.781928	72.68	3.10	298.1	59.4	155.1	148.0
J1901-1740	1.956858	24.40	–	–	18.2	24.2	21.9
J1903-0632	0.431887	195.61	–	–	53.4	46.5	42.0
J1904-1224	0.750808	118.23	–	–	15.5	20.0	22.1
J1918-0642	0.007646	26.55	0.58	11.1	56.3	50.7	46.5

Table A.2: Weak pulsars only detected by direct folding. The columns of the table are: pulsar name based on J2000 coordinates, pulsar spin period (P), dispersion measure (DM), flux density at an observing frequency of 1400 MHz (S_{1400}), theoretical S/N (Theory) and folded S/N when using published values (Dir).

Pulsar	P	DM	S_{1400}	Theory	Dir
J0746-4529	2.791025	134.57	0.20	18.2	9.7
J0901-4624	0.441995	198.80	0.46	26.7	9.4
J0934-4154	0.570409	113.79	—	—	7.1
J0957-5432	0.203557	226.10	0.18	9.6	8.6
J1002-5559	0.777501	426.00	0.12	6.5	6.8
J1006-6311	0.835797	195.99	—	—	6.9
J1021-5601	0.670026	212.00	0.37	7.0	6.5
J1028-5819	0.091403	96.53	0.36	60.9	10.7
J1052-5954	0.180592	491.00	0.15	6.0	6.5
J1055-6022	0.947558	590.00	0.16	6.1	6.1
<hr/>					
J1055-6236	0.448635	149.70	0.12	8.1	6.7
J1115-6052	0.259777	228.20	0.38	14.9	9.9
J1130-5826	0.162323	261.10	0.18	7.6	9.8
J1156-5707	0.288409	243.50	0.19	13.1	9.9
J1201-6306	0.592136	683.00	0.13	6.5	8.1
J1216-6223	0.374047	786.60	0.15	7.2	8.2
J1233-6344	0.756892	495.00	0.07	6.0	7.2
J1235-6354	0.256778	439.90	0.16	4.8	8.4
J1248-6344	0.198335	433.30	0.12	3.8	6.5
J1302-6313	0.967846	500.00	0.18	6.2	8.0
<hr/>					
J1309-6526	0.398292	340.00	0.15	10.2	8.7
J1321-5922	1.279058	383.00	0.19	14.1	8.5
J1337-6306	0.207953	777.70	0.11	4.3	7.0
J1354-6249	2.951938	254.00	0.24	10.9	8.0
J1403-7646	1.306198	100.60	—	—	9.3
J1406-6121	0.213075	542.30	0.36	7.0	9.0
J1418-5945	1.672596	369.00	0.18	9.8	8.1
J1425-5759	0.707868	325.00	0.09	6.7	8.1
J1429-5935	0.763915	456.70	0.11	5.1	5.9
J1514-5925	0.148796	194.10	0.27	10.7	8.4
<hr/>					
J1515-5720	0.286646	482.00	0.20	4.5	8.5
J1518-5415	0.214925	167.20	0.08	6.7	6.9
J1529-5355	0.891265	292.00	0.37	8.8	8.4
J1529-5611	0.822249	149.00	0.14	4.4	7.1
J1531-4012	0.356849	106.65	—	—	8.0
J1537-5153	1.528124	93.00	0.07	4.5	7.0
J1538-5732	0.341213	152.70	0.35	6.8	7.8
J1539-5521	1.004958	380.00	0.14	6.2	8.1
J1540-5736	0.612916	304.50	0.24	7.9	7.6
J1542-5303	1.207568	265.70	0.35	9.7	9.6

Table A.2 – Continued

Pulsar	P	DM	S ₁₄₀₀	Theory	Dir
J1543-5013	0.644255	211.00	0.17	10.1	8.8
J1601-5335	0.288457	194.60	0.22	7.2	7.5
J1625-4904	0.460339	684.80	0.20	7.1	7.3
J1632-4509	1.046810	412.00	0.16	6.1	7.5
J1636-4440	0.206649	449.00	0.38	8.5	7.3
J1637-4816	0.837365	738.00	0.74	9.5	8.3
J1640-4951	0.739099	411.40	0.15	9.1	11.7
J1643-4505	0.237383	484.00	0.28	6.5	10.0
J1654-2713	0.791822	92.31	0.10	5.0	10.7
J1657-4432	0.609607	375.30	0.38	11.8	7.8
<hr/>					
J1702-3932	0.390328	530.00	0.30	7.9	9.4
J1702-4428	2.123506	395.00	0.38	12.4	11.1
J1703-1846	0.804341	49.55	0.70	29.1	18.1
J1706-3839	0.586287	626.00	0.20	6.2	9.2
J1706-4310	0.616979	656.10	0.28	12.5	8.7
J1707-44	5.763752	380.00	—	—	11.8
J1708-3827	1.225782	788.00	0.42	11.6	9.4
J1709-3841	0.586986	356.00	0.31	9.6	10.8
J1718-4539	0.590473	254.00	0.08	5.5	9.9
J1722-4400	0.218554	219.30	0.22	9.6	8.2
<hr/>					
J1726-3530	1.110132	727.00	0.30	4.8	8.0
J1728-3733	0.615538	281.50	0.19	11.6	10.8
J1731-3123	0.753048	354.00	0.29	10.4	7.2
J1733-3030	0.362052	636.00	0.20	6.9	7.8
J1738-2955	0.443398	223.40	0.29	7.8	8.4
J1738-3316	0.730373	273.00	0.55	7.0	8.7
J1741-2719	0.346797	361.90	0.20	6.2	9.9
J1741-2945	0.223558	310.30	0.60	11.2	10.1
J1742-3957	1.016349	186.00	0.14	3.1	8.3
J1745-2229	1.160593	299.00	0.13	7.7	9.2
<hr/>					
J1751-2516	0.394836	556.00	0.22	5.2	7.7
J1753-2240	0.095138	158.60	0.15	6.4	7.0
J1755-2534	0.233541	590.00	0.17	3.6	5.3
J1758-2630	1.202893	328.00	0.41	13.5	6.7
J1759-1903	0.731505	467.00	0.16	5.7	7.1
J1802+0128	0.554262	97.97	—	—	8.8
J1803-1920	0.443649	436.10	0.27	7.1	9.1
J1805-2447	0.661402	269.00	0.27	13.3	7.6
J1809-0743	0.313886	240.70	0.29	10.4	7.7
J1809-1850	1.124481	598.00	0.20	6.3	7.2
<hr/>					
J1814-0618	1.377868	168.00	0.58	20.0	15.8
J1815-1738	0.198436	728.00	0.25	3.0	10.3
J1815-1910	1.249924	547.80	0.32	12.5	7.7
J1818-1116	0.544800	422.00	0.50	14.0	7.9

Table A.2 – Continued

Pulsar	P	DM	S₁₄₀₀	Theory	Dir
J1823-1807	1.636792	330.00	0.39	23.1	9.3
J1831-1423	0.507945	352.00	0.19	5.7	8.4
J1832-28	0.199300	127.00	–	–	9.9
J1835-0522	1.087749	456.00	0.23	8.3	10.1
J1836-0517	0.457245	564.00	0.15	6.5	7.1
J1839-0321	0.238778	449.10	0.27	11.6	8.0
J1839-0459	0.585319	243.00	0.30	15.4	9.1
J1840-1122	0.940962	311.00	0.13	10.0	6.5
J1843-0702	0.191614	228.10	0.17	8.2	8.2
J1844-0244	0.507722	429.00	0.87	2.1	6.3
J1845-0316	0.207636	500.00	0.35	7.1	9.0
J1845-1351	2.618918	197.40	0.33	29.6	9.4